A Novel Approach to High-Speed Electrical Impedance Tomography with Frequency Division Multiplexing : From Theoretical Development to Industrial Application

Mathieu Darnajou

École Doctorale : Physique et Sciences de la Matière (ED352)

C.E.A. Cadarache
Laboratoire de Thermohydraulique et d'Hydromécanique
analytique du Coeur et des Circuits

THÈSE DE DOCTORAT

pour obtenir le grade de

DOCTEUR de l'ÉCOLE CENTRALE de MARSEILLE

Discipline : Physique, Instrumentation

A Novel Approach to High-Speed Electrical Impedance Tomography with Frequency Division Multiplexing

From Theoretical Development to Industrial Application

par

DARNAJOU Mathieu

Directeur de thèse : BOURENNANE Salah
Co-directeur : RICCIARDI Guillaume
Co-Encadrant : BELLIS Cédric

Soutenue le 1er octobre 2020
devant le jury composé de :

M. Takei	Professeur, Chiba University	Rapporteur
H-M. Prasser	Professeur, ETH Zürich	Rapporteur
S. Mylvaganam	Professeur, University College of Southeast Norway	Examinateur
N. Polydorides	Professeur, University of Edinburgh	Examinateur
U. Hampel	Professeur, Helmholtz-Zentrum Dresden-Rossendorf	Examinateur
M. de Buhan	Chargée de Recherche CNRS, Uni. Paris Descartes	Examinatrice
H. Schmidt	Head of PKL and INKA, Framatome GmbH	Invité
S. Bourennane	Professeur, Ecole Centrale Marseille	Directeur de thèse
G. Ricciardi	Expert senior, C.E.A.	Co-directeur
C. Bellis	Chargé de Recherche CNRS, LMA	Co-encadrant

A
Abstract

The investigation of quickly-evolving flow patterns in high-pressure and high-temperature flow rigs is crucial due to inherent hazards. There is a dire need for a high-speed, non-intrusive imaging technique to identify characteristic flow phenomena to alleviate these hazards. Electrical Impedance Tomography (EIT) enables reconstruction of the admittivity distribution of the flowing medium(s), facilitating the characterisation of its/their flow.

Apart from the development of the Data Acquisition (DAQ) system, a crucial interest is the design of the detector device which contains a ring of electrodes, tangential with the inner surface of the pipe. The main concern is the determination of the electrode length to maximise the energy at their surface.

A numerical simulation was carried out to quantify the leakage of current which depends on the electrode area and the isolation layer thickness between the up-stream and down-stream conductive pipes and the electrodes. A maximum of the measurement energy was found for electrodes with 84% of the length of the EIT device. Another interest also developed in this work is the counterintuitive behaviour of the sensitivity map of measurements. This behaviour is validated by an independent computational method.

The requirement for images at high frame-rates led to simultaneous voltage excitations over electrodes on the periphery of the flow associated to Frequency Division Multiplexing (FDM), doped ONe Excitation for Simultaneous High-speed Operation Tomography (ONE-SHOT) method. A first approach demonstrates the possibility of the full implementation of simultaneous excitations and measurements strategies for EIT, which maximise the number of measurements for 16 electrodes. These preliminary results confirm the relevance and the feasibility of simultaneous Multi-Frequency (MF) excitations and measurements in EIT as a means to significantly increase the imaging rate.

This work details the proposed method and the signal generation/acquisition firmware based on a Field Programmable Gate Array (FPGA) DAQ system. The hardware and software integration and the signal processing involved in implementing the ONE-SHOT method for EIT are also detailed. It is shown that the 240 simultaneously generated signals are successfully discriminated and used for image reconstruction, at a rate up to 3906 frames per second (fps). The associated signal-to-noise ratio varies in the 55.6 dB–

69.1 dB range, depending on the generated frequency in the range of 3.906 kHz–468.7 kHz. The ONE-SHOT method were successfully operated in two experiments to measure flow characters in a Loss-Of-Coolant Accident (LOCA) in the hot leg of a Pressurised Water Reactor (PWR).

Finally, the novel Continuous Overlapping operations with Linear trigonometric Response ANalysis for EIT (COLTRANE) method is introduced and implemented for a 16 and a 32 electrodes EIT sensor in a FPGA based DAQ system. This novel method uses simultaneous trigonometric excitation patterns to increase the DAQ rate of EIT up to 32 250 fps. These novel ultra high rate systems open EIT toward new domains of application.

Keywords : Electrical Impedance Tomography, Frequency Division Multiplexing, FPGA, ONE-SHOT, COLTRANE, Signal Processing, Two-phase Flow.

Résumé

L'analyse des régimes d'écoulement évoluant rapidement dans des plateformes hydrauliques à haute pression et haute température est cruciale du fait de certains risques intrinsèques. Il est urgent de développer une technique d'imagerie non intrusive et à haut rendement d'images pour identifier les phénomènes d'écoulements caractéristiques et palier ces risques. La Tomographie par Impédance Electrique (EIT) permet de reconstruire la distribution de l'admittance du ou des milieu(x) en écoulement, facilitant sa/leur caractérisation.

Hormis le développement du système d'Acquisition de Données (DAQ), un intérêt crucial concerne la conception du détecteur lui-même, qui contient un anneau d'électrodes, tangentiel à la surface interne du conduit hydraulique. La principale préoccupation est de déterminer la longueur des électrodes qui maximise leur énergie de surface.

Une simulation numérique a été menée pour quantifier les fuites de courant qui dépendent de la surface des électrodes, ainsi que de l'épaisseur d'isolation entre les électrodes et les brides conductrices en amont et en aval. Un maximum de l'énergie de mesure a été trouvé pour des électrodes dont la longueur est de 84% la longueur du détecteur EIT. Un autre intérêt également développé dans ce travail concerne le comportement contre-intuitif de la carte de sensibilité des mesures. Ce comportement est validé par une méthode de calcul indépendante.

La nécessité d'acquérir des images à haut taux a amené à considérer des excitations simultanées en voltage imposées sur les électrodes en périphérie de l'écoulement. Ces excitations sont associées au Multiplexage en Division de Fréquences (FDM) selon la méthode ONE-SHOT (ONe Excitation for Simultaneous High-speed Operation Tomography). Une première approche démontre la possibilité d'une implémentation complète de stratégies d'excitations et de mesures simultanées pour l'EIT, qui maximise le nombre de mesures pour 16 électrodes. Ces résultats préliminaires confirment la pertinence et la faisabilité d'excitations et de mesures simultanées et Multi-Fréquentielles (MF) en EIT comme moyen pour augmenter significativement le taux d'images.

Ce travail détaille la méthode proposée ainsi que le système DAQ contenant un firmware pour la génération/acquisition des signaux basé sur un Réseau Logique Programmable (FPGA). L'intégration des logiciels et du matériel informatique ainsi que le traitement du signal impliqué dans l'implémentation de la méthode ONE-SHOT pour l'EIT est éga-

lement détaillée. Il est démontré que 240 signaux simultanés ont été générés, discriminés avec succès et utilisés pour reconstruire des images, au taux de 3906 images par secondes (fps). Le signal-sur-bruit associé varie de 55.6 dB à 69.1 dB, en fonction de la fréquence générée de 3,906 kHz à 468,7 kHz. La méthode ONE-SHOT a été exploitée avec succès dans deux expériences pour mesurer les caractéristiques des écoulements dans la branche chaude d'un Réacteur à Eau Pressurisée (PWR) en scénario d'Accident de Fuites de Réfrigérant Primaire (LOCA).

Finalement, la nouvelle méthode COLTRANE (Continuous Overlapping operations with Linear Trigonometric Response ANalysis for EIT) est introduite et implémentée dans un système DAQ basé sur FPGA pour des détecteurs EIT de 16 et 32 électrodes. Cette nouvelle méthode utilise des patrons d'excitations trigonométriques et simultanées dans le but d'augmenter le taux d'acquisition jusqu'à 32 250 fps. Ces nouveaux systèmes à taux ultra rapides ouvrent l'EIT vers de nouveaux domaines d'application.

Mots clés : Tomographie par Impédance Electrique, Multiplexage en Division de Fréquences, FPGA, ONE-SHOT, COLTRANE, Traitement du Signal, Écoulement Diphasique.

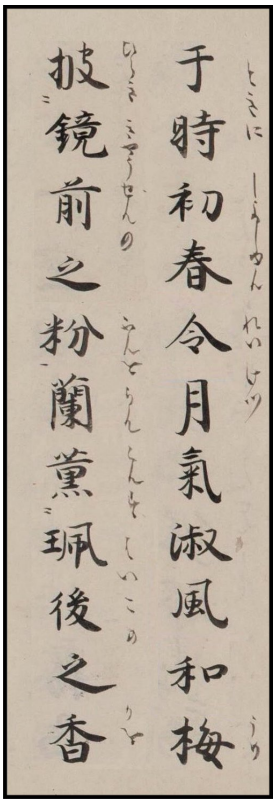

時は令月、
空気は美しく、風は和やかで、
梅は鏡の前の美人が白粉で装うように花咲き、
蘭は身を飾る衣に纏う香のように薫らせる。

万葉集、天平宝字三年

Voici le beau mois du début de printemps,
L'air est doux et la brise légère,
Le prunier a déployé ses fleurs blanches comme poudre d'une belle à son miroir,
L'orchidée répand une odeur suave comme poche à parfums.

Man'yōshū, 759

夏子と新之へ。

À Natsuko et à Nino.

A

Acknowledgments

Most of this thesis have been written during the lock down due to the COVID-19. At first, I would like to thank all the essential workers and in particular the healthcare professionals for their investment during the crisis.

I would like to express my sincere gratitude to Professor Masa Takei and to Professor Horst-Michael Prasser for reviewing this thesis. I would like to acknowledge the committee members, Professor Nick Polydorides, Professor Uwe Hampel and Dr. Maya de Buhan for accepting to examine my work. I wish to show my gratitude to Dr. Holger Schmidt and all the PKL team for our successful collaboration. Last but not least, I would like to pay my special regards to Professor Saba Mylvaganam for your support in many ways.

Un immense merci à mon encadrant CEA, Guillaume Ricciardi, pour ces années de bonheur réunissant bien-être et dépassement de soi. Merci également de partager tes intuitions brillantes, de l'idée du sujet de cette thèse jusqu'aux travaux futurs. Un très grand merci à mon co-encadrant Cédric Bellis pour ta grande disponibilité et ton aide précieuse tout au long de cette thèse. Enfin, j'adresse de chaleureux remerciements à mon directeur de thèse, Salah Bourennane, pour ton aide tout au long de ces trois années. J'ai eu une chance exceptionnelle de travailler avec vous trois.

Je remercie également toute l'équipe des laboratoires LTHC et LETH pour votre bonne humeur permanente. C'était un plaisir de travailler à vos côtés. Je souhaite en particulier remercier Marie-Hélène Arpaia pour toute ton aide.

My sincere thanks to all the former and current students of the LTHC for the stimulating discussions and for all the fun we have had in the last three years. I would like to thanks particularly my research partner Chunhui Dang for your support, advises and friendship. I will closely follow your future career and sincerely hope to work with you again. Many thanks to the former student interns, Ying Zhuang and Aleksander Tokle Poverud, for their support and their great interest in this project.

Merci aux ingénieurs de National Instruments, en particulier Yacine Addou et Salah Ismail pour leur grande aide dans ce projet. Je tiens a remercier particulièrement Eric Payen qui m'a aidé à poser les premières briques.

日本の友人に深く感謝申し上げます。特に川崎誉氏、原永千尋氏、橋本優憲

氏、Driss Harass氏、Ziane Izri氏、三明萌美氏、佐瀬和也氏、佐藤千尊氏、野口昭代氏、また九州かフランスでで会うことを本当に楽しみにしております。

Merci aux amis de Montréal, en particulier Etienne St Pierre et Fabio Lefebvre que j'ai très hâte de retrouver.

Merci aux amis de Grenoble, Massimiliano Comin, Thibault Dabout, Hugo Muh, Xavier Cuttat, Grégoire Ledoux et bien d'autres. Je suis heureux de vous retrouver ponctuellement et d'apprécier notre amitié inchangée. Je me dois également de remercier Jonathan Gigmes, Nathalie et Philippe Bellaïche, Bernard Ciancia, Maurice Besson ainsi que Corinne Petiot.

Un grand Merci à toute la famille Coulet, en particulier Maiko et Jean-François pour votre accueil dans la région d'Aix et les innombrables moments de bonheur partagés ensemble. Merci à Bruno-Marie Mauviel et à son équipe de bons-vivants pour leurs enseignements spirituels et gustatifs. Enfin merci à Christine Legrand, Georges Pascal et Romain Boschel, pour partager votre amour de la nature.

Merci aux nombreux jazzmen avec qui j'ai pu jouer durant ces trois années. Merci en particulier à Jean-Gabriel Lapierre, Eric Le Cardinal et Florence Tu Hong pour leurs enseignements précieux, il faut travailler dur pour goûter à la liberté. Enfin merci au docteur Jujube et à ses noyaux, Gilles Barges, Florian Sidobre et Julien Grossi. Il n'y a plus de doute à avoir, c'est bien moi le docteur !

Merci à tous les marins avec qui j'ai navigué sur Ohana.

Merci aux amis du club d'escalade de l'Apéro Club Meyrarguais en particulier Yann Clavé, Gilou Vallier, Pierre Cherici, Alexis Gola, Emmanuel Freydier, Pascal Belin et Matthieu Rock. Je passe chaque semaine un moment exceptionnel avec vous.

Je tiens à remercier particulièrement la famille Begic pour votre précieuse amitié et votre générosité.

日本の家族に深く深謝しております。いつも日本で温かいおもてなしをありがとうございます。

Enfin un gigantesque merci à ma famille pour m'encourager sans limite dans chacun de mes choix.

MD

Contents

Abstract 5

Résumé 7

Acknowledgments 15

Contents 19

Nomenclature 25

Acronyms 31

Introduction 35
I.1 Scientific contribution highlights . . . 39
I.2 Notes and publications . . . 39
I.3 Context of the present work . . . 41
I.4 Thesis Organisation . . . 42

1 Electrical Impedance Tomography 45
1.1 Tomographic techniques . . . 47
1.1.1 X-Ray tomography . . . 48
1.1.2 Single Photon Emission Computed Tomography (SPECT) . . . 49
1.1.3 Positron Emission Tomography (PET) . . . 50
1.1.4 Magnetic Resonance Imaging (MRI) . . . 51
1.1.5 Ultrasonic tomography . . . 53
1.2 Electrical Tomography (ET) . . . 54
1.2.1 Electromagnetism in material . . . 55
1.2.2 Magnetic Induction Tomography (MIT) . . . 56
1.2.3 Electrical Impedance Tomography (EIT) . . . 57
1.2.4 Electrical Capacitance Tomography (ECT) . . . 59
1.3 EIT measurement and image reconstruction . . . 60
1.3.1 Excitation and measurement strategies . . . 61
1.3.2 Measurement duration . . . 63
1.3.3 Continuum model of the inverse problem . . . 64
1.3.4 Discretisation and resolution . . . 67

1.4 Towards high frame rate Electrical Impedance Tomography (EIT) imaging 71
1.4.1 Multiplexing . . . 71
1.4.2 Time Division Multiplexing (TDM) . . . 72
1.4.3 High rate ET based on TDM . . . 73
1.4.4 Frequency Division Multiplexing (FDM) . . . 75
1.4.5 Multi-Frequency (MF) and FDM for high rate ET . . . 76

2 EIT System - Electromagnetic Modeling and Simulations 81
2.1 Simulation softwares . . . 84
2.1.1 EIT reconstruction software . . . 84
2.1.2 Finite element method in C++ . . . 84
2.1.3 Weak formulation in a finite element space . . . 85
2.2 EIT images with several configurations . . . 86
2.2.1 Adequate number of electrodes . . . 86
2.2.2 Mesh generation . . . 87
2.2.3 Effects of noise on simulated EIT data . . . 91
2.3 Leakage of current . . . 93
2.3.1 The utilisable energy . . . 94
2.3.2 Quantification of the leakage of current . . . 97
2.3.3 Maximum of utilisable energy . . . 100
2.3.4 The role of the form factor $\mathcal{F}$ . . . 101
2.4 Sensitivity maps . . . 103
2.4.1 Continuous formulation of the sensitivity . . . 104
2.4.2 Computation of the sensitivity map . . . 106
2.4.3 Reconstruction with locally imposed conductivity variations . . . 107
2.4.4 Sensitivity of the full-scan strategy . . . 108
2.5 Effects of the leakage of current on the sensitivity . . . 111
2.5.1 Continuous formulation of the sensitivity map with leakage of current 111
2.5.2 3D simulations . . . 112

3 Frequency Division Multiplexing for EIT 117
3.1 Excitation and measurement strategy with FDM . . . 119
3.1.1 Need for increasing the imaging rate . . . 119
3.1.2 Introduction to simultaneous excitations in EIT . . . 120
3.1.3 The discrete Fourier transform . . . 122
3.2 The ONE-SHOT method . . . 127
3.2.1 General simultaneous excitation pattern . . . 128
3.2.2 Simultaneous excitation pattern for 16 electrodes . . . 129
3.2.3 Excitation frequencies based on the measurement time window . . . 129
3.2.4 Continuous formulation of the sensitivity map of the ONE-SHOT method . . . 131
3.3 The Data Acquisition (DAQ) system . . . 132
3.3.1 Load specifications and proposed DAQ system . . . 132

3.3.2 The EIT sensor . . . 134
3.3.3 The Printed Circuit Board (PCB) . . . 137
3.3.4 The DAQ controller . . . 138
3.3.5 Practical excitation and measurement strategy . . . 139
3.4 Preliminary experimental results . . . 140
3.4.1 Analysis of the error propagation . . . 141
3.4.2 Raw data . . . 143
3.4.3 Noise measurement . . . 146
3.4.4 Image reconstruction from 16 datasets . . . 147

4 Software development for the ONE-SHOT method 151
4.1 Analog signal generation and acquisition logics . . . 154
4.1.1 Excitation frequencies . . . 154
4.1.2 Excitation amplitudes . . . 155
4.1.3 Analog signal generation logics . . . 156
4.1.4 Analog signal acquisition logics . . . 157
4.2 Output data format . . . 160
4.2.1 Standard EIT data . . . 160
4.2.2 Data from FPGA based ONE-SHOT method . . . 161
4.2.3 Sign of the signal magnitudes . . . 163
4.2.4 Spectral analysis of the impedance . . . 164
4.3 The ONE-SHOT method software . . . 165
4.4 Experimental results with static flows . . . 168
4.4.1 Static homogeneous medium . . . 168
4.4.2 Static inhomogeneous medium . . . 169
4.4.3 Contact impedance . . . 171

5 Application to accidental scenarios in nuclear power-plants 175
5.1 The Lost Of Coolant Accident (LOCA) in the hot leg . . . 177
5.1.1 Accidental scenarios and design of nuclear power-plants . . . 177
5.1.2 The Large LOCA Break (LBLOCA) scenario . . . 180
5.1.3 Electrical conductivity in the hot leg during LOCA . . . 180
5.1.4 Simulation of EIT measurements of accidental flows . . . 182
5.2 Fastly evolving flows experiment . . . 184
5.2.1 Experimental setup . . . 184
5.2.2 Modelling of Small LOCA break (SBLOCA) . . . 185
5.2.3 Modelling of Large LOCA break (LBLOCA) . . . 189
5.2.4 Flow patterns experiments . . . 189
5.3 High pressure and high temperature flows experiment . . . 192
5.3.1 Primary circuit modelling flow rigs . . . 192
5.3.2 The EIT sensor for high pressure and high temperature measurements 194
5.3.3 Dimensional variations due to temperature and pressure . . . 199
5.3.4 EIT measurements on the Benson loop . . . 200

6 The COLTRANE method **203**
6.1 Excitation strategy and software implementation . . . 205
6.1.1 General Spatial trigonometric excitation pattern . . . 205
6.1.2 General simultaneous trigonometric excitation pattern . . . 206
6.1.3 Practical implementation . . . 206
6.2 Measurement and output data format . . . 207
6.2.1 Measurement with FDM . . . 207
6.2.2 Practical excitation and measurement strategy . . . 208
6.2.3 Data format . . . 209
6.2.4 Sign of the signal magnitudes . . . 210
6.2.5 Experimental results from the COLTRANE method . . . 211
6.3 Implementation of the COLTRANE method for 32 electrodes . . . 213
6.3.1 Evolution of the hardware . . . 214
6.3.2 Excitation setting and data format . . . 216
6.3.3 Implementation and execution issues . . . 217

Conclusion **221**
C.1 Research prospects . . . 225

List of Figures **229**

List of Tables **238**

Appendix **241**

I Functional and Fourier Spaces **243**
I.1 Functional spaces . . . 243
I.2 Fourier spaces . . . 244

II `EIDORS` Script **247**
II.1 `EIDORS V.3` features . . . 247
II.2 Script to simulate EIT measurements . . . 248

III `FreeFEM++` scripts **251**
III.1 `FreeFEM++` features . . . 251
III.2 Script for leakage simulation and energy estimation . . . 253
III.3 Script for generalisation with the form factor . . . 257
III.4 Script to estimate the sensitivity map of a single EIT measurement . . . 262
III.5 Script for the hand reconstruction of the sensitivity map . . . 264
III.6 Script for 3D simulations . . . 268

IV `MATLAB` scripts **275**
IV.1 Computation of the ONE-SHOT method excitation pattern coefficients . . . 275
IV.2 Script for image reconstruction inputs . . . 276

IV.3 Computation of the COLTRANE method sign matrix 278

V User guide of the ONE-SHOT method LabVIEW software **281**
V.1 Details of the HOST VI 282
V.2 Details of the FPGA AO 296
V.3 Details of the FPGA AI 306
V.4 Details of the FPGA FFT 312
V.5 Compilation of the FPGA VI 318

VI User guide of the COLTRANE method LabVIEW software **323**
VI.1 Details of the FPGA AO 323
VI.2 Compilation of the COLTRANE method software FPGA VI 328

Bibliography **331**

Nomenclature

A	Signal amplitude [V]
$\mathcal{A}$	Forward map
$\boldsymbol{B}(\boldsymbol{x}, t)$	Magnetic flux density field [Wb]
C^∞	Vector space of infinitely derivable functions
C_e	Double layer capacitance [F]
D_n^k	Elements of the data matrix
$\boldsymbol{D}$	Data matrix
$\boldsymbol{D}(\boldsymbol{x}, t)$	Electric displacement field [C.m^{-2}]
$\mathcal{D}$	Inner diameter of the pipe [m]
$\widetilde{\boldsymbol{D}}$	Signed data matrix
$E_{1,2}^{exc}$	Excitation electrodes 1 and 2
$E_{1,2}^{meas}$	Measurement electrodes 1 and 2
E_n	n^{th} electrode
$\boldsymbol{E}(\boldsymbol{x}, t)$	Electric field [V.m^{-1}]
$\mathbb{E}$	Set of strictly positive even numbers
$\mathcal{E}_{\Omega_E}$	Energy of the subsystem Ω_E [J]
$\mathcal{E}_\Omega$	Energy of the system Ω [J]
$\mathcal{E}_\Omega$	Total energy in the system Ω [J]
$\mathcal{E}_{source}$	Source energy [J]
$\mathcal{F}$	Form factor
f	Frequency [Hz]
f^{exc}	Excitation frequency [Hz]
f^{meas}	Measurement frequency [Hz]
f_0	Fundamental frequency [Hz]

f_1	Lowest frequency band [Hz]
f_N	Highest frequency [Hz]
f_i	i^{th} harmonics of f_1 [Hz]
f_m	Time frequency of a given trigonometric pattern of spatial frequency m [Hz]
f_{DAQ}	Data acquisition frequency [Hz]
f_{Nyq}	Nyquist limit [Hz]
$H^{\pm 1/2}$	Space of traces of functions with finite energy
$H^k(\Omega)$	Sobolev vector space of k^{th} derivative finite integral
$\boldsymbol{H}(\boldsymbol{x}, t)$	Magnetic field strength [T]
I_Γ	Leaking current from the grounded surfaces [A]
I_n	Current flowing through the n^{th} electrode [A]
I_n	Current injected from the n^{th} electrode [A]
$Im_n(\boldsymbol{k})$	Imaginary part of $\hat{V}_n^{meas}(t)$
$\boldsymbol{I}(\boldsymbol{x})$	Continuous Neumann boundary conditions
$\boldsymbol{I}_{meas}$	Current in the probing circuit (*outside* Ω) [A]
J_E	Current passing through one unit of the electrode surface [A.m^{-2}]
J_{leak}	Leaking current passing through one unit of the grounded surface [A.m^{-2}]
$\boldsymbol{J}(\boldsymbol{x}, t)$	Current density field [A.m^{-2}]
$\boldsymbol{j}(\boldsymbol{x})$	Current density [A.m^{-2}]
$\mathcal{J}$	Jacobian precomputed matrix
k	Fourier coefficient
L^2	Banach space of up-bounded squared functions
L^∞	Vector space of up-bounded functions
$\mathcal{L}_{EIT}$	Length of the electrical impedance tomography sensor [m]
$\mathcal{L}_E$	Length of the electrodes [m]
$\mathcal{L}_{TOT}$	Length of Ω on the z-axis [m]
M	Number of measurements
$M'_n(k)$	Magnitude of Φ_n with the addition of noise [V]
$M^0_n(k)$	Magnitude of $\hat{V}_n^{meas}(t)$ without any excitation [V]
$M_n(k)$	Magnitude of $\hat{V}_n^{meas}(t)$ [V]

m	Spatial frequency [m^{-1}]
N	Total number of independent excitations
$\boldsymbol{n}$	Unitary vector pointing outward at $\boldsymbol{x} \in \partial\Omega$
n	Electrode label
n_e	Number of electrodes
n_p	Number of periods
$\mathbb{O}$	Set of positive odd numbers
P	Number of points in fast Fourier transform sequence
p	Discrete time [s]
R	Resistance in the probing circuit (*outside* Ω) [Ω]
R^{FDM}	Frame rate with FDM [s^{-1}]
R^{TDM}	Frame rate with TDM [s^{-1}]
R_b	Bulk resistance [Ω]
R_e	Charge transfert resistance [Ω]
$Re_n(\boldsymbol{k})$	Real part of $\hat{V}_n^{meas}(t)$
$\mathcal{R}_\sigma$	Neumann-to-Dirichlet operator
S	Mass flow rate [$\mathrm{kg.s}^{-1}$]
S_n	Surface area of the n^{th} electrode [m^2]
S_{Γ_i}	Surface of the grounded pipes upstream and downstream [m^2]
S_Γ	Total surface of all grounded surfaces [m^2]
S_{FDM}	Number of data points with frequency division multiplexing
S_{single}	Number of data points per measurement
$S_{exc_{1,2}}$	Surfaces of the excitation electrodes 1 and 2 [m^2]
$\boldsymbol{S}^n$	Discrete approximation of the trigonometric functions
$\boldsymbol{S}_l^n$	Excitation signal pattern
$\mathcal{S}(\boldsymbol{x})$	Sensitivity coefficient
s	Standard deviation
T	Period of $\tilde{x}(t)$ [s]
$T_\alpha(\boldsymbol{m})$	Regularisation term
T_k	Triangle in a finite element space

t	Continuous time [s]
t_f	Time duration of a frame measurement [s]
t_m	Time duration of a single measurement [s]
$\mathcal{U}(\alpha)$	Dimensionless utilisable energy
$u(\boldsymbol{x})$	Electric potential [V]
u_{homo}	Homogenous potential field [V]
u_{inhomo}	Inhomogenous potential field [V]
$V(\boldsymbol{x})$	Continuous Dirichlet boundary conditions
$V_n^{exc}(t)$	Excitation potential imposed on the n^{th} electrode [V]
$V_n^{meas}(t)$	Measurement potential on the resistance in the n^{th} electrode channel [V]
V_Ω	Volume of the system Ω [m^3]
V_h	Finite element space
$V_n(t)$	Electric potential of the n^{th} electrode [V]
$V_{Drain}(t)$	Drain excitation voltage [V]
V_Γ	Constant grounded potential [V]
V_{Ω_E}	Volume of the subsystem Ω_E [m^3]
$\boldsymbol{V}$	Vector of potentials on the n_e electrodes [V]
$\boldsymbol{V}^{im}$	Vector of image voltages on the n^{th} electrode [V]
$\boldsymbol{V}^{ref}$	Vector of reference voltages on the n^{th} electrode [V]
$\hat{V}_n^{meas}(k)$	Fourier transform of $V_n^{meas}(t)$
w	Test function
X	Model Hilbert space
$X(\lambda)$	Reduced frequency transform
$X(f)$	Fourier transform of $x(t)$
$X(k)$	Fourier transform of $x(p)$
$Z(f)$	Impedance [Ω]
$\boldsymbol{x}$	Spacial coordinate in Ω [m^3]
$\tilde{X}_n$	Complex spectrum of the periodic signal $\tilde{x}(t)$
$\tilde{x}(t)$	Any periodic time dependent function
$x(p)$	Any finite and discrete time dependent function

$x(t)$	Any time dependent function
α	Regularisation parameter
$\gamma(\boldsymbol{x}, \omega)$	Complex electrical conductivity [S.m^{-1}]
γ_D	Trace operator
ΔV	Potential difference between two electrodes [V]
$\delta(j)$	Distinguishability coefficient
$\delta(x)$	Dirac delta function
δ_i^j	Kronecker symbol
$\delta_n(t)$	Gaussian additive noise [V]
$\delta_{RMS}(t)$	Root mean square of the Gaussian additive noise
$\epsilon(\boldsymbol{x}, \omega)$	Electrical permittivity [F.m^{-1}]
ζ_Γ	Contact impedance at the grounded surfaces [Ω]
ζ_n	Contact impedance at the surface of the n^{th} electrode [Ω]
θ	Arbitrary Fourier normalisation factor
θ_n	Angular coordinate of the electrode E_n [Rad]
Λ_σ	Dirichlet-to-Neumann operator
λ	Number of data taken for averaging the signal-to-noise ratio
$\mu(\boldsymbol{x}, \omega)$	Magnetic permeability [N.A^{-2}]
$\rho(\boldsymbol{x}, t)$	Free electric charge density [C.m^{-3}]
$\boldsymbol{\Sigma}_{n_e}$	Sign matrix for the data from n_e electrodes
$\sigma(\boldsymbol{x}, \omega)$	Real electrical conductivity [S.m^{-1}]
$\sigma_0(\boldsymbol{x}, \omega)$	Reference conductivity field [S.m^{-1}]
τ_0	Time constant associated with the electrode [s]
Φ_{exc}	Electric field produced by a unit current flowing in excitation electrodes [V.m^{-1}]
Φ_{meas}	Electric field produced by a unit current flowing in measurement electrodes [V.m^{-1}]
$\Phi_{n,l}$	Phase shift between the excitation voltage and the measured current [Rad]
$\phi_n(k)$	Phase of $\hat{V}_n^{meas}(t)$ [Rad]
χ	Steam quality
$\chi_n(\boldsymbol{x})$	Indicator function

Ψ_i	Sine function of frequency f_i [V]
Ω	Mathematical System
Ω_E	Subsystem of Ω limited in z by the electrodes
$\bar{\Omega}$	Closure of Ω
ω	Angular frequency [Hz]
$\partial\Omega$	Boundary of Ω

A
Acronyms

AI	Analog Input
AO	Analog Output
BRAM	Block Random Access Memory
CEA	French Alternative Energies and Atomic Energy Commission
COLTRANE	Continuous Overlapping operations with Linear Trigonometric Response ANalysis for EIT
CT	Computed Tomography
DAQ	Data Acquisition
DDS	Direct Digital Synthesis
DEMUX	Demultiplexer
DFT	Discrete Fourier Transform
DMA	Direct Memory Access
DtN	Dirichlet-to-Neumann
ECCS	Emergency Core Cooling System
ECT	Electrical Capacitance Tomography
EIDORS	Electrical Impedance Tomography and Diffuse Optical Tomography Reconstruction Software
EIT	Electrical Impedance Tomography
ERT	Electrical Resistance Tomography
ET	Electrical Tomography
FDM	Frequency-Division Multiplexing
FEM	Finite Element Method
FFT	Fast Fourier Transform
FIFO	First-In-First-Out
FPGA	Field Programmable Gate Array
Fps	Frames per seconds
FreeFEM++	FreeFEM Free Finite Element Method in C++
GD	Gamma ray Densitometry

I16	16-bits integer
IRQ	Interrupt Request
LBLOCA	Large LOCA Break
LOCA	Lost Of Coolant Accident
LTHC	Laboratory of analytical Thermohydraulics and Hydromechanics of Core and Circuits
LUT	Look-Up Table
MF	Multi-Frequency
MIT	Magnetic Induction Tomography
MRI	Magnetic Resonance Imaging
MS/s	Mega Samples per second
MUX	Multiplexer
NMS	Number of Measurements per Seconds
NOSER	Newton's One-Step Error Reconstructor
NtD	Neumann-to-Dirichlet
ONE-SHOT	ONe Excitation for Simultaneous High-speed Operation Tomography
OZS	Over Zero Switching
PCB	Printed Circuit Board
PDM	Phase Division Multiplexing
PEEK	Polyetheretherketone
PET	Positron Emission Tomography
PKL	*German* "PrimärKreisLauf", i.e. primary circulation
PMMA	Poly(methyl methacrylate)
PWR	Pressurized Water Reactor
ProME-T	*French* "Prototype pour Mesures Electriques par Tomographie"
RF	Radio Frequency
RMS	Root Mean Square
RT	Real Time
SBLOCA	Small LOCA Break
SCTL	Single Cycle Timed Loop
SMA	SubMiniature version A
SNR	Signal-to-Noise Ratio
SPECT	Single Photon Emission Computed Tomography
SVD	Singular Value Decomposition
TDM	Time-Division Multiplexing

TE	Echo Time
THD	Total Harmonic Distortion
TR	Repetition Time
TSVD	Truncated Singular Value Decomposition
U16	Unsigned 16-bits integer
U32	Unsigned 32-bits integer
U64	Unsigned 64-bits integer
USN	University College of South-eastern Norway
VI	Virtual Instrument
WDM	Wavelength Division Multiplexing

I

Introduction

In the context of high-pressure and high-temperature flow rigs, the timely identification of flow patterns helps by alerting the process engineers about hazardous salutations involving fast moving slugs or bubbles. For instance, the experimental study of accidental scenarios in Pressurised Water Reactors (PWR) helps to validate the simulation codes that aims at predicting the phenomenology. In these situations, the measurement technique must withstand the extreme conditions, while measuring the flows continuously and non-intrusively.

Especially in applications involving extreme process conditions in the flowing medium, tomography is a suitable non-intrusive technique for interrogating the medium continuously. This imaging technique is used to reconstruct the volume of an object from measurements of penetrating waves or particles on its external boundary.

Tomography is based on measurements of the boundary conditions of a system, where both the signal emitter and receiver have to be well known in space. Various tomography techniques exist using electromagnetic, acoustic waves, or electron and muon particles. Among the use of tomography in applications, the most well established is medical imaging using X-ray-based CT scans or electromagnetic waves in magnetic resonance imaging. Nevertheless, these techniques are not robust in this context, complex to implement, and expensive.

The complexity of using the main tomographic techniques in such extreme conditions encouraged to invest myself in the field of EIT [Breckon and Pidcock, 1987, Cheney et al., 1999, Borcea, 2002, Hanke and Bruhl, 2003]. The contrast with other tomographic method is that EIT consists of imposing (resp. measuring) an electrical current passing through a set of electrodes at the surface of a body, while measuring (resp. imposing) the electrical potential over another set of electrodes. Based on the difference in electrical characteristics of the liquid/gas phases, the impedance measurement provides an opportunity for non-intrusive measurement potentially applicable at high temperature and pressure. The use of multiple probes with a post processing of the associated measurements gives access to the spatial distribution of the void fraction [Dupré, A. and Ricciardi, G. and Bourennane, S., 2016, George et al., 2000].

The EIT data can be used in the solution of the potential and current boundary

conditions to solve the associated inverse problem of reconstructing the distribution of material properties such as the electric conductivity, permittivitity, etc, in the meter-head containing the fluids under test. EIT has the advantage of its applicability at high pressure and temperature, robustness, and relatively low cost.

EIT necessitates potentially a high data-frame acquisition rate, for instance in flow study involving rapidly-evolving flow regimes [Dupré et al., 2017b]. The application of EIT in such extreme processes raises the following problematic: *Developing a high imaging rate EIT system able to withstand high-pressure and high-temperature conditions.*

Several high-speed EIT systems of hundreds of frames per seconds (fps) have been proposed in the literature [Halter et al., 2008, Khan et al., 2015, Wang et al., 2005, Cui et al., 2011, Morales et al., 2015, Dupré, 2017]. All these systems are based on the concept of Time Division Multiplexing (TDM), where the excitation signal is routed to a single pair of electrodes at any given time. The sequential selection of these pairs of electrodes with multiplexers or electronic switching [Kauppinen et al., 2006] creates an excitation strategy and builds an EIT data frame, which includes the measurement data for all excitation pairs. [Dang et al., 2019].

The challenge is that increasing the number of frames per seconds (fps) reduces the measurement time, while a large number of measurements is required to limit the ill-posedness of the inverse problem. In addition, the sequential excitation of the electrodes in contact with ionic solutions results in significant difficulties caused by transient voltages due to the presence of capacitive components in the electrode–electrolyte interface [Zhang et al., 2010]. Therefore, the TDM sequential measurement procedure requires dead time, complex signal processing techniques, or hardware improvement to limit the effects of contact impedance [Wang and Ma, 2006, Wright et al., 2017]. Therefore, the systems introduced above reach high-speed at the price of a small number of electrodes, a partial scanning strategy, or short measurement times, often with a combination of these.

Equivalent to TDM, in the early stages of X-ray tomography, a single source/detector pair was rotated around a body to be imaged, resulting in a low acquisition rate. The improvement of X-ray tomography systems led to multiple emitter/receiver pairs that do not interact with each other as X-rays pass straight through the body. The sources and receivers are activated simultaneously, improving significantly the acquisition rate.

By analogy with the evolution of X-ray tomography, a solution for increasing the speed of EIT is to perform simultaneous measurements. However, the sensitivity regions within the body depend on the conductivity of the material, which is a priori unknown since it depends on the conductivity distribution inside the body, which is unknown. Therefore, simultaneous electrical emissions and measurements through surface electrodes result in a superposition of the signals in the measurement channels.

Based on simultaneous Multi-Frequency (MF) stimulations, the overlapping signals can be identified individually using Frequency Division Multiplexing (FDM). Employed in

telecommunications, FDM consists of dividing the total bandwidth available into a series of non-overlapping frequency bands, each of which is used to carry a separate signal. FDM has been partially implemented in the context of EIT [Granot et al., 2007, Dowrick and Holder, 2018, Mager et al., 2008], and simultaneous excitations at different frequencies are discriminated by demodulation, which allows simultaneous excitations and measurements at the same electrodes.

In [Dupré and Mylvaganam, 2018], a novel concept for soft-field tomography is reported based on simulation of a four-electrodes EIT system. This concept is build upon the multiple-excitation multiple-receiving capacitance tomography technique and the fully simultaneous excitation principle and is called the ONE-SHOT method, for ONe Excitation for Simultaneous High-speed Operation Tomography. The real breakthrough in the proposed signal processing methods, is the simultaneous excitation and measurement of all electrodes at once, with improved suppression of transients in high-speed operation. The ONE-SHOT method consists of single excitation pattern that can be set continuously, thereby eliminating problems due to contact impedance and transients. However in this preliminary work, the authors reports that the simulation results with the ONE-SHOT method are unstable. The most probable reason is the spectral leakage during Discrete Fourier Transform (DFT) computation.

In the present work, I focus on the *creation of a hardware system to test high-speed and simultaneous excitation method for EIT in the context of high-pressure and high-temperature flow rigs.*

The first step in this project is to analyse the dimensioning of the EIT sensor to be connected in the thermo-hydraulic loop. Depending on the diameter and length of the pipe, the size and number of electrodes have to be determined to improve the sensitivity and data quality of the EIT measurements. This topic is discussed in Chapter 2.

Then in Chapter 3, I aim at proving the feasibility of the ONE-SHOT method in a physical experiment. To do so, I focus on a reduced number of simultaneously generated signal frequencies imposed on a single electrode. The combined excitation signals with their simultaneous responses at the electrodes of the EIT module could theoretically be used to produce images.

The full implementation of the ONE-SHOT method is considered in Chapter 4 with a 16 electrodes EIT sensor and a total of 240 simultaneous excitations. The difficulty concerns the very high number of data to operate, including DFT in parallel over 16 channels.

The data acquisition system with the ONE-SHOT strategy have to be tested in an industrial experimental context to see the advantages of high rate imaging. In Chapter 5, I discuss the application to the study of accidental scenarios in PWR in two dynamic experiments.

Another novel solutions to significantly increase the imaging rate consists in fully simultaneous trigonometric excitations with FDM. The solution is called the COLTRANE method for Continuous Overlapping operations with Linear Trigonometric Response

ANalysis for EIT and will be introduced in Chapter 6.

The scientific contribution highlights are listed in Section I.1. My publications in scientific journals and conference proceedings are listed in Section I.2. The Section I.3 relates the context of my PhD. Finally, the organisation of this PhD thesis, in 6 chapters, is detailed in Section I.4.

I.1. Scientific contribution highlights

- Quantification of the leakage current for EIT measurements in thermo-hydraulic flow rigs. The electrode surface energy is maximised for an electrode length of 84% the length of the EIT sensor. This ratio is valid for any form factor [cp1, cp4].
- Computation of the sensitivity map of EIT measurements for a pattern containing a full set of excitations and measurements for several number of electrodes. The counterintuitive behaviour is validated with an indirect computation method [cp1, cp4]. The effects of the curent leakage to the sensitivity were investigated in a 3D simulation.
- Implementation of the novel ONE-SHOT method with simultaneous MF excitations and measurements with FDM. EIT images at 3 906 fps [ja1, ja2, ja3, ja4, ja6].
- Experiment at University of South-eastern Norway (USN) to test the ONE-SHOT method on fastly evolving two-phase flows [ja2, ja3].
- Experiment at the Framatome research center of Erlangen (Germany) to test EIT for the first time on high-pressure and high-temperature flow rigs.
- Implementation of the novel COLTRANE method with simultaneous trigonometric excitation patterns with MF and measurement with FDM. EIT data frames acquisition at 31 250 fps.
- Supervision of two master degrees:
  - A. Poverud, "Flow-Analytics using Multiphase Flow Rig with Multimodal Sensor Suite with focus on Void Fraction, Water-Cut and Flow Regimes", Faculty of Technology, University of South-Eastern Norway, Porsgrunn, 2019.
  - Y. Zhuang, "Etude Expérimentale des Fuites de Courant et de Sensibilité des Mesures de Tomographie par Impédance Electrique", Institut National des Sciences Appliqués (INSA) de Lyon, France, 2019.

I.2. Notes and publications

The interdisciplinary nature of current thesis work allows to communicate the findings to the scientific research communities in both sensor development area and nuclear thermal- hydraulics area. The journal papers and proceeding papers are listed separately as follows:

Scientific journal articles

[ja1] C. Dang, **M. Darnajou**, C. Bellis, G. Ricciardi, S. Mylvaganam, and S. Bourennane. Practical Comparisons of EIT Excitation Protocols with Applications in High Contrast Imaging. Measurement, Submitted

[ja2] C. Dang, **M. Darnajou**, C. Bellis, G. Ricciardi, S. Mylvaganam, and S. Bourennane. Real-time Imaging and Features Extraction of Air-Water Two-phase Flows Using High Speed EIT. Flow Measurement and Instrumentation, Submitted

[ja3] **M. Darnajou**, A. Dupré, C. Dang, G. Ricciardi, S. Bourennane, C. Bellis and S. Mylvaganam, "High Speed EIT with Multifrequency Excitation using FPGA and Response Analysis using FDM". IEEE Sensors, DOI 10.1109/JSEN.2020.2984388, 2020.

[ja4] **M. Darnajou**, A. Dupré, C. Dang, G. Ricciardi, S. Bourennane, and C. Bellis, "On the implementation of simultaneous multi-frequency excitations and measurements for electrical impedance tomography," MDPI Sensors, 1424-8220/19/17/3679, DOI 10.3390/s19173679, vol. 19, no. 17, August 2019.

[ja5] C. Dang, **M. Darnajou**, C. Bellis, G. Ricciardi, H. Schmidt and S. Bourennane, "Numerical and Experimental Analysis of the Correlation Between EIT Data Eigenvalues and Two-phase Flow Phase Fraction", Measurement Science and Technology, 10.1088/1361-6501/ab3d63, August 2019.

[ja6] A. Dupré, **M. Darnajou**, G. Ricciardi and S. Mylvaganam, "Simultaneous and Continuous Excitation Method for Electrical Impedance Tomography: Simulating Effects of Transients" Sensors (Basel, Switzerland), 538644, 2019 (Submitted)

Concerning [ja1, ja2], my contributions are conceptualisation, data curation, investigation, methodology, validation, visualisation, review and editing. Concerning [ja3, ja4], my contributions are conceptualisation, data curation, formal analysis, investigation, methodology, software, validation, visualisation and writing original draft. Concerning [ja5], my contributions are conceptualisation, formal analysis, investigation, methodology, review and editing. Finally, concerning [ja6], my contributions are data curation, formal analysis, investigation, methodology, software, validation, visualisation, review and editing.

International conference proceedings

[cp1] **M. Darnajou**, C. Dang, G. Ricciardi, S. Bourennane, C. Bellis, H. Schmidt, "Design of an Electrical Impedance Tomography Detector for Two-Phase Flow Measurements in the PKL experiment". In Proceedings of SWINTH-2019, Liverno, Italia, October, 2019.

[cp2] C. Dang, **M. Darnajou**, C. Bellis, G. Ricciardi, H. Schmidt, S. Bourennane, " Spectral and Eigenvalues Analysis of Electrical Impedance Tomography Data for Flow Regime Identification". In Proceedings of SWINTH-2019, Liverno, Italia, October, 2019.

[cp3] C. Dang, **M. Darnajou**, G. Ricciardi, S. Bourennane, C. Bellis, H. Schmidt, " Two-phase Flow Void Fraction Estimation from the Raw Data of Electrical Impedance Tomography Sensor". In Proceedings of ICAPP 2019, Juan-les-Pins, France, May, 2019.

[cp4] **M. Darnajou**; C. Dang; G. Ricciardi; S. Bourennane; C. Bellis; H. Schmidt, " The Design of Electrical Impedance Tomography Detectors in Nuclear Industry". WCIPT9, Bath, UK, 2-6 September 2018;

[cp5] C. Dang; **M. Darnajou**; G. Ricciardi; A. Beisiegel S. Bourennane; C. Bellis, " Performance Analysis of an Electrical Impedance Tomography Sensor with Two Sets of Electrodes of Different Sizes". WCIPT9, Bath, UK, 2-6 September 2018;

I.3. Context of the present work

The development of EIT for two-phase flow investigation at the French Alternative Energies and Atomic Energy Commission (CEA) of Cadarache has started with the PhD research of Antoine Dupré [Dupré, 2017] between October 2014 and October 2017. In his work, A. Dupré has developed a high speed EIT system called Pro-ME-T, able to acquire more than 800 fps based on TDM. In the year following the end of his PhD, A. Dupré has published in a conference proceeding [Dupré and Mylvaganam, 2018] the basic idea of the ONE-SHOT method for 4 electrodes. His work was the starting point of my research.

Two PhD subjects were created in 2017 by Guillaume Ricciardi (CEA) and Holger Schmidt (Framatome) in a collaboration to apply EIT to the analysis of accidental scenarios in PWR. One of this subject were developed by myself with a focus on the hardware and data acquisition. Regarding the complexity and the wide variety of methods for the reconstruction, the concerns about the quality of the EIT images in my work stops at the raw data level. The other subject were developed by my colleague Chunhui Dang, who focused on image reconstruction and eigenvalue analysis of EIT data. The thesis of C. Dang [Dang, 2020] contains various and interesting, analytical and experimental studies on image reconstruction and void fraction estimation for two phase flows [ja5, cp2, cp3, cp5].

The collaboration with Framatome has brought the possibility to test ProME-T and the ONE-SHOT method on high-pressure and high-temperature flow rigs. The creation of the EIT sensors able to withstand such extreme conditions with a large number of electrodes raised numerous problems that were discussed and solved thanks to the close collaboration with framatome. A successfull experiment were performed between June and July, 2019, proving the robustness of the sensors.

Finally, during the WCIPT8 conference in 2016, Antoine Dupré has started a collaboration with Saba Mylvaganam (USN). The laboratory of S. Mylvaganam focuses on two- and three-phase flow measurement with tomography coupled with deep learning. We organised with professor S. Mylvaganam, senior engineer Fredrik Hansen and master

student Aleksander Tokle Poverud an experiment to test the ONE-SHOT method on the USN facilities in October 2019.

I.4. Thesis Organisation

- The **Chapter 1** introduces in Section 1.1 the technique of tomography with a non-exhaustive overview of some main techniques. The description of these techniques is mathematical so the reader has a precise idea on what information is harvested concerning the object to image. The focus will then be turned on electrical tomography in Section 1.2. The section contains a remainder of electromagnetism and an exhaustive review of the different techniques for electrical tomography. Among these techniques, EIT is of interest in this thesis. The EIT measurement process and image reconstruction is detailed in Section 1.3. Finally, in Section 1.4, two concepts for multiplexing are explained with examples of EIT systems from the literature. One of this concept, Frequency-Division Multiplexing (FDM) is a key tool to significantly increase the data acquisition rate in EIT. The association of EIT and FDM is the core of the present thesis.
- In **Chapter 2**, simulations with two different softwares are used to find the optimal parameters for the sake of increasing the measurement performances. The Section 2.1 is an introduction to the softwares and methods used along this chapter. Section 2.2 contains the first approach to determine some dimensioning parameters. Section 2.3 relates the apparition of a leaking current from the electrodes to the neighboring pipes elements in the thermo-hydraulic loop. A simulation of the leakage currents at electrodes was used to find the adequate length of the electrodes that maximises the energy at their surfaces. Section 2.4 introduces the sensitivity map of the EIT measurements and validates the results with an independent computation approach. Finally, Section 2.5 presents the preliminary results for the integration of current leakage effects on the sensitivity in a 3D simulation.
- The **Chapter 3** introduces in Section 3.1, a first approach for simultaneous excitations and measurements strategy with FDM. Secondly, a general definition of the ONE-SHOT method is proposed in Section 3.2. The section provides details for its practical implementation. Thirdly, the high frame rate generates a large amount of data to process. In the past few years the development of electronics made it possible to handle systems enabling transfer of large measurement data [Kryszyn et al., 2017]. The estimation of the optimal data transfer rate and online computation speed is needed to choose the adequate hardware components, an issue that is discussed in Section 3.3. Finally, the Section 3.4 presents preliminary results of the demodulation of 15 simultaneous excitation frequencies to prove the feasibility of the ONE-SHOT method.
- The **Chapter 4** presents the strategy to implement the ONE-SHOT method in a physical experiment. The Section 4.1 introduces the logics used for analog signal generation and acquisition. The output data format is discussed in Section 4.2.

The Section 4.3 details the software to implement the ONE-SHOT method. Finally, the Section 4.4 contains the experimental results, obtain from the measurement of two-phase static flows.

- The **Chapter 5** discusses the application of EIT to measure the flow patterns in several accidental scenarios in the primary circuit of PWRs. These scenarios are introduced in Section 5.1, with a discussion of the applicability of EIT in a particular region of the primary circuit. The Section 5.2 relates the experimental results of measurements of fastly evolving two-phase flows in a horizontal pipe using the ONE-SHOT method. In a second experiment, introduced in Section 5.3, the ONE-SHOT method is tested on a high pressure and high temperature hydraulic loop.
- In **Chapter 6**, a novel approach with simultaneous trigonometric excitations for EIT is presented. The simultaneous trigonometric excitation strategy is discussed in Section 6.1, with the presentation of its software implementation. The measurement strategy and the output data format of the COLTRANE method are presented in Section 6.2, including experimental results. Finally, Section 6.3 discusses the preliminary work to develop the COLTRANE method for 32 electrodes.

A short history of Physics:
Aristote said a bunch of stuff that was wrong. Galileo and Newton fixed things up. Then Einstein broke everything again. Now, we've basically got it all work out, except for small stuff, big stuff, hot stuff, cold stuff, fast stuff, heavy stuff, dark stuff, turbulence, and the concept of time.

1

Electrical Impedance Tomography

Tomography is a widely used technique which consists in reconstructing the volume of a body from a series of measurements on its boundary. The result is the reconstruction of some physical properties inside the body, depending on the nature of the measurement. There exist numerous techniques, based on the measurement of particles, acoustic pressure, electromagnetic wave absorption, speed difference, polarisation of seismic waves...

Contents

1.1 Tomographic techniques 47
1.1.1 X-Ray tomography 48
1.1.2 Single Photon Emission Computed Tomography (SPECT) 49
1.1.3 Positron Emission Tomography (PET) 50
1.1.4 Magnetic Resonance Imaging (MRI) 51
1.1.5 Ultrasonic tomography 53
1.2 Electrical Tomography (ET) 54
1.2.1 Electromagnetism in material 55
1.2.2 Magnetic Induction Tomography (MIT) 56
1.2.3 Electrical Impedance Tomography (EIT) 57
1.2.4 Electrical Capacitance Tomography (ECT) 59
1.3 EIT measurement and image reconstruction 60
1.3.1 Excitation and measurement strategies 61
1.3.2 Measurement duration 63
1.3.3 Continuum model of the inverse problem 64
1.3.4 Discretisation and resolution 67
1.4 Towards high frame rate EIT imaging 71
1.4.1 Multiplexing 71
1.4.2 Time Division Multiplexing (TDM) 72
1.4.3 High rate ET based on TDM 73
1.4.4 Frequency Division Multiplexing (FDM) 75
1.4.5 Multi-Frequency (MF) and FDM for high rate ET 76

The chapter introduces in Section 1.1 the technique of tomography with a non-exhaustive overview of some main techniques. The description of these techniques is mathematical so the reader has a precise idea on what information is harvested concerning the object to image. The focus will then be turned on electrical tomography in Section 1.2. The section contains a remainder of electromagnetism and an exhaustive review of the different techniques for electrical tomography. Among these techniques, EIT is of interest in this study. The EIT measurement process and image reconstruction is detailed in Section 1.3. Finally, in Section 1.4, two concepts for multiplexing are explained with examples of EIT systems from the literature. One of this concept, Frequency Division Multiplexing (FDM) is a key tool to significantly increase the data acquisition rate in EIT. The association of EIT and FDM is the core of the present study.

1.1. Tomographic techniques

Tomography is widely used in astrophysics, geophysics and material sciences as well as application in medical imaging, destructive and non-destructive controls and thermo-hydraulics. One particular technique is not necessarily used in one particular domain of applications.

All these tomography techniques have in common to operate in three steps. Firstly the study volume is questioned, namely excited with an acoustic or electromagnetic signal. The second step consists in measuring the reaction signal of the matter. Those two steps are repeated in order to get a dataset containing the imposed and measured conditions for several independent measurements. The third step consists in solving the associated mathematical problem.

This third step on the mathematical problem, is decomposed into two steps. Firstly in the elaboration of a direct model which describes with a sufficient accurateness the physical phenomenons occurring inside the body. Secondly, it consists in determining an inverse problem used to determine the distribution of a physical quantity, based on the direct model.

Numerous reconstruction algorithms exists with various ways for solving the problem. Their are generally ordered in two categories:

- The *analytical algorithms* are based on a continuous representation of the problem given by a mathematical formula. Generally fast and simple algorithms, they do not necessarily provide an estimation of statistical phenomenons (noise) or other alterations imposed by the hardware.
- The *algebraical algorithms* are based on a discrete representation of the problem. These algorithms are often more elaborated and permit the use of a discrete model obtained from numerical simulation. A statistical modelling of the measurement gives probabilist methods to solve the inverse problem.

This section introduces a brief summary of the essential details of tomographic techniques, widely used in numerous applications. These techniques are quite far from the topic of this study, but the overview is interesting for the reader to realise the tremendous

variety of strategies for tomography. The following contains the overview of X-Ray Tomography in Section 1.1.1, Single Photon Emission Computed Tomography (SPECT) in Section 1.1.2, Positron Emission Tomography (PET) in Section 1.1.3, in Section 1.1.4 the very famous technique of Magnetic Resonance Imaging (MRI) and finally another interesting technique, Ultrasonic Tomography in Section 1.1.5.

1.1.1. X-Ray tomography

X-Ray tomography is an imaging technique to measure the absorption of X-Ray passing through a body and, with measurements from different angles, to reconstruct the inner structure of the body [Sijbers and Postnov, 2004, Dalrymple et al., 2005, Fishman et al., 2006, Silverstein et al., 2008, Berrington de Gonzalez et al., 2009, Boas and Fleischmann, 2011, Van Gompel et al., 2011, Pessis et al., 2013, Jha et al., 2014, Nieuwenhove et al., 2015]. Each reconstructed image represents a 2D slice of the body. In numerous applications such as the Computed Tomography (CT) scan in medical imaging (Figure 1.1a.), several slices are reconstructed together and associated with digital geometry processing to form a 3D image.

Although its main application is medical imaging [Oldendorf, 1978, Jacobs et al., 2008, Smith-Bindman et al., 2009], CT scan is used in numerous domains such as non-destructive control [Buffiere and Maire, 2014], security inspection [Megherbi et al., 2010, Flitton et al., 2013], research for nuclear fusion [Evans et al., 2015] or in archeology to image the contents of sarcophagi or ceramics [Payne, 2013]. The 1979 Nobel Prize in Physiology or Medicine was awarded for the development of computer assisted tomography to Allan M. Cormack and Godfrey N. Hounsfield [Richmond, 2004].

The basic principle of X-Ray tomography is to detect photons that are transmitted through an object. The X-Ray interact with matter following mechanisms that results in the production of charged particles. In the typical energy range of CT scan operation, there is three main physical processes for light/matter interaction:

- The *photoelectric absorption*: The incident photon is absorbed by an atom of the object and its energy is transmitted to an electron, ejected from its orbit. The reorganisation of the electrons in the electronic shell of the atom emit fluorescence or an Auger electron. Generally, the Auger electron is quickly reabsorbed by the material.
- The *Rayleigh (coherent) diffusion*: The incident photon is absorbed by an atom and reemitted with the same energy.
- The *Compton (incoherent) diffusion*: The incident photon interacts with a single electron, providing a part of its energy. The rest of the photon energy is transmitted to a diffused photon.

The probability of these effects depends on the energy of the incident photon and the nature of the medium. In application, the photoelectric absorption and the Compton diffusion are predominant.

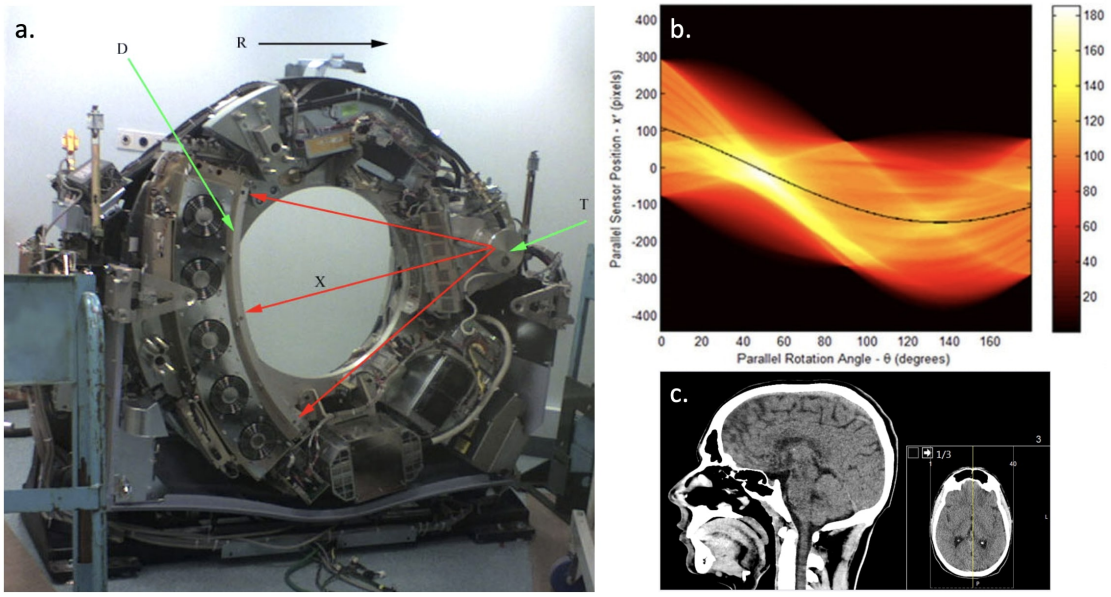

Figure 1.1. – a. CT scan with cover removed to show internal components. T: X-ray tube, D: X-ray detectors, X: X-ray beam, R: Gantry rotation. b. Sinogram (graphic representation) of the raw data obtained from a CT scan. [Jun and Yoon, 2017] c. Image sample of human brain, derived from the raw data.

The effects described above are responsible for the attenuation of the incident X-Ray through the material. The absorption coefficient μ [cm^{-1}] is a sum of all the attenuation effects, it characterises the attenuation of the X-Ray and represents the probability for a photon to be absorbed by length unit. The value of μ depends on the energy of the X photons, the density and the atomic number of the traversed material.

The attenuation law, or Beer-Lambert law, describes the basis of the X-Ray tomography for a single slice:

$$N_1 = N_0 \exp\left[-\int_{path} \mu(x, y_1)dx\right]. \tag{1.1}$$

The incident number of photons N_0 and the number of transmitted photons N_1 passing along the line y_1 are used to assess the integral of the absorption along the path:

$$\ln \frac{N_1}{N_0} = -\int_{path} \mu(x, y_1)dx. \tag{1.2}$$

The repetition of measurements along a sufficient number of linearly independent lines in a same slice gives the Radon transform (Figure 1.1b.). Based on the inverse of the Radon transform, it is possible to reconstruct the map of attenuation $\mu(x, y)$ of the slice from its projections (Figure 1.1c.).

1.1.2. Single Photon Emission Computed Tomography (SPECT)

SPECT is a medical imaging [Brooks and Di Chiro, 1976, D'Angelo et al., 1995, Tousignant et al., 1999]. It consists in injecting into the patient a radioactive substance,

which emits photons of well known energy. The photons emitted outside the body are measured with a photon detector array [Scuffham et al., 2012], rotating around the body. The rotation gives the image of the distribution of the radionuclides from several angles to reconstruct its precise position and concentration.

A naive description of the SPECT image reconstruction [National Research Council, 1996] is to simply consider the projections $p(t, \theta)$ of the radioactive emission as the simple Radon transform. For a two-dimensional distribution $f(x, y)$,

$$p(t, \theta) = c \int_{-\infty}^{+\infty} f(x, y) ds, \tag{1.3}$$

where t is the position on the projection array, θ is the angle and c is a gain factor that transforms the radioactivity concentration to detected signals.

In application, each photon is attenuated and scattered when traveling through the material. While the attenuation can be modelled by a coefficient, scattering has to take into consideration three-dimensional effects. The measured projections are two-dimensional and given by a more complicated Radon transform:

$$p(t, \theta) = c \int_{\Omega} h(s, \omega; \boldsymbol{r}) \int_{-\infty}^{+\infty} f(\boldsymbol{r}) e^{-\int_{r=0}^{+\infty} a(\boldsymbol{u}) ds'} ds d\omega, \tag{1.4}$$

where $a(\boldsymbol{u})$ is the three-dimensional attenuation coefficient distribution, $\int_{\boldsymbol{r}=0}^{+\infty} a(\boldsymbol{u}) ds'$ is the attenuation factor for photons originating from $\boldsymbol{u}$, traveling along the direction perpendicular to the detector array. $\boldsymbol{t} = (x, y)$ is a point on the two-dimensional projection image $p(\boldsymbol{t}, \theta)$, $f(\boldsymbol{r})$ is the three-dimensional radioactivity distribution in the object.

A widely used radionuclide is an isomer of technetium, ^{99m}Tc [Dougall et al., 2004], with a half life of 6.02 hours. During the decay of technetium, photons with energy 140.5 keV are emitted at 89% which is high enough to penetrate through the human body, but low enough to be measured by the photon detector.

The result brings precious information to study the organs behaviour and gives the opportunity to detect malfunctioning as early as possible. The SPECT is also used in industrial applications, for instance in the non-destructive control of fuel assemblies in nuclear power plants [Svard et al., 2005, Biard, 2013, Andersson and Holcombe, 2017].

1.1.3. Positron Emission Tomography (PET)

PET [Snyder and Miller, 1985, Vardi et al., 1985, Miller and Snyder, 1987, Snyder et al., 1987, Green, 1990, Miller and Roysam, 1991, Kuhl et al., 1999, Kelloff et al., 2005] is a nuclear imaging technique used in medical applications. It consists in injecting a radioactive tracer, radiopharmaceutical glucose solution labeled with a positron emitting isotope (^{11}C, ^{13}N,^{15}O and ^{18}F) into a patient. The distribution of the tracer is measured to create an image. The PET reveals areas where the glucose is consumed in excess such as in a growing tumor.

The lifetime of the emitter is an important parameter since it must be large enough to

allow its transportation from the production facility to the location where the patient is treated. On the contrary, it is required to not be too large so the radioactive material despairs quickly in the patient body. The radioactive tracer 2-[^{18}F]fluoro-2-deoxy-D-glucose (^{18}FDG) [Pacak et al., 2001] is widely used for nuclear medical imaging. The radioactive element, the ^{18}F decays via positron with a half time of 110 minutes. The FDG is a sugar analogue which has the property to accumulate in the organs where the glucose is used, essentially the brain and the heart.

The distribution of the positron-emitting tracer is calculated [National Research Council, 1996] by tomographic reconstruction methods from

$$P = e^{-\int a(s)ds} \int f(s)ds, \tag{1.5}$$

where P is the projection data, $a(s)$ the linear attenuation coefficient and $f(s)$ the isotope distribution. The exponential coefficient in (1.5) takes into consideration the attenuation effects of the two photons inside the patient's body. In this description, the scattering effects are ignored but an approach similar to (1.4) can be considered.

The detectors in the PET scanners are made of scintillation blocs placed on a ring, placed around the body. The diameter of the ring defines the distance between the detectors, which influences the spatial resolution of the imaging. Hence, reducing the diameter increases the resolution, but it also increases random coincidences [Leroy and Rancoita, 2009]. About fifteen rings can be operated simultaneously to form an array of detector to permit three-dimensional imaging. The images [Shepp and Vardi, 1982, Qi and Leahy, 2006] reach a resolution of about 6mm in each direction.

1.1.4. Magnetic Resonance Imaging (MRI)

The most known tomography technique is probably the MRI [Erasmus et al., 2004, Buxton, 2009, Chavhan et al., 2009, Uecker et al., 2010, Abeida et al., 2013, Landheer et al., 2020]. Compared to the SPECT and PET, MRI has the advantage that it does not need radioactive material but uses the non-zero spin property of the hydrogen isotope ^{1}H nuclei.

A magnetic field $\boldsymbol{B}$ is imposed in a body. The nucleus and electron spins tend to align with the field, oscillating around the field direction and producing a sequence of radio-frequency pulses. The frequency of the oscillation depends on the magnetic field and the physical properties of the particles, making them identifiable through the pulse response.

The energy difference between the up state $S_z = +\frac{1}{2}$ and the down state $S_z = -\frac{1}{2}$ of the spin of the hydrogen nuclei is:

$$\Delta E = h\gamma B \tag{1.6}$$

where h is Planck's constant, γ is the gyro-magnetic ratio which is a characteristic of

each atom. The resonance, or the Larmor frequency, is given by

$$\nu = \gamma B \tag{1.7}$$

which is 85.16 MHz for hydrogen in a 2T magnetic field.

The net magnetisation of the system is

$$\boldsymbol{M} = \sum \boldsymbol{\mu} \tag{1.8}$$

with $\mu = e\pi\gamma \boldsymbol{S}$. The individual magnetisation held with the nucleus. When a magnetic field is applied, most of the nuclei will align in the same direction according to Boltzmann distribution:

$$\frac{N_-}{N_+} = \exp\left(-\frac{\Delta E}{kT}\right). \tag{1.9}$$

A Radio Frequency (RF) wave called saturation pulse or 90° impulsion is imposed through the body to balance the populations N_+ and N_-, giving a net magnetisation $M_z = 0$. After a saturation pulse, the system will return to its equilibrium depending on the spin-lattice relaxation time T_1 (Figure 1.2a.b.) according to:

$$M_z = M_0\left(1 - e^{-t/T_1}\right). \tag{1.10}$$

The 90° impulsion brings the net magnetisation in the x-y plane, the equilibrium is reached as:

$$M_{xy} = M_{xy_\tau}\left(e^{-t/T_2}\right), \tag{1.11}$$

where T_2 is the spin-spin relaxation time and τ is the time marking the end of the impulsion. The decreasing effect is coming from the interaction between the nuclei magnetic fields.

To be able to reconstruct an image, the frequency ω, the spin-lattice T_1 and the spin-spin T_2 relaxation times are extracted. Due to the exponential nature of the signal, it is hard to extract these values directly. For this reason an echo is produced.

Among several methods to extract the values [Hurd and John, 1991, Brown et al., 1995], the most direct one is called spin-echo method (Figure 1.2d.e.) and considers only RF waves to create the echo. A sequence used is a 90° impulsion followed by a saturation pulse after a time $t = TE/2$ there TE is the echo time. This pattern is repeated after a time t. The height of the echo signal is:

$$S = k\rho\left(1 - e^{-TR/T_1}\right)e^{-TR/T_2} \tag{1.12}$$

where ρ is the non-zero spin nuclei density and k is a proportionality constant that depends on the measuring device. From ρ is extracted the information for tomographic images inside the body.

The MRI can be associated to other tomographic techniques such as PET imaging [Wagenknecht et al., 2013] or CT-scan [Semelka et al., 2007]. As for CT-scan, MRI

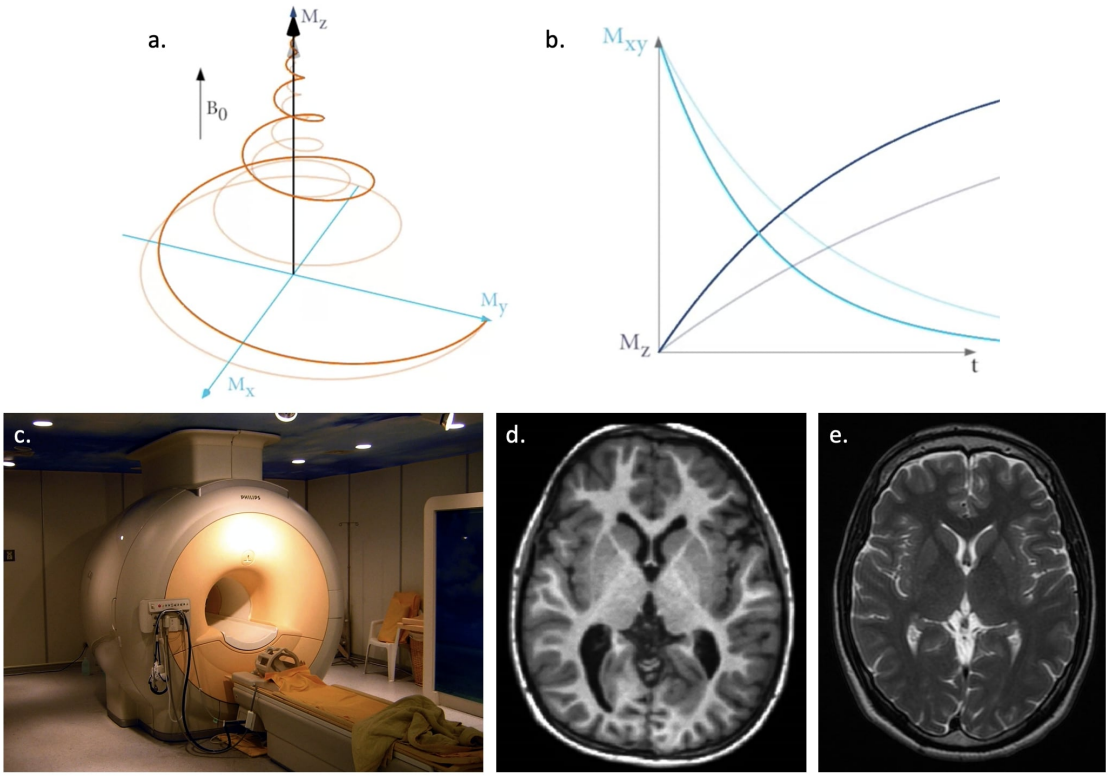

Figure 1.2. – a. Visual representation of the spin of a proton in a constant magnetic field B_0, then subject to a RF wave. The two colours represents two typical behaviours. b. Visualisation of the relaxation times T_1 and T_2. c. IRM machine in closed geometry. d. Spin-echo, T_1 weighted. MRI of the head measuring spin-lattice relaxation by using a short Repetition Time (TR) and Echo Time (TE). e. Spin-echo, T_2 weighted. Measuring spin-spin relaxation by using long TR and TE times.

has application not only in medical imaging [Erasmus et al., 2004, Masselli and Gualdi, 2012, Necus et al., 2019] but in a wide range of applications such as in physics experiments [Mansfield and Grannell, 1975], in palaeontology [Giovannetti et al., 2016] or ornithology [Liu et al., 2007].

1.1.5. Ultrasonic tomography

Ultrasonic Tomography [Munk and Wunsch, 1979, Greenleaf and Bahn, 1981, National Research Council, 1996, Kak and Slaney, 2001, Goncharsky and Romanov, 2013, Arakawa et al., 2018, Mita and Takiguchi, 2018, Takiguchi, 2019] uses ultrasound waves as physical phenomenon for imaging. It is mostly used for soft tissue medical imaging, especially breast imaging.

A sound wave is generated with Piezoelectric ultrasound transducers and transmitted in the direction of the object to measure. The response of the system is a sound wave, that is measured with the same or other piezoelectric transducers around the object. This response sound wave carries information about the object.

Let us consider an object $\Omega \in \mathbb{R}^n$ with a reflective index γ, and $\gamma = 1$ outside. Planar sound waves are generated in the direction of the object θ :

$$e^{-ikt}u_\theta(x), \quad u_\theta(x) = e^{-ikx\cdot\theta} \tag{1.13}$$

where $k = 2\pi/\lambda$ is the wave number and λ the wave length. The response is the wave $e^{-ikt}u(x)$ which satisfies the reduced wave equation:

$$\Delta u + k^2(1+f)u = 0, \quad f = \gamma^2 - 1. \tag{1.14}$$

Assuming the boundary conditions :

$$g(x,\theta) = u(x), \quad \theta \in \mathbb{R}^{n-1} \tag{1.15}$$

to be known outside the object. The inverse problem to be solve consists in determining f inside Ω.

The generally assumed method to solve this problem consists in linearisation of (1.14), with methods such as Born and Rytov approximation. Let us assuming $n = 3$, ones rewrites (1.14) as

$$u(x) = u_\theta(x) - k^2 \int_\Omega G(x-y)f(y)u(y)dy, \tag{1.16}$$

where

$$G(\boldsymbol{x}) = \frac{e^{ik|\boldsymbol{x}|}}{4\pi|\boldsymbol{x}|} \tag{1.17}$$

is an appropriate Green's function. The Born approximation consists in considering $u \sim u_\theta$ in (1.16), giving

$$g(\boldsymbol{x},\theta) = u_\theta(\boldsymbol{x}) - k^2 \int_\Omega G(\boldsymbol{x}-\boldsymbol{y})f(\boldsymbol{y})u_\theta(\boldsymbol{y})dy, \quad \boldsymbol{x} \notin \Omega \tag{1.18}$$

Ultrasonic Tomography has the benefit to provide multiple information on the object to image: the attenuation coefficient from the wave's sound pressure, the speed of sound from the time-of-flight and the echogenicity (i.e. refraction index, surface morphology...) from the scattered wave.

1.2. Electrical Tomography (ET)

ET aims at reconstructing an electrical quantity to form a tomographic image. Prior to introduce the ET techniques, let us remind the basis of electromagnetism in Section 1.2.1. There is three different ET techniques: Magnetic Induction Tomography (MIT), Electrical Impedance Tomography (EIT) and Electrical Capacitance Tomography (ECT). These techniques are overviewed in Section 1.2.2, Section 1.2.3 and Section 1.2.4, respectively.

1.2.1. Electromagnetism in material

The principle of ET is based on the theory of electromagnetism. The three-dimensional description of the electromagnetic field in a physical body starts from the Maxwell's equations. [Mueller and Siltanen, 2012, Monk, 2003, Cheng et al., 1989]:

$$\nabla \times \boldsymbol{E} = -\partial_t \boldsymbol{B} \qquad \text{Faraday's law,} \tag{1.19}$$

$$\nabla \times \boldsymbol{H} = \boldsymbol{J} + \partial_t \boldsymbol{D} \qquad \text{Ampere's law,} \tag{1.20}$$

$$\nabla \cdot \boldsymbol{B} = 0 \qquad \text{Gauss's law for magnetism,} \tag{1.21}$$

$$\nabla \cdot \boldsymbol{D} = \rho \qquad \text{Gauss's law.} \tag{1.22}$$

Here, $\boldsymbol{E}(\boldsymbol{x}, t)$ is the electric field, $\boldsymbol{B}(\boldsymbol{x}, t)$ the magnetic flux density, $\boldsymbol{H}(\boldsymbol{x}, t)$ the magnetic field strength, $\boldsymbol{D}(\boldsymbol{x}, t)$ the electric displacement field and $\rho(\boldsymbol{x}, t)$ the free electric charge density, described for a point $\boldsymbol{x} \in \mathbb{R}^3$ at time t. In ET, a periodic excitation of the form $e^{i\omega t}$, with ω the temporal angular frequency, is generally applied at the surface of the body. The application of a periodic excitation affects the electromagnetic fields such that:

$$\begin{cases} \boldsymbol{E}(\boldsymbol{x}, t) = \boldsymbol{E}(\boldsymbol{x}) e^{i\omega t}, \\ \boldsymbol{H}(\boldsymbol{x}, t) = \boldsymbol{H}(\boldsymbol{x}) e^{i\omega t}, \\ \boldsymbol{B}(\boldsymbol{x}, t) = \boldsymbol{B}(\boldsymbol{x}) e^{i\omega t}, \\ \boldsymbol{D}(\boldsymbol{x}, t) = \boldsymbol{D}(\boldsymbol{x}) e^{i\omega t}, \\ \rho(\boldsymbol{x}, t) = \rho(\boldsymbol{x}) e^{i\omega t}, \\ \boldsymbol{J}(\boldsymbol{x}, t) = \boldsymbol{J}(\boldsymbol{x}) e^{i\omega t}. \end{cases} \tag{1.23}$$

The particular case of an applied periodic current affects the Faraday's law (1.19) and the Ampere's law (1.20) in the way that:

$$\nabla \times \boldsymbol{E}(\boldsymbol{x}) = -\partial_t [\boldsymbol{B}(\boldsymbol{x}) e^{i\omega t}] = -i\omega \boldsymbol{B}(\boldsymbol{x}), \tag{1.24}$$

$$\nabla \times \boldsymbol{H}(\boldsymbol{x}) = \boldsymbol{J}(\boldsymbol{x}) + i\omega \boldsymbol{D}(\boldsymbol{x}). \tag{1.25}$$

Assuming the electric and magnetic response of the body is linear and anisotropic, the following relationship is verified:

$$\boldsymbol{D} = \epsilon(\boldsymbol{x}, \omega) \boldsymbol{E}, \tag{1.26}$$

$$\boldsymbol{B} = \mu(\boldsymbol{x}, \omega) \boldsymbol{H}, \tag{1.27}$$

and Ohm's law implies:

$$\boldsymbol{J} = \sigma(\boldsymbol{x}, \omega) \boldsymbol{E}. \tag{1.28}$$

Here, $\epsilon(\boldsymbol{x}, \omega)$ is the electric permittivity, $\mu(\boldsymbol{x}, \omega)$ the magnetic permeability and $\sigma(\boldsymbol{x}, \omega)$ the real conductivity.

1.2.2. Magnetic Induction Tomography (MIT)

MIT uses the Foucault's current effect to image the passive electromagnetic properties of an object: conductivity, permittivity and permeability [Telford et al., 1976, Peyton et al., 1996, Korjenevsky et al., 2000, Scharfetter et al., 2001, Binns et al., 2001, Soleimani and Lionheart, 2006, Wei and Soleimani, 2012]. As ECT and EIT, it has the advantage to be contactless and non-intrusive. The applications of MIT are broad in domains such as geophysics, metal flow visualisation in metal working processes, non-destructive testing as well as medicine and process industry.

The principle of MIT is to apply a magnetic field from a coil at the surface of an object [Saiful et al., 2015]. The magnetic field disturbed by a perturbation is measured by sensing coils at the periphery of the object [Ziolkowski and Gratkowski, 2009], as illustrated in Figure 1.3.

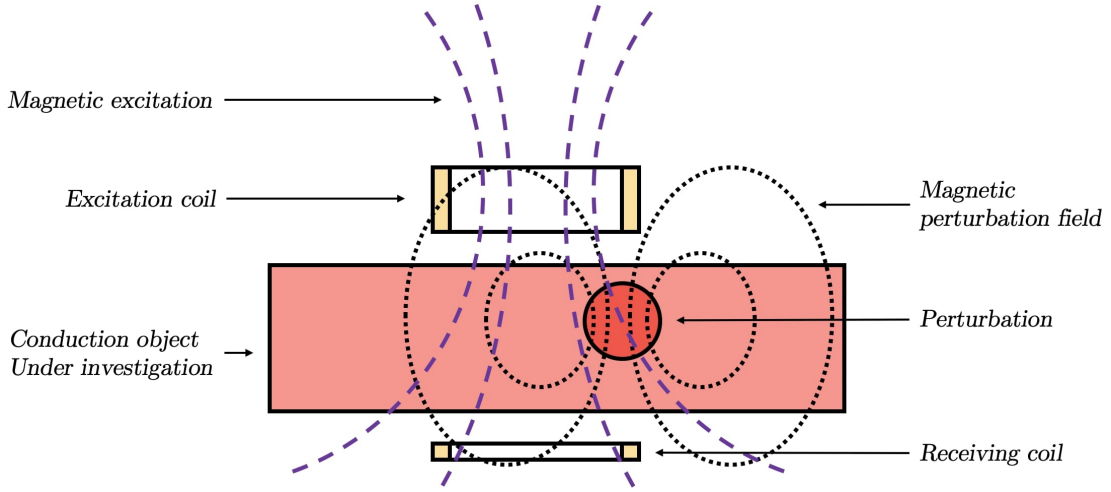

Figure 1.3. – The principle of magnetic induction tomography [Igney et al., 2005].

When the object or biological tissu is exposed to the excitation magnetic field $\boldsymbol{B}$, the object creates Foucault's currents resulting from the electromagnetic induction [Zinan Liu et al., 2008]. It results a perturbation of the magnetic fiels $\Delta\boldsymbol{B} \in \mathbb{C}$ which modifies the strength and the spatial distribution of the magnetic field. The detection coils are used to mesure the perturbed magnetic field $\tilde{\boldsymbol{B}} = \Delta\boldsymbol{B} + \boldsymbol{B}$ as follows [Griffiths, 2001]:

$$\tilde{\boldsymbol{B}} \propto \omega(\omega\epsilon_0\epsilon_r - i\sigma) \tag{1.29}$$

where ω is the angular frequency of the excitation signal, ϵ_0 the vacuum permittivity, ϵ_r the relative permittivity and σ is the conductivity of the object. The perturbation creates a phase ϕ between $\boldsymbol{B}$ and $\tilde{\boldsymbol{B}}$. The real part of $\Delta\boldsymbol{B}$ is due to the displacement currents which is in linear relationship with the permittivity inside the object. The imaginary part is related to its impedance. MIT requires a phase sensitive measurement to get the conductivity inside the material and reconstruct an image.

The strength of MIT is its capacity to measure three dielectric properties of material:

conductivity σ, permeability μ and permittivity ϵ [Trakic et al., 2012, Zakaria et al., 2012]. However, the literature generally focuses on the conductivity measurement because the quantities involved are relatively higher.

1.2.3. Electrical Impedance Tomography (EIT)

EIT is a type of non-intrusive technique widely used in medical, geo-physical, and industrial imaging. From the information of electrical current and potential on the boundary of an object, the Calderón's inverse problem aims at determining the complex conductivity distribution inside the object. A close technique consists in reconstructing the real conductivity and is called Electrical Resistance Tomography (ERT). This section introduces the mathematical aspects of EIT as generally reported in the literature.

As for the MRI, EIT were firstly developed for medical applications. Much of the fundamental work was done at Rensselaer Polytechnique Institute starting in the 1980s [Cheney et al., 1990, Gisser et al., 1990, Cheney and Isaacson, 1995, Cheney et al., 1999]. The method [Borcea, 2002, Hanke and Bruhl, 2003, Cheney et al., 1999] uses a set of electrodes, placed on the surface of the body, with a low frequency current passing through, below the human perception (Figure 1.4a.). This results in a voltage distribution on the electrodes which can be measured. Based on the fact that the electrical conductivity and permittivity of the human tissues vary significantly, the application of an excitation pattern between several pairs of electrodes associated with the voltage measurement results in a current-to-voltage map. This map serves as data for the *inverse conductivity problem* to compute the tomography of the electrical properties of the tissue and to assess its structure.

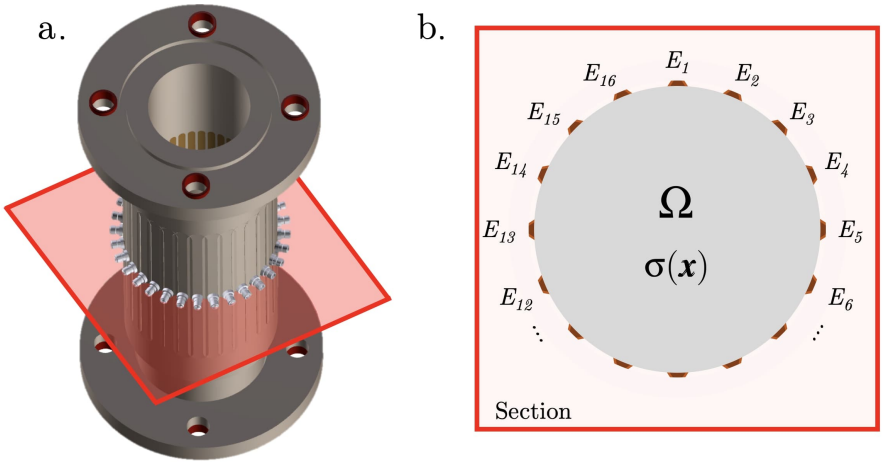

Figure 1.4. – a. Scheme of the EIT sensor prototype of height 336 mm, external diameter 120 mm, and inner diameter 80 mm containing 32 electrodes of length 150 mm and width 6 mm. This prototype is used for experiments in the following chapters. b. Representation of the 16 electrodes in the cross-section of the EIT sensor.

More precisely, the system $\Omega \subset \mathbb{R}^3$ in which the image reconstruction is considered is cylindrical (Figure 1.4b.). EIT is a technique to solve the inverse problem of determining

the conductivity function $\gamma(\boldsymbol{x},\omega) = \sigma(\boldsymbol{x}) + i\omega\epsilon(\boldsymbol{x})$ within the interior of Ω [Cheney et al., 1999, Borcea, 2002, Hanke and Bruhl, 2003]. Here, $\sigma(\boldsymbol{x})$ is the isotropic electrical conductivity field, $\epsilon(\boldsymbol{x})$ the permittivity, and ω the angular frequency. EIT operates at $\omega \ll 1$ GHz, so the imaginary part of γ can be neglected $\gamma(\boldsymbol{x},\omega) \to \sigma(\boldsymbol{x})$. The closure of Ω is denoted as $\bar{\Omega}$, and its boundary is $\partial\Omega$.

In EIT, the conductivity function $\sigma(\boldsymbol{x})$ is unknown and has to be determined from simultaneous excitations and measurements of the potential $u(\boldsymbol{x})$ and the current $\boldsymbol{j}(\boldsymbol{x}) = \sigma(\boldsymbol{x})\nabla u$, on the boundary.

Since the magnetic permeability of water, air, oil, human tissus and earth are very low compared for instance to metallic materials, it is possible in every fields of application of EIT to linearise $\boldsymbol{E}$ and $\boldsymbol{B}$ around $\mu = 0$. Respectively,

$$\boldsymbol{E}(\boldsymbol{x},\omega;\mu) = \boldsymbol{E}(\boldsymbol{x},\omega;0) + \partial_\mu \boldsymbol{E}(\boldsymbol{x},\omega;\mu)\mu + \frac{1}{2!}\partial_\mu^2 \boldsymbol{E}(\boldsymbol{x},\omega;\mu)\mu^2 + ... \tag{1.30}$$

$$= \boldsymbol{E}_0 + \mu\boldsymbol{E}_1 + \mu^2\boldsymbol{E}_2 + ..., \tag{1.31}$$

and

$$\boldsymbol{B}(\boldsymbol{x},\omega;\mu) = \boldsymbol{B}_0 + \mu\boldsymbol{B}_1 + \mu^2\boldsymbol{B}_2 + ... \tag{1.32}$$

In the approximation at leading order, the Faraday's law (1.19) becomes:

$$\nabla \times \boldsymbol{E}_0(\boldsymbol{x}) = -i\omega\boldsymbol{B}_0(\boldsymbol{x}), \tag{1.33}$$

However, it follows from the approximation $\mu = 0$ and the (1.27) that $\boldsymbol{B}_0 = \boldsymbol{0}$ and then :

$$\nabla \times \boldsymbol{E}_0(\boldsymbol{x}) = \boldsymbol{0}. \tag{1.34}$$

The electric field is expressed in this particular case as the gradient of the electric potential u, defined so that:

$$\boldsymbol{E}_0(\boldsymbol{x}) = -\nabla\boldsymbol{u}. \tag{1.35}$$

Alternatively, starting from the Ampere's law under a periodic current (1.25), and considering (1.26) and (1.28), it follows that:

$$\nabla \times \boldsymbol{H} = (\sigma + i\omega\epsilon)\boldsymbol{E}, \tag{1.36}$$

and,

$$\nabla \cdot (\nabla \times \boldsymbol{H}) = \nabla \cdot [(\sigma + i\omega\epsilon)\boldsymbol{E}] = 0, \tag{1.37}$$

Since the divergence of a curl is null. At zero order, (1.37) becomes:

$$\nabla \cdot [(\sigma + i\omega\epsilon)\boldsymbol{E}_0] = 0, \tag{1.38}$$

The generalized Laplace equation is obtained by considering (1.35):

$$\nabla \cdot [(\sigma(\boldsymbol{x}) + i\omega\epsilon(\boldsymbol{x}))\nabla u(\boldsymbol{x})] = 0. \tag{1.39}$$

for $\boldsymbol{x} \in \Omega$, where $\Omega \subset \mathbb{R}^3$ is the bounded domain in which the problem is considered. This equation conditions the mathematical problem for the image reconstruction. We will see in more details the reconstruction problem of EIT in Section 1.3.

The material to operate EIT is available in real-time application and is cost-effective. Furthermore, the low current and voltage being able to penetrate a wide variety of materials without damaging them, makes EIT an attractive technique. Nevertheless, the ill-posedness of the inverse problem associated with its discretisation due to the finite size of the electrodes makes the inverse conductivity problem very sensitive to modelling errors and measurement noise, necessitating a Data Acquisition (DAQ) system that operates with low measurement errors and fast computational resources. To conclude, the application of EIT techniques is a complicated task at all levels: physical, instrumentational, mathematical, computational and interpretational.

1.2.4. Electrical Capacitance Tomography (ECT)

ECT [Kortschak et al., 2006, Soleimani et al., 2007, Makkawi and Ocone, 2007, Liu et al., 2008, Niedostatkiewicz et al., 2009, Hamidipour and Larachi, 2010, Wang and Yang, 2010, Rimpilainen et al., 2011, Rimpilainen et al., 2012, Banasiak and Soleimani, 2010] is similar to EIT but uses the dependence of the capacitance on the permittivity value of a material. To obtain a spatially resolved image of the permittivity distribution inside the pipe, multiple electrodes are arranged at its surface. The difference with EIT is that in ECT, the electrodes are not necessary in contact with the fluid but distributed on the tube and all inter-electrode capacitances are measured. Substances of differing dielectric properties can be distinguished by means of this method.

The forward problem solves the capacitance values from a given permittivity distribution [Yang and Peng, 2002, Ortiz-Aleman et al., 2004, Fang, 2004, Soleimani and Lionheart, 2005, Changhua et al., 2005, Lei et al., 2013]. The relationship between capacitance and the permittivity distribution can be formulated by:

$$C = \frac{Q}{V} = -\frac{1}{V}\int_{\Gamma} \epsilon(\boldsymbol{x})\nabla\phi(\boldsymbol{x})d\Gamma \tag{1.40}$$

where Q is the electric charge, V the potential difference between two electrodes, Γ is the electrode surface, $\epsilon(\boldsymbol{x})$ is the permittivity and $\phi(\boldsymbol{x})$ the electrical potential distributions.

From the given capacitance data, the inverse problem aims at estimating the permittivity distribution. In real applications, the static linearisation image reconstruction model can be simplified as:

$$\boldsymbol{SG} = \boldsymbol{C} + \boldsymbol{r} \tag{1.41}$$

where $\boldsymbol{S}$ is the Jacobian matrix or Sensitivity matrix of dimension $m \times n$, $\boldsymbol{G}$ is an vector of length n standing for the normalised permittivity distributions, $\boldsymbol{C}$ is a vector of length

m indicating the normalised capacitance values and $\boldsymbol{r}$ is a vector of size m representing the capacitance measurement noises. The Jacobian matrix $\boldsymbol{S}$ can be formulated by:

$$S_{i,j}(\boldsymbol{x}) = -\int_{p(\boldsymbol{x})} \frac{E_i(\boldsymbol{x})}{V_i} \cdot \frac{E_j(\boldsymbol{x})}{V_j} d\boldsymbol{x} \tag{1.42}$$

where $S_{i,j}(\boldsymbol{x})$ defines the sensitivity between the i^{th} electrode and the j^{th} electrode at $p(\boldsymbol{x})$, $E_i(\boldsymbol{x})$ is the electric field distribution inside the sensing domain when the i^{th} electrode is activated as an excitation electrode by applying a voltage V_i to it.

The application of suitable algorithms yields the permittivity distribution inside the pipe. Common ECT systems are based on the above description which is itself based on the approximation of a linear relationship between capacitance and permittivity values. Such systems are fast but the reconstruction is not strongly accurate since the true relationship between capacitance and permittivity is strongly nonlinear and cannot be approximated by a linear mapping for high-quality reconstruction purposes [Yang et al., 1999, Warsito and Fan, 2001, Jang et al., 2006, Takei, 2006, Wang et al., 2007, Lei et al., 2011].

1.3. EIT measurement and image reconstruction

We now focus on EIT. There is a large contrast between EIT and other tomographic techniques based on Radon transformation such as CT scan, SPECT or PET. The three main differences are:

- the **worse conditioning of the inverse problem**. This is due to the discretisation of the boundary conditions due to a finite number of electrodes.
- a **more complexe resolution**: EIT constitutes a non-linear inverse problem which makes its resolution much more difficult than in the linear case of Radon transforms.
- the **non straightforward propagation of current through the object**. This is particularly contrasting with X-Ray tomography technique where the photons travels through matter in straight lines.

The discretisation due the electrodes allows several excitation and measurement strategies. The choice on the strategies is important since it directly impacts the ill-posedness of the inverse problem.

In the following, we will firstly review these excitation and measurement strategies for EIT in Section 1.3.1 and the corresponding measurement-times in Section 1.3.2. In a second part, we provide an overview of the image reconstruction principles in EIT. The continuum model of the inverse problem in Section 1.3.3 and the discretisation and resolution of the problem in Section 1.3.4.

1.3.1. Excitation and measurement strategies

There are several excitation strategies, that can be configured with multiplexers (Section 1.4). For a one electrode ring EIT system, the most common excitation patterns are the adjacent and the opposite excitation, measured simultaneously (Figure 1.5) on all available electrodes. However numerous strategies are available:

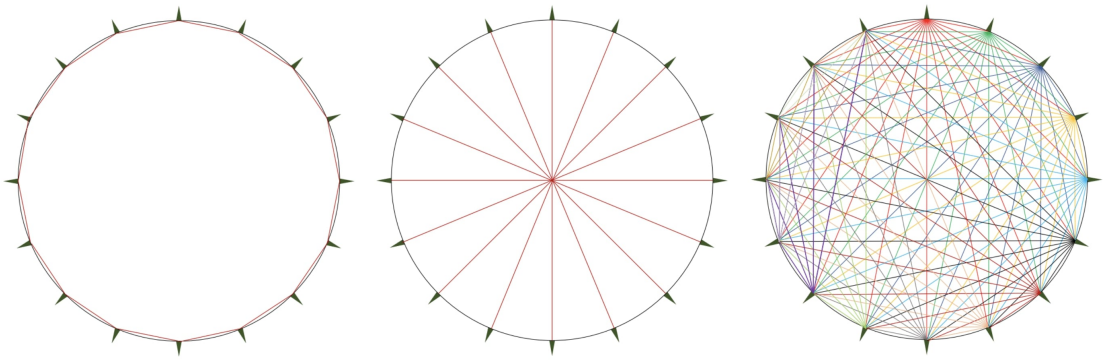

Figure 1.5. – Illustration of the Adjacent excitation pattern (Left), the Opposite (Center) and the Full-Scan (Right) for 16 electrodes. The lines on the schematic are used to show the pairs of excitation electrodes and have no physical meaning. In the last, several colours were used for clarity to show the 120 patterns.

- The **adjacent** (also called **neighbouring**) data collection strategy considers pairs of adjacent electrodes for the excitation. Considering n_e electrodes, the excitation signal of amplitude A follows:

$$\boldsymbol{S}_l^n = \begin{cases} A, & l = k, k = 1, ..., n_e, \\ -A, & l = k+1, k = 1, ..., n_e - 1, \\ -A, & l = 1, k = n_e, \\ 0, & \text{Otherwise.} \end{cases} \tag{1.43}$$

  Note that $\boldsymbol{S}_l^n$ denotes the excitation signal and in applications it can refer to the excitation potential or the excitation current. The measurements concerning 1 or 2 current-injection electrodes are discarded because they are potentially biased by the voltage drop within the electrodes. The strategy yield a good sensitivity in the regions near the electrodes, but is almost insensitive to the centre of the study volume.

- The **cross** strategy is similar to the adjacent strategy, but is skips at least one in two electrodes for the excitation.

- The **opposite** strategy employs pairs of opposite electrodes for current injection.

The excitation pattern follows:

$$\boldsymbol{S}_l^n = \begin{cases} A, & l = k, k = 1, ..., n_e, \\ -A, & l = k + n_e/2, k = 1, ..., n_e/2, \\ -A, & l = m, k = n_e - m, m = 0, ..., n_e/2, \\ 0, & \text{Otherwise.} \end{cases} \tag{1.44}$$

- The **adaptive** strategy [Gamio, 2002] optimises the excitation voltage to maximise the potential on the measurement electrodes on a designated region. It enables simultaneous current flows from all the electrodes which complexifies greatly the experimental set-up.
- The **walsh** strategy [Mueller and Siltanen, 2012] uses simultaneously all the electrodes for the excitation:

$$\boldsymbol{S}_l^n = \begin{cases} A, & l = n \bmod(n_e), ..., (n + \frac{n_e}{2}) \bmod(n_e), \\ -A, & l = (n + \frac{n_e}{2} + 1) \bmod(n_e), ..., (n + n_e - 1) \bmod(n_e), \end{cases} \tag{1.45}$$

- The **full-scan** strategy (Figure 1.5) considers the excitation and measurement of all available pairs of electrodes. This strategy has the benefits that it allows to measure the flow on the edge but also in the center of the pipe with a nearly homogenous sensitivity distribution over the cross-section. The number N of measurements for this strategy is :

$$N = \frac{n_e(n_e - 1)}{2}, \tag{1.46}$$

  giving $N = 120$ for 16 electrodes.
- The **trigonometric** strategy. On a system containing n_e electrodes, there are only $n_e - 1$ linearly independent excitation patterns. Therefore, any other pattern will be a linear combination of these. The Fourier basis functions $e^{in\theta}/\sqrt{2\pi}$ are a natural choice to describe the linearly independent patterns:
  The excitation signal patterns follows:

$$\boldsymbol{S}_l^n = \begin{cases} A\cos(n\theta_l), & n = 1, ..., n_e/2 - 1, \\ A\cos(\pi l), & n = n_e/2, \\ A\sin((n - n_e/2)\theta_l), & n = n_e/2 + 1, ..., n_e - 1. \end{cases} \tag{1.47}$$

  The vector $\boldsymbol{S}^n$ is a discrete approximation of the trigonometric functions on the boundary. More details concerning this excitation pattern can be found in Chapter 6, as a practical implementation is introduced.

The excitation amplitude imposed on the electrodes for some patterns is illustrated in Figure 1.6

Concerning the acquired data, it is either the current passing through the electrodes or the potential between pairs of electrodes that is measured. The strategies can consider

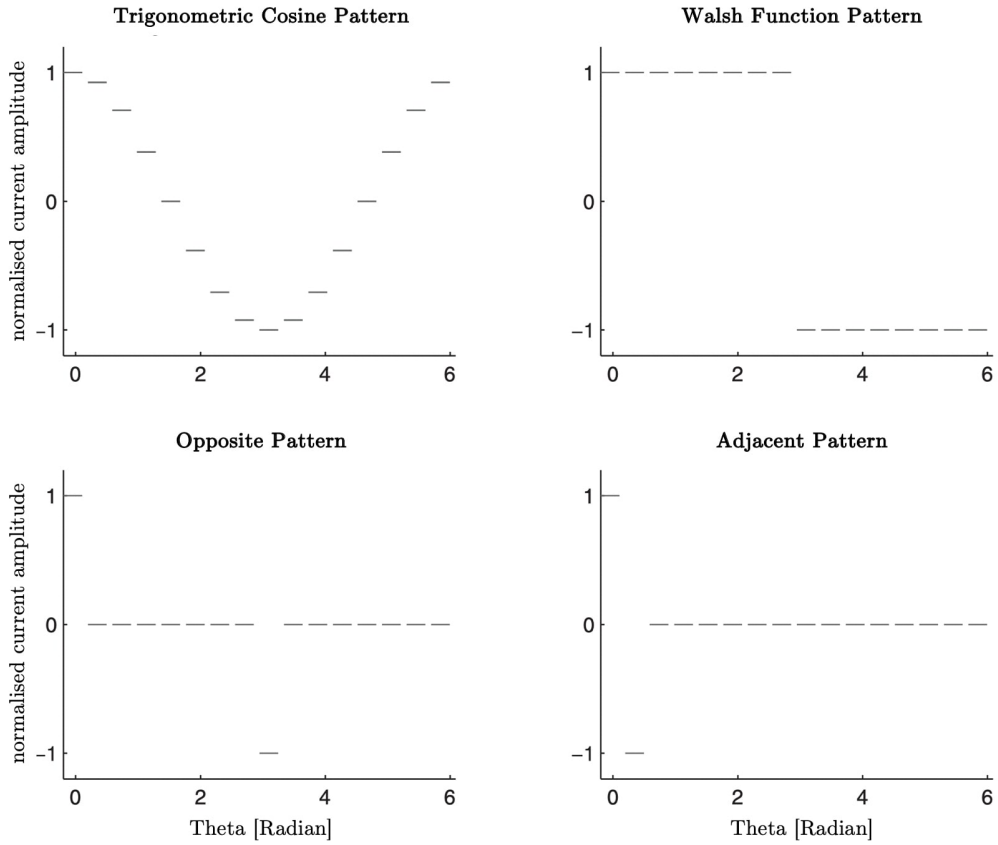

Figure 1.6. – Illustration of four excitation patterns corresponding to a 16 electrode system [Mueller and Siltanen, 2012]. Theta is the angular coordinate of the electrodes.

the measurement at all the electrodes or only at a subset of electrodes. Furthermore, the measurement can be sequential or simultaneous.

The choice of the applied and measured current or potential is very important for distinguishability [Isaacson, 1986, Cheney and Isaacson, 1992, Gisser et al., 1990]. The distinguishability $\delta(j)$ is the ability to detect an object. It depends on the shape and location of this object, the conductivity profile as well as the applied excitation pattern and is defined as:

$$\delta(\sigma_1, \sigma_2, j) = \frac{||\Delta V(\sigma_1, \sigma_2, j)||_{L^2}}{||j||_{L^2}} \tag{1.48}$$

with ΔV the voltage difference and j the current density. The distinguishability is an important parameter to assess the maximum theoretical precision of an EIT system and the best current pattern to apply for a given application.

1.3.2. Measurement duration

We are interested in the typical time to operate the three main excitation patterns: *adjacent*, *opposite* and *full-scan*.

Let's consider n_e electrodes and N to be the number of patterns in one frame. A frame

contains all the excitation and measurement configurations in a given pattern. For the adjacent and opposite excitation strategies, $N = n_e$ and $N = n_e/2$, respectively. For the full-scan strategy, the total set of independent measurements is given by (1.46). It is easy to obtain the total time to measure one frame:

$$T_f = N \times t_m, \tag{1.49}$$

from the time duration t_m of a single measurement, and by considering the excitation strategy and the number of electrodes.

The table 1.1 shows a rough estimation of the time needed to measure one frame for several number of electrodes and strategies. The timing values consider a typical excitation between a pair of electrodes: two sinusoidal period at frequency 50 kHz [Dupré, 2017]. Then, the time for one measurement in this typical situation is $t_m = 4.10^{-5}$ s.

	$n_e = 8$	$n_e = 16$	$n_e = 32$	$n_e = 64$
Adjacent	$N = 8$	$N = 16$	$N = 32$	$N = 64$
	$t_f = 0.3$ ms	$t_f = 0.6$ ms	$t_f = 1.3$ ms	$t_f = 2.6$ ms
Opposite	$N = 4$	$N = 8$	$N = 16$	$N = 32$
	$t_f = 0.2$ ms	$t_f = 0.3$ ms	$t_f = 0.6$ ms	$t_f = 1.3$ ms
Full-Scan	$N = 28$	$N = 120$	$N = 496$	$N = 2016$
	$t_f = 1.1$ ms	$t_f = 4.8$ ms	$t_f = 19.8$ ms	$t_f = 80.6$ ms

Table 1.1. – Number of measurement and time for one frame under several excitation strategies and number of electrodes.

In two phase flow experiments, these values are to be compared with the typical time the flow passes through the detector. If the measurement time is greater, it means that the flow can completely change and comeback to its original state without being identified.

1.3.3. Continuum model of the inverse problem

The boundary conditions can be either imposed in voltage (Dirichlet) or in current (Neumann). Both are linked by the Ohm's law to the electrical properties of the system. In the case where $\sigma(\boldsymbol{x})$ is known, the direct problem of reconstructing the voltage from the imposed current (or equivalently reconstructing the current from the imposed voltage) is called the forward problem and is well-posed.

Let us consider the continuous function m, that contains the imposed and measured boundary conditions. The mathematical model is the following:

$$m = \mathcal{A}(\sigma) + \epsilon \tag{1.50}$$

where $\mathcal{A}$ is the forward map, a nonlinear function of the conductivity field σ, and ϵ is the measurement error. A problem is well posed if it satifies the Hadamard conditions:

- **Existence**: There should be at least one solution.

- **Uniqueness**: There should be at most one solution.
- **Stability**: The solution must depend continuously on data.

Otherwise it is called ill-posed. In practical $\sigma(\boldsymbol{x})$ is unknown and can be reconstructed, knowing the imposed conditions (Dirichlet or Neumann) associated with the measured conditions (Neumann or Dirichlet). In this situation, reconstructing $\sigma(\boldsymbol{x})$ is an inverse problem that is ill-posed, meaning that at least one of the above condition fails.

This section focuses on the ideal situation of a continuous measurement of the voltage-to-current operator (the Dirichlet-to-Neumann map Λ_σ) and the current-to-voltage operator (the Neumann-to-Dirichlet map $\mathcal{R}_\sigma$) in the context of continuum model of EIT. The two dimensional case is also considered with one ring EIT systems. In this situation, EIT is the inverse conductivity problem associated with the Laplace equation (1.39):

$$\nabla \cdot [\sigma(\boldsymbol{x}) \nabla u(\boldsymbol{x})] = 0. \tag{1.51}$$

in $\Omega \subset \mathbb{R}^2$.

The Dirichlet-to-Neumann map

The Dirichlet boundary conditions are imposed with a voltage distribution on the boundary $\partial\Omega$ of the domain Ω:

$$u(\boldsymbol{s}) = V(\boldsymbol{s}) \quad \text{for } \boldsymbol{s} \in \partial\Omega. \tag{1.52}$$

In parallel, the current density distribution j is measured on $\partial\Omega$:

$$j(\boldsymbol{s}) = \sigma(\boldsymbol{s}) \frac{\partial u(s)}{\partial \boldsymbol{n}}, \quad \text{with } \boldsymbol{s} \in \partial\Omega, \tag{1.53}$$

and $\boldsymbol{n}$ the outward-facing unit normal on the boundary. An additional requirement is dictated by Kirchhoff's law of conservation of charges. The Kirchhoff's law imposes that the integral of the current is zero on the border:

$$\int_{\partial\Omega} J da = \int_{\partial\Omega} \sigma \frac{\partial u}{\partial \boldsymbol{n}} da = \int_{\Omega} \nabla\sigma \cdot \nabla u d\boldsymbol{s} = 0, \tag{1.54}$$

by using Green's formula. The so-called Dirichlet-to-Neumann (DtN) map Λ_σ is an operator that links the imposed potential (1.52) to the measured current (1.53) on the boundary:

$$\Lambda_\sigma : u|_{\partial\Omega} \longmapsto \sigma \frac{\partial u}{\partial \boldsymbol{n}}\bigg|_{\partial\Omega} \tag{1.55}$$

By analogy with (1.50), the DtN map is the key to determine the current-density distribution arising from any given voltage distribution over the boundary.

The Neumann-to-Dirichlet map

Equivalently, the Neumann boundary conditions can be imposed, considering u to be the unique solution of (1.39):

$$\sigma \frac{\partial u}{\partial \boldsymbol{n}} = g, \quad \text{on } \partial\Omega, \tag{1.56}$$

with the additional requirement that:

$$\int_{\partial\Omega} u ds = 0 \tag{1.57}$$

in order to define a unique solution. The Neumann-to-Dirichlet (NtD) map $\mathcal{R}_\sigma$ is necessary to assess the voltage distribution from any given current-density distribution:

$$\mathcal{R}_\sigma : \sigma \frac{\partial u}{\partial \boldsymbol{n}}\bigg|_{\partial\Omega} \longmapsto u|_{\partial\Omega} \tag{1.58}$$

By opposition with the photons of X-ray tomography passing through the study domain in straight lines, the propagation of electromagnetic waves in EIT depends on the medium and the "path" is unknown when the composition of the medium is unknown. Hence, u is itself a function of σ and the DtN and NtD maps are nonlinear functions of the electrical conductivity [Mueller and Siltanen, 2012]. The fact that EIT data has a nonlinear dependency on the conductivity is a major difference with the situation of X-ray tomography data that depends linearly on the distribution of the absorption spectrum over the domain.

Functional spaces

Considering k an integer, a function f is in $H^k(\Omega)$ if the squared k^{th} derivative has a finite integral over Ω. The Sobolev spaces with non-integers or negative powers are defined by taking the Fourier transform, multiplying by a power of frequency and requiring that the result is square integrable. Concerning the potential, it must satisfy:

$$\int_\Omega |\nabla u|^2 dV < \infty. \tag{1.59}$$

The physical meaning is to require, provided the conductivity is finite, that the ohmic power dissipated is finite. Sobolev spaces are useful to express the smoothness of a function and its derivatives. These spaces can be also endowed with an inner product since they are Hilbert spaces.

The condition of finite power requires the Dirichlet boundary data $\phi|_{\partial\Omega} \in H^{1/2}(\partial\Omega)$ and the Neumann data $j \in H^{-1/2}(\partial\Omega)$. The DtN operator is then a transformation $H^{1/2}(\partial\Omega) \longmapsto H^{-1/2}(\partial\Omega)$. By opposition, the NtD is $H^{-1/2}(\partial\Omega) \longmapsto H^{1/2}(\partial\Omega)$. We observe that the current density is one derivative less smooth than the potential on the boundary.

For the sake of simplicity, the transformation can be considered as $L^2(\partial\Omega) \longmapsto L^2(\partial\Omega)$

since the Fourier bases is defined on $\partial\Omega$. Some information on Sobolev spaces are deferred to the Appendix I.

1.3.4. Discretisation and resolution

The continuum model (1.50) is an idealization. Namely, the current-density cannot be applied or measured continuously over the surface of the body. In practice, the only accessible measurements are currents along wires that are attached to electrodes at the surface of the system. On the other hand, it is also only possible to measure the voltage on these electrodes. Therefore, the model must include the discretisation of the boundary conditions.

Modeling of voltage and current distributions on the electrodes

The simplest electrode model, the gap model consists in a sub-division of the boundary $\partial\Omega$ into n_e electrodes on which potentials including constant values over the electrodes are given or measured. This is possible to assume that the electrode material is a perfectly conducting. By analogy with (1.52):

$$V = \begin{cases} V_n & \text{for } s \in e_n, \quad n = 1, 2, ..., n_e \\ 0 & \text{for } s \notin \bigcup_{n=1}^{n_e} E_n. \end{cases} \tag{1.60}$$

Here, V_n is the potential on E_n, the n^{th} electrode. Concerning the current in the gap model and starting from (1.56):

$$\sigma \frac{\partial u}{\partial \boldsymbol{n}} = j = \begin{cases} I_n / S_n & \text{for } s \in E_n, \quad n = 1, 2, ..., n_e \\ 0 & \text{for } s \notin \bigcup_{n=1}^{n_e} E_n \end{cases} \tag{1.61}$$

with S_n the surface area and I_n the current of the n^{th} electrode E_n. In this situation, (1.54) and (1.57) become respectively:

$$\sum_{n=1}^{n_e} I_n = 0 \quad \text{and} \quad \sum_{n=1}^{n_e} V_n = 0. \tag{1.62}$$

Using the gap model, the inverse problem ains at finding the conductivity σ inside the body from all possible current patterns $\boldsymbol{I} = (\boldsymbol{I}_1, ..., \boldsymbol{I}_N)$ and their corresponding voltage patterns $\boldsymbol{V} = (\boldsymbol{V}_1, ..., \boldsymbol{V}_N)$ where $\boldsymbol{I}_m$ and $\boldsymbol{V}_m$ with $1 \leq m \leq N$ are vectors of lengths n_e, describing a given excitation and measurement in a strategy containing N patterns [Cheney et al., 1999].

The gap model approximation of constant current-densities over the electrodes is appealing because of its simplicity. However, the electrode material providing a highly conductive path for the current, shunting effects appears when the electrodes of finite area come into contact with the surface of the medium being imaged [Somersalo et al., 1992]. For this reason, the definition of the applied or measured current (1.61) must be

written in terms of a non-constant current-density over the electrodes as:

$$\int_{E_n} \sigma \frac{\partial u}{\partial \boldsymbol{n}} = I_n \quad \text{for } s \in E_n \text{ and } n = 1, 2, ..., n_e \tag{1.63}$$

$$\text{and} \quad \sigma \frac{\partial u}{\partial \boldsymbol{n}} = 0 \text{ for } s \notin \bigcup_{n=1}^{n_e} E_n \tag{1.64}$$

On the other hand, electrochemical effects between the electrodes and the material may cause a thin and highly resistive layer resulting in a *contact impedance* ζ. To account for this phenomenon, another model, the *complete model* were developed [Borcea, 2002, Somersalo et al., 1992, Isaacson and Cheny, 1991] for a more accurate definition of the voltage distribution of (1.60):

$$V_n = u + \zeta_n \sigma \frac{\partial u}{\partial \boldsymbol{n}} \quad \text{on } E_n, \quad n = 1, 2, ..., n_e \tag{1.65}$$

$$\text{and} \quad \sigma \frac{\partial u}{\partial \boldsymbol{n}} = 0 \text{ for } s \notin \bigcup_{n=1}^{n_e} E_n \tag{1.66}$$

where ζ_n is the contact impedance at the surface of the n^{th} electrode.

Finally, (1.39) together with either equations (1.63) and (1.64) or (1.65) and (1.66) and associated with the corresponding condition of (1.62) gives a forward problem with a unique solution, close to the measurement data [Cheng et al., 1989, Somersalo et al., 1992, Isaacson et al., 1991].

The continuum definition (1.50) need to be approximated by a discrete model of the form

$$\boldsymbol{m} = A\boldsymbol{f} + \epsilon, \tag{1.67}$$

where $m \in \mathbb{R}^k$, $A \in \mathbb{R}^{k \times n}$ is a matrix and $\boldsymbol{f}$ is a vector of dimension n.

Singular Value Decomposition

The Singular Value Decomposition (SVD) of the matrix A in (1.67) is a useful tool to inverse the problem in the discretised form [Kerrouche et al., 2001, Bellis et al., 2012]. Matrix algebra stipulates that any matrix A can be expressed on the form:

$$A = UDV^T \tag{1.68}$$

where $U \in \mathbb{R}^{k \times k}$ and $V \in \mathbb{R}^{n \times n}$ are orthogonal matrices and $D \in \mathbb{R}^{k \times n}$ is a diagonal matrix. A is badly conditioned, i.e.:

$$\frac{dn}{dr} \gg 1, \tag{1.69}$$

with $r = \text{rank}(M)$. The elements d_j with $j = 1, ..., r$ on the diagonal of D are the singular values of A:

$$D = \begin{bmatrix} d_1 & & & & \\ & \ddots & & 0 & \\ & & d_r & & \\ & & & 0 & \\ & 0 & & & \ddots \\ & & & & & 0 \end{bmatrix} \tag{1.70}$$

Thanks to the SVD, the continuous inverse problem becomes an eigenfunction problem. From (1.67), writing $\boldsymbol{f} \in \mathbb{R}^n$ as a linear combination:

$$\boldsymbol{f} = \sum_{j=1}^{n} a_j V_j = V\boldsymbol{a}, \tag{1.71}$$

the goal is to find the coefficients $a_1, ..., a_n$ by choosing $\boldsymbol{f}$ to be a minimum norm solution.

Assuming $\boldsymbol{m}' = U^T\boldsymbol{m} \in \mathbb{R}^k$ and using the orthogonality of U, we have:

$$\begin{aligned} ||A\boldsymbol{f} - \boldsymbol{m}||^2 &= ||UDV^TV\boldsymbol{a} - U\boldsymbol{m}'||^2 \\ &= ||D\boldsymbol{a} - \boldsymbol{m}'||^2 \\ &= \sum_{j=1}^{r}(d_j a_j - \boldsymbol{m}'_j)^2 + \sum_{j=r+1}^{k}(\boldsymbol{m}'_j)^2. \end{aligned} \tag{1.72}$$

Given d_j and $\boldsymbol{m}'_j$, the norm in (1.72) reaches its minimum for $a_j = \boldsymbol{m}'_j/d_j$ for $j = 1, ..., r$. A least-square solution is any $\boldsymbol{f}$ of the form:

$$\boldsymbol{f} = V \begin{bmatrix} d_1^{-1}\boldsymbol{m}'_1 \\ \vdots \\ d_r^{-1}\boldsymbol{m}'_r \\ a_{r+1} \\ \vdots \\ a_n \end{bmatrix}. \tag{1.73}$$

where $a_{r+1}, ..., a_n$ are unconstrained coefficients.

The Tikhonov regularisation method

In EIT, the discretisation of the problem is associated to its instability. In other words, a small error ϵ on the data in (1.50) can create very large error in the computed solution $\sigma(\boldsymbol{x})$. To overcome ill-posedness in EIT, two main types of regularisation techniques are commonly used. One is projection methods, such as Truncated Singular Value Decomposition (TSVD). The other is penalty methods, such as the Tikhonov regularisation method which is details in this section.

A priori information can be introduced in the problem to restore its stability. The general way is to find a function $\delta(\epsilon) \to 0$ as $\epsilon \to 0$ such that the stability is satisfied. Considering (1.67), let the data $\boldsymbol{m}^\epsilon \in Y$, with Y a Hilbert space, such that $||\boldsymbol{m}-\boldsymbol{m}^\epsilon|| \leq \epsilon$, and let $A\boldsymbol{f}^\epsilon = \boldsymbol{m}^\epsilon$, then :

$$||\sigma - \sigma^\epsilon|| \leq \delta(\epsilon). \tag{1.74}$$

The degree of ill-posedness is reflected by the behaviour of $\delta(\epsilon)$ as $\epsilon \to 0$. There is no ill-posedness in the case where $\delta(\epsilon)$ is of order ϵ. On contrary, the problem is severely ill-posed if $\delta(\epsilon)$ tends to zero very slowly, such as $\delta(\epsilon) = 1/\log(1/\epsilon)$. These problems are extremely difficult to solve and only approximations of the true solution can be obtain.

Regularisation methods are any method verifying (1.74) to solve the inverse problem from an element M of f^ϵ. Among these methods, the Tikhonov regularisation method is commonly used for linear problems. It consists in considering $M = \{f \in X : ||f-f_0|| \leq \rho\}$ for some $f_0 \in X$, where X is the model Hilbert space and ρ positive. The solution is the vector $T_\alpha(\boldsymbol{m}) \in \mathbb{R}^n$ which is obtained by minimising

$$||AT_\alpha(\boldsymbol{m}) - \boldsymbol{m}||^2 + \alpha||T_\alpha(\boldsymbol{m})||^2 \tag{1.75}$$

in X. Here, $\alpha \in \mathbb{R}$ and $\alpha > 0$ is the regularisation parameter, a penalty coefficient for the regularisation term $||T_\alpha(\boldsymbol{m})||$. We denote

$$T_\alpha(\boldsymbol{m}) = \underset{\boldsymbol{z}\in\mathbb{R}^n}{\operatorname{argmin}} \left(||A\boldsymbol{z} - \boldsymbol{m}||^2 + \alpha||\boldsymbol{z}||^2 \right). \tag{1.76}$$

The Tikhonov regularised solution for the discrete equation (1.67) is

$$T_\alpha(\boldsymbol{m}) = V\mathcal{D}_\alpha^+ U^T \boldsymbol{m}, \tag{1.77}$$

where $A = UDV^T$ is the SVD and

$$\mathcal{D}_\alpha^+ = \operatorname{diag}\left(\frac{d_1}{d_1^2 + \alpha}, ..., \frac{d_{min(k,n)}}{d_{min(k,n)}^2 + \alpha} \right) \in \mathbb{R}^{n\times k}. \tag{1.78}$$

The proof of (1.78) can be found in [Mueller and Siltanen, 2012].

In the context of EIT, the problem (1.75) consists in determining T_α that minimises [Cheney et al., 1990, Gisser et al., 1990, Cheney and Isaacson, 1995, Cheney et al., 1999]:

$$\frac{1}{2}||\boldsymbol{U}(\boldsymbol{\sigma}) - \boldsymbol{V}||^2 + \alpha||\boldsymbol{T}_\alpha(\boldsymbol{\sigma} - \boldsymbol{\sigma}_0)||^2 \tag{1.79}$$

where $\boldsymbol{U}$ is a vector of simulated measurements on the boundary, $\boldsymbol{V}$ concentenates the actual boundary measurements on the electrodes. Moreover, $\boldsymbol{\sigma}$ is the discrete conductivity field and $\boldsymbol{\sigma}_0$ is a reference conductivity field.

The Gauss-Newton iterative method can be used to solve (1.79) with the update $\delta\boldsymbol{\sigma}^i$

of the conductivity profile $\boldsymbol{\sigma}^i$ at the i^{th} iteration being given by

$$\delta\boldsymbol{\sigma}^i = -\frac{\boldsymbol{J}^T\delta\boldsymbol{V} + \alpha\boldsymbol{T}_\alpha^T\boldsymbol{T}_\alpha(\boldsymbol{\sigma} - \boldsymbol{\sigma}_0)}{\boldsymbol{J}^T\boldsymbol{J} + \alpha\boldsymbol{T}_\alpha^T\boldsymbol{T}_\alpha}, \tag{1.80}$$

where "δ" denotes the update of a quantity at each iteration. Here, $\boldsymbol{J} = \delta\boldsymbol{U}(\boldsymbol{\sigma}^i)/\delta\sigma^i$ is the Jacobian matrix and $\delta\boldsymbol{V} = \boldsymbol{V} - \boldsymbol{U}(\boldsymbol{\sigma}^i)$.

Finally, the Gauss-Newton method can be heavy to implement since the Jacobian is updated at each iteration of the algorithm. The Newton's One-Step Error Reconstructor (NOSER) [Cheney et al., 1990] is a method to reduce the computation heaviness. To do so, it considers the penalisation on the diagonal elements of the Jacobian on a single iteration:

$$\Delta\boldsymbol{\sigma} = -\frac{\boldsymbol{J}^T}{\boldsymbol{J}^T\boldsymbol{J} + \alpha\cdot\mathrm{diag}(\boldsymbol{J}^T\boldsymbol{J})}\Delta\boldsymbol{V} \equiv -\mathcal{J}\Delta\boldsymbol{V}. \tag{1.81}$$

Since there is only one iteration, the values are updated once and "δ" is replaced with "Δ". The advantage of this method is that the inverse matrix $\mathcal{J}$ can be pre-computed and implemented for online applications. For this reason, in the present study, this reconstruction algorithm is exclusively considered.

1.4. Towards high frame rate EIT imaging

Developing a fast EIT system and DAQ procedures with an adequate strategy and data frame acquisition rate is a real challenge. The development for fast EIT can be improved on numerous levels and over the past years numerous approaches have been considered. Nevertheless since the 2000's, the main strategy opted to increase the data frame acquisition rate is parallel sampling of all measurement channels.

In this study, I focus on the association of parallel measurements with parallel excitations. In the following, the excitation strategies are classified into two categories that represents two important concepts for EIT and more generally for ET. These concepts are Time-Division Multiplexing (TDM) and Frequency Division Multiplexing (FDM).

This section firstly introduces the concept of multiplexing in Section 1.4.1. Then, TDM is introduced in details in Section 1.4.2 with a bibliography of ET systems based on this strategy in Section 1.4.3. Following an introduction on FDM in Section 1.4.4 with examples of ET systems reported in the literature in Section 1.4.5. We will see the advantages of FDM and why do I have considered this approach in the present study.

1.4.1. Multiplexing

Most of the data-communicating devices typically require a modest amount of data. The communication media usually have a much more effective bandwidth and are used far below their capacities. Moreover, in EIT the data coming from many electrodes compete to access the network and some techniques are essential to use efficiently the datalink.

In the situation where the datalink bandwidth can support all the individual channels

to be transmitted, the datalink medium can be shared by more than one channel. This process of using several channels on the same datalink is called *multiplexing*. Several techniques of multiplexing are available to make the most effective use of the datalink bandwidth capacity. For efficiency, the datalink capacity is shared among a number of communicating sub-links. The most common use of multiplexing is in long-haul communication using coaxial cables, microwave and optical fibers [Kharagpur, 2018].

The general function of multiplexers is illustrated in Figure 1.7. The multiplexer combines the data from n channels and transmit them through the datalink which have a high capacity. In EIT, the channels are the links to the individual electrodes. The combined data can be then demultiplexed at another end to deliver to the appropriate output lines.

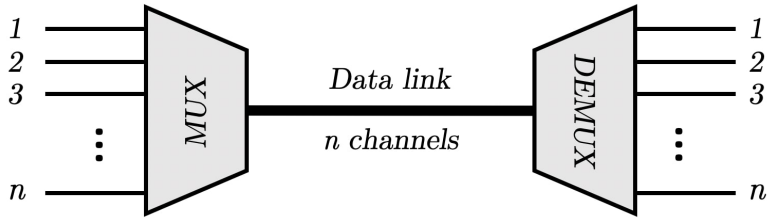

Figure 1.7. – The basic concept of multiplexing. The Multiplexer (MUX) combines the data from n channels, then the data is separated into n channels with the Demultiplexer (DEMUX).

Several techniques for multiplexing can be categorised in the two following types:

- **Time Division multiplexing (TDM)** consists in a time separated distribution of the channels into the datalink. This technique is commonly used for multiplexing of digitised stream. Each channel uses exclusively the datalink for a short burst of time.
- **Frequency Division multiplexing (FDM)** is widely used in radio and TV transmission. The technique consists in divising the frequency spectrum into several logical channels. Each channel has the exclusive possession of a particular frequency band.

The following sections details these two techniques. For each technique, we will overview examples on corresponding ET systems and their performances in term of imaging rate.

1.4.2. Time Division Multiplexing (TDM)

TDM operates with the same frequency at different times. A composite base band signal is formed by an electronic commutator sequentially samples and combines all channel data sources. The composite signal travels through the datalink and is demultiplexed into independent channels with the appropriate timely identification.

During the multiplexing operation, the data is briefly buffered as each buffer is one bit or one character length. The buffers are scanned sequentially to form a composite stream of data from the incoming channels. The scanning operation is fast enough to empty the buffer before the multiplexer re-fill it with new data. Therefore, to assure that

all the data is transmitted, the composite data rate must be at least equal to the sum of the individual data rates. The TDM multiplexing operation is illustrated in Figure 1.8.

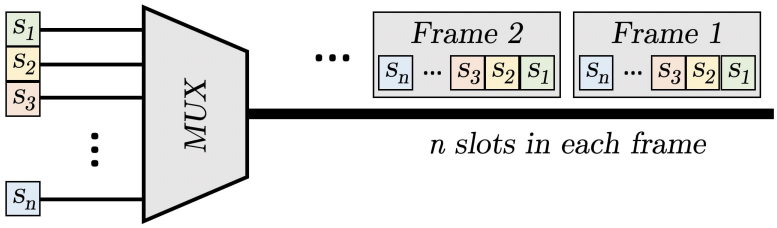

Figure 1.8. – Illustration of the TDM operation. the s_1, ... , s_n are packets of data that are send individually on the datalink. At any given time, the datalink transmit a single packet.

A fundamental task is the synchronisation of the transmission sampling. To do so, one synchronising pulse of time t^p is sent in each cycle along with the sampled pulses. These data pulses together with the control information form a frame where each frame contains a cycle of time slot t^f. In each frame, one or more time slots t^s are dedicated to each source channel. The composite signal in TDM has the disadvantage of including *dead times* between the successive packets t_d^s and between the successive frames t_d^f. This is mandatory to prevent inter-channel cross talks. The frame rate R^{TDM} is then

$$R^{TDM} = \frac{1}{t^f + t_d^f} = \frac{1}{\sum_{i=1}^{n} t^{s_i} + nt_d^s + t_d^f}, \tag{1.82}$$

assuming that the dead time is of same length between all packets. In TDM, the maximum frame transmission rate is at least equal to the data rate of the sources.

In this technique, the time slots are transmitted to the datalink even if there is no data to send in a particular channel. For this reason the technique explained above is also called *synchronous TDM* since each time slot is preassigned to a fixed source. This effect can result in wasted channel capacity depending on the nature of the data to transmit. An efficient alternative consists in dynamically allocating the time slots on demand to separate input channels. This alternative is called *asynchronous TDM*.

1.4.3. High rate ET based on TDM

As in Section 1.3.1 and Section 1.3.2, the time of measurement and performances depends greatly on the excitation strategy. In TDM, the successive measurements implies that increasing the number of independent measurement (i.e. improving the description of boundary conditions) necessarily increases the time.

A disadvantage of TDM is the error imposed by the contact impedance. At the time where the multiplexer switches the curent injection to another electrode, the residual voltage potential on the previous electrode source decays with AC coupling time constant. This effect appears at the electrode/electrolyte interface and has been modelled in [Pollak, 1974, Wang and Ma, 2006]. In most systems, the DAQ procedure would wait the parasitic effects to fade off before starting a new excitation. This process imposes dead times

between each excitations, and reduces greatly the DAQ rate, especially in data taking strategies containing a large number of measurements. In [Wang, 2005], the Authors reports to use a direct coupling, a higher order filter or a clamping and discharging circuit.

Several high-speed EIT systems of hundreds of fps have been proposed in the literature. In [Halter et al., 2008], a multichannel architecture system was presented, containing a control module that manages and synchronises 64 channels capable of generating and measuring voltages and currents. The system was able to collect 182 frames per seconds when acquiring 15 spatial patterns with a Signal-to-Noise Ratio (SNR) from 65.5–96 dB when averaging the signal from 32 samples.

A high performance EIT system is reported by Leeds University [Wang et al., 2005]. The originality of this system is explained by the parallel acquisition of voltage measurements on all 16 channels while using the TDM with an AC sinusoidal current injection. The article reports the use of a novel Over Zero Switching (OZS) scheme which is implemented to limit the transient effects caused by residual potentials arising after the multiplexers switch. The OZS consists in controlling the operation of the multiplexers at the peak value of the current to limiting the amplitude of the transient potential. However, OZS does not reduce its decay time. The measurement is required to capture at least one full period of a sinusoidal signal waveform. The reconstruction of the complex impedance requires at least 4 points per period, imposing that the upper limit of the excitation frequency is a quarter of the sampling frequency. The DAQ rate is reported to be up to 1164 fps with the adjacent data collection strategy.

Another high frame rate EIT system is reported by Cape Town University in [Wilkinson et al., 2005]. The technique uses a DC current pulse to generate the excitation signal. The novel idea of this system is to measure the differential potential between the positive and negative half-cycles. This process cancels out the transient potentials and results in a double-layer capacitance and solution interface. As in [Wang et al., 2005], the systems is reported with parallel data sampling over all measurement channels. The cross data collection strategy is used, with 14 excitation patterns per frames to reach a rate of 1000 fps.

An interesting system is the "Prototype pour Mesures Electriques par Tomographie" (ProME-T, *French*) [Dupré, A. and Ricciardi, G. and Bourennane, S., 2016, Dupré et al., 2017a, Dupré, 2017] EIT system developed by the French Alternative Energies and Atomic Energy Commission (CEA). This system uses a complex multiplexing strategy using two multiplexers to operate the full-scan excitation strategy. The measurement are simultaneously taken on the adjacent pairs of the 16 electrodes. Its design was conceived for a maximal acquisition frame rate of 833 fps with for each image, a total of 1960 data points.

Another EIT system proposed in [Khan et al., 2015] allows capturing over 100 frames per seconds with a SNR of 90 dB when averaging the signal.

Concerning ECT, several systems were also reported in [Wang et al., 2005, Cui et al., 2011, Morales et al., 2015] with high frame rate. In particular, a system called EVT4 is

reported in [Kryszyn et al., 2017] with a design claiming to provide 10000 fps. However, only 30 fps have been demonstrated with 16 electrodes.

All these systems have in common that high speed is reached at the price of a small number of electrodes, a partial scanning strategy, or short measurement times.

1.4.4. Frequency Division Multiplexing (FDM)

By opposition with TDM, the data-link available bandwidth in FDM is subdivided into several smaller spectral bands which are independent frequency channels. Each band carries an independent message signal. These signals are injected into a frequency band thanks to modulation techniques, which are combined by the multiplexer by a linear summing operation (Figure 1.9). The resulting composite signal is transmitted through the single datalink and discriminated by a process called *demultiplexing*. The carriers used to modulate the individual signals are called *sub-carriers*, as shown as $f_1, f_2, ..., f_n$ in the top right of Figure 1.9.

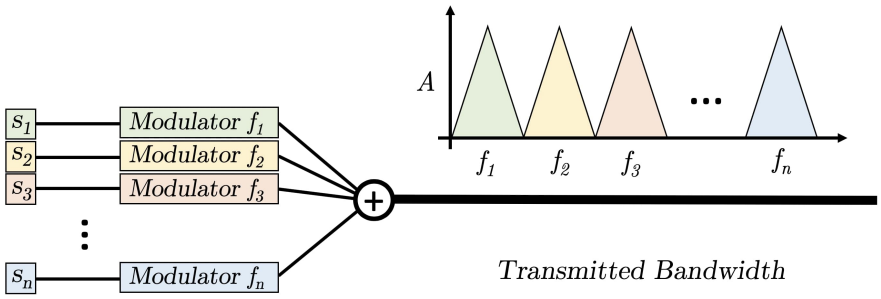

Figure 1.9. – FDM multiplexing process.

In the receiving signal (Figure 1.10), the sub-carriers are separated with a bank of band-pass filters into their individual frequency channels. After each filter, the output is then demodulated and distributed to the output channels.

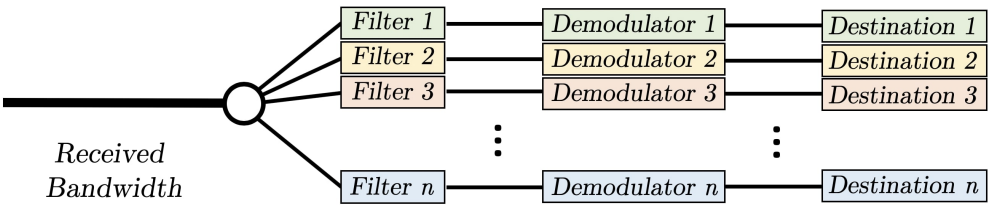

Figure 1.10. – FDM demultiplexing process

The channels in the composite signal must be separated by strips of unused bandwidth, called *guard bands*, to prevent inter channel cross-talk. The analogy of the guard bands are the dead times in TDM. The advantage here is that guard bands do not increase the measurement time. The frame rate in FDM is simply given by:

$$R^{FDM} = f_1, \tag{1.83}$$

where f_1 is the lowest frequency band. This frequency depends on the performances of the DAQ system and can be very high by comparison with R^{TDM}.

The main application of FDM can be found in radio broadcasts and TV communications. Each radio or TV channel in a certain broadcast area is allocated to a certain frequency band, so that several independent channels can be transmitted simultaneously. For example, the AM radio uses 540 to 1600 KHz and the FM radio uses 88 to 108 MHz frequency bands. The receiving user applies a filter in a particular frequency band to choose a channel.

Another example of FDM is the telephone. The typical telephone cable has a frequency bandwidth of 48 KHz in the 70 to 108 KHz range. Considering that the frequency band used for voice transmission in telephone network is 4 KHz, twelve sub channels can be carried by the telephone cable.

Another concept close to FDM is Wavelength Division Multiplexing (WDM) for optical signal transmission in optical fibres. The concept of combining different frequency signals is the same, however in WDM, the implied frequencies are very high. The bands of light channels in the combined signal are very narrow, and are multiplexed with a prism. At the receiving end, another prism is used to decompose the signal.

1.4.5. Multi-Frequency (MF) and FDM for high rate ET

FDM is based on the generation of MF excitation signals. We will first overview ET systems in which MF operations is considered. Then we will focus on the specific use of FDM for EIT.

MF ET systems

Numerous ET systems have been developed based on a MF excitations and measurements. These techniques do not necessarily use FDM, but depending on the applications, the effects of MF on the system response can give additional information on the measurement.

MF EIT has been used in reconstructing the distribution of conductivity of the region of investigation by fusing the spatiotemporal data of tissue conductivity measured at different frequencies [Osterman et al., 2000, Wi et al., 2014, Malone et al., 2014, Zhou et al., 2015, Yang and Jia, 2017, Goren et al., 2018]. In ECT, simultaneous excitation strategies have been applied in multiphase flow studies [Wang et al., 2009, Yang and Peng, 2013, Zhang and Soleimani, 2016, Yang et al., 2017b]. MF tomography has been used in tomographic applications involving other sensor modalities, e.g. magnetic induction, acoustic and acousto-optic modalities. [Wu et al., 1994, Scharfetter et al., 2008, Donadio et al., 2008].

Besides, MF bioelectrical impedance analysis [Baumgartner et al., 1989, Salmi, 2003, Utter and Lambeth, 2010, Palle et al., 2016] was introduced mainly in medical applications and especially in sports medicine. Multiple frequency bioelectrical impedance analysis was used in obtaining bioimpedance data at several different frequencies for quantification

of extracellular water at low but spot frequencies (1.0 kHz and 5.0 kHz), and total body water at higher spot frequencies (100 kHz, 200 kHz, or 500 kHz). Bioimpedance spectroscopy presented in the same study for bioimpedance measurements across a range of frequencies (5 kHz - 1000 kHz).

An interesting study describing numerical techniques relevant for anomaly distribution using MF EIT is presented in [Ammari et al., 2017].

In all MF systems described above, the purpose is somewhat different from our topic of increasing the imaging rate by improving the DAQ strategy with MF.

FDM for EIT systems

By opposition to TDM, increasing the number of measurements in FDM does not directly increase the measurement time but the number of involved frequencies. There is few example of FDM applied to EIT in the literature. To the best of my knowledge, the following content is an exhaustive bibliography on EIT studies that considers the implementation of FDM.

The concept of FDM in EIT applications was introduced in [Teague, 2002] with the use of a dual-plane impedance tomography system to calculate the individual mass flow rates of the components in an air-gravel-seawater mixture. A dual-plane 16-electrode FDM impedance tomography system has been developed that operates at an online real-time frame rate of approximately 280 fps for a two-phase image reconstruction or three-phase volume fraction prediction. In this system, 8 electrodes have been used for excitation and the 8 others for measurement. In this work, it has been shown that this technique provides a means for performing online real-time reconstructions at a far higher frame rate than standard TDM EIT systems with minimal loss in resolution for a given number of electrodes. Subsequently, it enables tomography to be used in industrial applications where previously the limited frame-rates of tomography systems were a hindrance, such as online multi-phase flow meters.

In [Granot et al., 2007], a similar excitation strategy based on FDM is considered. The interest of FDM in this particular biomedical applications is that using different frequencies has important implications due to dispersions as the tissue's electrical properties change with frequency. The study includes a noise analysis, image reconstruction comparison with simulation, and confrontation of the results with time division multiplexing EIT and trigonometric excitation strategy. A prototype was built and tested to show that the method with FDM can give results that are comparable with TDM methods. The prototype contains 16 electrodes where 8 are used for current injection and 8 others for voltage measurement. The excitations are seven sinusoidal signal waveforms of seven frequencies, imposed on seven excitation electrodes while the remaining one is grounded. The conclusion confirms that it is possible to inject several currents concurrently, even within a narrow frequency band, and still separate them and treat them independently.

In [Dowrick and Holder, 2018], Phase Division Multiplexing (PDM) is used where multiple out of phase signals can be injected at each frequency and investigated to increase temporal resolution. TDM, FDM and PDM were compared in head tank experiments,

to compare transfer impedance measurements and spatial resolution between the three techniques. The temporal resolution presents improvement of an order of magnitude the TDM approach, and the approach addresses the limited spatial resolution of FDM by increasing the number of simultaneous EIT injections, reducing the spectral band of the combined data.

The hardware and software used along with the hardware-software integration in these MF EIT, ECT, other tomographic applications and bio-imepedance measurements set-up are somewhat different to those presented in this thesis since they do not answer our main problematic of significantly increasing the imaging rate. This objective requires to simultaneously measure a large number of independent measurement. Therefore to valid the discriminability of several signals simultaneously imposed on a single electrode.

In [Dupré and Mylvaganam, 2018], a proof-of-principle experiment predicted the feasibility of the demodulation of simultaneous excitations on a single electrode with respect to their frequencies, based on a four-electrode EIT system. The study reports a novel concept for soft-field tomography, building upon the Multiple-excitation multiple-receiving capacitance tomography technique and the fully simultaneous excitation principle.

The method is called ONE-SHOT, for ONe Excitation for Simultaneous High-speed Operation Tomography and will be detailed in Chapter 3. Using "off-the-shelf-modules", a dedicated hardware is designed allowing for simultaneous excitation of all electrodes with linear superposition of multiple sinusoidal waves at different AC frequencies and simultaneously monitoring the current in the sensing resistors. Digital demodulation of sampled signals is proposed to extract the frequency components of interest in the system response. As compared to the sequential excitation technique, an increasing number of samples is available for digital demodulation leading to considerable reduction in the effects of white noise in the system response. The real breakthrough in the proposed signal processing methods is the simultaneous excitation of all electrodes at once, which improved suppression of transients in high-speed operation. The ONE-SHOT method consists in single excitation pattern that can be set continuously, thereby eliminating problems due to contact impedance and transients in many high-speed EIT applications.

The benefit of the method regarding the insensitivity to transients has been further analysed with SPICE circuit simulation models in [Dupré and Mylvaganam, 2018]. While high speed operation with the TDM method can be strongly affected by transient voltage bias caused by contact impedance, the ONE-SHOT method is insensitive to transients since the excitation is set continuously. However in this preliminary work, the Authors reports that the SPICE simulation results with the ONE-SHOT method are unstable. The most probable reason is the spectral leakage during DFT computation. Estimates based on averaging were used to compensate the numerical artefacts.

"What does it mean to be a good person?" — *Aristote*
"What does it mean to be?" — *Descartes*
"What does it mean?" — *Nietzsche*
"What does 'it' mean?" — *Bertrand Russel*
"What does it?" — *C.S. Lewis*
"What?" — *M. Darnajou (working on this chapter)*

2

EIT System - Electromagnetic Modeling and Simulations

The research presented in this work focuses on the non-invasive measurement of fastly evolving two-phase flows in an hydraulic loop with EIT. The EIT sensor (Figure 1.4) is a cylinder that is plugged in the loop. it includes one or several rings of electrodes. When designing an EIT sensor, the requirements relative to the pipe itself (diameter, length, connection...) must fit in the measurement position that is imposed or chosen at the very beginning of the experiment. Another task in designing an EIT detector concerns the determination of the physical characteristics of the electrodes. Furthermore, the robustness of the device (material, thickness, deformation...) considers the environment (pressure, temperature, chemistry, radioactivity...) inside and outside the pipe. In any cases, it is required for the interior layer of the pipe in the EIT system to be insulated to avoid perturbing the measurement...

Contents

2.1 Simulation softwares . . . 84
2.1.1 EIT reconstruction software . . . 84
2.1.2 Finite element method in C++ . . . 84
2.1.3 Weak formulation in a finite element space . . . 85
2.2 EIT images with several configurations . . . 86
2.2.1 Adequate number of electrodes . . . 86
2.2.2 Mesh generation . . . 87
2.2.3 Effects of noise on simulated EIT data . . . 91
2.3 Leakage of current . . . 93
2.3.1 The utilisable energy . . . 94
2.3.2 Quantification of the leakage of current . . . 97
2.3.3 Maximum of utilisable energy . . . 100
2.3.4 The role of the form factor $\mathcal{F}$ . . . 101
2.4 Sensitivity maps . . . 103
2.4.1 Continuous formulation of the sensitivity . . . 104
2.4.2 Computation of the sensitivity map . . . 106
2.4.3 Reconstruction with locally imposed conductivity variations . . . 107
2.4.4 Sensitivity of the full-scan strategy . . . 108
2.5 Effects of the leakage of current on the sensitivity . . . 111
2.5.1 Continuous formulation of the sensitivity map with leakage of current 111
2.5.2 3D simulations . . . 112

All the parameters concerning the physical dimensions of the EIT sensor can be divided into the following three categories.

The first category of parameters concerns the fundamental constraints of the experiment. These constraints are imposed at the very beginning since they correspond to the experimental context. More precisely, they are given by the characteristics of the thermo-hydraulic loop in which I plan to install the EIT sensor. These parameters are:

- the **diameter of the pipe** $\mathcal{D}$,
- the **length of the test section** $\mathcal{L}_{EIT}$,
- the **temperature**,
- the **electro-chemical characteristics of the flow**, including its real electrical conductivity σ.

Another parameter that is not necessarly included is the electromagnetic noise in the laboratory. The dimensioning of the sensor itself is not affected directly by this parameter but it can imply discussions on the length of the cables or the necessity for shielded signals.

The second category of parameters concerns the software integration for the image reconstruction. These are:

- the **number of degrees of freedom**,
- the **Geometric features** (Smaller on the boundaries, Adaptive, ...).

There is other parameters that belongs to this category such as the reconstruction method, the regularisation parameter α... This Chapter focuses on the hardware dimensioning and not determination of these other parameters. The literature reports a wide variety of methods for the reconstruction [Mueller and Siltanen, 2012].

Finally, the third category of parameters concerns the load specifications for the EIT sensor itself. These are:

- the **material** (electrodes and insulated layer)
- the **number** n_e of electrodes,
- the **angular size** of the electrodes,
- the **length** $\mathcal{L}_E$ of the electrodes,

Since the electric potential is imposed during measurements, the image reconstruction quality is a-priori optimised with the largest area of the electrodes.

In this chapter, simulations with two different softwares are used to find the optimal parameters for the sake of increasing the measurement performances. The Section 2.1 is an introduction to the softwares and methods used along this chapter. Section 2.2 contains the first approach to determine some dimensioning parameters. Section 2.3 relates the apparition of a leaking current from the electrodes to the neighbouring pipes elements in the thermo-hydraulic loop. A simulation of the leakage of current at electrodes was used to find the adequate length of the electrodes that maximises the energy at their surfaces. Section 2.4 introduces the sensitivity map of the EIT measurements and validates the

results with an independent computation approach. Finally, Section 2.5 presents the preliminary results for the integration of current leakage effects on the sensitivity in a 3D simulation.

2.1. Simulation softwares

This section is a short overview of the softwares used for the following numerical simulations. Firstly, a software specially used for EIT simulations is introduced in Section 2.1.1. Then, a `C++` software based on the Finite Element Method (FEM) is presented in Section 2.1.2. Finally, a fundamental mathematical tool for numerical simulation, the weak formulation of equations, is explained in Section 2.1.3 with a practical example.

2.1.1. EIT reconstruction software

The results obtained in the following Section 2.2 are based on `EIDORS` for Electrical Impedance and Diffuse Optical tomography Reconstruction Software, a code for EIT simulations. `EIDORS` provides software algorithms for forward and inverse modelling for EIT and diffusion based optical tomography, in medical and industrial settings. It aims to solve the following problem [Barber and Brown, 1984] : By applying a current on the surface S of a body B and measuring the induced voltages at the surface, reconstruct the image of the conductivity inside the body.

The original version, `EIDORS V.1` [Vauhkonen et al., 1998, Vauhkonen et al., 2001], is implemented as a package for two-dimensional mesh generation on `MATLAB`, solving the forward problem and reconstruction to display the images. A three-dimensional mesh generation, `EIDORS3D`, has been implemented in [Polydorides and Lionheart, 2002]. The last version, `EIDORS V.3` [Adler and Lionheart, 2006], provides features that are detailed in Appendix II.

2.1.2. Finite element method in C++

The numerical calculations performed in the following Section 2.3, Section 2.4 and Section 2.5 uses the `C++` open source software `FreeFEM++` [Hecht, 2012] for Free Finite Element Method in `C++`. This freeware uses the FEM to solve partial differential equations numerically. It is not a package but an integrated product with its own high level programming language. This software runs on all `UNIX OS` (with `g++ 3.3` or later, and `OpenGL`) , on `Window XP`, `Vista` and 7,8,10 and on `MacOS 10 intel`.

The strongness of `FreeFEM++` is its high adaptability to handle arbitrary finite element spaces and adapt meshes. It is suitable to simulate the phenomenology of electromagnetism in EIT. The characteristics of `FreeFEM++` are detailed in Appendix III.

2.1.3. Weak formulation in a finite element space

The design of `FreeFEM++` requires the problem to be expressed in its variational or weak formulation. The weak formulation of equations is an important tool for the mathematical analysis. It permits to extrapolate concepts from linear algebra to solve a wide variety of problems in other fields such as diferential equations.

The weak formulation consists in expressing a weak solution with respect to a test function, or test vector. Let V be a Banach space and let us consider the equation

$$Au = f \tag{2.1}$$

where $A : V \to V'$, $f \in V'$ and V' the dual of V. Finding a solution $u \in V$ in (2.1) is equivalent to find $u \in V$ such that for all test function, or test vector $v \in V$ holds:

$$[Au](v) = f(v). \tag{2.2}$$

The weak formulation on its generic form consists in finding $u \in V$ such that

$$a(u, v) = f(v) \quad \forall v \in V. \tag{2.3}$$

with $a(u, v)$ the bilinear form defined as:

$$a(u, v) = [Au](v). \tag{2.4}$$

As an example, let's consider the Poisson problem

$$-\nabla^2 u = f, \tag{2.5}$$

on a domain $\Omega \subset \mathbb{R}^d$ with $u = 0$ on its boundary. The weak formulation uses the L^2-scalar product

$$\langle u, v \rangle = \int_\Omega uv dx. \tag{2.6}$$

Testing with differentiable function v gives:

$$-\int_\Omega (\nabla^2 u) v dx = \int_\Omega f v dx. \tag{2.7}$$

By integrating by parts, using the Green identity and assuming that $v = 0$ on $\partial\Omega$, we get the weak formulation of Poisson's equation:

$$-\int_\Omega \nabla u \cdot \nabla v dx = \int_\Omega f v dx. \tag{2.8}$$

The generic form is obtained by:

$$a(u, v) = \int_\Omega \nabla u \cdot \nabla v dx \tag{2.9}$$

and

$$f(v) = \int_{\Omega} f v dx. \tag{2.10}$$

In `FreeFem++` the variational formula is directly input in the code, defined in a finite element space.

A finite element space V_h is a space of polynomial functions on elements, here triangles, with certain matching properties at edges, vertices etc. In `FreeFEM++`, V_h is the space of continuous functions which are affine in x, y on each triangle T_k with $k = 1, ..., n_t$ and n_t the number of triangles. V_h has certain matching properties at edges or boundary conditions. As it is a linear vector space of finite dimension, basis can be found. The canonical basis is made of functions, called the hat functions ϕ_k which are continuous piecewise affine and are equal to 1 on one vertex and 0 on all others. Then,

$$V_h(\mathcal{T}_h, P_1) = \left\{ w(x,y) \middle| w(x,y) = \sum_{k=1}^{D} w_k \phi_k(x,y), w_k \in \mathbb{R} \right\} \tag{2.11}$$

where $\mathcal{T}_h$ refers to the family $\{T_k\}_{k=1,...,n_t}$, D is the dimension of V_h, i.e. the number of vertices. The w_k are called the degree of freedom of w and D is the number of the degree of freedom.

In (2.11), P_1 refers to the behaviour of the continuous functions at the edge of the triangles [Hecht, 2012]. Among a long list of available functions given in Appendix III, the balance between satisfactory images and computational speed were found by using `P2` continuous piecewise quadratic functions.

2.2. EIT images with several configurations

In the following, `EIDORS` is used in order to simulate the first approach for reconstructing an image from impedance measurement. In the following analysis, the images of several flow patterns are reconstructed using several designs and number of electrodes to compare them. An example of script used in the following can be found in Appendix II. The analysis presented in this Section 2.2 was accomplished during the very first few months of the PhD as a way to understand the behaviour of EIT under different configurations. The results are known matter in the field of EIT and not necessary used in the rest of this work.

In Section 2.2.1, the simulation with several number of electrodes shows the differences on the expected image reconstruction. The Section 2.2.2 is an analysis on the mesh design and density to reconstruct the image. Finally, the effects of noise on the EIT data is investigated in Section 2.2.3.

2.2.1. Adequate number of electrodes

As discussed in Section 1.3, a large number of measurements is required to well condition the inverse problem for an accurate and stable solution. Consider an EIT

device containing a set of n_e electrodes. The maximum number of measurements is:

$$M = N \times n_e, \tag{2.12}$$

where N is the total number of independent excitation pairs, i.e.:

$$N = \frac{n_e\ (n_e - 1)}{2}. \tag{2.13}$$

As $M \sim n_e^3$, the dataset size increases rapidly as the number of electrodes increases. One can expect that larger values of the parameter n_e lead to images of better quality.

To evaluate this, synthetic data of several flow patterns with EIT sensors containing $n_e = 8$, 16, and 32 electrodes are computed with `EIDORS`. The data are associated with an image based on the linear back projection reconstruction algorithm (Section 1.3). This non-iterative method projects the set of voltage variations $[\delta V_n]$ between homogenous and an inhomogeneous conductivity data onto the maps of conductivity change $\delta\sigma(\boldsymbol{x})$ with a set of sensitivity coefficients S calculated with a linearised version of the inverse problem [Kotre, 1993].

In the simulations of Figure 2.1, the domain is filled with homogenous water of conductivity 0.5 S.m^{-1} with the addition of steam bubbles of conductivity 1×10^{-5} S.m^{-1}. Three patterns are represented in the figure. The number of measurements is $M = 224$ for $n_e = 8$, $M = 1\ 920$ for $n_e = 16$, and $M = 15\ 872$ for $n_e = 32$. For every pattern, increasing n_e improves the image quality, as expected. However, the situation $n_e = 32$ does not give much more accuracy than $n_e = 16$, even if the number of measurements is multiplied by more than eight.

In the following Chapter 3, Chapter 4 and Chapter 6, a high frame rate EIT system is created and brings an important amount of data. From the result of Figure 2.1, the balance between high image accuracy and low data size led to develop an EIT system with a specific number of 16 electrodes. According to (2.13), the full set of excitations for an EIT system of 16 electrodes is $N = 120$.

2.2.2. Mesh generation

We are now interested in the mesh refinement effects on the image. In this Section, an air bubble in water is simulated with different mesh refinements using `EIDORS` in EIT sensors containing 16 electrodes.

The function `MK_COMMON_MODEL` creates mesh for common EIT FEM models (Figure 2.2). By using this function, the user do not need to re-write common code. The input parameters are:

- `a-j` → Mesh density
- `2d` → 2D Distmesh model
- `0-4` → element refinement
- `c` or `s` → Circular or square model.

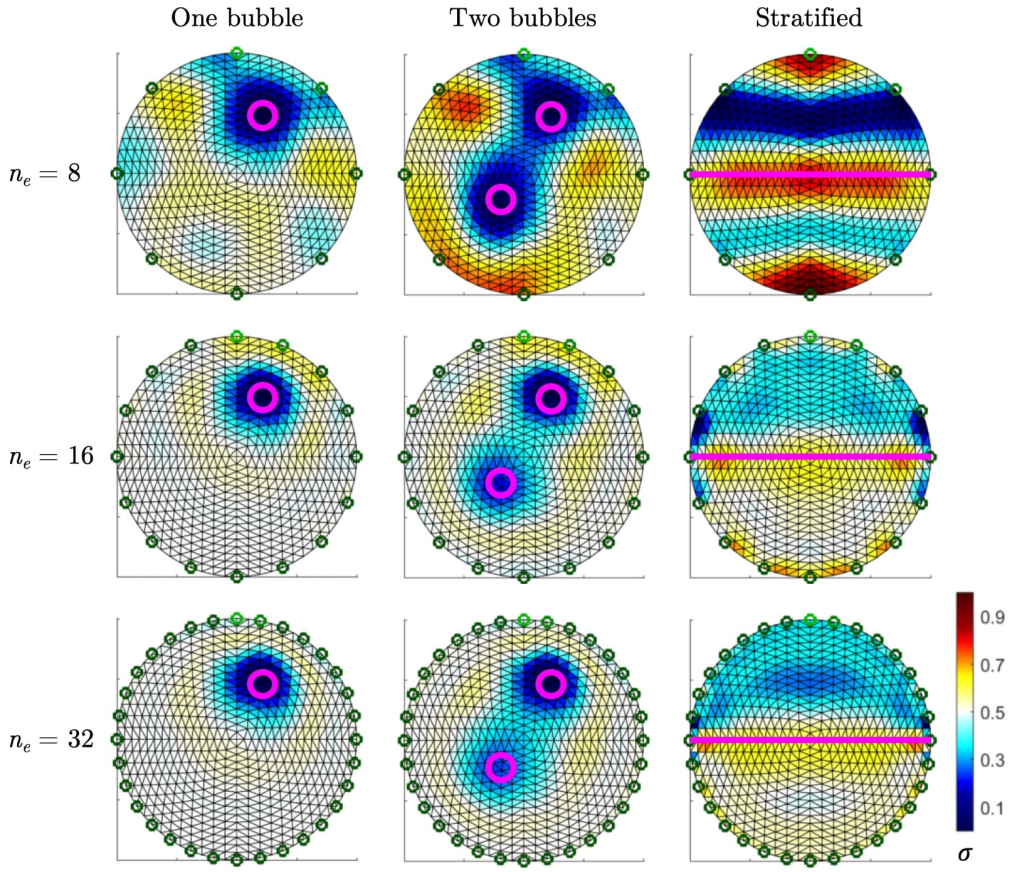

Figure 2.1. – Image reconstruction using linear back projection from simulated data of bubbles in liquid for EIT detectors containing 8, 16, and 32 electrodes, represented with the green circles. On the left, one bubble of diameter 0.1 $\mathcal{D}$, with $\mathcal{D}$ being the diameter of the pipe. In the middle, two bubbles of the same diameter. On the right, stratified flow. The gas–liquid interface is shown with the purple line.

In the last, `c` are models with point like electrodes and `C` use the complete electrode model, with two nodes per electrode. The code also provides thorax model for medical application as well as 3D models.

Mesh density

The following 2D circular models with 16 electrodes were simulated with a bubble of size $0.1\mathcal{D}$ with $\mathcal{D}$ the inner diameter of the pipe. Several mesh densities are investigated as listed in Table 2.1. The Figure 2.3 shows the real image and the reconstructed image for several mesh densities. As discussed in Section 1.3.1, the number of patterns for the full-scan is equal to the number of independent measurements and is given by (2.13). The target number N of mesh elements is 120 in the case of Figure 2.3, with 16 electrodes. The other images with higher mesh refinement shows smoother variation at the periphery of the bubble. In fact these images overdetermine the problem since there is more mesh elements than independent measurement. The image may be smoother but actually, the

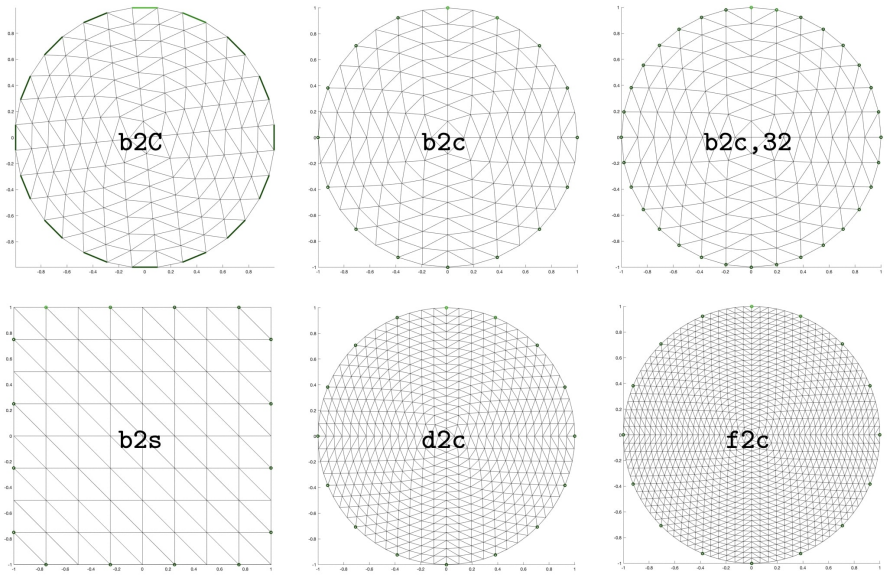

Figure 2.2. – The function `MK_COMMON_MODEL` for different shapes and number of electrodes.

Table 2.1. – List of function inputs and the resulting output for the mesh generation.

Function Input	**Mesh output**
`MK_COMMON_MODEL(a2C,16)`	2D circ model (64 elems)
`MK_COMMON_MODEL(b2C,16)`	2D circ model (256 elems)
`MK_COMMON_MODEL(c2C,16)`	2D circ model (576 elems)
`MK_COMMON_MODEL(d2C,16)`	2D circ model (1024 elems)
`MK_COMMON_MODEL(e2C,16)`	2D circ model (1600 elems)
`MK_COMMON_MODEL(f2C,16)`	2D circ model (2304 elems)

results brings no additional information on the bubble position and shape. Furthermore, a higher number of degrees of freedom elements increases the reconstruction time.

On the other hand, a number of simulated mesh smaller than N, results in a loss of informations. The design target should be a number of degrees of freedomh as close as possible to N.

Finally, another result of the simulation concerns tiny bubbles. It is observed that with 16 electrodes, the size of the smallest detectable objet is $0.05\mathcal{D}$.

Mesh design

The geometric features of the mesh that indicates the conductivity is also important. It will be introduced in Section 2.4 that the measurement is more sensitive near the boundary. Therefore, it is preferable to take smaller mesh elements on the edge of the domain. On the other hand, the mesh elements cannot be taken too small [Cheney et al., 1990]. In the case where an element is significantly smaller than the smallest

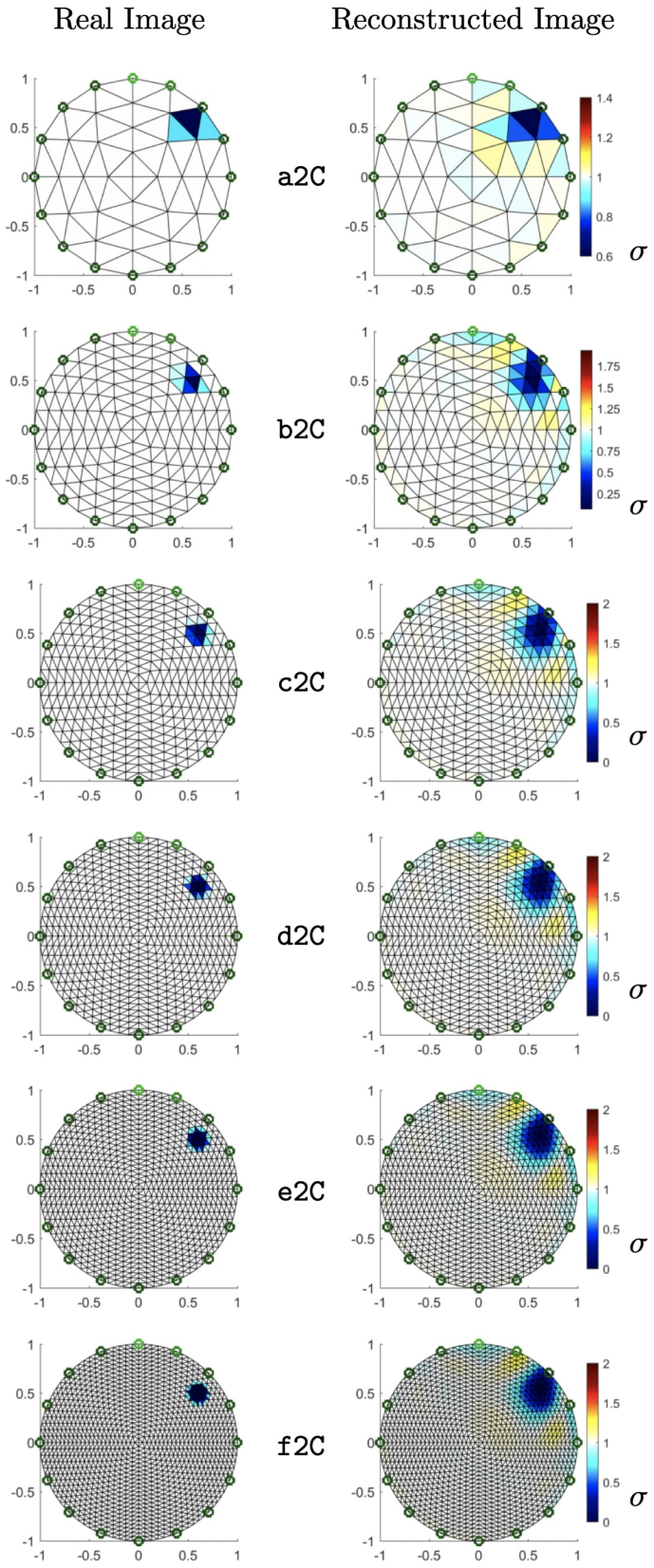

Figure 2.3. – The image of a bubble (with conductivity 1×10^{-5} S.m^{-1}) of diameter $1/10\mathcal{D}$ in a medium of constant conductivity value 0.5 S.m^{-1}.

detectable object, then several conductivity distributions will result in the same data and the reconstruction problem may have several solutions: it may be badly conditioned.

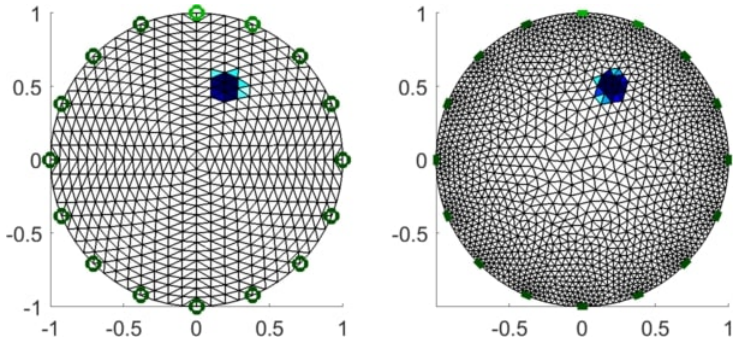

Figure 2.4. – On the left, system with mesh size independent of the radius. On the right, mesh refinement on the edges, where the sensitivity is higher.

In Figure 2.4, two mesh designs were chosen and compared to reconstruct the image of an air bubble in water with an EIT sensor containing 16 electrodes.. The liquid phase in the bottom is considered with an arbitral conductivity of $\sigma = 0.5$ S.m^{-1} and the gas phase with $\sigma = 1 \times 10^{-5}$ S.m^{-1}. The first simulation were created with 2635 elements and constant mesh density over the pipe radius, the second simulation contains 3270 elements with a density gradient. The image in the second design shows a better contrast.

2.2.3. Effects of noise on simulated EIT data

Let's now consider the case where we apply on the electrodes a set of current $\boldsymbol{I}^1$, $\boldsymbol{I}^2$, ... , $\boldsymbol{I}^k$ with $\boldsymbol{I}^k = (I_1^k, I_2^k, ..., I_L^k)$. If we knew the conductivity, we could compute the voltages that would be produced by the applied current pattern.

Unlike in the numerical simulation, the signals at the electrodes during real acquisition are much more chaotic, the signal at fundamental frequency is overlapping with higher order harmonics, background noises, etc. To assess the strength of noises, two parameters with a unit of decibels (dB) are introduced: Total Harmonic Distortion (THD) and Signal to Noise Ratio (SNR).

$$THD = 10 \cdot log_{10} \left(\frac{P_{\text{fundamental freq.}}}{\sum P_{\text{higher order harmonics}}} \right). \tag{2.14}$$

$$SNR = 10 \cdot log_{10} \left(\frac{P_{\text{fundamental freq.}}}{\sum P_{\text{all other freq.}}} \right). \tag{2.15}$$

The graph of SNR/THD changing with signal amplitude (Figure 2.5) were obtained [Dupré et al., 2017b] after analysing the signals of various amplitudes measured on the 16 channels at $f_{exc} = 5kHz$. In this experiment, the results are obtained using the hardware that will be detailed in Chapter 3. As we can see, the fundamental signal power is far lower than the noise. While according to [Dupré et al., 2017b], most of the noises can be

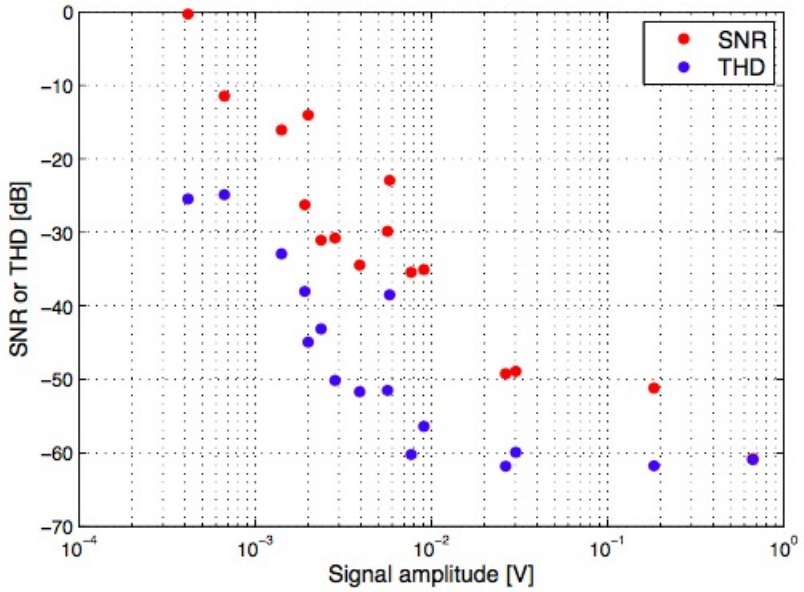

Figure 2.5. – THD and SNR of signals on 16 measurement channels for 1 VAC 5 kHz excitation

filtered mathematically by applying Fourier Transform to the original signals (transferring from time domain to frequency domain) and abandoning the signals of all frequencies other than excitation frequency. Thus, the signals used for image reconstruction have quite a low noise level, and might be neglected.

In this simulations, four different levels of SNR noises (different values of standard deviation) are added to the signal, that is, 1 dB, 5 dB, 10 dB, 20 dB (n dB noise means that the noise power is $10^{\frac{n}{10}}$ times of the fundamental signal power). A number of electrodes n_e =16, 32 and 64 with adjacent excitation and measurement strategy are set up, some results are showed in Figure 2.6. As we can see, for all cases the quality of the reconstructed image is strongly affected by noise, and with a higher number of electrodes, the reconstructed image is robuster with noise. With 10 dB noise, 16 electrodes cannot give a distinguished bubble at default bubble position, while for 64 electrodes the default bubble is reconstructed even at 20 dB noise. As to 3 bubbles cases, the same results can be obtained as shown in Figure 2.7.

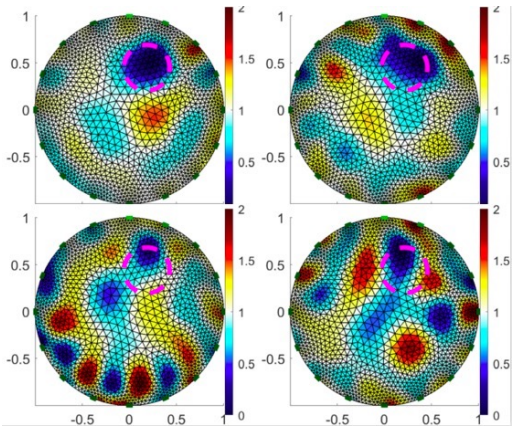

a. Default bubble with 16 electrodes

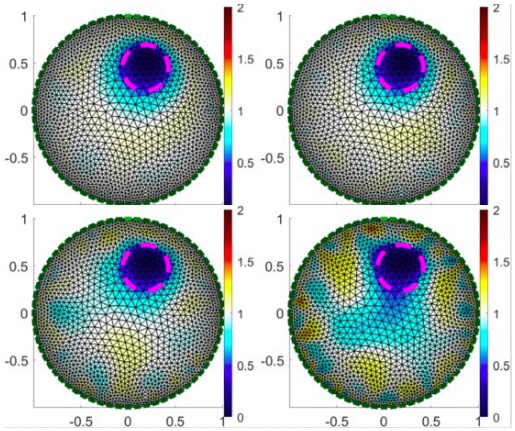

b. Default bubble with 64 electrodes

Figure 2.6. – 4 levels of noises added to default bubble cases. The pink dashed circles show the position and size of the bubbles.

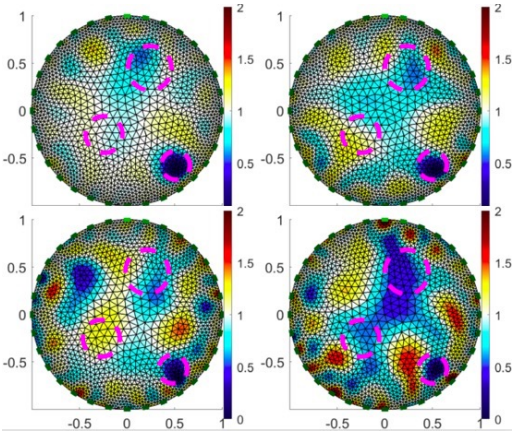

a. 3 bubbles with 16 electrodes

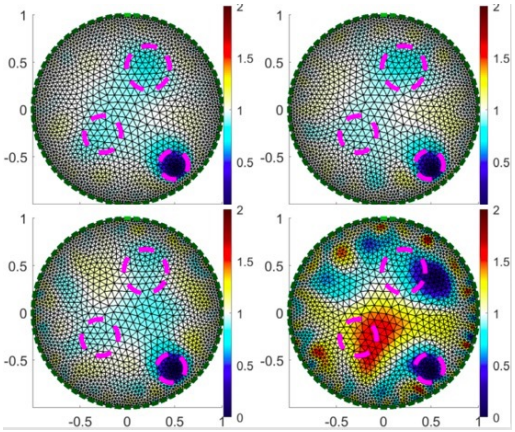

b. 3 bubbles with 64 electrodes

Figure 2.7. – 4 levels of noises added to 3 bubbles cases. The pink dashed circles show the position and size of the bubbles.

Besides, from [George et al., 2000], the ill-conditioning of the case and sensitivity to noise are increasing with the number of electrodes, so more investigations is necessary when applying a high number of electrodes.

2.3. Leakage of current

In the introduction of this chapter, the parameters concerning the physical dimensions of the EIT sensor were divided in three categories. The parameters of the first category are imposed by external constraints. The parameters of the second category are implemented

in the software. The third category contains free parameters and corresponds to the load specifications for the EIT sensor itself.

The **material** of the EIT sensor must consider the experimental conditions. In this thesis I have used Poly(methyl methacrylate) (PMMA) for low pressure and low temperature experiments and stainless steel with a Polyetheretherketone (PEEK) inner layer for insulation in high pressure and high temperature experiments. The material for the electrodes is stainless steel. The **number** of electrodes were discussed in Section 2.2. In the following simulations, I compare the cases with $n_e = 4$, 8, 16, 32 and 64 to generalise the results. The **angular size** of the electrodes have to be as large as possible but small enough so they do not overlap.

The remaining parameter is the **length** $\mathcal{L}_E$ of the electrodes. Previous studies [Gisser et al., 1988, Gisser et al., 1990] have shown that the electrodes of the EIT system on which the current (or voltage) is imposed should fill as much of $\partial\Omega$ as possible. Therefore, the electrodes have to be as long as possible in order to maximise the sensitive surface area. Nevertheless, in the case of industrial tomographic imaging, the EIT detector is commonly installed in an electrically conducting stainless pipe circuit as shown in Figure 2.8. Therefore, the electric potential induced by excitation electrodes E_{exc_1} and E_{exc_2} can be affected compared with the situation of a non-conductive pipe system. Namely, the conductive pipes upstream and downstream (Figure 2.8) are expected to induce a leakage of current.

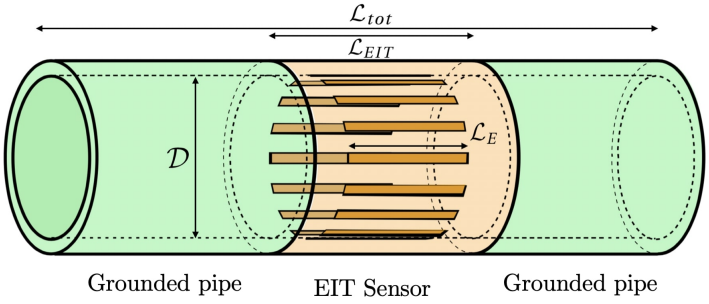

Figure 2.8. – Layout of a 16 electrodes EIT detector, surrounded by grounded stainless pipes.

In Section 2.3.1, the utilisable energy is introduced. To estimate this quantity, the leaking current is quantified for several length of electrodes in Section 2.3.2. Furthermore, the maximum of energy is estimated for an adequate lengths of electrodes in Section 2.3.3. Finally, the Section 2.3.4 generalises the results with the introduction of the form factor.

2.3.1. The utilisable energy

Mathematically, the leakage of current should not affect the measured potential ΔV between two measurement electrodes E_{meas_1} and E_{meas_2}. Instead, is spreads the total electrical energy $\mathcal{E}_\Omega$ over the system Ω of volume V_Ω with:

$$V_\Omega = \mathcal{L}_{tot} \times \pi \left(\frac{\mathcal{D}}{2}\right)^2, \tag{2.16}$$

where the length $\mathcal{L}_{tot}$ of the system Ω is arbitrarily set so the electrical energy goes to zero on the right and left boundaries, considered infinitely far away. The Figure 2.9 is an illustration of this phenomenon.

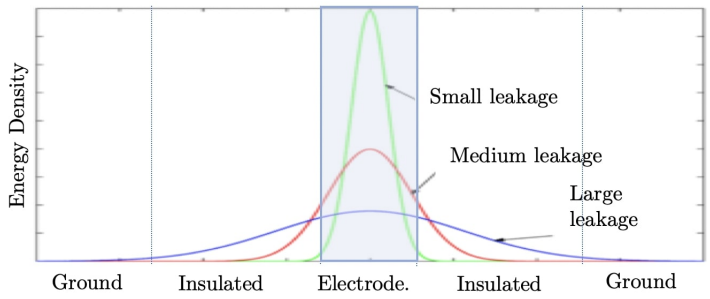

Figure 2.9. – Illustration of the behaviour of the energy with the presence of leakage. This figure is only to report a general behaviour and do not contain any numerical data.

The total electrical energy is defined as:

$$\mathcal{E}_\Omega = \frac{1}{2V_\Omega} \int_\Omega \sigma \ |\nabla u|^2 \ dx. \tag{2.17}$$

This energy is given to the system through the two excitation electrodes E_{exc_1} and E_{exc_2}. The Ohm's law:

$$\boldsymbol{j}(\boldsymbol{x}) = \sigma(\boldsymbol{x}) \nabla u, \tag{2.18}$$

gives the following form to the total electrical energy:

$$\mathcal{E}_\Omega = \frac{1}{2V_\Omega} \int_\Omega \boldsymbol{j} \cdot \nabla u \ (\boldsymbol{x}) dx. \tag{2.19}$$

Integrating (2.19) by parts gives:

$$\mathcal{E}_\Omega = \frac{1}{2V_\Omega} \left(\int_{\partial\Omega} \boldsymbol{j} \cdot \boldsymbol{n} \ u \ ds - \int_\Omega (\text{div } \boldsymbol{j}) \ u \ dx \right). \tag{2.20}$$

In the other hand, the conservation law specifies that:

$$\text{div} \boldsymbol{j} = 0, \tag{2.21}$$

and associated with (2.20) gives the definition of $\mathcal{E}_{source}$, the source energy:

$$\mathcal{E}_\Omega = \frac{1}{2V_\Omega} \int_{E_{exc_1} \cup E_{exc_2}} \boldsymbol{j}^g \cdot \boldsymbol{n} \ u \ dx \equiv \mathcal{E}_{source}. \tag{2.22}$$

Here, the integral is computed over the union $E_{exc_1} \cup E_{exc_2}$ of the surfaces of the excitation electrodes because the surface current $\boldsymbol{j} \cdot \boldsymbol{n}$ is zero on the insulated areas *and* on the measurement electrodes. On the other hand, the potential u is zero on grounded areas. Therefore, $\boldsymbol{j}^g$ is defined as the given current from the excitation electrodes E_{exc_1} and E_{exc_2} to the system, $\boldsymbol{j}^g$ being the cause of the source energy $\mathcal{E}_{source}$ which is an important

quantity because measurable in the experiment.

The interest here is to quantify the electrical energy in the sensitive region Ω_E of volume V_{Ω_E}, defined similarly as in (2.16), but delimited on the z-axis of cylindrical coordinates by the electrodes of length $\mathcal{L}_E$:

$$V_{\Omega_E} = \mathcal{L}_E \times \pi \left(\frac{\mathcal{D}}{2}\right)^2. \tag{2.23}$$

The energy in the electrodes region is then:

$$\mathcal{E}_{\Omega_E} = \frac{1}{2V_{\Omega_E}} \int_{\Omega_E} \sigma(\boldsymbol{x}) |\nabla u(\boldsymbol{x})|^2 d\boldsymbol{x}, \quad \text{for} \quad -\frac{\mathcal{L}_E}{2} \leq z \leq +\frac{\mathcal{L}_E}{2}, \tag{2.24}$$

with the origin taken at the center of the EIT detector. Here, $u \in H^1(\Omega)$, the Sobolev space of field of finite energy in Ω, then u and ∇u are square integrable. Therefore, the energy $\mathcal{E}_\Omega$ (*and likewise for* $\mathcal{E}_{\Omega_E}$) is finite:

$$||u||_{H^1(\Omega)} = \left(\int_\Omega (|u(\boldsymbol{x})|^2 + |\nabla u(\boldsymbol{x})|^2) dx\right)^{1/2} < +\infty, \tag{2.25}$$

then, $\mathcal{E}_\Omega < +\infty$.

The relation between $\mathcal{E}_\Omega$ and $\mathcal{E}_{\Omega_E}$ is expressed, considering two subdomains of Ω: the sensitive region Ω_E of length $\mathcal{L}_E$ delimited by the electrodes (Figure 2.8) and the remaining region, not directly contributing to the measurement, $\Omega \backslash \Omega_E$ (i.e. Ω without Ω_E). Starting from the definition of $\mathcal{E}_\Omega$ in (2.17):

$$\mathcal{E}_\Omega = \frac{1}{2V_\Omega} \frac{V_{\Omega_E}}{V_{\Omega_E}} \int_\Omega \sigma |\nabla u|^2 dx. \tag{2.26}$$

By respect with (2.24),

$$\mathcal{E}_\Omega = \frac{V_{\Omega_E}}{V_\Omega} \left(\mathcal{E}_{\Omega_E} + \frac{1}{2V_{\Omega_E}} \int_{\Omega \backslash \Omega_E} \sigma |\nabla u|^2 dx\right), \tag{2.27}$$

and considering (2.16) and (2.23),

$$\mathcal{E}_\Omega = \frac{\mathcal{L}_E}{\mathcal{L}_{tot}} (\mathcal{E}_{\Omega_E} + \mathcal{E}_{lost}) = \mathcal{E}_{source}. \tag{2.28}$$

Where

$$\mathcal{E}_{lost} = \frac{1}{2V_{\Omega_E}} \int_{\Omega \backslash \Omega_E} \sigma |\nabla u|^2 dx, \tag{2.29}$$

is called the lost energy because it is not located within the sensor region, it does not directly contribute to the EIT measurement. In addition, the energies defined above verifies the following:

$$\mathcal{E}_{\Omega_E} \leq \mathcal{E}_{source}, \quad \text{and} \quad \mathcal{E}_{lost} \leq \mathcal{E}_{source}. \tag{2.30}$$

Finally, the following relation can be deduced from (2.28):

$$1 = \mathcal{U}(\alpha) + \frac{\mathcal{L}_E}{\mathcal{L}_{tot}} \frac{\mathcal{E}_{lost}}{\mathcal{E}_{source}}, \tag{2.31}$$

with the introduction of the function of dimensionless utilisable energy $\mathcal{U}(\alpha)$:

$$\mathcal{U}(\alpha) = \alpha \frac{\mathcal{L}_{EIT}}{\mathcal{L}_{tot}} \frac{\mathcal{E}_{\Omega_E}}{\mathcal{E}_{source}}, \tag{2.32}$$

and

$$\alpha = \mathcal{L}_E / \mathcal{L}_{EIT}. \tag{2.33}$$

To assess why a decrease of $\mathcal{U}(\alpha)$ affects the measurement, it is necessary to clarify how ΔV is probed without affecting the Dirichlet conditions. This implies that the current at the surface of *measurement* electrodes $\boldsymbol{j}^m$ must be significantly smaller than the given current: $|\boldsymbol{j}^m| \ll |\boldsymbol{j}^g|$. To do so, the probe uses a very high resistance $R^m \gg 1/\sigma_t$ where σ_t is the electrical conductivity of the typical liquid phase inside the system Ω. Considering R^m large enough, the measurement circuit current $\boldsymbol{j}^m$ is not zero, but very low in comparison with the current between E_{meas_1} and E_{meas_2} passing through Ω. If $\mathcal{U}(\alpha)$ decreases, ΔV remains theoretically the same, but $\boldsymbol{j}^m$ (*which is already low*) decreases as well, altering significantly the measurement accuracy.

2.3.2. Quantification of the leakage of current

In the following, I consider the case of the EIT detector that fits the PKL primary circuit, between the Reactor Pressure Vessel and the Steam Generator. This application will be discussed in Chapter 5. The interior diameter $\mathcal{D}$ of the pipe is 128.20 mm, the exterior diameter is 286 mm and the EIT sensor length $\mathcal{L}_{EIT}$ is 170 mm. Nevertheless, the numerics developed for this paper and the corresponding results can be conveniently adapted to any size.

The first step in order to quantify the energy is to estimate the current leakage. A 3D approach have shown that 3D simulation is computationally heavy and not necessary to quantify the leakage: a 2D model is applied. The Figure 2.10a. and b. shows the plan of two chosen excitation electrodes (E_{exc_1} and E_{exc_2}), simulated using `FreeFEM++`. The boundary conditions are the following:

1. On E_{exc_1} *and* E_{exc_2}: $u(\boldsymbol{x}) = \pm 1$ V.
2. On the *insulated* border: $\boldsymbol{j} \cdot \boldsymbol{n} = \sigma(\boldsymbol{x}) \nabla u \cdot \boldsymbol{n} = 0$ A.
3. On the *grounded* border: $u(\boldsymbol{x}) = 0$ V.
4. The *left* and *right* borders are taken sufficiently far away in order to not perturb the field $\boldsymbol{j}(\boldsymbol{x})$ in the simulation domain.
5. All over Ω: $\sigma(\boldsymbol{x}) = 1$ S.m^{-1} .

The iso-potential regions for this excitation are shown in Figure 2.10c. The current J_E passing through one unit of the surfaces S_{exc_1} and S_{exc_2} (respectively the surfaces of

E_{exc_1} and E_{exc_2}) is defined as following:

$$J_E = \frac{1}{S_{exc_1} + S_{exc_2}} \left[\left(\int_{S_{exc_1}} |\boldsymbol{j} \cdot \boldsymbol{n}| \, dx \right) + \left(\int_{S_{exc_2}} |\boldsymbol{j} \cdot \boldsymbol{n}| \, dx \right) \right]. \tag{2.34}$$

The leakage of current J_{leak} is defined similarly, on the grounded surface element S_{Γ_i} of the upstream and downstream grounded pipes:

$$J_{leak} = \frac{1}{S_\Gamma} \left(\sum_{S_{\Gamma_i}} \int_{S_{\Gamma_i}} |\boldsymbol{j} \cdot \boldsymbol{n}| \, dx \right), \tag{2.35}$$

where S_Γ is the total surface of all grounded surfaces. The current density field is shown in Figure 2.10d., in the image we can clearly see the leaking current from the electrode to the grounded surface.

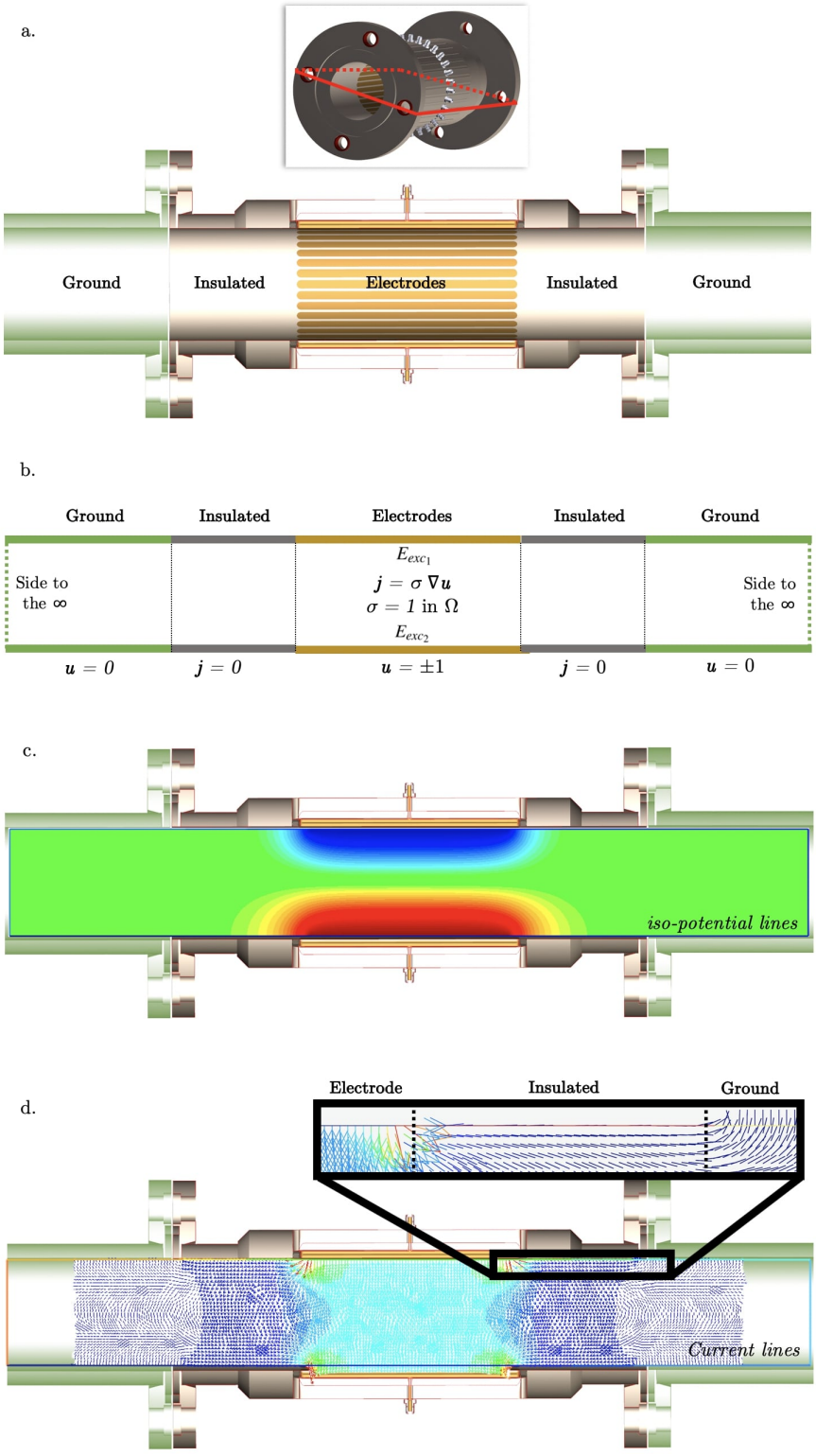

Figure 2.10. – a. Illustration of the simulation domain in the plan of the two excitation electrodes. b. Scheme of the boundary conditions for the 2D leakage simulation. c. Iso-potential lined in the medium during an excitation. d. Current lines that let appear the leaking component from the electrodes to the ground surfaces.

The results (Figure 2.11) show the ratio J_{leak}/J_E as a function of the ratio α of the electrodes length $\mathcal{L}_E$ to the EIT detector length $\mathcal{L}_{EIT}$. The script developed to obtain this result can be found in Appendix III. This output were computed as an average over all independent measurements by considering the distances between every pair of electrodes in EIT systems containing $n_e = 4$, 8, 16, 32 or 64 electrodes. The leakage of current are computed for each distance available between any pair (E_{exc_1}, E_{exc_2}) and weighted to the number of time this relative distance appears in the complete set of independent measurements.

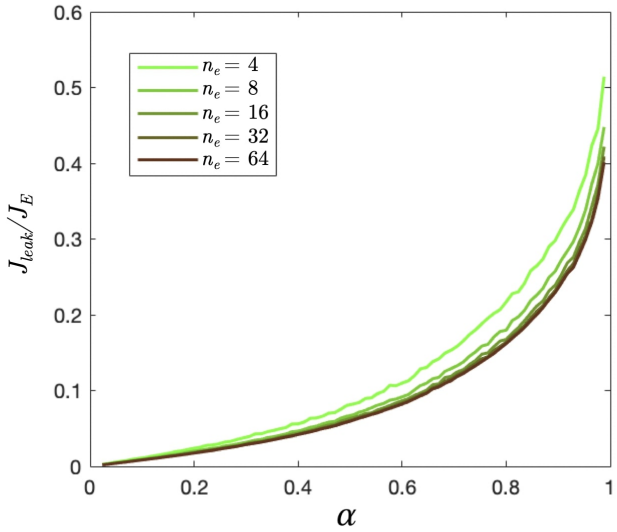

Figure 2.11. – Leakage of current versus the electrode length for EIT detectors containing $n_e = 4$, 8, 16, 32 or 64 electrodes.

As expected, the larger the electrode length, the thiner the isolation layer and the larger the leakage of current. An important observation is the decreasing leakage of current with the increasing number of electrodes. J_{leak}/J_E appears to approach a saturation level for $n_e = 64$ electrodes configuration.

2.3.3. Maximum of utilisable energy

Because a potential is measured on the electrodes, the larger the measurement electrode surfaces, the larger the current $\boldsymbol{j}^m$. Therefore, the utilisable energy $\mathcal{U}(\alpha)$ is expected to increase with these parameters (2.24). In the extreme case of infinitely thin electrodes ($\alpha \to 0$), the utilisable energy $\mathcal{U}(0) = 0$. On the other hand, the larger $\mathcal{L}_E$, the thiner the insulated layer and the greater the leakage. In the other extreme case of very large electrodes ($\alpha \to 1$), it is also expected that $\mathcal{U}(1) = 0$. This observation leads to expect a maximum of energy at an adequate length of electrodes. The load specification of the EIT device should take into account this length in order to optimise the measurement performances. In the results illustrated in Figure 2.12, a maximum is observed for a length of electrodes that is 0.84 times the length of the test section.

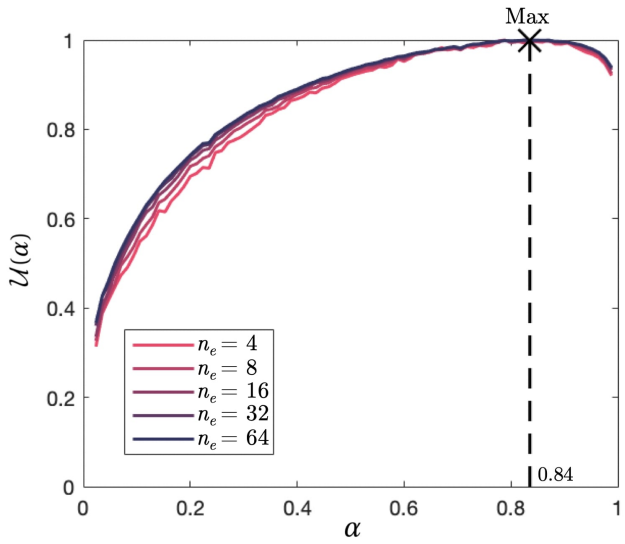

Figure 2.12. – Normalized utilisable energy versus the electrode length for EIT detectors containing $n_e = 4$, 8, 16, 32 or 64 electrodes.. The maximum of $\mathcal{U}(\alpha)$ is given at $\alpha = 0.84$.

To conclude, the design of the EIT detector is mainly imposed by the specifications of the external experimental constraints. Concerning the electrodes, since the electric potential is imposed during measurements, the image reconstruction quality of the images is optimised for the largest area of the electrodes. The **angular size** is maximised, limited by technical constraints. The **length** $\mathcal{L}_E$ of the electrodes affects the leakage of current that spreads the energy outside the sensitive region. From the results of this section, a maximum of energy were found in the sensitive region for electrodes length of 84% of the distance between those conductive pipes.

2.3.4. The role of the form factor $\mathcal{F}$

The previous results were constrained by the diameter $\mathcal{D}$ and test section length $\mathcal{L}_{EIT}$ for a particular application. The topic of this section is to generalise these results by associating these requirements into a form factor:

$$\mathcal{F} = \frac{\mathcal{D}}{\mathcal{L}_{EIT}}. \tag{2.36}$$

The results of the simulation (Figure 2.13) were computed with the script of Appendix III.III.3. The computation covers several length of electrodes, including the ratio of 0.84 that maximises the energy in the previous analysis (Section 2.3.3). An important observation is that the ratio $\mathcal{L}_{Elec}/\mathcal{L}_{EIT} = 0.84$ seems to be a golden ratio that gives a maxima of energy for all form factors. Furthermore, the energy increases significantly in the region where $\mathcal{F} \leq 1$. It is therefore preferable to have a test section that is longer than the diameter of the pipe.

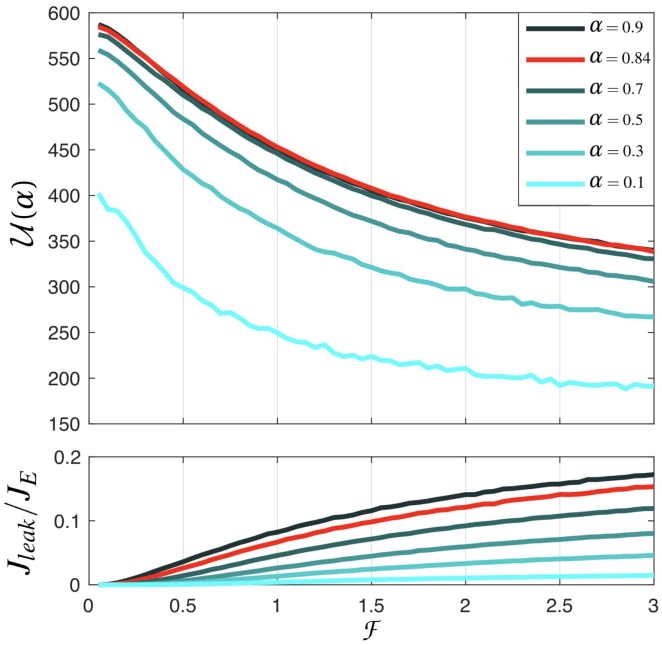

Figure 2.13. – Current leakage and Energy, varying with the Form Factor $\mathcal{F}$. The dependency is shown for several ratio of electrode lengths to the EIT detector length.

As in Figure 2.13, the energy is larger for a long EIT detector and a naive conclusion might be that maximising the length of the detector optimises its performances. Nevertheless, it is important to point out that long electrodes covers a large region of the pipe, which is less efficient to measure local changes in the flow pattern. It is important to keep in mind that the time to measure all frames of EIT measurement should be faster than the time for the flow to pass through the detector. The results of Figure 2.13 have to be confronted to a discussion on the requirements of the measurement resolution over the z-axis.

The set of parameters that defines completely the design of an EIT detector in the current problem is given by the physical characteristics of the test section and the EIT system:

$$\mathcal{P} = \{\mathcal{L}_{tot}, \mathcal{L}_E, \mathcal{D}, \mathcal{L}_{EIT}\}. \tag{2.37}$$

The dependency of the utilisable energy to those parameters can be express, starting from (2.31):

$$\mathcal{U} = 1 - \frac{\int_{\Omega\setminus\Omega_E} \sigma|\nabla u|^2 dx}{\sum_{\text{elec.}} \boldsymbol{j}^d \cdot \boldsymbol{n}u} \tag{2.38}$$

$$= 1 - \frac{\int_{\Omega\setminus\Omega_E(\{\mathcal{P}\})} \sigma|\nabla u(\{\mathcal{P}\})|^2 dx}{\sum_{\text{elec.}} \boldsymbol{j}^d \cdot \boldsymbol{n}u}. \tag{2.39}$$

The complexity of the dependency of $\mathcal{U}(\{\mathcal{P}\})$ makes extremely difficult to find the equation that fully describes the behavior of the utilisable energy. In order to assess a the general behavior of the dependencies of the utilisable energy to the form factor, a

dimensional analysis is proposed, based on the Vaschy-Buckingham theorem. The method is commonly used to find a reduced number of combinations of parameters, only based on the consideration of their physical dimensions. The utilisable energy is a function of the following form:

$$\mathcal{U} = f_U(\sigma, u, j, \mathcal{L}_{tot}, \mathcal{L}_E, \mathcal{D}, \mathcal{L}_{EIT}) \tag{2.40}$$

The result of further simulation analysis have shown that the general behavior, especially the maxima, do not depends on the conductivity function or the boundary conditions. This is true for reasonable values of α. Indeed, in the case where α is close to 1, strong shunting effects can rise from the source electrode to the grounded pipes. In the case where α goes to 0, the source energy $\mathcal{E}_{source}$ gets tiny and the current may be completely absorbed by the medium of the system. In the physical situation of these cases, the current may behave differently than as described in the current simulation and the definition of $\mathcal{U}$ in (2.32) may not stand.

The utilisable energy dependence to the physical lengths of the EIT experiment can be rewritten in terms of non-dimensional parameters:

$$\mathcal{U} = \beta \left(\frac{\mathcal{L}_E}{\mathcal{L}_{tot}} \right)^{\gamma_1} \alpha^{\gamma_2} \mathcal{F}^{\gamma_3}. \tag{2.41}$$

As in (2.32), the dependency of $\mathcal{U}$ to $\mathcal{L}_E/\mathcal{L}_{tot}$ is trivial and $\gamma_1 = 1$.

2.4. Sensitivity maps

We are now interested in the sensitivity of EIT. As discussed in Chapter 1, the EIT principle is to impose Dirichlet (Neumann) conditions on the closure of the domain $\bar{\Omega}$ and to measure the potentials (current) on $\bar{\Omega}$. These boundary conditions are imposed by a pair of excitation electrodes E_{exc_1} and E_{exc_2} with the responses measured at the measurement electrodes E_{meas_1} and E_{meas_2}. The sensitivity of the measurement relates the magnitude of a change in voltage $\Delta V \to \Delta V + \delta(\Delta V)$ measured between E_{meas_1} and E_{meas_2} to the change in conductivity $\sigma(\boldsymbol{x}) \to \sigma(\boldsymbol{x}) + \delta\sigma(\boldsymbol{x}_0)$ of a small volume element at $\boldsymbol{x}_0$ which has given rise to it [Kotre, 1989]:

$$\mathcal{S}(\boldsymbol{x}_0) = \frac{\delta(\Delta V)}{\delta\sigma(\boldsymbol{x}_0)}. \tag{2.42}$$

This value is affected by the position of the change $\delta\sigma(\boldsymbol{x}_0)$ within the current density field, and with respect to E_{meas_1} and E_{meas_2}.

The following numerical work starts with the continuous formulation of the sensitivity, in Section 2.4.1. From this formulation, the Section 2.4.2 contains the results of the sensitivity map from a continuous equation. The results are validated by an independent computation method in Section 2.4.3. Finally, the sensitivity map of the full-scan excitation strategy is presented in Section 2.4.4.

2.4.1. Continuous formulation of the sensitivity

In a domain $\Omega \subset \mathbb{R}^2$ with an admittivity distribution $\gamma(\boldsymbol{x}) \in \mathbb{C}$ and $\boldsymbol{x} \in \Omega$, the electric potential u satisfies the elliptic partial differential equation

$$\nabla \cdot [\gamma(\boldsymbol{x}) \nabla u(\boldsymbol{x})] = 0. \tag{2.43}$$

In the frame of EIT, the imaginary part is generally neglected $\gamma = \sigma$. The continuous derivation of (2.42) uses the weak form of (2.43) with any w:

$$\int_\Omega \sigma \nabla u \cdot \nabla w dV = \int_{\partial\Omega} w\sigma \frac{\partial u}{\partial n} dS, \tag{2.44}$$

using the Green identity. Here, dV and dS respectively measure a volume of Ω and a surface of $\partial\Omega$. The power conservation formula is obtained for $w = u$:

$$\int_\Omega \sigma |\nabla u|^2 dV = \int_{\partial\Omega} u\sigma \frac{\partial u}{\partial n} dS = \sum_n \int_{E_n} \left(V_n - \zeta_n \sigma \frac{\partial u}{\partial n} \right) \sigma \frac{\partial u}{\partial n} dS \tag{2.45}$$

Here, ζ_n is the contact impedance at the electrode E_n, and V_n is the constant voltage on electrode E_n:

$$V_n = u|_{\partial\Omega} + \zeta_n \sigma \frac{\partial u}{\partial n}, \quad \text{on } \partial\Omega. \tag{2.46}$$

Thus,

$$\int_\Omega \sigma |\nabla u|^2 dV + \sum_n \int_{E_n} \zeta_n \left(\sigma \frac{\partial u}{\partial n} \right)^2 dS = \sum_n V_n I_n \tag{2.47}$$

where I_n is the current injected from the n^{th} electrode E_n:

$$I_n = \int_{E_n} \sigma \frac{\partial u}{\partial n} dS. \tag{2.48}$$

The equation (2.47) simply states that the power input is either dissipated by the contact impedance or in the domain Ω.

Considering, as in (2.42), the small perturbation $\sigma(\boldsymbol{x}_0) \to \sigma(\boldsymbol{x}_0) + \delta\sigma$ at $\boldsymbol{x}_0 \in \Omega$ of the conductivity [Calderón, 2006]. It results in a change of the potential field $u(\boldsymbol{x}_0) \to u(\boldsymbol{x}_0) + \delta u$, implying a perturbation on the electrode potential $V_n \to V_n + \delta V_n$. However, the current I_n passing the electrode E_n is left unchanged. The perturbation of (2.47) is

$$\int_\Omega \sigma |\nabla u|^2 dV + 2 \int_\Omega \sigma \nabla u \cdot \nabla \delta u dV + 2 \sum_n \int_{E_n} \zeta_n \left(\sigma \frac{\partial u}{\partial n} \right) \delta \left(\sigma \frac{\partial u}{\partial n} \right) dS = \sum_n \delta V_n I_n \tag{2.49}$$

where the higher order terms are neglected. From (2.46), the current change on electrode E_n verifies:

$$\delta \left(\sigma \frac{\partial u}{\partial n} \right) = \frac{1}{\zeta_n} (\delta V_n - \delta u|_{\partial\Omega}), \tag{2.50}$$

which associated to the weak formulation of (2.49) with $w = \delta u$ gives:

$$\int_\Omega \delta\sigma|\nabla u|^2 dV + 2\int_{\partial\Omega} \delta u\sigma\frac{\partial u}{\partial n}dS - 2\sum_n \zeta_n \int_{E_n} \frac{\delta u}{\zeta_n}\sigma\frac{\partial u}{\partial n}dS \\ +2\sum_n \delta V_n \int_{E_n} \sigma\frac{\partial u}{\partial n}dS = \sum_n \delta V_n I_n. \tag{2.51}$$

Concerning the second term of the above equation, the integral is taken over the boundary $\partial\Omega$. However, the current goes to zero at the insulated boundary and the Kirchhoff's law gives:

$$\int_{\partial\Omega} \delta u\sigma\frac{\partial u}{\partial n}dS = \sum_n \zeta_n \int_{E_n} \frac{\delta u}{\zeta_n}\sigma\frac{\partial u}{\partial n}dS. \tag{2.52}$$

Furthermore, integrating over the electrode E_n gives:

$$\sum_n \delta V_n \int_{E_n} \sigma\frac{\partial u}{\partial n}dS = \sum_n \delta V_n I_n. \tag{2.53}$$

Therefore, from (2.51), (2.52) and (2.53), we obtain the total change in power:

$$\int_\Omega \delta\sigma|\nabla u|^2 dV = -\sum_n \delta V_n I_n. \tag{2.54}$$

The experimental interpretation of this results necessitates as in (2.42), to quantify the voltage change ΔV observed on a given measurement electrode E_{meas}, when a current pattern is imposed on one or several electrodes of the EIT system. To do so, the dependancy of the potential on a vector of electrode current $\boldsymbol{I} = (I_1, ..., I_{n_e})$ is referred as $u(\boldsymbol{I})$. Therefore, for a given excitation/measurement configuration, the hypothetical excitation potential is $u(\boldsymbol{I}_{exc})$ and measurement potential is $u(\boldsymbol{I}_{meas})$. The power perturbation formula of (2.54) can be applied to $u(\boldsymbol{I}_{exc}) + u(\boldsymbol{I}_{meas})$ and $u(\boldsymbol{I}_{exc}) - u(\boldsymbol{I}_{meas})$ and subtract to obtain [Polydorides and Lionheart, 2002]:

$$\Delta V_{em} = -\int_\Omega \delta\sigma\nabla u(\boldsymbol{I}_{exc}) \cdot \nabla u(\boldsymbol{I}_{meas})dV. \tag{2.55}$$

The computation of the Jacobian matrix necessitates the discretisation of the conductivity. A finite element computation suggest that the conductivity change is uniform over a single voxel of the mesh located at $\boldsymbol{x}_0$ and of area α. The sensitivity of that element, (2.42), is then given by the following:

$$\frac{\Delta V_{em}}{\delta\sigma(\boldsymbol{x}_0)} = -\int_\alpha \nabla u(\boldsymbol{I}_{exc}) \cdot \nabla u(\boldsymbol{I}_{meas})dV. \tag{2.56}$$

The method of optimisation in EIT generally necessitates the complete matrix of partial derivatives of voltages with respect to the conductivity distribution [Lionheart, 2004]. The Newton method for solving the inverse problem uses the Jacobian matrix, which is determined from (2.56). The matrix contains as many $\boldsymbol{I}_{exc}$ and $\boldsymbol{I}_{meas}$ as the

excitation and measurement configurations considered in the EIT data frame.

2.4.2. Computation of the sensitivity map

The sensitivity coefficient for the element at $\boldsymbol{x}_0$ can be calculated [Breckon and Pidcock, 1987] as the inner product of the field $\Phi_{exc} = u(\boldsymbol{I}_{exc})$ produced by a unit current flowing in E_{exc_1} and E_{exc_2} and the field $\Phi_{meas} = u(\boldsymbol{I}_{meas})$ produced by a unit current flowing in E_{meas_1} and E_{meas_2}, (2.56) is rewritten:

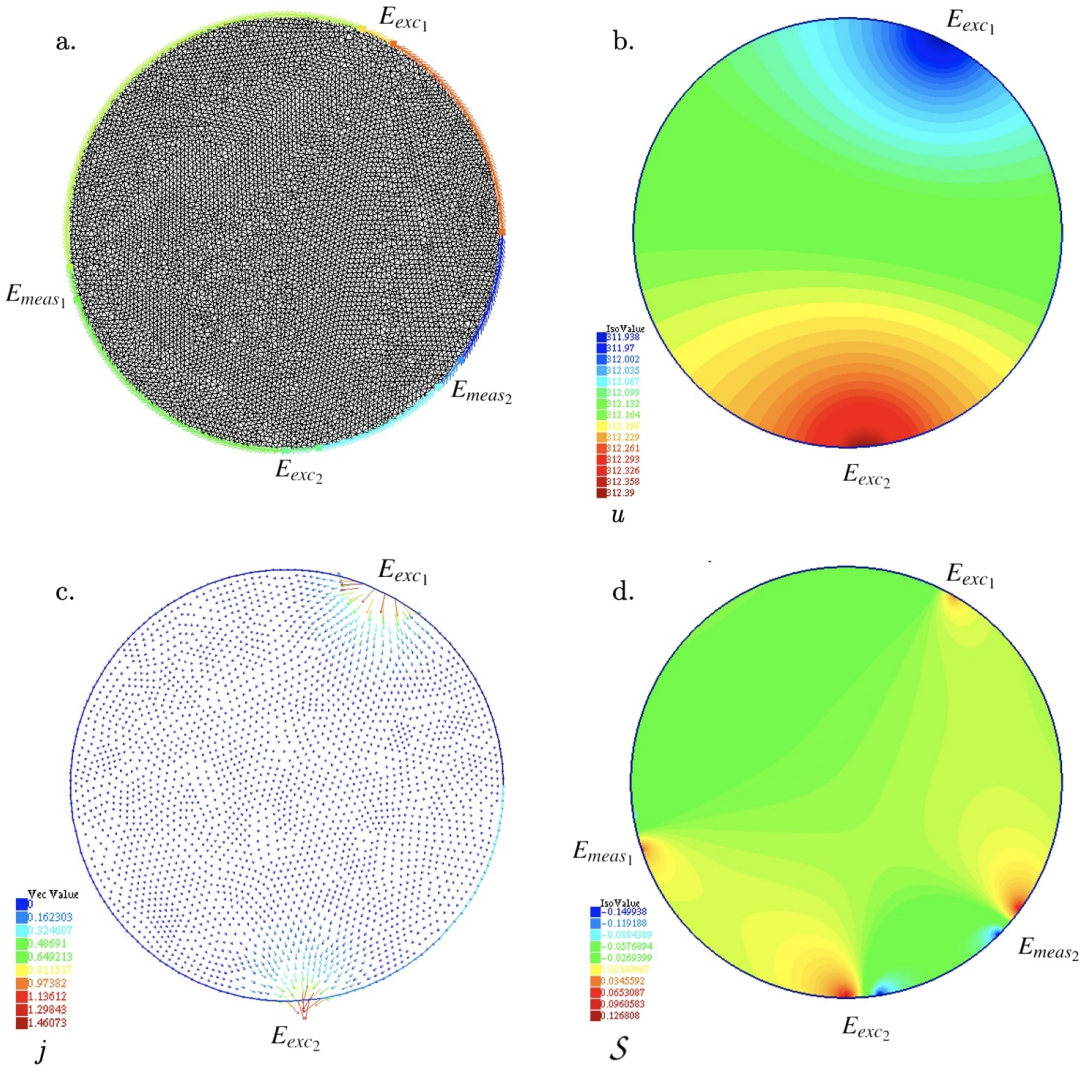

Figure 2.14. – a. Contour and mesh for the simulation with arbitrary position of the excitation electrodes E_{exc_1}, E_{exc_2} and the measurement electrodes E_{meas_1}, E_{meas_2}. The mesh contains 14158 Triangles and 7234 Vertices. b. Iso-potential regions in the simulation domain for an excitation of ±1 V between the excitation electrodes. c. Representation of the current vector filed fot the same excitation. d. The sensitivity map for a set of excitations and measurements on four electrodes with arbitrary position.

$$\mathcal{S}(\boldsymbol{x}_0) = \int_a \nabla\Phi_{exc} \cdot \nabla\Phi_{meas}\ da. \tag{2.57}$$

The integral is made over [1] the volume a of the element at $\boldsymbol{x}_0$.

The sensitivity is computed over the finite element space and the boundary regions of Figure 2.14a. The mesh uses the Delaunay-Voronoi algorithm: The inner point density is proportional to the density of points on the boundaries [George, 1996], chosen to be constant on the whole periphery with a total of 314 nodes. There is a total of 14158 triangles and 7234 vertices over the domain. The excitation potential field Φ_{exc} and the current density field are shown in Figure 2.14b. and Figure 2.14c., respectively.

The sensitivity map shown in Figure 2.14d. was computed with the script of Appendix III.III.4. The method were to impose a potential between two excitation electrodes E_{exc_1} and E_{exc_2} and to measure the potential between E_{meas_1} and E_{meas_2} to reconstruct the sensitivity as in (2.57). In Figure 2.14d., the sensitivity has a positive and negative components depending on the position in the domain. The logarithmic representation of the sensitivity map is shown in Figure 2.15. The result is strongly counterintuitive as the minimal sensitivity of the EIT measurement corresponds to the path between the excitation and measurement electrodes.

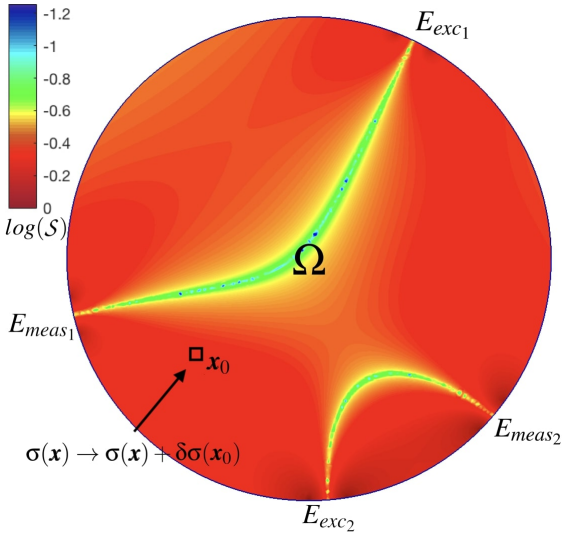

Figure 2.15. – Log of the Sensitivity map normalised to $Max(\mathcal{S}) = 1$ for two pairs of excitation and measurement electrodes of width $\pi/20$. Each point $\boldsymbol{x}_0$ of the map is estimated from a small change over the area a centred at $\boldsymbol{x}_0$ of the electrical conductivity σ.

2.4.3. Reconstruction with locally imposed conductivity variations

The unexpectedness of the result above raised the necessity for a numerical confirmation using an independent computational method. In order to establish the facts, an indirect reconstruction method of the sensitivity map is proposed in this section. The purpose

1. Or over the area of the element at $\boldsymbol{x}_0$ for the following 2D simulations.

consists to manually change locally the conductivity map $\sigma(\boldsymbol{x}) \to \sigma(\boldsymbol{x}) + \delta\sigma(\boldsymbol{x}_0)$ on small elements at $\boldsymbol{x}_0$ of area a to reconstruct the sensitivity with (2.42).

An electrical field is simulated by imposing the potential ±1V between a pair of excitation electrodes E_{exc_1} and E_{exc_2} of arbitral position. In our case, the positions are chosen to be as in Figure 2.15 for comparison. A differential potential ΔV is computed from the condition above between two measurement electrodes E_{meas_1} and E_{meas_2}. The value of ΔV is modified by the introduction of a bubble of conductivity $\sigma_{bubble} = 10^{-2}\ \sigma_{pipe}$ and size $0.1\mathcal{D}$, with $\mathcal{D}$ the diameter of the pipe, that were simulated in the pipe section of the electrode region, filled with a liquid of arbitral conductivity $\sigma_{pipe} = 1$ S/m. The sensitivity $\mathcal{S}$ were computed from (2.42) with the bubble centred at a number of 7,845 different points in Ω, illustrated in Figure 2.16 as pixels of width $1/100\mathcal{D}$.

The correspondence between the Figure 2.15 and Figure 2.16 is direct. However, the region of lower sensitivity ($\mathcal{S} \approx -0.7$) is larger in the indirect reconstructed map. This is due to the size of the mesh, that had to be taken larger due to the large number of computation involved. Nevertheless, the point in this result is to validate the existence of two valleys of low sensitivity between excitation and measurement electrodes.

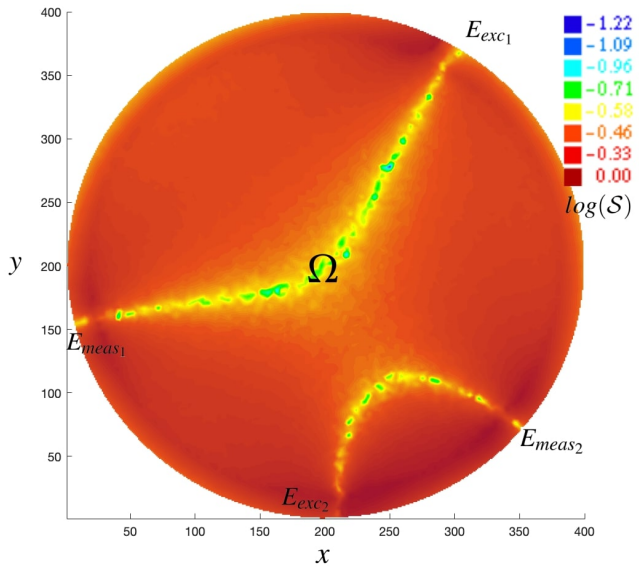

Figure 2.16. – Log of the reconstructed sensitivity map normalised to $Max(\mathcal{S}) = 1$ for two pairs of excitation and measurement electrodes of width and positions as in Figure 2.15. The sensitivity is reconstructed for bubbles at positions (x, y).

2.4.4. Sensitivity of the full-scan strategy

In the above simulation, the position of the electrodes is arbitrary. It represents the sensitivity of a single excitation between two electrodes associated with a single measurement on two other electrodes. As discussed in Section 1.3.1, there is several ways to select pairs of electrodes for the excitation and the measurement and therefore increase

the number of independant measurements for a better description of the boundary conditions.

We are interested in the sensitivity of several independent excitation and measurement set. In particular the full-scan strategy, since this strategy is preferred in the following two chapters.

Four sensitivity maps of full-scan were computed for EIT sensor with $n_e = 4$, 8, 16 or 32 electrodes. As in (2.12), a total of M excitation/measurement configurations has to be considered for each sensor type. For each configuration, an equivalent of Figure 2.15 is computed. All the generated sensitivity maps are averaged out.

The code is adapted for each EIT sensor configuration. It contains a set of functions that is organised in two categories: *Shared functions* and *Electrode number selected functions*. The shared functions are called in the following order at each implementation of the code.

- `Main` (86 lines): The main code calls all the other functions. In a first part it calls the three following shared functions before to initialise the finite element space. Due to the large number of sensitivity maps, the mesh contains 686 triangles and 376 vertices. In a second part, the main code calls the two electrode number selected functions.
- `FullScanBorderdef` (191 lines): This function creates the boundary of the sensor, depending on the input number of electrodes.
- `FullScanplot` (57 lines): Plots the boundary.
- `FullScanMesh` (51 lines): Creates the mesh. The number of degrees of freedomh is defined as the total number of points on the boundary.

In total, the shared functions contains 385 lines of code.

The second category of functions are the electrode number selected functions. There is two functions called for each configuration of the simulated EIT sensor for a total of eight functions. These are:

- `Solve_ne_elec`: This function creates and solve the weak form of the Laplace equation for the M excitation and measurement electrodes. Due to the very large number of lines, it has been written with a script.
- `Solve_ne_elecSum`: This function averages out all the configuration computed above.

To realise the size of this simulation codes, each function with its number of lines is listed in Table 2.2.

The result shown in Figure 2.17 relates that the sensitivity is much higher in the neighbouring of the electrodes and drastically reduced in the middle, as observed experimentally. This simulation code can be improved to analyse alternative implementation of scanning strategies as for instance the full-scan without neighbouring electrode excitation.

The implementation of the code for 64 electrodes requires a high performance and parallelised computed resources. The code could be fully parallelised since the sensitivity maps for each configuration is independent to the others. I suggest to implement a

Table 2.2. – Number of lines of code for the full-scan simulation of the sensitivity for different number of electrodes.

n_e	Shared	`Solve_ne_elec`	`Solve_ne_elecSum`	**Total**
4	385	132	40	**557**
8	385	1119	291	**1795**
16	385	7679	2172	**10236**
32	385	55551	16877	**72813**
64	385	$\sim$ 400000	$\sim$ 12000	$\sim$ **520000**

parallelised version of the code with thiner mesh refinement in suggestion for further development.

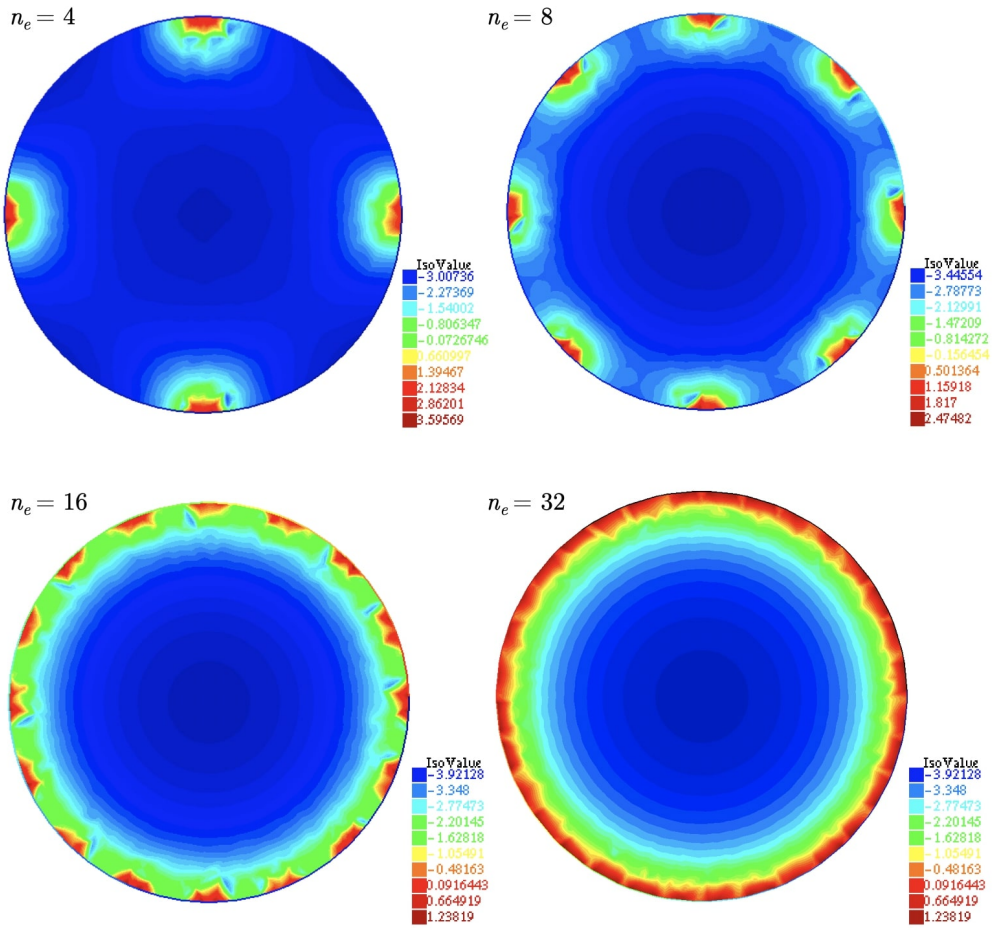

Figure 2.17. – Log of the sensitivity map average out from M excitations in the full-scan strategy.

2.5. Effects of the leakage of current on the sensitivity

This sections contains preliminary results on the numerical estimation of the effects of the leakage of current on the sensitivity map. In Section 2.5.1, the continuous formulation of the sensitivity map with leakage of current is derived with a new perturbation theory. The Section 2.5.2 introduces the results based on a 3D simulation.

2.5.1. Continuous formulation of the sensitivity map with leakage of current

With the presence of two conducting elements of surface S_Γ upstream and downstream, the equation of power conservation, (2.45) has an additional term:

$$\int_\Omega \sigma|\nabla u|^2 dV = \sum_n \int_{E_n} \left(V_n - \zeta_n \sigma \frac{\partial u}{\partial n}\right) \sigma \frac{\partial u}{\partial n} dS + \int_{S_\Gamma} \left(V_\Gamma - \zeta_\Gamma \sigma \frac{\partial u}{\partial n}\right) \sigma \frac{\partial u}{\partial n} dS \quad (2.58)$$

where V_Γ is the constant potential and ζ_Γ is the contact impedance of the grounded surfaces. Thus,

$$\int_\Omega \sigma|\nabla u|^2 dV + \sum_n \int_{E_n} \zeta_n \left(\sigma \frac{\partial u}{\partial n}\right)^2 dS + \int_{S_\Gamma} \zeta_\Gamma \left(\sigma \frac{\partial u}{\partial n}\right)^2 dS = \sum_n V_n I_n + V_\Gamma I_\Gamma \quad (2.59)$$

with I_Γ, the leaking current from the grounded surfaces. By applying the following set of perturbations at $\boldsymbol{x}_0 \in \Omega$ and on the electrode E_n:

$$\begin{cases} \sigma(\boldsymbol{x}_0) & \to \sigma(\boldsymbol{x}_0) + \delta\sigma(\boldsymbol{x}_0) \\ u(\boldsymbol{x}) & \to u(\boldsymbol{x}) + \delta u(\boldsymbol{x}) \\ V_n & \to V_n + \delta V_n \\ I_n & \to I_n, \text{invariant} \\ V_\Gamma & \to V_\Gamma, \text{invariant} \\ I_\Gamma & \to I_\Gamma + \delta I_\Gamma \end{cases} \quad (2.60)$$

it results:

$$\begin{aligned} \int_\Omega \sigma|\nabla u|^2 dV + 2\int_\Omega \sigma \nabla u \cdot \nabla \delta u dV + 2\sum_n \int_{E_n} \zeta_n \left(\sigma \frac{\partial u}{\partial n}\right) \delta \left(\sigma \frac{\partial u}{\partial n}\right) dS \\ +2\int_{S_\Gamma} \zeta_\Gamma \left(\sigma \frac{\partial u}{\partial n}\right) \delta \left(\sigma \frac{\partial u}{\partial n}\right) dS = \sum_n \delta V_n I_n + V_\Gamma \delta I_\Gamma \end{aligned} \quad (2.61)$$

where the higher order terms are neglected. The potential on electrode E_n is given by (2.50). We deduce the potential on the grounded surfaces:

$$\delta \left(\sigma \frac{\partial u}{\partial n}\right) = -\frac{\delta u}{\zeta_\Gamma}. \quad (2.62)$$

The weak formulation with $w = \delta u$ is then:

$$\begin{aligned}\int_\Omega \delta\sigma|\nabla u|^2 dV + 2\int_{\partial\Omega} \delta u\sigma\frac{\partial u}{\partial n}dS - 2\sum_n \zeta_n \int_{E_n} \frac{\delta u}{\zeta_n}\sigma\frac{\partial u}{\partial n}dS \\ +2\sum_n \delta V_n \int_{E_n} \sigma\frac{\partial u}{\partial n}dS - 2\zeta_\Gamma \int_{S_\Gamma} \frac{\delta u}{\zeta_\Gamma}\sigma\frac{\partial u}{\partial n}dS = \sum_n \delta V_n I_n + V_\Gamma \delta I_\Gamma\end{aligned} \tag{2.63}$$

The second, third and fifth terms are cancelling under the Kirchhoff's law:

$$\int_{\partial\Omega} \sigma\frac{\partial u}{\partial n}dS = \sum_n \int_{E_n} \sigma\frac{\partial u}{\partial n}dS + \int_{S_\Gamma} \sigma\frac{\partial u}{\partial n}dS \tag{2.64}$$

Therefore, from (2.63), (2.64) and (2.53):

$$\int_\Omega \delta\sigma|\nabla u|^2 dV = V_\Gamma \delta I_\Gamma - \sum_n \delta V_n I_n \tag{2.65}$$

Finally, defining the ground state $V_\Gamma = 0$ leads to an equation similar to (2.54).

By analogy with the discussion of Section 2.4.1, the quantification of the voltage change ΔV observed on a given measurement electrode takes into account the dependancy of the potential on a vector of electrode current $\boldsymbol{I} = (I_1, ..., I_{n_e})$. Nevertheless, the potential also depends on the effects of the leaking current I_Γ and is referred as $u(\boldsymbol{I}, I_\Gamma)$. The sensitivity of a conductivity change $\delta\sigma(\boldsymbol{x}_0)$ at $\boldsymbol{x}_0$ over a voxel of area α with the presence of leaking current effects is given by:

$$\frac{\Delta V_{em}}{\delta\sigma(\boldsymbol{x}_0)} = -\int_\alpha \nabla u(\boldsymbol{I}_{exc}, I_\Gamma) \cdot \nabla u(\boldsymbol{I}_{meas}, I_\Gamma) dV. \tag{2.66}$$

With the addition of leaking current effects induced by the addition of ground surfaces on the boundary $\partial\Omega$, the sensitivity map is modified only by the effects on the excitation and measurement potential fields. The excitation and measurement potentials in (2.66) must take into account the leaking current on the grounded surfaces, by imposing $u(\boldsymbol{x}) = 0$ over $\boldsymbol{x} \in S_\Gamma \subset \partial\Omega$.

2.5.2. 3D simulations

The modelling of the effects of current leakage on the sensitivity requires a 3D simulation since one is in the $x - y$ plane and the other in the $x - z$ plane. The structure of the 3D domain (Figure 2.18) is build based on the two-dimensional disc for the simulation of the sensitivity. The mesh of the disk are duplicated on both sides of the z-axis over the total length $\mathcal{L}_{tot}$ of the system Ω, arbitrarily set so the electrical energy goes to zero on the right and left boundaries, considered infinitely far away. The position of the electrodes were chosen to be uniformly distributed on the circumference of the cylinder.

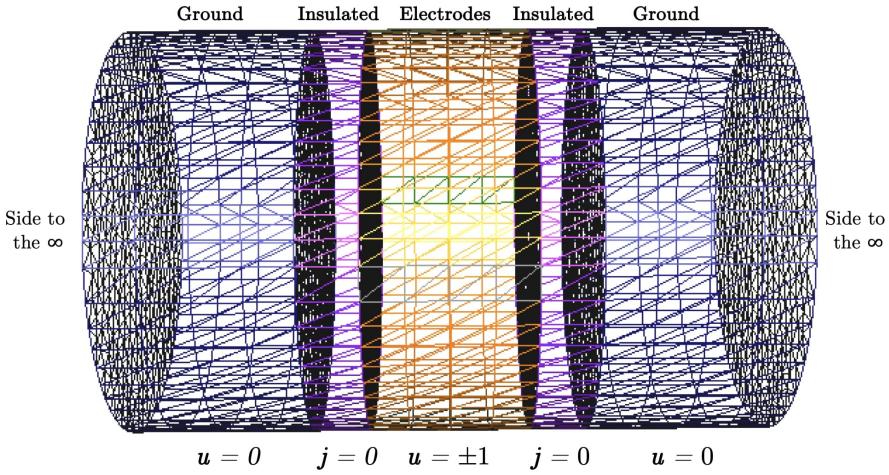

Figure 2.18. – The domain of the 3D simulation with the boundary conditions as in Figure 2.10.

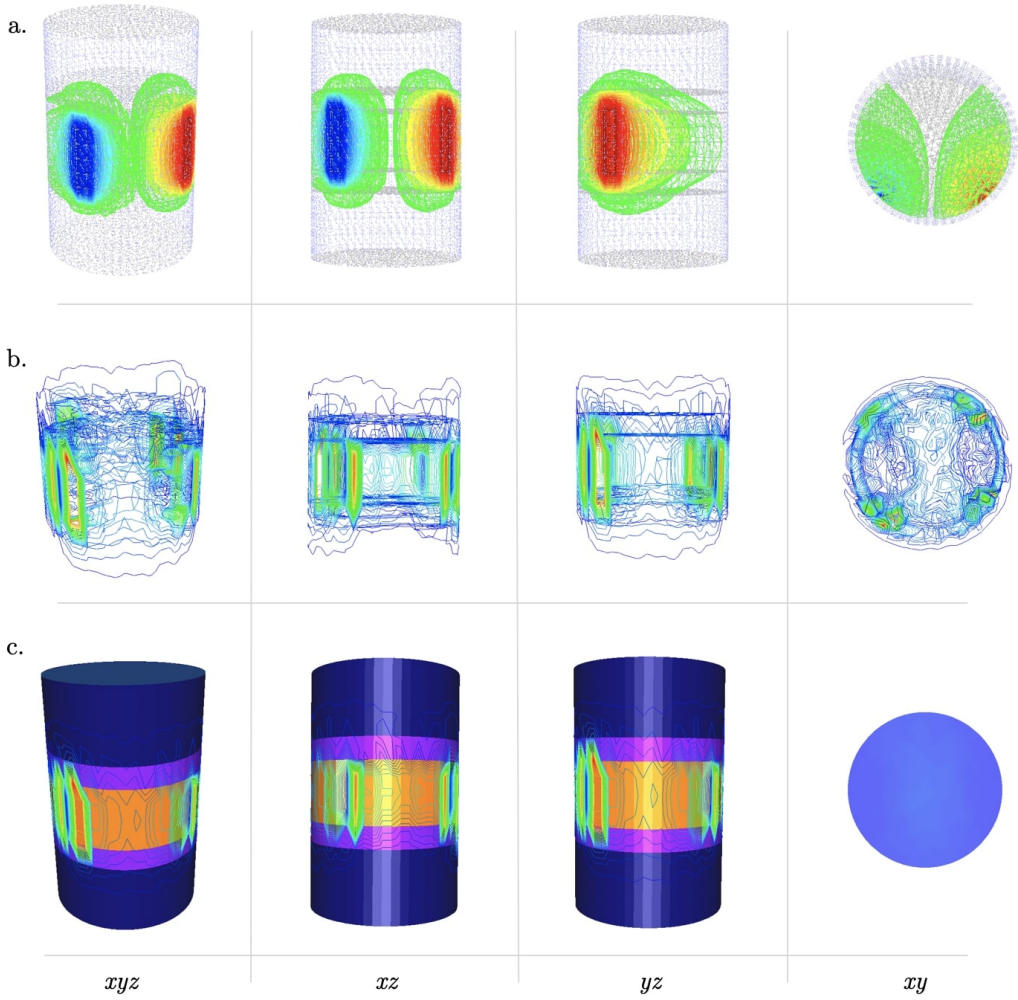

Figure 2.19. – Four representations in of the 3D simulations of a 4 electrode EIT sensor in the $x-y-z$ space and in the $x-z$, $y-z$ and $x-y$ plans for a. The iso-potential surfaces b. Log of the sensitivity c. Log of the sensitivity with the cylindrical boundary.

On each duplicated disc, the boundary conditions are set independently wether the boundary mesh are located on an excitation electrode, a measurement electrode, an insulated surface or a grounded surface. The iso-potential surfaces for an excitation of $\pm$1V between the pair of excitation electrodes is shown in Figure 2.19 in four point-of-views. From this excitation, the estimated sensitivity map is also shown in the Figure. The script which were written to obtain these results can be found in Appendix III.6.

This results are preliminary and the extension of this thesis is required to assess the effect of leakage on the sensitivity. To do so, this modelling requires the implementation of several electrode lengths configuration as in Section 2.3. Furthermore, the extension of the number of electrodes and independent measurement patterns as in Section 2.4.4 can bring interesting results for analysing the sensitivity map. The EIT image is reconstructed on the $x-y$ plan while the current flows in the z-direction as well so the system is sensitive to objects that are not necessary between the electrodes.

In the Figure 2.20a., a cavity is created inside the same cylinder. This cavity has an electrical conductivity of zero to represent an air bubble. The iso-potential lines are shown in Figure 2.20b. for an excitation between two electrodes with the cavity. The Figure 2.20c. is the difference $\Delta u = u_{homo} - u_{inhomo}$ between the homogenous potential field u_{homo} of Figure 2.19b. and the inhomogenous potential field u_{inhomo} with the cavity.

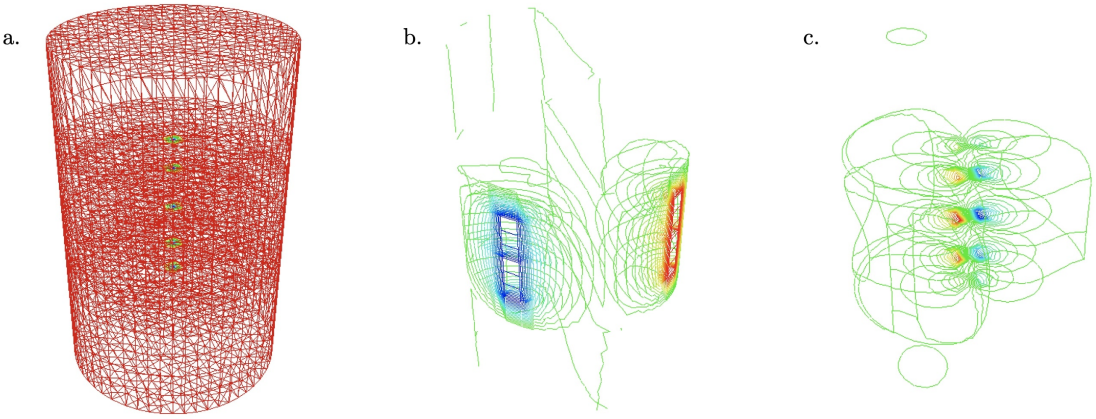

Figure 2.20. – 3D simulations of a 4 electrode EIT sensor with a cavity in the center of conductivity zero. a. The conductivity field on the mesh elements, the green lines are $\sigma = 0$ and the red lines are $\sigma = 1$. b. The iso-potential lines with the cavity c. The iso-potential lines of the potential field Δu.

The heaviness of the computation in 3D simulation imposed in this thesis to work with large mesh. The implementation of parallelised computation is possible with `FreeFEM++`. This task is also a suggestion for further work.

Prospects and indication for further work

The following prospects are proposed for future developments. The prospects that are estimated as most interesting/important are given at the top of the list.

- The development of 3D simulations to assess the effects of leaking current on the sensitivity map. This simulations must include a high number of nodes to compute the sensitivity with a high precision.
- The trigonometric excitation pattern is implemented in Chapter 6 with the COLTRANE method. This pattern has the particularity to inject the current from all the electrodes. From the results of Section 2.4, an interesting research topic would be to compute the sensitivity map of trigonometric excitations.
- An experiment can be setup to prove the simulation results on the leakage. The purpose is to measure the leaking current from electrodes of several lengths and to compute the corresponding energy.
- Another experiment is analog to the indirect reconstruction of the sensitivity map (Section 2.4.3). The method is to insert low conductivity sticks at $\boldsymbol{x}_0$ in an EIT sensor containing an electric potential induced by two excitation electrodes. Subsequently, to measure the changes in ΔV on two chosen measurement electrodes to reconstruct the sensitivity $\mathcal{S}$ at $\boldsymbol{x}_0$. These two experiments have been developed by a master student of INSA Lyon, Ying Zhuang, in an internship at LTHC during spring/summer 2019.
- The computation time to obtain the full-scan sensitivity map is very large. This time could be reduced with a parallelised computation strategy. The implementation of parallel computation is possible since each maps are independent.

"I'm smart enough to know that I'm dumb" *Richard Feynman*

3

Frequency Division Multiplexing for EIT

This third chapter proposes a practical implementation of FDM for a large number of simultaneous measurements. I will introduce the ONe Excitation for Simultaneous High-speed Operation Tomography (ONE-SHOT) method, an innovative method for simultaneous excitations for EIT. The method was introduced in [Dupré and Mylvaganam, 2018] for four electrodes; however, in practice, EIT systems usually contain eight electrodes or more for better performances. Furthermore, the method as it is introduced in [Dupré and Mylvaganam, 2018] is theoretical and does not contain details on technical issues for its practical implementation. In this chapter, I propose solutions with a physical experiment to prove its applicability to EIT...

Contents

3.1 Excitation and measurement strategy with FDM . . . 119
3.1.1 Need for increasing the imaging rate . . . 119
3.1.2 Introduction to simultaneous excitations in EIT . . . 120
3.1.3 The discrete Fourier transform . . . 122
3.2 The ONE-SHOT method . . . 127
3.2.1 General simultaneous excitation pattern . . . 128
3.2.2 Simultaneous excitation pattern for 16 electrodes . . . 129
3.2.3 Excitation frequencies based on the measurement time window . . . 129
3.2.4 Continuous formulation of the sensitivity map of the ONE-SHOT method . . . 131
3.3 The Data Acquisition (DAQ) system . . . 132
3.3.1 Load specifications and proposed DAQ system . . . 132
3.3.2 The EIT sensor . . . 134
3.3.3 The Printed Circuit Board (PCB) . . . 137
3.3.4 The DAQ controller . . . 138
3.3.5 Practical excitation and measurement strategy . . . 139
3.4 Preliminary experimental results . . . 140
3.4.1 Analysis of the error propagation . . . 141
3.4.2 Raw data . . . 143
3.4.3 Noise measurement . . . 146
3.4.4 Image reconstruction from 16 datasets . . . 147

As a first step, the Section 3.1 is a first approach for simultaneous excitations and measurements strategy with FDM. Secondly, a general definition of the ONE-SHOT method is proposed in Section 3.2. The section provides details for its practical implementation. Thirdly, the high frame rate generates a large amount of data to process. In the past few years the development of electronics made it possible to handle systems enabling transfer of large measurement data [Kryszyn et al., 2017]. The estimation of the optimal data transfer rate and online computation speed is needed to choose the adequate hardware components, an issue that is discussed in Section 3.3. Finally, the Section 3.4 presents preliminary results of the demodulation of 15 simultaneous excitation frequencies to prove the feasibility of the ONE-SHOT method.

3.1. Excitation and measurement strategy with FDM

The basic principle of simultaneous excitations is to consider several excitation frequencies. In the measurement channel, the combined signal can be decomposed in the Fourier space.

The necessity to increase the data frame acquisition rate is discussed in Section 3.1.1. A simulation presents the effects of low rate measurement on fastly evolving flows. As an introduction to EIT with FDM, two simple examples of simultaneous excitations are given in Section 3.1.2. The Section 3.1.3 is an overview on the Fourier transforms, and their use in a physical experiment.

3.1.1. Need for increasing the imaging rate

The determination of the number of electrodes n_e in the EIT system is a central question as it will impact the number of measurement for a given excitation strategy (Section 1.3.1). The simulation results of Section 2.2.1, obtained in the early work of the PhD, showed that a system with more than 16 electrodes gives better accuracy and higher contrast.

We have seen in Section 1.3.2 that the time of measurement depends greatly on the number of electrodes and on the excitation strategy. The full-scan excitation strategy brings a maximum of independent measurements to well-pose the reconstruction problem. Considering this strategy, the corresponding measuring time for one frame increases as n_e^2.

In applications to thermo-hydraulic circuits, if we consider the full-scan strategy and electrodes that are 1 cm long in the flow direction, it becomes impossible to have an image of a bubble flowing faster than ~ 2 m.s^{-1} for n_e =16 electrodes and ~ 0.5 m.s^{-1} for n_e =32 electrodes. These values are lower than the typical velocity of flows in industrial pipelines.

The effects of slow measurement of fast flows are simulated with `EIDORS` (Section 2.1.1). The output data for each measurement is a matrix containing the voltage measurements of all channel (in x) for every voltage measurement in time (in y). A fast bubble were simulated using the combination of two data matrices, from two simulated static flows

measurements.

The Figure 3.1a. illustrates two bubbles of different shapes passing through the cross plan of a pipe. The static measurements of these bubbles can be assimilated to very fast measurements, taken in very short measurement times Δt_1 and Δt_2. The reconstructed images of these two bubbles are shown in Figure 3.1b. and Figure 3.1c.

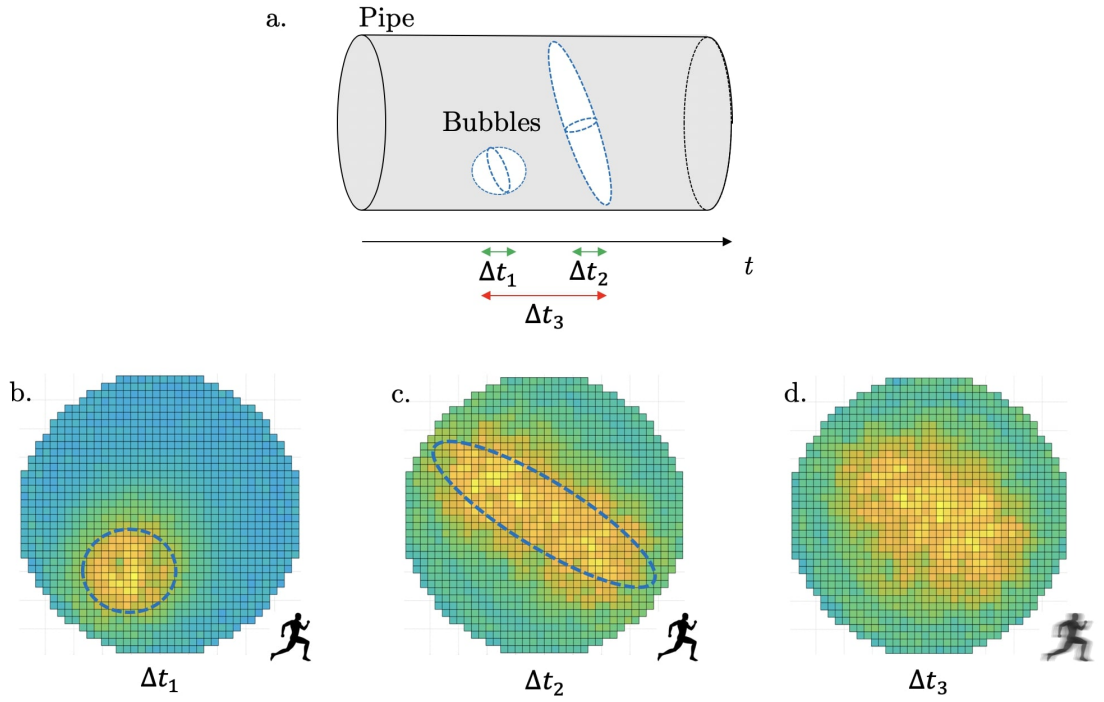

Figure 3.1. – a. Representation of two bubbles of different shapes passing through the cross section of the pipe. b. Simulated image of a bubble measured in a very short time Δt_1. c. Image of another bubble measured in a very short time Δt_2. d. Reconstructed image from the hybrid simulated data matrix.

A slow measurement time Δt_3 is illustrated in the Figure 3.1a. During this time interval, the two bubbles are passing through the pipe cross section. To simulate this, a hybrid data matrix, containing half of each static measurement is build. This hybrid data matrix corresponds to a flow that changes faster that one frame measurement. The reconstructed image of the hybrid matrix is illustrated in Figure 3.1d. In this blurred image, the shapes of the two bubbles are lost.

3.1.2. Introduction to simultaneous excitations in EIT

The solution I suggest in the necessity for increasing the imaging rate of EIT is to consider simultaneous excitations.

As an example, let us consider an EIT system containing a small number of electrodes: $n_e = 6$ electrodes $(E_1, ..., E_6)$ of arbitrary positions on the edge $\partial\Omega$ of a system Ω (Figure 3.2a.). For the sake of simplicity, the electrodes E_1 to E_4 are only used for

excitation and E_5 and E_6 only for the measurement. This section contains two simple examples of simultaneous excitation based on this 6 electrodes EIT system.

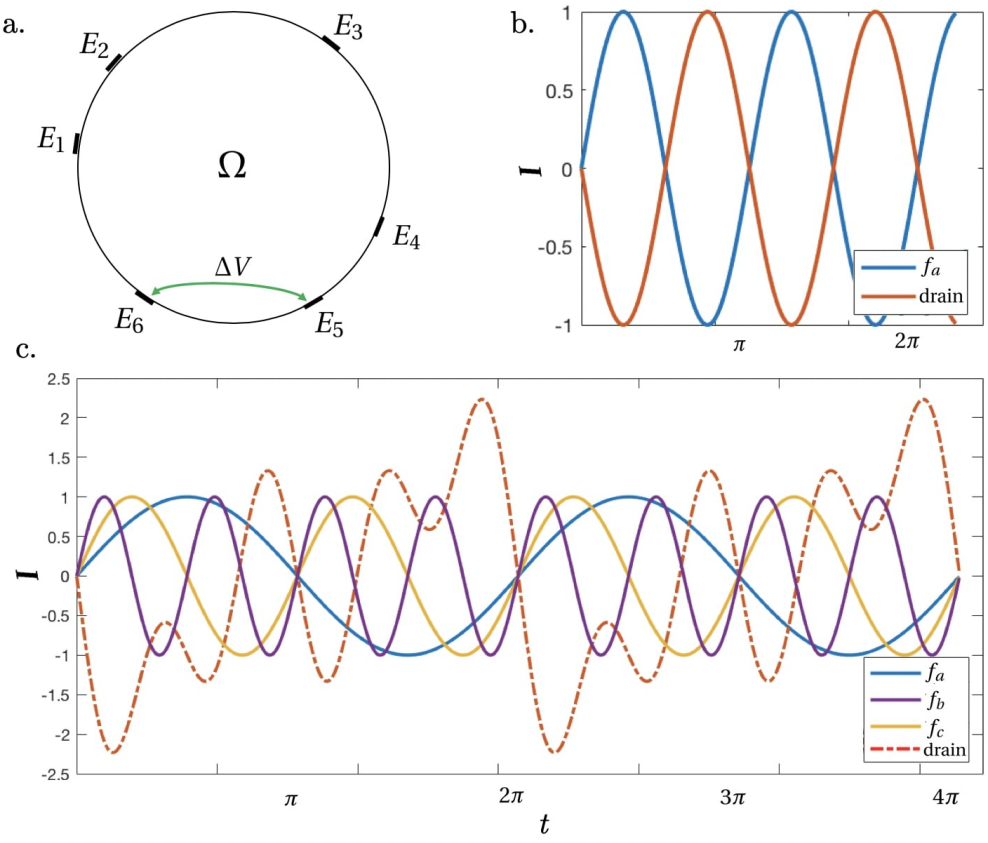

Figure 3.2. – a. Layout of a 6 electrodes EIT system: E_1 to E_4 are used for current excitation while the potential is measured between E_5 and E_6. b. Alternative excitation current between two excitation electrodes as used in the Adjacent, Opposite and Full-Scan Strategies. c. New MF excitation pattern between 4 electrodes.

Simultaneous excitations between two pairs of electrodes

Let's impose the Neumann boundary conditions by inducing a sinusoidal current of frequency f_a between E_1 and E_2 and another sinusoidal current of frequency f_b between E_3 and E_4. As discussed in Section 1.3.3 and Section 1.3.4, the conservation of current imposes:

$$\sum_{i=1}^{n_e} I_i = 0, \tag{3.1}$$

on all electrodes. This suggests that the excitation between two electrodes is composed of a *source* and a *drain* as illustrated in Figure 3.2b.

As a result, the Dirichlet boundary conditions are obtained by measuring the voltage ΔV between the two remaining electrodes E_5 and E_6. In this case, ΔV is expected to have a period p which is a function of f_a and f_b.

Due to the linearity of electromagnetism, the voltage ΔV is expected to be a superposition of the voltage ΔV_a induced by the current between E_1 and E_2 at frequency f_a and the voltage ΔV_b induced by the current between E_3 and E_4 at frequency f_b. The adequate use of Fourier transforms allows to decompose ΔV into its sub-components ΔV_a and ΔV_b.

The situation above introduces the basic idea of the simultaneous measurement with Multi-Frequency (MF). The reader may realise that this one measurement in MF contains the data of two independent measurements from the adjacent excitation strategy, reducing by twice the measurement time, without considering the multiplexing transition time between two successives excitations.

Three simultaneous excitations on four electrodes

In the above example, we are limited to two simultaneous measurements. By considering four electrodes for the excitation, it is possible to increase the number of simultaneous excitations by increasing the number of involved frequencies.

Let us now impose the Neumann boundary conditions by inducing a sinusoidal current of frequency f_a on E_1, f_b on E_2 and f_c on E_3, as illustrated in Figure 3.2c. The conservation of current is respected by imposing a current pattern of the form:

$$I_{Drain} = -\sin(2\pi f_a t) - \sin(2\pi f_b t) - \sin(2\pi f_c t) \tag{3.2}$$

on the remaining electrode E_4, labelled as *drain*.

In this situation, the resulting voltage ΔV measured between E_5 and E_6 is a superposition of the voltage ΔV_a induced by the current between E_1 and E_4 at frequency f_a, the voltage ΔV_b induced by the current between E_2 and E_4 at frequency f_b and the voltage ΔV_c induced by the current between E_3 and E_4 at frequency f_c.

In this new situation, it is interesting to consider $f_c > f_a$ and $f_c > f_b$ so the measurement time between E_3 and E_4 is shorter than the other measurements. By comparaison with the previous situation with two frequencies, we have now three independent measurements, taken in the same interval of time.

The Section 3.2 proposes to maximise the number of simultaneous measurements with the so-called ONE-SHOT method.

3.1.3. The discrete Fourier transform

We will see in the following that the excitation strategy in the ONE-SHOT method considers a high number of superposed signals. The decomposition of these signals in a physical experiment requires the implementation of highly performing Fourier transforms.

Signals in nature are continuous in time. The use of computer to manipulate signal transformation introduces the necessity of discrete numerical methods. This section introduces the continuous transformations and their discrete equivalent, as used in the signal processing in the frame of this work to decompose the measured signals.

Every signal has two representations: in time and frequency. Firstly the time representation $y(t)$ or $y(p)$ is used for a continuous time t or a discrete time with p the period between two steps of a discrete sequence. Secondly, the frequency representation of a signal addresses a key role for the pure frequencies which constitute a basis for the representation of the signals. The duality between discrete and continuous time and their corresponding representations in frequency domain results in four classes of signals that are associated to four transformation families:

- The signals with continuous time and frequency are linked with the Fourier transform. This transform acts on time signals of dimension [s] to its frequency representation of dimension $[\mathrm{s}^{-1}] = [\mathrm{Hz}]$.
- Periodic signals has a particular status since their frequency representation is composed of discrete values that are associated to the harmonics of a fundamental frequency. The representation of these signals are the Fourier series.
- The discrete signals are represented in a continuous frequency domain with the Z-transform. The introduction of the reduced frequency transform gives an intuitive representation of the frequencies.
- Finally, the signals of discrete time and frequency are treated with the Discrete Fourier Transform (DFT) that can be fastly implemented with the Fast Fourier Transform (FFT) algorithm.

In the following, we briefly overview the four transforms and focus on the DFT and FFT which are widely used in this work.

The Fourier transform

Let $x(t) \in L^2$ a finite non periodic signal with

$$\int_{-\infty}^{+\infty} |x(t)|^2 dt < \infty. \tag{3.3}$$

The Fourier transform $X(f)$ of the signal gives the complex spectrum of $x(t)$:

$$X(f) = \mathcal{F}[x(t)] \tag{3.4}$$

$$= \int_{-\infty}^{+\infty} x(t) e^{-2\pi i f t} dt \tag{3.5}$$

The real and imaginary parts of the spectrum are then:

$$Re[X(f)] = \int_{-\infty}^{+\infty} x(t) \cos(-2\pi i f t) dt \tag{3.6}$$

and

$$Im[X(f)] = \int_{-\infty}^{+\infty} x(t) \sin(-2\pi i f t) dt, \tag{3.7}$$

respectively. The spectrum is generally represented in terms of its magnitude:

$$|X(f)| = (Re[X(f)]^2 + Im[X(f)]^2)^{1/2} \tag{3.8}$$

and its phase:

$$\phi_X(f) = \arctan\left(-\frac{Im[X(f)]}{Re[X(f)]}\right). \tag{3.9}$$

Another property of the Fourier transform is its invertibility. The signal $x(t)$ can be completely reconstructed from the knowledge of its complex spectrum $X(f)$ with: The Fourier transform $X(f)$ of the signal gives the complex spectrum of $x(t)$:

$$x(t) = \mathcal{F}^{-1}[X(f)] \tag{3.10}$$

$$= \int_{-\infty}^{+\infty} X(f)e^{-2\pi ift}df. \tag{3.11}$$

Finally the two functions $x(t)$ and $X(f)$ represents the same physical quantity but from different representation. This observation is closely related to the impossibility of the humain brain to watch the nature without deforming it [1].

The Fourier transform of periodic signals

Let us considering the periodic function $\tilde{x}(t) \in L^2$ of period T. As a periodic function, it can be represented by the following Fourier series:

$$\tilde{x}(t) = \frac{a_0}{2} + \sum_{n=1}^{\infty}[a_n \cos(2\pi n f_0 t) + b_n \sin(2\pi n f_0 t)], \tag{3.12}$$

with $f_0 = 1/T$ the fundamental frequency of the signal $\tilde{x}(t)$. Here, $a_0/2$ is the continuous component of the periodic signal. The coefficients a_n and b_n are given by:

$$a_n = \frac{2}{T} + \int_{-\frac{T}{2}}^{+\frac{T}{2}} \tilde{x}(t)\cos(2\pi n f_0 t), \tag{3.13}$$

$$b_n = \frac{2}{T} + \int_{-\frac{T}{2}}^{+\frac{T}{2}} \tilde{x}(t)\sin(2\pi n f_0 t), \tag{3.14}$$

From (3.12), the complex numbers

$$\tilde{X}_n = \frac{1}{2}(a_n - ib_n) \tag{3.15}$$

and

$$\tilde{X}_{-n} = \frac{1}{2}(a_n + ib_n) \tag{3.16}$$

1. Note: This is one interpretation of the duality principle of quantum physics as introduced by Heisenberg in 1927.

gives the complex Fourier series:

$$\tilde{x}(t) = \sum_{-\infty}^{\infty} \tilde{X}_n e^{-2\pi i n f_0 t}, \tag{3.17}$$

with the introduction of $\tilde{X}_n$, the complex spectrum of the periodic signal $\tilde{x}(t)$:

$$\tilde{X}_n = \frac{1}{T} \int_{-\frac{T}{2}}^{+\frac{T}{2}} \tilde{x}(t) e^{-2\pi i n f_0 t} dt, \tag{3.18}$$

which let appear the positive ($n > 0$) and negative ($n < 0$) frequencies. Similarly to (3.6) to (3.9), the exponential component is used to find the magnitude and the phase spectrums.

We introduce the frequency Dirac comb function:

$$\delta_{f_0} = \sum_{-\infty}^{\infty} \delta(f - f_0) \tag{3.19}$$

with the Dirac delta function $\delta(x)$ which is $+\infty$ for $x = 0$ and 0 otherwise. The Dirac delta function verifies the property $\int \delta(x)dx = 1$. Thus, (3.17) becomes:

$$\tilde{x}(t) = \int_{-\infty}^{\infty} \left[\sum_{-\infty}^{\infty} \tilde{X}_n \delta(f - f_0) \right] e^{-2\pi i n f_0 t} dt, \tag{3.20}$$

and the distribution

$$\tilde{X}(f) = \sum_{-\infty}^{\infty} \tilde{X}_n \delta(f - f_0) \tag{3.21}$$

is the Fourier transform of the periodic function $\tilde{x}(t)$. In the frequency spectrum, the representation of such periodic functions is formed from peaks, related to the harmonics of the fundamental frequency f_0. We will see later that this point is very important since it is the basis of the determination of the whole set of excitation frequencies in the ONE-SHOT method.

The Fourier transform is a linear operation. It has numerous properties that are not enumerated in this work. The reader can find more details in [Max and Lacoume, 2004].

The Fourier transform of discrete signals

The numerical transformation of signals, including Fourier transforms, necessitates discrete operations. The sampling of a natural and continuous signal by a numerical device results in a sequence defined on a discrete time scale, that can be transformed with the reduced frequency transform.

To transpose the continuous Fourier transform of (3.5) into a discrete operation, the integral is replaced by a series, and the time t to a discrete time p. For the sampling

period T_s, the product ft becomes fpT_s and the non-dimensional reduced frequency is:

$$\lambda = fT_s. \tag{3.22}$$

The Fourier transform of a discrete signal $x(p)$ becomes

$$X(\lambda) = \mathcal{F}[x(p)] \tag{3.23}$$

$$= \sum_{p=-\infty}^{+\infty} x(p)e^{-2\pi i\lambda p}. \tag{3.24}$$

and similarly, the discrete signal can be reconstructed from the reduced frequency Fourier transform:

$$x(p) = \int_{-\frac{1}{2}}^{+\frac{1}{2}} X(\lambda)e^{-2\pi i\lambda p}d\lambda. \tag{3.25}$$

The discrete Fourier transform

In a physical experiment, the discrete signals are of finite lengths and are represented by a P-point sequence. Typically, in a discrete Fourier transform the signal which is bounded within $0 \leq p \leq P$ is extended to the real axis, and p grows from $-\infty$ to $+\infty$. As explained above, the frequency representation of such discrete and finite signals $x(p)$ is given by the reduced frequency transform $X(\lambda)$. However, the extension of the signals to the whole real axis makes it acts as a periodic function of period P resulting in a sampling in time and in frequency. The Fourier transform $X(k)$ of a finite and discrete signal $x(p)$ is:

$$X(k) = \mathcal{F}[x(p)] \tag{3.26}$$

$$= \theta \sum_{p=0}^{P-1} x(p)e^{\frac{-2\pi ikp}{P}}. \tag{3.27}$$

With θ an arbitrary normalisation factor, typically chosen to be $\theta = 1$ or $\theta = 1/P$. Similarly, the inverse DFT is given by:

$$x(p) = \mathcal{F}^{-\infty}[X(k)] \tag{3.28}$$

$$= \beta \sum_{p=0}^{P-1} X(k)e^{\frac{-2\pi ikp}{P}}. \tag{3.29}$$

with $P\beta\theta = 1$. A wise choice for the arbitrary terms is $\theta = \beta = 1/\sqrt{N}$ in order to respect the symettry between the DFT and its inverse operation.

Real-time fast Fourier computation

The DFT is a method that is widely used in spectral analysis, necessitating eventually a fast implementation of the algorithm. The FFT algorithm [Good et al., 1997] were

developed in this direction. In general, the FFT is computed over a sequence containing a number of points P that is a power of 2: $P = 2^n$.

In a direct computation of the DFT as in (3.27), each value of $X(k)$ necessitates P additions and P complex multiplications. Therefore, the whole computation of the DFT necessitates a total of P^2 additions and complex multiplications. By supposing $P = 2^n$, it is possible to distinguish the sum over even samples and odd samples. For $0 \leq k \leq P/2$:

$$X_P(k) = \theta \sum_{l=0}^{\frac{P}{2}-1} x(2l) e^{\frac{-2\pi i l p}{P/2}} + \theta e^{\frac{-2\pi i l p}{P}} \sum_{l=0}^{\frac{P}{2}-1} x(2l+1) e^{\frac{-2\pi i l p}{P/2}} \tag{3.30}$$

and

$$X_P\left(k + \frac{P}{2}\right) = \theta \sum_{l=0}^{\frac{P}{2}-1} x(2l) e^{\frac{-2\pi i l p}{P/2}} - \theta e^{\frac{-2\pi i l p}{P}} \sum_{l=0}^{\frac{P}{2}-1} x(2l+1) e^{\frac{-2\pi i l p}{P/2}}, \tag{3.31}$$

such that the DFT over the $P/2$ even samples is

$$X_{e\frac{P}{2}}(k) = \theta \sum_{l=0}^{\frac{P}{2}-1} x(2l) e^{\frac{-2\pi i l p}{P/2}} \tag{3.32}$$

and over the $P/2$ remaining odd samples is

$$X_{o\frac{P}{2}}(k) = \theta \sum_{l=0}^{\frac{P}{2}-1} x(2l+1) e^{\frac{-2\pi i l p}{P/2}}. \tag{3.33}$$

Finally we have,

$$X_P(k) = X_{e\frac{P}{2}}(k) + e^{\frac{-2\pi i l p}{P}} X_{o\frac{P}{2}}(k) \tag{3.34}$$

and

$$X_P\left(k + \frac{P}{2}\right) = X_{e\frac{P}{2}}(k) - e^{\frac{-2\pi i l p}{P}} X_{o\frac{P}{2}}(k). \tag{3.35}$$

The procedure above shows that it is possible to compute the DFT of a P-points sequence from two DFT over $P/2$ points. These sub-sequences can also be decomposed into $P/4$ points sequences. Choosing p as a power of two makes possible to decompose up to a sequence of two points, reducing significantly the number of operations to compute the DFT. The number of operations for the FFT is proportional to $P.\log_2(P)$ against P^2 for the DFT. The FFT algorithm is a central tool to use FDM and is widely used along this thesis to treat the measured signals.

3.2. The ONE-SHOT method

The ONE-SHOT method was introduced in [Dupré and Mylvaganam, 2018], which contains motivating results that predict the feasibility of the demodulation of simultaneous excitations with respect to their frequencies. Nevertheless, the proof-of-principle experiment is based on a four-electrode EIT system. The number of independent pairs of

excitation for such systems is six, implying six simultaneous excitations at six different frequencies. In practical EIT, the number of electrodes is an important parameter since it allows more measurements and a better conditioning of the inverse problem. Usually, EIT systems contain more than eight electrodes.

The need for more simultaneous measurements is the motivation to evolve the ONE-SHOT method with the increased number of electrodes and, consequently, the number of excitation frequencies. This section discusses the generalisation of the ONE-SHOT method excitation strategy to any number of electrodes in Section 3.2.1 and then adapted for 16 electrodes in Section 3.2.2. This process increases significantly the number of independent pairs and the complexity of the corresponding excitation patterns. Finally, choosing the frequencies is a challenging task. A choice is proposed in Section 3.2.3 to ensure discriminability, a high rate, and adaptivity to high-speed hardware systems. Finally, the sensitivity map of measurements with the ONE-SHOT method is discussed in Section 3.2.4.

3.2.1. General simultaneous excitation pattern

The ONE-SHOT method has to be adapted for a larger number of electrodes. The total number of independent measurements

$$N \;=\; \frac{n_e\,(n_e-1)}{2}. \tag{3.36}$$

defines the number of frequencies that have to be generated simultaneously to maximise the number of measurements for a given system. The excitation is a set of voltages imposed on the electrodes and is generated from a basis of N sinusoidal signals. Moreover, as discussed in Section 1.3.3 and Section 1.3.4, the excitation pattern ensures that the sum of boundary voltages is zero at any time.

One defines the signal Ψ_i as:

$$\Psi_i(t) = A\sin(2\pi f_i^{exc} t). \tag{3.37}$$

Then, given an arbitrary number n_e of electrodes, one defines the excitation voltage $V_n^{exc}(t)$ at an arbitrary electrode $n \in \{1,\dots,n_e\}$ using the following recurrence relation:

$$V_n^{exc}(t) = -\sum_{j=1}^{n-1} \left[V_j^{exc}(t)\right]_{n-1} + \sum_{\ell=\ell_n^{\min}}^{\ell_n^{\max}} \Psi_\ell(t) \tag{3.38}$$

where:

$$\ell_n^{\min} = (n-1)n_e - \frac{n(n-1)}{2} + 1 \qquad \text{and} \qquad \ell_n^{\max} = n\;n_e - \frac{(n+1)n}{2} \tag{3.39}$$

and with $\left[V_j^{exc}(t)\right]_{n-1}$ designating the $(n-1)^{\text{th}}$ element of the identity defining the voltage $V_j^{exc}(t)$, under the convention that the terms Ψ_i are always ordered with increasing index i

in such an identity. Moreover, in (3.38), we adopt the convention that a sum is identically zero if the value of the starting index is larger than that of the ending one.

The validation of (3.38) is made with the `MATLAB` script of Appendix IV.1.

3.2.2. Simultaneous excitation pattern for 16 electrodes

We are now interested in applying (3.38) in the situation of $n_e = 16$ electrodes. In this situation, $N = 120$ and the set of excitation voltages $[V_n^{exc}(t)]$ contains signals that are distributed by respect with the excitation matrix (IV.1.1):

$$\left\{\begin{array}{lcccccccc} V_1^{exc}(t) & = & +\Psi_1 & +\Psi_2 & +\Psi_3 & + & ... & +\Psi_{14} & +\Psi_{15} \\ V_2^{exc}(t) & = & -\Psi_1 & +\Psi_{16} & +\Psi_{17} & + & ... & +\Psi_{28} & +\Psi_{29} \\ V_3^{exc}(t) & = & -\Psi_2 & -\Psi_{16} & +\Psi_{30} & + & ... & +\Psi_{41} & +\Psi_{42} \\ V_4^{exc}(t) & = & -\Psi_3 & -\Psi_{17} & -\Psi_{31} & + & ... & +\Psi_{53} & +\Psi_{54} \\ & \vdots & & & & & & & \\ V_{15}^{exc}(t) & = & -\Psi_{14} & -\Psi_{28} & -\Psi_{41} & - & ... & -\Psi_{118} & +\Psi_{120} \\ V_{16}^{exc}(t) & = & -\Psi_{15} & -\Psi_{29} & -\Psi_{42} & - & ... & -\Psi_{119} & -\Psi_{120} \end{array}\right. \tag{3.40}$$

where the frequency f_{120}^{exc} is the N^{th} frequency for $n_e = 16$. Finally, the verification of the Dirichlet boundary requirement (Section 1.3.4):

$$\sum_{i=1}^{n_e} V_i^{exc} = 0. \tag{3.41}$$

from the excitation pattern of (3.40) is straightforward.

3.2.3. Excitation frequencies based on the measurement time window

The main advantage in the use of a continuous MF excitation method is the absence of transients between successive projections, resulting in a diminution of the measurement error from the absence of the residual voltage in the electrode–electrolyte contact impedance. Concerning ONE-SHOT, the values of the frequencies remain as free parameters. In this section, I suggest suitable values based on the performances of the DAQ system.

The first observation is that in order to ensure continuous excitations and measurements in parallel, the frequencies of the excitation signals have to be harmonics of a fundamental frequency f_0, as discussed in Section 3.1.3. A wise choice is to define f_0 as the frequency of the DFT of a P-point measurement sequence $\{V_n^{meas}(p)\}$ and p the discrete time. The discretisation of the time is due to the sampling rate of the DAQ system at the frequency f_{DAQ}, with the discretisation time interval $\Delta p = 1/f_{DAQ}$, implying:

$$f_0 = \frac{f_{DAQ}}{P}. \tag{3.42}$$

The DFT (3.27) of the real-valued sequence $\{V_n^{meas}(p)\}$ in the $1 \leq n \leq n_e$ measurement channel is:

$$\hat{V}_n^{meas}(k) = \mathcal{F}[V_n^{meas}(p)] \;=\; \theta \sum_{p=0}^{P-1} V_n^{meas}(p) e^{-ik\beta_p}, \quad k = 0, ..., P-1, \tag{3.43}$$

with $\theta = 1/P$, $\beta_p \;=\; 2\pi p/P$, and a synchronous sampling is assumed. The real and imaginary parts of $\hat{V}_n^{meas}(k)$:

$$Re_n(k) \;=\; \frac{1}{P} \sum_{p=0}^{P-1} V_n^{meas}(p) \cos(k\beta_p) \tag{3.44}$$

and:

$$Im_n(k) \;=\; -\frac{1}{P} \sum_{p=0}^{P-1} V_n^{meas}(p) \sin(k\beta_p) \tag{3.45}$$

define the module $M_n(k)$ and the phase $\phi_n(k)$ of each frequency domain sample $\hat{V}_n^{meas}(k)$:

$$M_n(k) \;=\; \sqrt{R_n^2(k) + I_n^2(k)} \tag{3.46}$$

and:

$$\phi_n(k) \;=\; \arctan\left(\frac{I_n(k)}{R_n(k)}\right). \tag{3.47}$$

The adequate situation where the frequencies f_i^{exc} of the generated sinusoidal signals Ψ_i are multiples of f_0 leads to the following observation: To each k-coefficient is associated a frequency f_k^{meas}, which is linked to the DFT computation frequency f_0 by $f_k^{meas} \;=\; kf_0$, for $k = 0, ..., P-1$, and the following difference, which defines the resolution in the Fourier space:

$$\Delta f_k^{meas} \;=\; f_{k+1}^{meas} - f_k^{meas} = f_0. \tag{3.48}$$

Choosing the generated frequencies as harmonics of f_0 leads to a match between f_i^{exc} and f_k^{meas} such that $f_i^{exc} \;=\; f_k^{meas} \;=\; f_i$, for $i = k$ and $i = 0, ..., P-1$.

This observation is particularly interesting as with a given magnitude $M_n(k)$ is associated a frequency f_k^{meas}, which corresponds to one and only one generated signal frequency f_i^{exc} on the electrode n. Therefore, the set of $[M_n(k)]$ for all n and k is one frame of the EIT data. The frame is acquired at the frequency f_0 and contains the full set of independent excitations and measurements to define the Dirichlet or the Neumann boundary conditions.

A first remark is that the highest frequency f_N^{exc} is constrained below the Nyquist limit: $f_N^{exc} \leq f_{DAQ}/2$. A second remark concerns the phase shift, which describes the difference in radians when two or more alternating quantities reach their maximum or zero values. The phase shift of an electric signal passing through a material depends on the frequency [Dupré, 2017]. In ONE-SHOT, the continuous generation of signals makes the phase shift independent of the Fourier magnitude. This is true because of the choice

of the generated signals that are harmonics of the Fourier computation time window.

In standard EIT based on TDM, the measurement associated with one excitation configuration corresponds to a voltage or current input over one or several periods of an alternative excitation at a given fixed frequency. The corresponding data are a set of tens of points per measurement, which multiplied by M (2.12) gives the total number of samples per frame. On the other hand, in the Fourier space, the corresponding data for the same measurement becomes a single element $M_n(k)$ with n and k defined. Building a data frame with the Fourier elements reduces significantly the data size.

Finally, the determination of the frequencies for the application of a 16-electrode ONE-SHOT method excitation strategy strongly depends on the acquisition rate f_{DAQ} of the DAQ system and the choice for the number of measurement points P used to compute the DFT.

3.2.4. Continuous formulation of the sensitivity map of the ONE-SHOT method

The ONE-SHOT method consists in the simultaneous excitation in voltage of pairs of electrodes at several frequencies and the measurement in current. The sensitivity of this strategy is computed by analogy with Section 2.4.

The measured current on an electrode is changed by a perturbation $\sigma(\boldsymbol{x}_0) \to \sigma(\boldsymbol{x}_0)+\delta\sigma$ of the conductivity. We reinterpret (2.47), with V_n^{exc} the imposed potential on electrode E_n and I_n, (2.48), the measured current passing through E_n.

The set of perturbations becomes:

$$\begin{cases} \sigma(\boldsymbol{x}_0) & \to \sigma(\boldsymbol{x}_0) + \delta\sigma(\boldsymbol{x}_0) \\ u(\boldsymbol{x}) & \to u(\boldsymbol{x}) + \delta u(\boldsymbol{x}) \\ V_n^{exc} & \to V_n^{exc}, \text{invariant} \\ I_n & \to I_n + \delta I_n \end{cases} \tag{3.49}$$

and the first order of the perturbation of (2.47) is:

$$\int_\Omega \sigma|\nabla u|^2 dV + 2\int_\Omega \sigma\nabla u\cdot\nabla\delta u dV + 2\sum_n \int_{E_n} z_n \left(\sigma\frac{\partial u}{\partial n}\right)\delta\left(\sigma\frac{\partial u}{\partial n}\right) dS = \sum_n V_n^{exc}\delta I_n \tag{3.50}$$

And the weak formulation with $w = \delta u$ gives:

$$\int_\Omega \delta\sigma|\nabla u|^2 dV + 2\int_{\partial\Omega} \delta u\sigma\frac{\partial u}{\partial n} dS + 2\sum_n \int_{E_n} z_n \left(\sigma\frac{\partial u}{\partial n}\right)\delta\left(\sigma\frac{\partial u}{\partial n}\right) dS = \sum_n V_n^{exc}\delta I_n. \tag{3.51}$$

From (2.50),

$$\delta\left(\sigma\frac{\partial u}{\partial n}\right) = \frac{1}{z_n}(\delta V_n^{exc} - \delta u|_{\partial\Omega}) = \left.\frac{-\delta u}{z_n}\right|_{\partial\Omega}, \tag{3.52}$$

and the total change in power is:

$$\int_{\Omega} \delta\sigma |\nabla u|^2 dV = \sum_n V_n^{exc} \delta I_n. \tag{3.53}$$

By opposition with the case of Sec. 2.4.1, the experimental interpretation of (3.53) is to quantify the current variation δI_n observed on electrode E_n for a potential imposed on one or several electrodes. The dependency of the potential to a vector of potentials $\boldsymbol{V} = (V_1, ..., V_{n-e})$ is denoted $u(\boldsymbol{V})$. For an excitation/measurement configuration, the excitation potential field is $u(\boldsymbol{V}^{exc})$ and the measurement potential field is $u(\boldsymbol{V}^{meas})$. Therefore, the power perturbation formula of (3.53) is applied to $u(\boldsymbol{V}^{exc}) + u(\boldsymbol{V}^{meas})$ and $u(\boldsymbol{V}^{exc}) - u(\boldsymbol{V}^{meas})$ and subtracted:

$$\Delta I_{em} = \int_{\Omega} \delta\sigma \nabla u(\boldsymbol{V}^{exc}) \cdot \nabla u(\boldsymbol{V}^{meas}) dV. \tag{3.54}$$

Finally, the sensivity at $\boldsymbol{x}_0$ of the finite element voxel of area α is:

$$\frac{\Delta I_{em}}{\delta\sigma(\boldsymbol{x}_0)} = \int_{\alpha} \nabla u(\boldsymbol{V}^{exc}) \cdot \nabla u(\boldsymbol{V}^{meas}) dV. \tag{3.55}$$

3.3. The Data Acquisition (DAQ) system

The DAQ system to implement the ONE-SHOT method with 16 electrodes has stricts requirements in terms of performance. These requirements for each component that led to the choice of this particular DAQ system are discussed in Section 3.3.1. The three main parts of this system the EIT Sensor, the Printed Circuit Board (PCB) and the DAQ Controller are presented in Section 3.3.2, Section 3.3.3 and Section 3.3.4, respectively. Finally, the Section 3.3.5 discusses the optimal characteristic of the signals based on this particular DAQ system.

3.3.1. Load specifications and proposed DAQ system

The starting point in creating a physical experiment for simultaneous EIT excitations and measurements is to establish the requirements on the DAQ system. The DAQ system is required to verify the following tasks :

- **High rate**: The sinusoidal output signals of an electronic device are generated by a succession of points. The time between two points is limited by the highest rate the system can handle. In order to reconstruct properly the Fourier transform of a signal, the Nyquist theorem requires that each periods contains at list 2 points. The excitation frequency window is between 1 and 500 kHz. Hence, the generation of a 500 kHz excitation signal requires that the system handle a minimum rate of 1 MHz.
- **High number of I/Os**: The MF data taking strategy requires the DAQ system to operate in parallel n_e output excitation signal and n_e input measurement signals.

The number of electrodes n_e being higher than 16 for a good signal reconstruction (Section 2.2.1).

- **Fast computation**: In MF DAQ, the input signals are decomposed online in parallel. The use of a Field Programmable Gate Array (FPGA) is adequate to compute DFT with a high rate. However the numerous computations in parallel requires an FPGA with a very large memory.
- **Operational at distance** for experiments in high pressure and high temperature environments.

The concretisation of an experiment to implement the ONE-SHOT method is based on the proposed hardware system presented in Figure 3.3. It is composed of three elements: the EIT sensor that contains the electrodes, the PCB to distribute the signals, and the DAQ controller to manage the excitations and measurements:

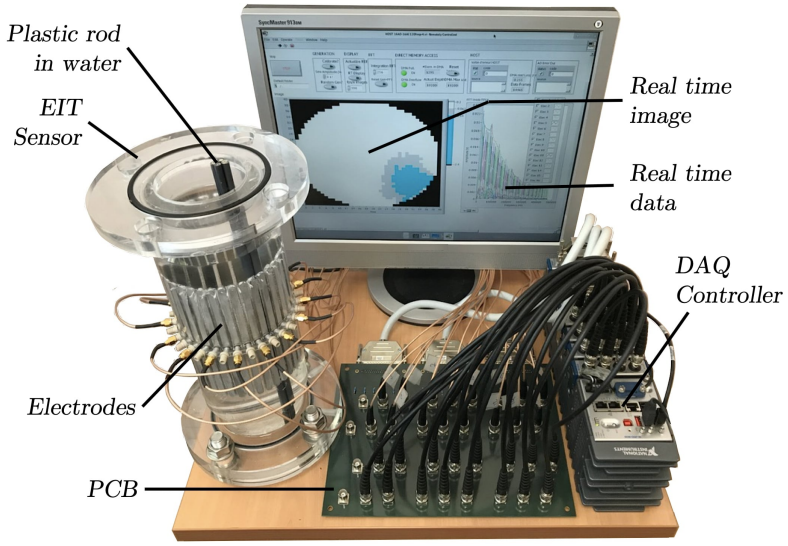

Figure 3.3. – The system implementing the ONE-SHOT method as used for static experiment. The EIT sensor is filled with water and a plastic rod of low conductivity is inserted to mimic non-conductive inclusions. The software provides a 2D real time image of the probed medium.

- **The EIT sensor:** contains a set of 16 electrodes (Figure 3.3) tangential to the inner surface of the pipe and in contact with the fluid. The electrodes are used for excitation and measuring the response of the medium.
- **The PCB:** used for the 16 excitation signals fed to the 16 electrodes. The material distribution is estimated using reconstruction algorithms from voltage measurements over 16 resistors on the PCB.
- **The DAQ controller:** manages both AO excitations and Analog Input (AI) measurements. The DAQ controller provides 16 voltage AO channels and 16 voltage AI channels.

The following details the issues and solutions found for the conception of these different components.

3.3.2. The EIT sensor

The EIT sensor is composed of a ring of electrodes in contact with the fluid and is non-intrusive. The electrodes must be insulated from each other and made in a conductive and robust material. In addition, the excitation and measurement signals at the electrodes are possibly of low amplitude.

The EIT sensor prototype used in my experiment is shown in photo in Figure 3.3 and in scheme in Figure 3.4.

It was a 336 mm-long cylinder PMMA prototype with an internal diameter of 80 mm containing a set of 32 electrodes (Figure 3.5 and Figure 3.6). The electrodes (Figure 3.7) were chosen to be made of stainless steel. They were 150 mm long and 6 mm wide, and their surface was tangential to the inner pipe surface and collinear to the axis of the cylinder. In the experimental setting considered, only one over two, 16 electrodes were connected. The characteristics of the detector were chosen for future tests on static and dynamic flow measurements at the Laboratory of analytical Thermohydraulics and Hydromechanics of Core and Circuits (LTHC). More details on the design of the EIT for flow measurement applications can be found in [Darnajou et al., 2017].

The signal was routed to the electrodes using shielded coaxial cables. The EIT sensor provided SMA (Sub-Miniature version A) connectors (Figure 3.8) to ensure the connection of the electrodes with the inner wire of the coax and the insulation of the shielding.

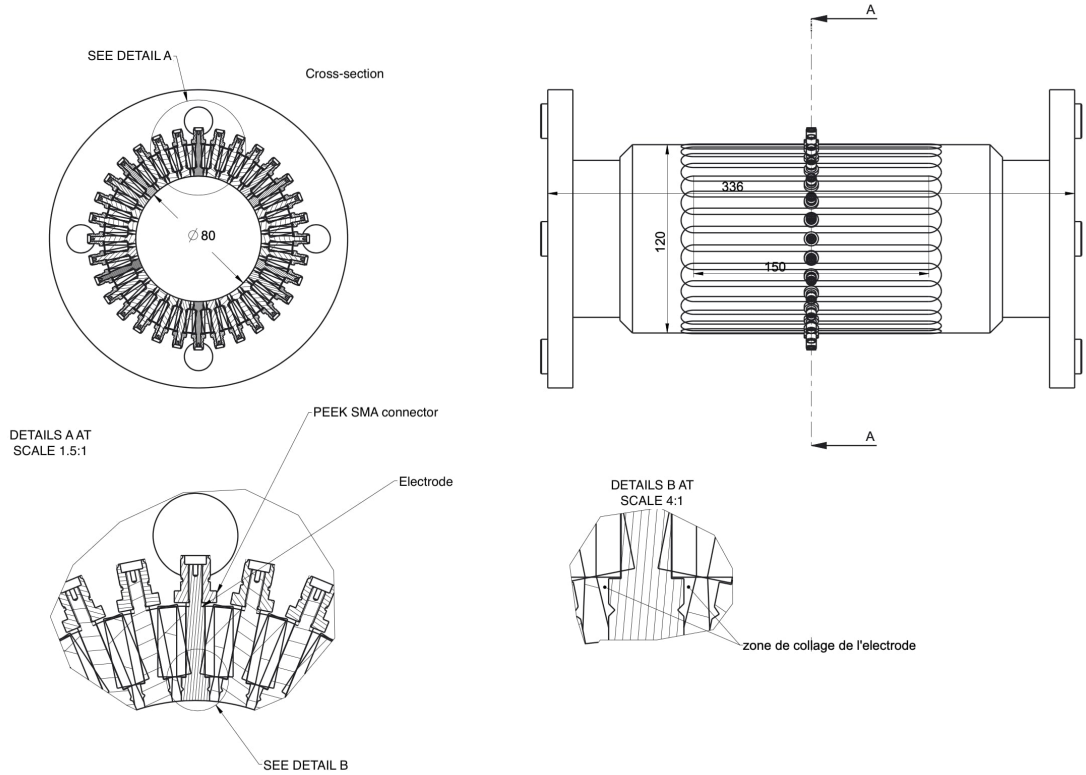

Figure 3.4. – Scheme of the EIT sensor used for low pressure and low temperature tests. This sensor is composed of four parts: The body in Figure 3.5, the pipe connectors in Figure 3.6, the electrodes in Figure 3.7 and the SMA adaptors in Figure 3.8.

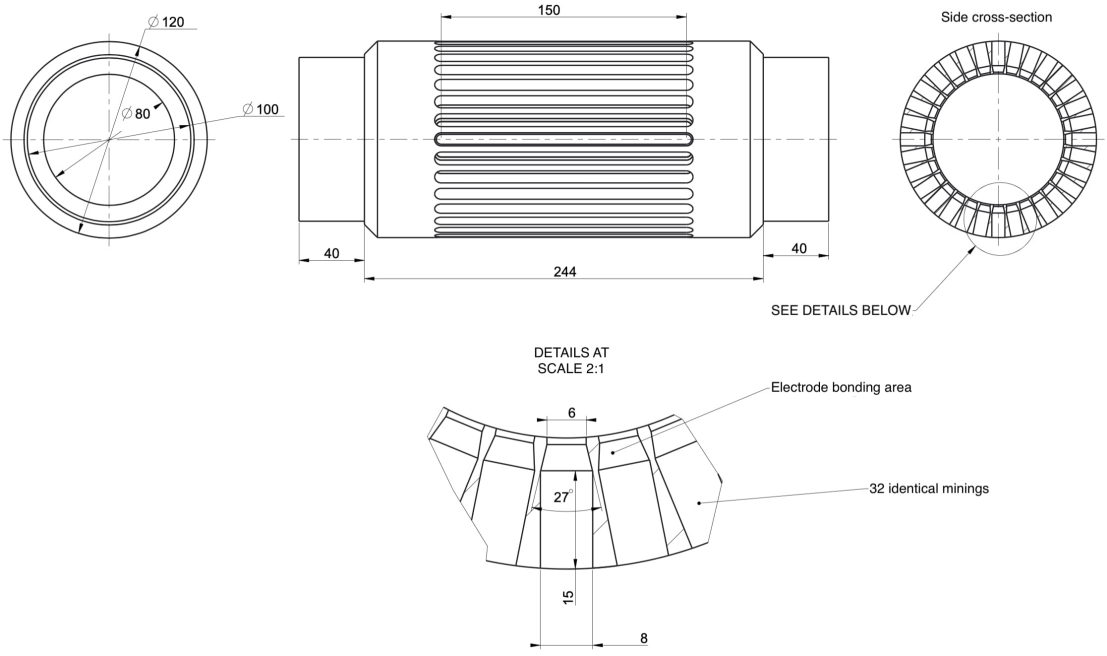

Figure 3.5. – PMMA body of the EIT sensor.

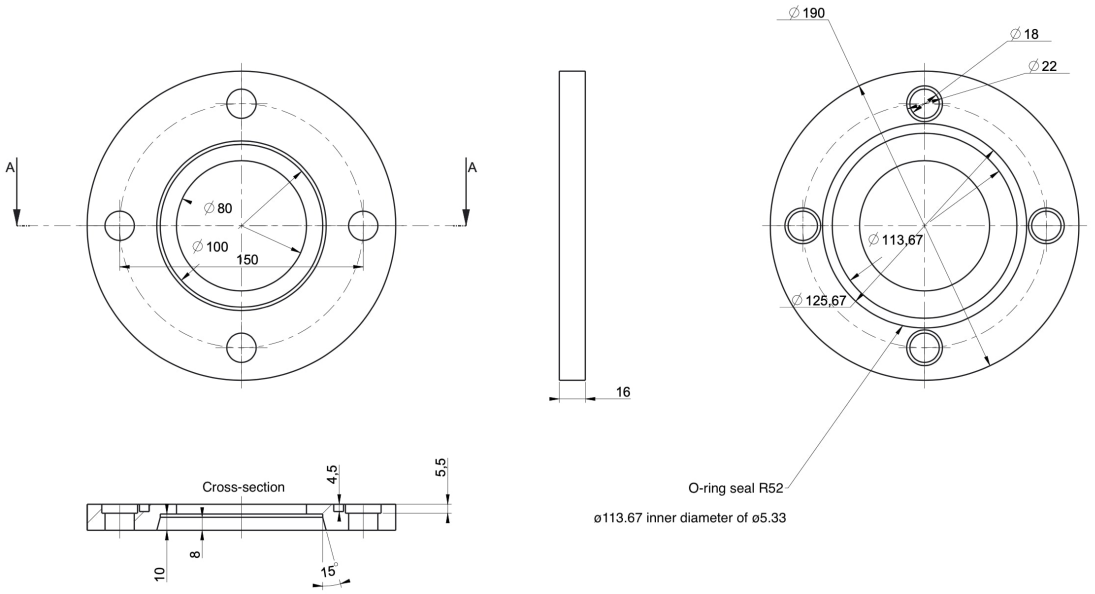

Figure 3.6. – PMMA pipes connector for inner diameter 80 and ISO standard pn10.

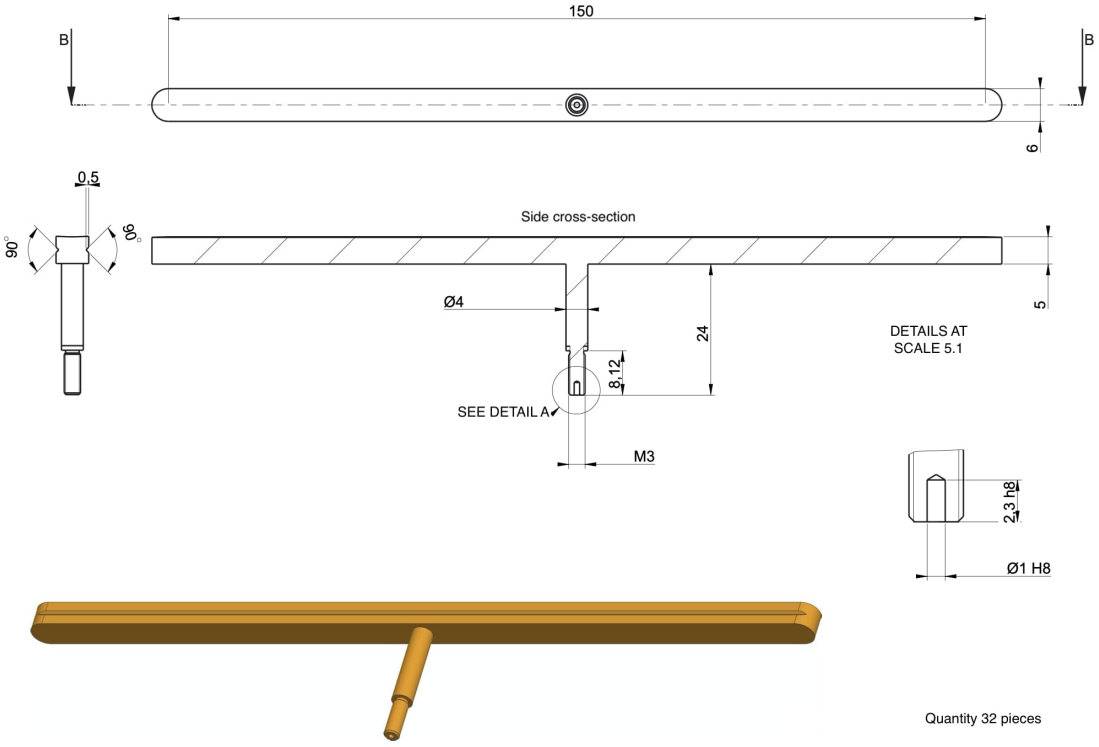

Figure 3.7. – Stainless steal electrodes.

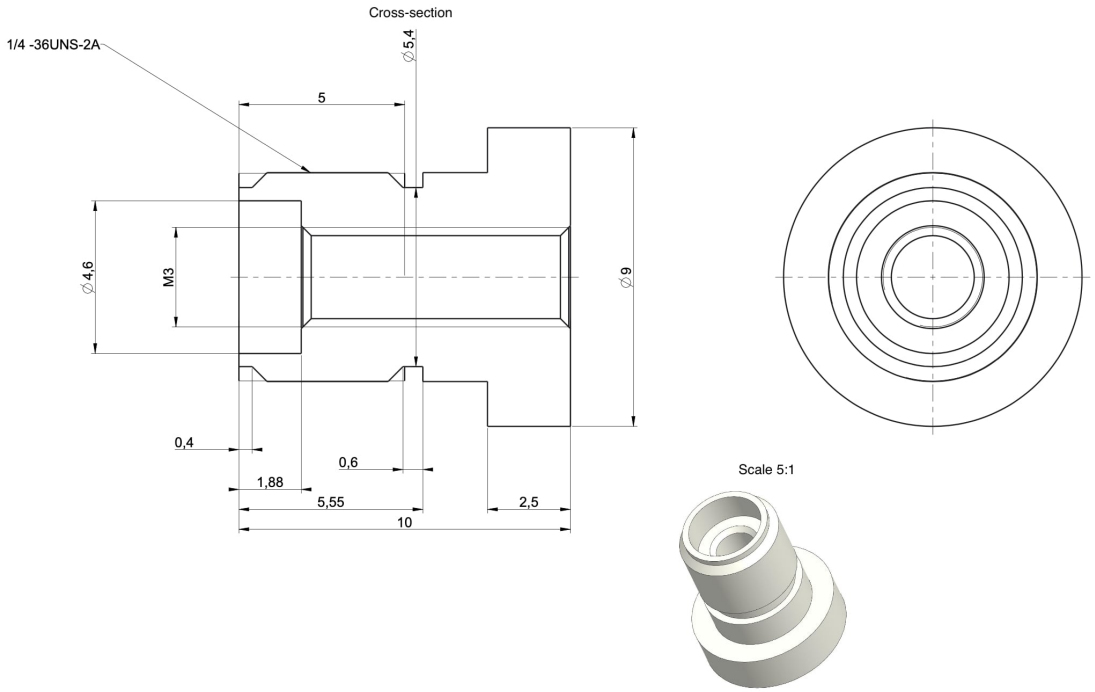

Figure 3.8. – PEEK SMA connectors.

3.3.3. The Printed Circuit Board (PCB)

The main motivation in using the ONE-SHOT method strategy is its high data acquisition rate. The natural choice for the hardware is to provide a very high sampling rate for excitation and measurement. As in Section 1.2.3, EIT relies on imposing or measuring either a voltage or a current on the boundary. However, the sampling rate for generation and acquisition of current is usually much slower than for the voltage.

A one-layer PCB (Figure 3.9) was designed to manage the voltage excitations and, in parallel, the current measurements. The currents passing through the electrodes (Neumann boundary conditions) were reconstructed from voltage measurements over 16 sense resistors of 100 Ω in the 16-electrode circuits on the PCB. This allowed current measurement using an analog voltage sampling at the DAQ level for a high sampling rate. Moreover, the PCB provided coaxial connectors and ensured the signal shielding with a ground connection.

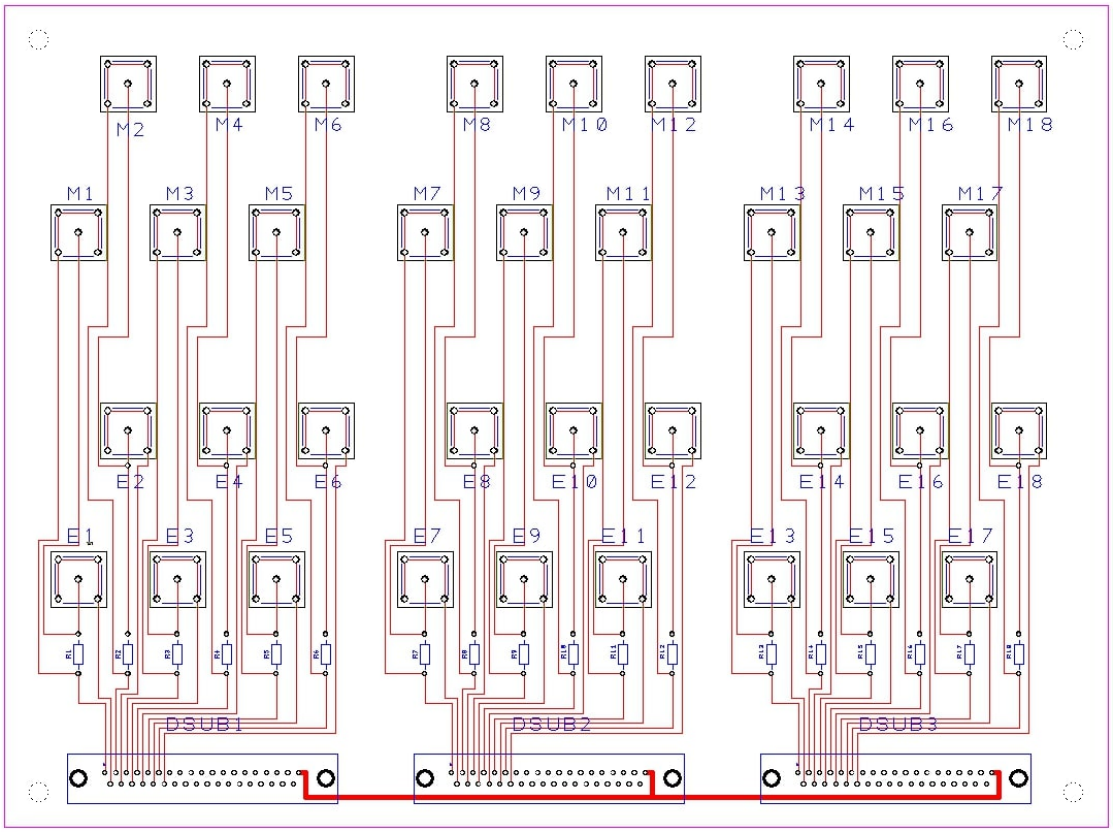

Figure 3.9. – Layout of the PCB design including 18 independent circuits for voltage excitation and current measurements. The M1 to M18 BNC connectors are differential measurements over the R1 -R18 100Ω resistors and connected to the NI-9223 modules. The E1 to E18 BNC connectors send the excitation signal to the electrodes, the circuit assures a shielding of the coax cables. On the bottom, 3 DSUB connectors for the excitation signals, the common ground assures the same ground reference for the 3 NI-9262 modules.

3.3.4. The DAQ controller

The DAQ controller was required to perform 16 voltage excitations and 16 voltage measurements in parallel at high rate with great accuracy. The output configuration contained the generation of 120 sinusoidal signals at 120 different frequencies and a distribution onto the 16 electrodes under (3.40). The input configuration computed the DFT online for each electrode signal at a high rate, based on the FFT algorithm. Finally, the DAQ controller was required to perform fast data storage.

Apart from the performance requirements, the DAQ controller must be robust and light weight for transportation purposes in future prospects of experiments on several hydraulic loops. It also has to be controllable at a distance for an application to high pressure and high temperature flow experiments.

The strict requirements of fast computations in both output and input for multiple channel operations, including FFT, suggest the use of a FPGA. In recent years, the number of logic blocks contained in an FPGA chip increased, and the generation of a

large number of arbitrary signals became feasible.

DAQ chassis

A suitable device for the DAQ controller in the ONE-SHOT method hardware system is the National Instruments CRIO-9039 [NI-9039 Documentation, 2016] controller, which includes a 1.91-GHz Quad-Core CPU, 2 GB of DRAM, and the `Xilinx`'s FPGA `Kintex-7 325T` [Xilinx325T Documentation, 2019]. The FPGA includes 326,080 logic cells, 840 digital signal processing slices, and 16,020 block RAM elements. The main advantage of the FPGA is that it includes a large number of logic cells and large block RAM, which are required in my experiment to perform the operations described in Section 3.2. The adequate use of the FPGA allows fast DFT for a minimal data frame size, which allows efficient data transfer and reduces storage.

The CRIO-9039 DAQ controller includes a Linux host computer that operates the ONE-SHOT method with `LabView` Real-Time and FPGA. The monitoring of the ONE-SHOT method results in a large amount of data over numerous channels. The fast data monitoring is based on Direct Memory Access (DMA), a buffer to send the data to the host computer. In addition, the CRIO-9039 provides 8 slots in which Analog Output (AO) and AI modules are connected.

Output and input configuration

Regarding the necessity for fast and accurate operations, the AO was managed with the NI-9262 [NI-9262 Documentation, 2017] module to provide the voltage outputs. The six-channel module had a typical output voltage range of ± 10.742 V, including an internal noise of 150 µV RMS per channel. In the system, three NI-9262 modules were connected to the 16-output excitations.

Concerning the AI, the NI-9223 [NI-9223 Documentation, 2016] module is suitable to provide voltage inputs. The NI-9223 includes four channels with a typical input voltage range of ± 10.6 V with a noise of 229 µV RMS per channel. A total of four NI-9223 modules were required to connect the 16 input measurements.

Finally, the digitalized data format for both AO and AI modules were (20,5) fixed points: 20 bits allocated to the number including 5 precision digits. The data were operated at a sampling rate of 1 Mega Samples per second (MS/s) for both AO and AI, which is very competitive in terms of the performance requirements.

3.3.5. Practical excitation and measurement strategy

The Figure 3.10 is a scheme of the DAQ system with the software logic blocs. The software of the ONE-SHOT method will be detailed in the Chapter 4.

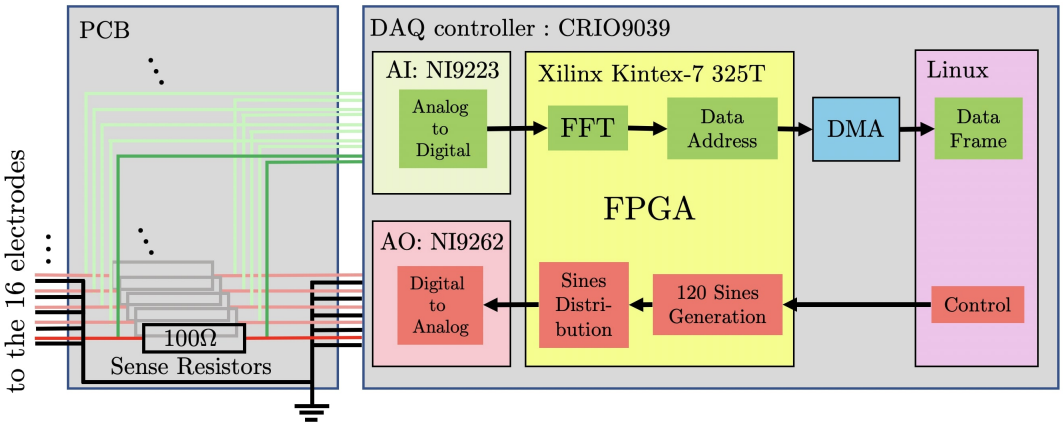

Figure 3.10. – Layout of the DAQ system. On the left, details of the PCB that includes 16 independent circuits for voltage measurements over 100 Ω resistors. On the right, the FPGA-based CRIO-9039 configuration containing four NI-9223 AI modules, three NI-9262 AO modules, and a DMA buffer all controlled by the host, operated by Linux. In red, the excitation circuit. In green, the measurement circuit.

In Figure 3.10, the excitation circuit is detailed in red. The host computer controls the FPGA to provide a fast generation of 120 sinusoidal signal signals. A second function inside the FPGA distributes the sinusoidal signals to the electrodes as in (3.40). The 16 signals are transformed from 1 MS/s digital to analog signals using the NI-9262 modules and sent with coaxial cables to the electrodes through the resistors of the PCB.

In parallel, the measurement circuit, shown in green in Figure 3.10, contains AI modules to digitalize the voltages taken over the 16 resistances on the PCB. The FPGA-based DFT computation provides the signal magnitude and phase for each Fourier coefficient at the high rate of 1 MS/s. The electrode label n and Fourier coefficient k are associated with the magnitude value to provide its address: the host computer uses the address as x and y coordinates for the magnitude to build the data matrix. The FPGA sends the data with a DMA to ensure fast operations and reliability.

Considering the sampling rate of 1 MS/s of the DAQ system, one solution for the frequencies of the generated signals (3.40) in the situation of a 16-electrode EIT sensor consists of $f_i^{exc} = if_0$ for $1 \leq i \leq N$ and $N = 120$. Furthermore, the DFT computation can be chosen to be over $P = 512$ points and results in a data frame acquisition rate of $1 \times 10^6/512 = 1953$ fps. This choice implies the lowest sinusoidal signal frequency f_1^{exc} to be the same as the DFT computation frequency. The highest frequency $f_N^{exc} = f_{120}^{exc}$ is 234.375 kHz, below the Nyquist limit of 500 kHz for the considered system.

3.4. Preliminary experimental results

As discussed in the introduction, the imaging rate of the well-established X-ray tomography suddenly increased when considering several pairs of emitters and receptors for simultaneous measurements. The novel idea, which consists of applying simultaneous excitations and measurements in EIT, brings new challenges due to the fundamental

differences existing between such hard field and soft field systems. Apart from the radical difference in solving the inverse problem (Section 1.3.4), MF excitations and measurements have to be considered with the association of TDM in the ONE-SHOT method strategy.

In Section 3.4.1, the error propagation through the FDM is estimated in this context based on two quantitative numerical simulations. The discriminability of the raw data is discussed in Section 3.4.2 in two harmonic ranges. In Section 3.4.3, the noise measurement is shown with a discussion of the SNR of the measured data. Finally, Section 3.4.4 introduces the images reconstructed from a set of measurement data.

3.4.1. Analysis of the error propagation

Besides the hardware configuration, the measurement performances strongly depend on the DFT algorithm, which may have an influence on the uncertainty of the output data [Betta et al., 2000]. Consequently, there is a great interest in evaluating the systematic uncertainty in the DFT reconstruction. Two simulations are proposed, firstly without noise to assess the systematic uncertainty due to the discretisation of the DFT into $P = 512$ points and, secondly, another simulation with a noisy signal to assess the propagation of noise in the DFT by quantifying the magnitude change in the Fourier space.

Noise-free sinusoidal signal simulation

In the first step, the experiment focused on a limited number of frequencies. Let us impose 16 voltage excitation signals over the electrodes: 15 sinusoidal signals V_n^{exc} of frequencies f_i^{exc} and amplitude A such that:

$$V_n^{exc} = A\sin(2\pi f_i^{exc} p), \quad \text{for } n = 1, ..., 15 \text{ and } i = n \tag{3.56}$$

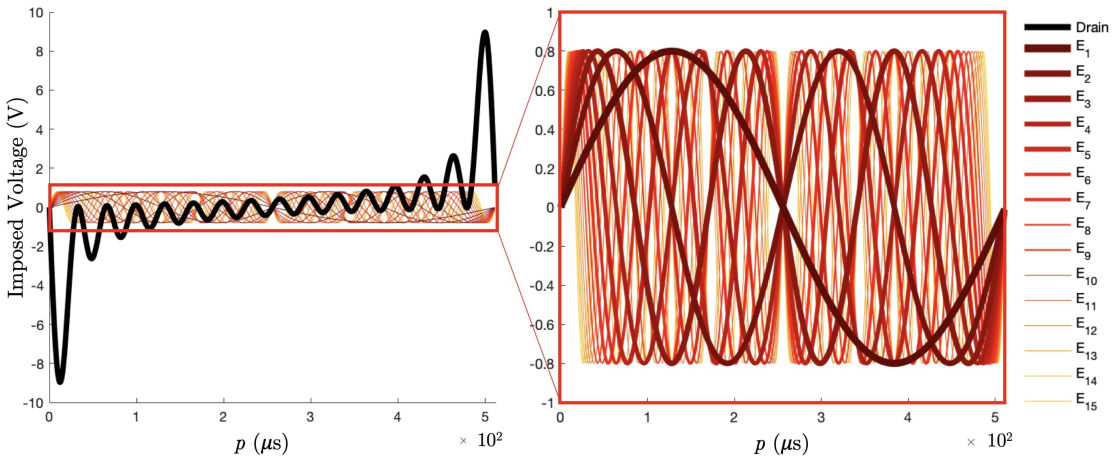

Figure 3.11. – The 15 excitation signals V_n^{exc} imposed on electrodes E_n of frequencies if_1^{exc} for $1 \leq i \leq 15$, and $f_1^{exc} = (512\ \mu s)^{-1}$. The drain excitation signal is shown in black on the left plot.

over the electrodes E_n. In addition, the definition of the ground (3.41) suggests a drain voltage:

$$V_{Drain}^{exc} = -A \sum_i \sin(2\pi f_i^{exc} p) \tag{3.57}$$

imposed on the remaining electrode E_{16} (Figure 3.11).

The lowest frequency is defined such that it corresponds to the frequency of the DFT computation time window (Section 3.2.3). The DAQ system described in Section 3.3 has a sampling frequency of 1 MS/s, resulting in $f_1^{exc} = (512\ \mu s)^{-1} = 1953.125$ Hz, which is also the resolution in the frequency space. Furthermore, the frequencies f_i^{exc} are the harmonics of f_1^{exc} such that $f_i^{exc} = i f_1^{exc}$. The amplitude A is 0.8 V, so the drain signal remains in the NI-9262 AO module range limit of ± 10.742 V.

The reconstruction of the magnitudes is shown in Figure 3.12. The systematic uncertainty due to the 512 points discretisation of the DFT was of the order of $O(1 \times 10^{-15})$ V.

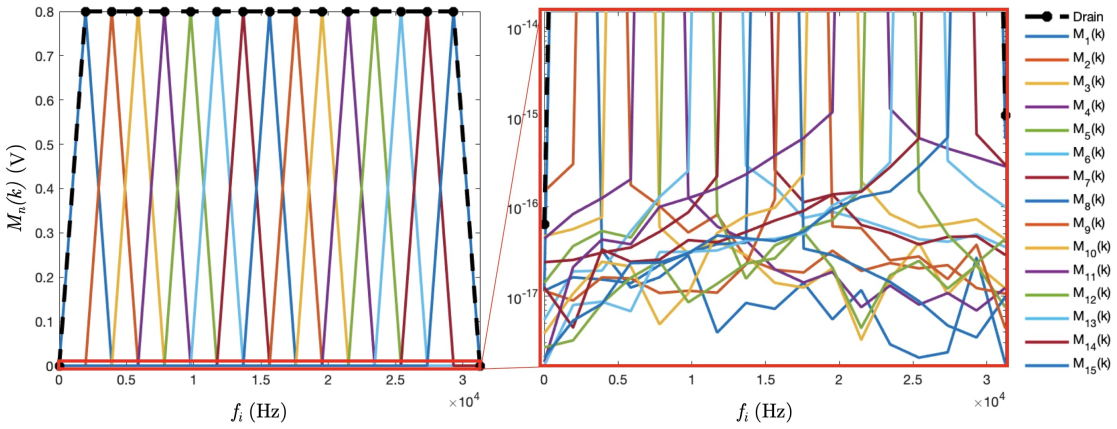

Figure 3.12. – Simulation of the magnitudes of the 15 frequencies plus the drain at the 16 channels. On the right, rescaled zoom in the bottom part in the logarithmic scale of the DFT plot to show the tails of the peaks due to the discretisation onto 512 points.

Sinusoidal signals with Gaussian additive noise

The second objective was to assess the magnitude of the distortion of the k^{th} harmonic due to the noise in the measured signal. In the time domain, the noisy signal $\tilde{V}_n^{meas}(p)$ in the circuit of electrode E_n contained a true signal V_n^{meas} and a Gaussian additive noise δ such that:

$$\tilde{V}_n^{meas}(p) = V_n^{meas}(p) + \delta(p). \tag{3.58}$$

Since the Fourier transform is linear, the addition of noisy signal gives the following magnitude in the k^{th} harmonic of the measurement on the n^{th} electrode, as in

Equations (3.43)–(3.46):

$$\tilde{M}_n(k) = \left[\left(\frac{1}{P} \sum_{p=0}^{P-1} (V_n^{meas}(p) + \delta(p)) \cos(k\beta_p) \right)^2 + \left(\frac{1}{P} \sum_{p=0}^{P-1} (V_n^{meas}(p) + \delta(p)) \sin(k\beta_p) \right)^2 \right]^{1/2}. \tag{3.59}$$

A simulation was proposed to assess the effects of a noisy signal by quantifying the magnitude change $\Delta M_n(k) = \tilde{M}_n(k) - M_n(k)$. The probability function, δ, of the Gaussian-distributed noise pattern reads:

$$\delta(p) = \frac{1}{s\sqrt{2\pi}} e^{-\frac{1}{2}(\frac{p}{s})^2}. \tag{3.60}$$

Several noise amplitudes with various standard deviation s were generated and added to the signal V_n^{meas} of Figure 3.11. The DFT coefficients of four different frequencies of low and high harmonic range are shown in Figure 3.13. On the abscissa, the Root Mean Square (RMS) of the generated noise δ_{RMS} is compared with the amplitude A of the generated sinusoidal signal as in Equation (3.37).

Due to signal filtering in the DFT computation, the error of the DFT magnitude for a given coefficient remains small by comparison with the original signal. However, the above simulation is based on white noise, which is well filtered by the DFT computation. Nevertheless, in the experimental case, it is important to detect possible constructing interference patterns in the noise, which could correspond to a generated frequency. The lengths of the cables in the DAQ system for instance have to be taken into account to not generate electromagnetic noise at one of the generated frequencies.

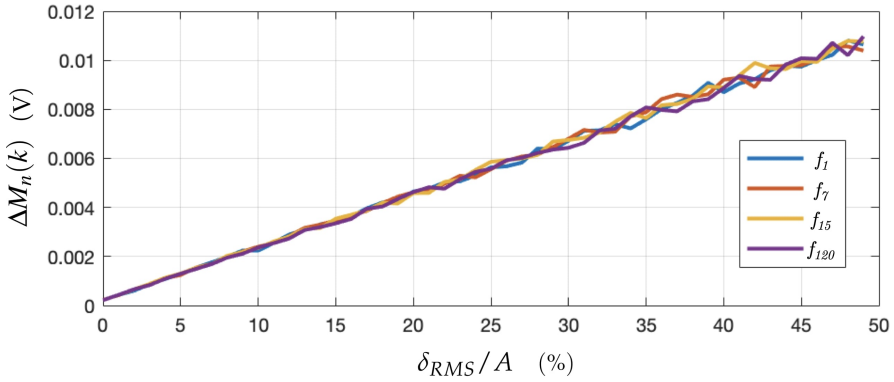

Figure 3.13. – Propagation of the Gaussian white noise through DFT computation for four generated frequencies. The Noise RMS was computed from 1000 Gaussian white noises and averaged out. The four curves follow the same linear interpolation: $y = 2.14 \times 10^{-4}\, x + 1.81 \times 10^{-4}$.

3.4.2. Raw data

The ONE-SHOT method excitation strategy has as its goal one single excitation for all independent pairs of electrodes, resulting in the generation of 240 positive and negatives

sinusoidal signals (3.40) of 120 different frequencies for 16 electrodes. Implementing the ONE-SHOT method is a challenging task as it requires fast voltage excitations of arbitrary signals and FFT computation of current measurements, all in parallel over numerous channels. Nevertheless, the simulation results in Section 3.4.1 are a great incentive to build the experiment as described in Section 3.3.

The preliminary results in this experiment are presented to prove the feasibility of using TDM in EIT, based on the simultaneous excitation of 30 positive and negative sinusoidal signals at 15 frequencies and the experimental DFT reconstruction of the same voltage excitation pattern as in Figure 3.11. Two frequency domains are investigated: the low harmonic range where the 15 positives sinusoidal signals are the 15 first harmonics of the DFT frequency f_0 (Section 3.2.3). Furthermore, the high harmonic range contains the harmonics 106–120: as discussed above, these higher frequencies are planned to be generated in the future development of a full simultaneous excitation set, as concretised in Chapter 4.

Experimental results in the low harmonic range

An experiment was set up to measure a homogenous field of conductivity 300 µS/cm. The results in the low harmonic range (Figure 3.14) are the DFT magnitudes $M_n(k)/R$ of the 16 experimental measurement signals computed from $P = 512$ data points, at a frequency of 1953.125 Hz for a data sampling of 1 MS/s. The results are shown as the current by including $R = 100\ \Omega$, the resistance in the measurement channel on the PCB. I observe a good accordance with the simulations of Section 3.4.1. The comparison of the experimental results (Figure 3.14) with the simulated DFT reconstruction of pure sinusoidal signals (Figure 3.11) led to the following observations:

- The readers familiar with EIT may expect the following phenomenon. In the experimental data, at the bottom of Figure 3.14 and Figure 3.15, non zero currents were measured over electrodes that were not excited at the corresponding frequency. Let us consider an electrode E_n with $1 \leq n \leq 15$ excited by a single sinusoidal signal of frequency f_i^{exc}. In the Fourier space (Figure 3.14 and Figure 3.15), the measured current passing through an electrode gives non-zero values for other frequencies. The reason comes from the electric potential difference that appears between the excited electrode E_n with an imposed potential V_n^{exc} with $-A \leq V_n^{exc} \leq +A$ and a non-excited electrode E_m whose potential is $V_m^{exc} = 0$ for a given frequency f_i^{exc} in the Fourier space (Figure 3.12). This effect is particularly large for the current in the adjacent measurement of the drain electrode in E_1 and E_{15}. These data depend on the electrical conductivity distribution inside the body and have to be considered as well.
- The magnitudes of the Fourier coefficients in the experimental results were lower for the mid-range harmonics than f_1^{exc} and f_{15}^{exc}: Considering the finite electrical conductivity inside the system, the current resulting from the potential imposed between two neighboring electrodes was larger than the current resulting from the

same potential imposed between two opposite electrodes in the circular shape of the EIT sensor [Dupré, 2017].

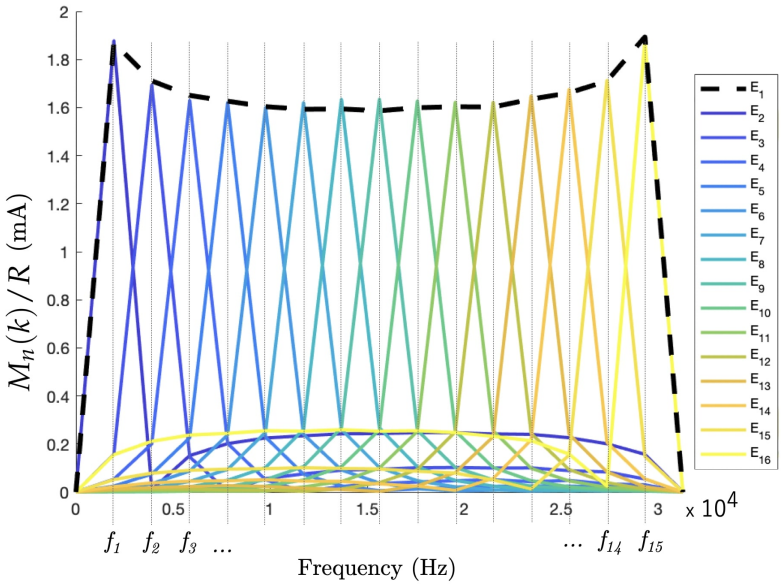

Figure 3.14. – Measured current, represented as the magnitude of the DFT of 16 voltages over resistances in the excitation circuit of the 16 electrodes. This result corresponds to excitations in the low harmonic domain.

Experimental results in the high harmonic range

The main prospect of the ONE-SHOT method excitation strategy is to consider simultaneous excitations at 120 different frequencies for the EIT sensor of 16 electrodes. As in Section 3.2.3, the frequencies were chosen to be harmonics of the fundamental frequency f_0. The 120th harmonic f_{120}^{exc} was then 234.357 kHz. I have investigated the performance of the ONE-SHOT method in this higher harmonic range.

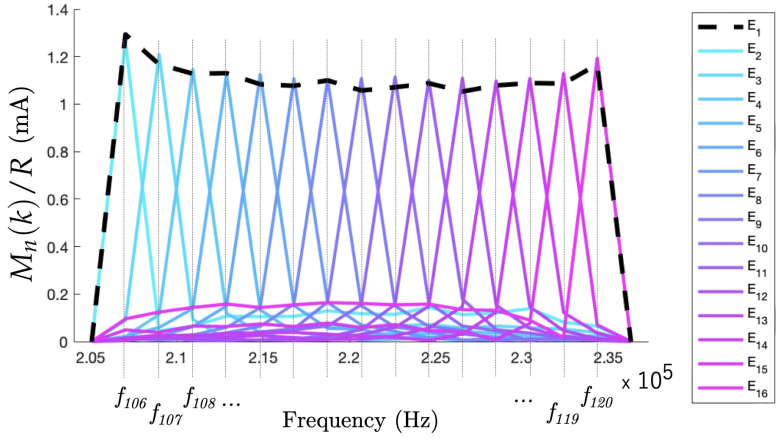

Figure 3.15. – Magnitudes of the DFT from excitations in the high harmonic domain.

The experimental measurement resulted in the high harmonic range from f_{106}^{exc}–f_{120}^{exc} is shown in Figure 3.15. The discrimination of the signals by frequency offered equivalent performances to the low harmonic case. However, an important remark is that the signal amplitudes in the high harmonic range were lower than previously due to the impedance of water, which depends on the excitation frequency. The result was a weaker response in amplitude in the high harmonic range for the same conductivity change in the system. The calibration of the amplitude of the generated sinusoidal signals have been developed in order to have a similar response in every harmonic when considering a full set of 120 excitations. However, this calibration reenforce the noise and is not used in the following.

3.4.3. Noise measurement

A set of voltage magnitudes $M_n^0(k)$, defined as in (3.46), was experimentally measured without any excitation to identify the noise spectrum. The results in Figure 3.16 show localized peaks in the noise amplitude beyond the high harmonic frequency domain.

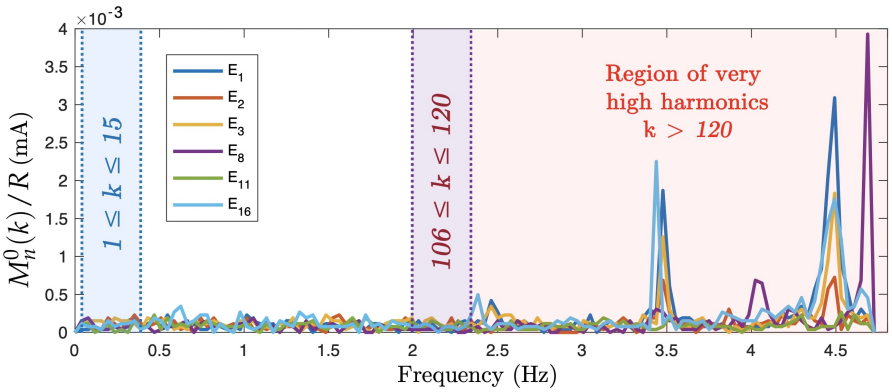

Figure 3.16. – Noise measured over the full spectrum available for the sampling rate of 1 MS/s. The results show five of the 16 electrode channels. The low, high, and very high harmonic ranges are also shown.

The SNR of a signal measured at a given electrode n and tagged with a given frequency k is defined as follows:

$$SNR_n(k) = \log_{10}\left[\frac{\sum_\lambda [M_n(k)]_\lambda / R}{\sum_\lambda ([M_n(k)]_\lambda / R)^2 + \sum_\lambda ([M_n^0(k)]_\lambda / R)^2}\right] \tag{3.61}$$

where λ is the number of data taken for averaging. The noise in the low harmonic range resulted in an SNR of the raw signal of 69.1 dB in the lowest frequency magnitude in the excitation electrode channels when averaging the signal from $\lambda = 20$ samples. In a non-excited channel, the signal was O(0.1) weaker, resulting in an SNR of about 60 dB depending on the signal magnitude. In the high harmonic range, the SNR was 59.6 dB for the highest harmonic.

The very high frequencies 250 $\leq$ 500 kHz, bounded above by the Nyquist limit, is

considered as excitation frequencies in the next chapter. However, a proper shielding of the DAQ system must be investigated. A large part of the noise was caused by electrical noise in the PCB. For this reason, a new PCB has been manufactured in Chapter 6. Finally, the results showed that the noise completely covered the DFT systematic uncertainty (Section 3.4.1), which is completely negligible.

3.4.4. Image reconstruction from 16 datasets

The main objective of the present work is the implementation of a method to obtain a very fast EIT data frame acquisition rate. From such data, the user can then reconstruct an image with any given reconstruction algorithm in post-processing, a step that I consider to be distinct from the main goal. As an example, we are interested in the image reconstruction of the above data. However, the datasets are incomplete by comparison with the ONE-SHOT method excitation prospects of (3.40). A solution consists of reconstructing the full dataset in the post-processing.

The results described above contained a complete set of excitations for the drain electrode. It is possible to consider another drain electrode and another frequency set to obtain another set of measurements, independent of location and frequency.

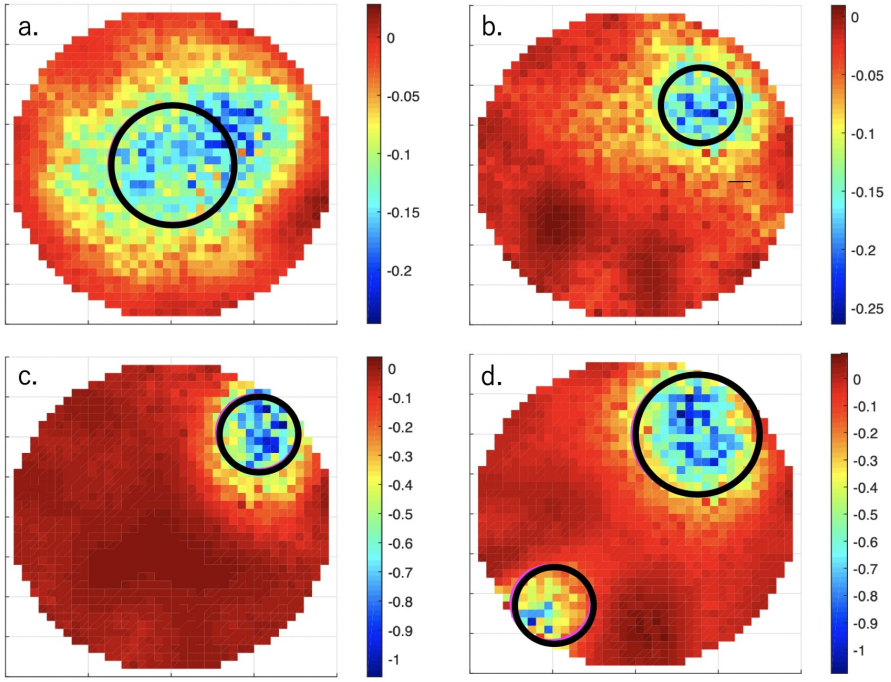

Figure 3.17. – Electrical conductivity indicator function. Two non-conductive rods of diameter 20 and 30 mm, shown with black circles, are inserted in the test section filled with salt water. a. A 30-mm rod at the center. b. A 20-mm rod half way to the edge. c. A 20-mm rod on the edge. d. Two rods on the edge.

The rotation of the drain over the 16 electrodes resulted in $16 \times 15 = 240$ pairs of excitations. The symmetry suggested to consider only half of the data. The full dataset

was deduced and contained the decomposition of 240 signals from 120 excitation pairs, measured over the 16 resistances of the PCB. Therefore, the full dataset included a total of 1920 elements. To sum up, the sequential excitations with the drain located on each of the 16 electrodes resulted in a dataset equivalent to the one expected by the full implementation of the ONE-SHOT method.

Several datasets were measured from the inclusion of non-conducting PMMA rods in the test section of Figure 3.3 filled with tap water with a conductivity of $\sigma = 635$ µS·m^{-1}. The one-step least-squares iterative reconstruction method [Yorkey et al., 1987, Kim et al., 2001] was implemented, and the results are shown in Figure 3.17.

The results showed similar image reconstruction performances as another EIT system [Dupré, 2017] based on TDM and using the same reconstruction algorithm. As usual in EIT, the sensitivity was much higher close to the electrodes. This effect resulted in sharp gradients when imaging the inclusions inserted at the edge.

Finally, the frame rate of the ONE-SHOT method system can be changed by integrating the FFT over more or less data points. For instance, choosing the FFT to be computed over 512 points as considered in this chapter resulted in the frame rate of 1953 fps. In this case, the 120 frequencies can fill all the discrete values from 1953 Hz to the Nyquist limit of 500 kHz with $\Delta f = 1/512$ µs $= 1953$ Hz the minimal gap between two neighboring values. The high frame rate was at the cost of a large frequency bandwidth.

Example of real-time application:
A pizza is a real-time pie chart of how much pizza is left.

4

Software development for the ONE-SHOT method

The goal of this research is to achieve high speed acquisition of data frames to image multiphase flows. Each frame contains the maximum number of linearly independent excitations and measurements for a given set of 16 electrodes, using a set of MF signals for the excitation of 16 electrodes. From the state of the art along with the findings of my work presented in Chapter 3 and in [Darnajou et al., 2019]*, three major issues need to be addressed to improve performances and achieve this high-speed data acquisition...*

Contents

4.1 Analog signal generation and acquisition logics . . . 154
4.1.1 Excitation frequencies . . . 154
4.1.2 Excitation amplitudes . . . 155
4.1.3 Analog signal generation logics . . . 156
4.1.4 Analog signal acquisition logics . . . 157
4.2 Output data format . . . 160
4.2.1 Standard EIT data . . . 160
4.2.2 Data from FPGA based ONE-SHOT method . . . 161
4.2.3 Sign of the signal magnitudes . . . 163
4.2.4 Spectral analysis of the impedance . . . 164
4.3 The ONE-SHOT method software . . . 165
4.4 Experimental results with static flows . . . 168
4.4.1 Static homogeneous medium . . . 168
4.4.2 Static inhomogeneous medium . . . 169
4.4.3 Contact impedance . . . 171

The three major areas that need to be addressed for improved performance in achieving this high-speed data acquisition are:

Analog signal generation

The first aspect is the generation of continuous signals at 120 distinct frequencies. An important task in this process is the selection of suitable frequencies for good performance of the FDM. A possible solution according to [Lockstone, 1993, Max and Lacoume, 2004] is to generate harmonics based on FFT frequency components and their amplitudes matching the frequencies/amplitudes of the generated frequencies. This solution results in a large bandwidth for 120 frequencies, while the signal frequencies are restricted by the Nyquist sampling limit determining the proper detection of the signals at the sensing electrodes. Moreover, harmonics of low frequency interfere with the signals in the upper frequency range, as discussed in [Quirás-Olozábal et al., 2016]. We need to address effects of the available bandwidth on the possible data acquisition rates. An alternative scheme for signal generation based on periods based on prime numbers is also presented.

The determination of the signal amplitudes is based on experimental observations. The DAQ system used in my experiments operates within ±10 V for AO, [Darnajou et al., 2019, NI-9039 Documentation, 2016, NI-9262 Documentation, 2017, NI-9223 Documentation, 2016]. The simultaneous generation of the 120 signals implies large values for the temporal derivative of the voltages (dV/dt), imposing restrictions on the output voltage levels in the DAQ system. We discuss, based on experimental observation, methods of maximising the signal output voltage to increase the SNR while keeping good discrimination of the signals at different frequencies for implementing the FDM.

Moreover, the firmware is extended from 15 frequencies to 120 frequencies using a larger Block Random Access Memory (BRAM), which is beyond the capacity of single FPGA chip, given the implementation strategy described in [Darnajou et al., 2019]. There are at least two solutions for extending the capacity of the FPGA. An array of FPGA chips can be used to increase the BRAM. First option enabling the fast operation for high data frames rate necessitates a robust and fast synchronisation strategy, as discussed in [Sanchez Correa and David, 2018]. Second option is the generation of the signals point by point from a pre-computed Look-Up Table (LUT), saved in the FPGA. The second option using the LUT saved in the FPGA is adopted here. For achieving the high-speed operations, LUTs are integrated in the FPGA firmware. This gives no flexibility in selecting the signal generation patterns, once the firmware is compiled.We propose to use one LUT for two AO channels. By using two accumulators incremented in a loop at high speed, I was able to extract two signals at two different frequencies from the same LUT. This strategy permits the firmware to fit into a single FPGA chip while keeping the same flexibility for the signal generation.

Analog signal acquisition

The second task is to build a firmware architecture to acquire 16 analog signals in

parallel and apply FFT at the high rate of 1 MS/s. The full implementation of the ONE-SHOT method requires each FFT operation to extract 120 Fourier coefficients per channel. In this architecture, I associate parallel FFT computing and large data transfer, based on DMA, like the work described in [Kidav et al., 2019].

Output data format

The excitations are based on the association of positive and negative sinusoidal signals used for excitation. The signs of the magnitudes are usually determined from the phase of the Fourier transforms. However, the phase-shift of the signal spreading in the domain is potentially large, creating phase wrapping effects. A solution proposed by [Yang et al., 2017a] is to extract the wrapped phase in image processing with Gabor filter. However, in EIT, the discretisation from the electrodes creates large phase discontinuities and the Gabor filtering cannot be used. In this chapter, I bring a novel solution, based on an intuitive estimation based on the sign matrix of the measured Fourier coefficients.

Finally, the full implementation of the ONE-SHOT method at maximum rate necessitates high performance data buffer to handle up to 75 MB/s of data. This requirement of the data buffer led to the implementation of a high-performance data storage system.

This chapter presents the strategy to implement the ONE-SHOT method in a physical experiment. The Section 4.1 introduces the logics used for analog signal generation and acquisition. The output data format is discussed in Section 4.2. The Section 4.3 details the software to implement the ONE-SHOT method. Finally, the Section 4.4 contains the experimental results, obtain from the measurement of two-phase static flows.

4.1. Analog signal generation and acquisition logics

In [Darnajou et al., 2019], I demonstrated the feasibility of discriminating 15 voltage signals, simultaneous pairwise excitation of 16 electrodes. The implementation of the ONE-SHOT method in an EIT module with 16 electrodes requires a set of 120 signals of different frequencies. The complexity for generating a large number of frequencies is balanced by the benefit of a full set of excitation pairs which increases in turn the well-posedness of the inverse problem for a given number of electrodes. In the following, we discuss in Section 4.1.1, the requirements on the frequencies and the constraints for the generation of the signals. Section 4.1.2 concerns the amplitude of the generated sinusoidal signals. Finally, Section 4.1.3 and Section 4.1.4 details the firmware structure and logics of the generation and the acquisition, respectively. In this section, the AO and AI logics are simplified for the reader to get an overview of the strategy. For a complete description of the software, please refer to the Section 4.3.

4.1.1. Excitation frequencies

The discrimination of the excitation signals is achieved using FFT. The number of points considered for the FFT as well as the sampling frequency of the DAQ system

suggest the following restrictions on the generated signals.

Firstly, the Nyquist sampling theorem limits the highest usable output frequency. In practice, to avoid aliasing or harmonics noise and ensure the quality of the output signal, the minimum number of samples in a single sinusoid period to compute the FFT is two. For the acquisition system operated at $f_{DAQ} = 1$ MS/s, the theoretical maximum excitation/acquisition frequency is the Nyquist limit: $f_{Nyq} = f_{DAQ}/2 = 500$ kHz for a DAQ system operated at 1 MS/s.

Secondly, the residual voltage resulting from the energy stored in the electrode-electrolyte contact impedance is a great source of error in EIT [Wang et al., 2005, Wilkinson et al., 2005, Dupré et al., 2017a]. However, if a continuous signal is generated, the spurious signals due to contact impedances are eliminated. The solution is to chose the lowest generated signal frequency f_1 to be equal to the FFT computation frequency, which depends on the number of integrated samples. The other frequencies are then chosen such that an entire number $k \in \mathbb{N}$ of periods fits inside f_1. Thus, k is the absolute Fourier coefficient as well as the harmonic index and is associated to the frequency $f_k = kf_1$. Note that the FFT magnitude does not depend on the phase shift, which is an advantage.

In an early stage of the implementation of the ONE-SHOT method, only prime numbers of sinusoid period were considered in order to avoid resonances from lower to higher frequencies. Experimentally, the amplitude of the resonance peaks were measured to be about 1% of the fundamental harmonics. In the current system that excites the 120 independent pairs of electrodes at 120 frequencies, the 120^{th} prime number, 661, gives a generated sinusoid frequency of 1.2 MHz (0.60 MHz) for an FFT over 512 points (1024 points), which is beyond the maximal frequency f_{Nyq}. Furthermore, the 661^{th} resonance of an FFT computed over 2048 points is 0.20 MHz and this option could be considered to avoid effects of harmonics in the measurements. The frame rate in the last case is 488 fps which, for 16 electrodes, is the typical rate of the available fast EIT systems based on TDM.

4.1.2. Excitation amplitudes

The voltage generation and acquisition modules are constrained within the range ±10 V. Considering the generation patterns given in [Darnajou et al., 2019], the amplitude A of the sinusoids must be much lower than the generated sum of sinusoids due to constructive interferences between them. On the other hand, the signal amplitude must remain as large as possible in order to reduce the SNR.

Another limit is the maximum variation allowed between two successive generated voltages. A real-time control in the DAQ system allowed to set the adequate value of $A = 0.15$ V, giving resonance peaks at ±2.25 V. The fast transition between negative and positive signal values cancels the apparition of electrolytic effects [Dupré et al., 2017a, Dupré and Mylvaganam, 2018].

4.1.3. Analog signal generation logics

This section details the coding strategy for managing the excitation signals. We give an overview of the software logic blocks, step by step.

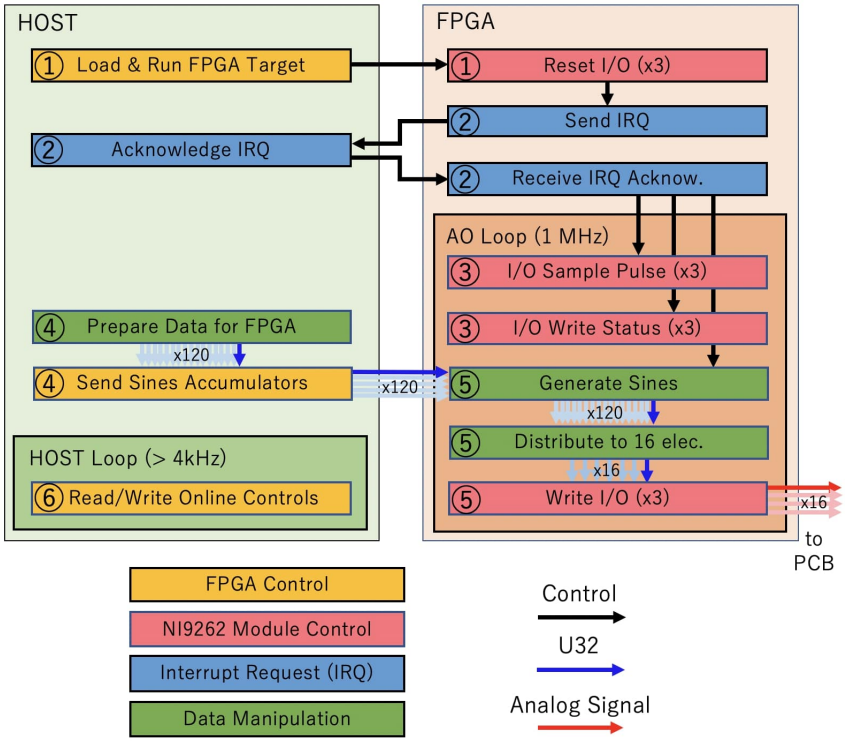

Figure 4.1. – Layout of AO Logic. The colours of the boxes and arrows indicate respectively the nature of the VIs used and the formats of the data transfer.

The `LabVIEW` code for the generation and distribution of the 120 sinusoids of different frequencies is based on two levels: HOST and FPGA. While the HOST sends continuously the frequencies and amplitude parameters to the FPGA, the latter takes the data points 16 by 16 in a loop cadenced at the high rate of 1 MS/s to create 16 analog signals. The following details the firmware structure including the layout of the `LabVIEW` based AO logic in Figure 4.1.

(1) When starting the execution, the FPGA is blank and requires the information to structure itself. The *Load and Run FPGA Target* function is implemented by the HOST prior to call the *Reset I/O* function of the three NI-9262 AO modules. When this call completes, the FPGA is ready to perform the other VIs for the NI-9262 AO modules control.

(2) The acquisition of the data has to be ready before generating any signal. An Interrupt Request (IRQ) is used to warn the HOST that the FPGA is ready to begin acquiring data and is waiting to start the acquisition until the HOST acknowledges it. This is necessary to ensure that the DMA First-In-First-Out (FIFO) in the acquisition firmware (see Section 4.1.4) has been started.

③ Call the *Generate Sample Pulse* to start generating data points. The rate at which the pulse is called determines the sampling rate for the generation, so that a loop timer is used to enforce the desired sampling period of 1 MS/s. In parallel, the *Write I/O Status* is called at the same rate to check the status of every generated sample. If an overwrite occurs, the generation is stopped and an error message is reported to the HOST.

④ The HOST *Prepare Data for FPGA* contains two sub-VIs: *Generate Harmonic Parameters*, *Generate Sines Parameters*. As discussed in Section 4.1.1, the frequencies of the generated signals are harmonics of the FFT frequency. To ensure an accurate correspondence, the 120 frequencies are set up using integers, representing the order of the harmonics k of the fundamental frequency. In the next step, the sub-VI *Generate Sines Parameters* uses Direct Digital Synthesis (DDS) to translate the harmonic numbers into 120 sinusoids accumulator increments at the Unsigned 32-bits integer (`U32`) format for the FPGA. The sub-VI also provides the amplitude calibration of the NI-9262 AO modules by setting the adequate scaling parameters. To ensure that the FPGA loop starts after receiving the values from the accumulators, these are sent to the FPGA prior acknowledging the IRQ.

⑤ Each `U32` accumulator contains 13 bits to address the 8192 elements stored in a LUT, saved on the FPGA chip. The LUT outputs the addressed element, linearly interpolated between one address and the next one, given by the 16 remaining bits of the `U32` accumulator. The LUT returns a 16-bits Integer (`I16`) by truncating the fractional bits resulting from the interpolation operation. The obtained value is scaled with the signal amplitude. There is a total of 240 positive and negative sinusoidal signals that are dispatched to the 16 electrodes. To avoid a large BRAM on the FPGA, only 60 LUTs are stored on the FPGA. Each LUT is read in a loop at 2 MHz and two values are extracted independently at 1 MHz from two accumulators. The benefit is to control individually the channels in RT, without necessitating a renewed compilation of the firmware.

⑥ The HOST contains online control functions to confirm that signals are generated, to report loop iteration speed and to report eventual errors at HOST or FPGA levels in RT.

4.1.4. Analog signal acquisition logics

The measurement of voltages over resistors on the PCB gives access to Neumann boundary conditions for the image reconstruction algorithm. The high rate acquisition at 1 MS/s over 16 channels corresponds to a large data transfer rate of 320 MB/s. We found two positive aspects in using FFT: the first is to reduce the data size without altering the data quality by considering only the Fourier coefficients that are related to a generated signal. The second is to act as an efficient bandpass filter. However, the computation of 16 FFTs online requires very high speed computations. The FPGA is a suitable device for this task since it allows the online and parallel transformation of the

signals into its Fourier components over multiple channels.

This section details the coding strategy used for the task of acquiring the signals and transforming them into their FFT components. The HOST generation functions ①, ② and ⑥ are also used to monitor the acquisition. The AO and AI FPGA firmwares are implemented together on the single FPGA chip and run in parallel.

The following details the algorithm scheme of Figure 4.2:

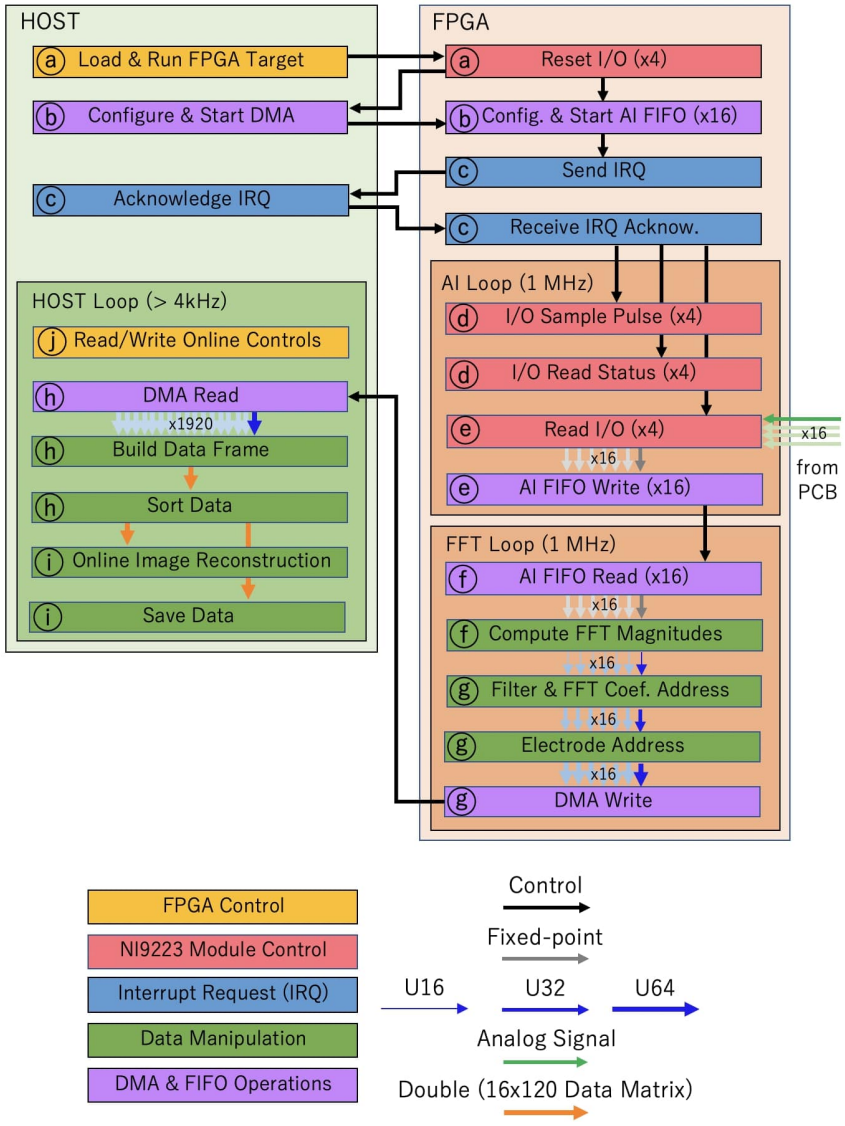

Figure 4.2. – Layout of AI Logic representing the HOST software, shared with the AO and the FPGA firmware including two loops operating in parallel at 1 MHz. The colours of the boxes and arrows indicate respectively the nature of the functions used and the formats of the data transfer.

ⓐ The *Load and Run FPGA Target* is shared with the AO logic. In parallel to the AO firmware, the FPGA calls the *Reset I/O* function of the four NI-9223 AI modules. Once this function is called, the NI-9223 AI modules are ready to acquire analog

signals and proceed to their digitalisation.

ⓑ The large AI data transfer from the FPGA to the HOST is based on a DMA strategy. At the very start of the compilation, the HOST *Configures and starts the DMA*. Subsequently, the FPGA *Configures and starts the AI FIFOs*. These 16 FIFOs are used to ensure the communication from the 16 measurement channels to their FFT computations.

ⓒ As in the AO firmware, the IRQ is used to ensure that the DMA and AI FIFOs are ready before generating and acquiring data.

ⓓ By analogy with the NI-9262 AO modules, the *Generate Sample Pulse* function is called to control the sampling rate. In parallel, the *I/O Read Status* is called at the same rate to check the status of every acquired sample and report an eventual error to the HOST.

ⓔ The *Read I/O* function is configured to read a single sample from each channel on each NI-9223 AI module. This function is called at 1 MHz and regulated by the *Generate Sample Pulse* function.

ⓕ The FFT of each channel is computed in a loop operated at the iteration speed of 1 MHz, as the AI loop. The computation time is managed by the number P of points considered for the FFT. Once all the P measurement data points sequence is transferred for FFT computations, the function outputs the P Fourier coefficients one by one at each iteration of the FFT loop. In a second step, the magnitude of the FFT coefficients are computed at a rate of 1 MHz.

ⓖ The extraction of the data through FFT acts as an efficient bandpass filter since only the harmonics of the FFT computation time are considered. Each data point magnitude is of format `U32` and addressed with the corresponding Fourier coefficient and channel both at the format Unsigned16-bits integer (`U16`). The association creates an addressed 64-bits Unsigned integer (`U64`) data element. At each iteration of the FFT loop, 16 elements for the 16 channels are written in the DMA to be transferred to the HOST computer. More details on the data format will be introduced in Section 4.2.

ⓗ The HOST waits for the DMA to collect at least 1920 elements representing one full data frame. The address of the n^{th} electrode and the Fourier coefficient associated with the FFT magnitude M are used to build a data matrix denoted as $\boldsymbol{D}$.

ⓘ The data are either used for online image reconstruction or stored. The image is based on the one step least square iterative reconstruction algorithm [Yorkey et al., 1987, Kim et al., 2001], implemented using a `MATLAB` interface in `LabVIEW`. The computation time is much slower than the data frame rate obtained with the ONE-SHOT method. Online imaging can be achieved at around a hundred of frames per seconds. For this reason, the data are stored independently in a binary file to assure fast operation.

ⓙ As in the signal generation step, the firmware reports errors and checks the synchronisation of AO and AI.

4.2. Output data format

In EIT, the data for one measurement are a set of points describing the sinusoidal voltage over one or several periods. However, in practice, only the magnitude of the signal is of importance and the data size can be significantly reduced in the post processing. The computation of the FFT within the FPGA has two additional advantages: Firstly, the output data matrix contains only the magnitudes and its size is significantly reduced. Secondly, the magnitudes of the Fourier coefficients not corresponding to an excitation signal frequency are discarded. This section discusses first a single standard EIT measurement data followed by the full set of measurements case in Section 4.2.1. Then, the ONE-SHOT method dataset developed in [Dupré and Mylvaganam, 2018, Darnajou et al., 2019, Darnajou et al., 2020] is recalled in Section 4.2.2, detailing the advantages of using a FPGA-based system for the measurements. The Section 4.2.3 discusses the sign of the measured data points from the ONE-SHOT method. Finally, Section 4.2.4 contains a spectral analysis of the impedance in the bandwidth of the excitation frequencies.

4.2.1. Standard EIT data

In TDM EIT, a single measurement (Figure 4.3) is the association of a single excitation pair of electrodes $E_{n,m}$ for $1 \leq n \leq n_e$, $1 \leq m \leq n_e$ and $n \neq m$ with a single pair of measurement electrodes. The signal is typically a sinusoidal signal of frequency f, recorded over a finite number of periods n_p. The acquisition signal contains a finite number of points, recorded over a time n_p/f, at the rate equal to the acquisition frequency f_{DAQ} which is constrained by the hardware system.

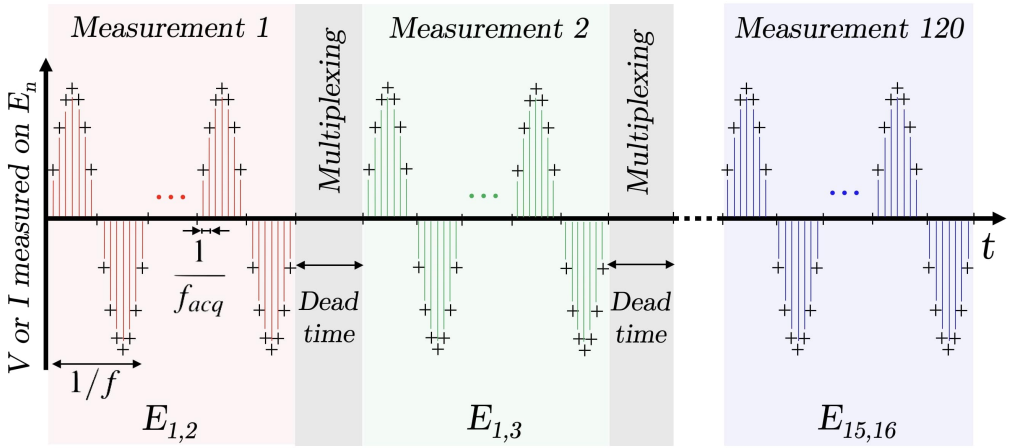

Figure 4.3. – Representation of a full dataset for the standard TDM EIT acquisition process for 16 electrodes. The full dataset contains 120 single measurements, and here, only three are shown. The dead time dedicated to multiplexing is usually longer than the above representation.

A single measurement dataset contains

$$S_{single} = f_{DAQ}\frac{n_p}{f} \tag{4.1}$$

measurement points, typically 10 to 100. The measurement over each electrode gives a similar dataset for the total number n_e of electrodes.

A large measurement set improves the inverse problem conditioning for image reconstruction. Therefore, maximising the number of measurements improves the description of the boundary conditions for a given set of electrodes. For an EIT system with n_e electrodes, there is two ways to maximise the number of measurement. Firstly, by considering excitations between the N independent pairs of electrodes with

$$N \;=\; \frac{n_e\;(n_e-1)}{2}. \tag{4.2}$$

Secondly, by considering measurements over every electrode, as shown in Figure 4.3.

Therefore, from equations (4.2) and (4.1), the total number of elements for all excitations and measurements is:

$$S_{TDM} \;=\; S_{single}\;n_e\;N \;=\; \frac{f_{DAQ}\;n_p\;n_e^2(n_e-1)}{2f}. \tag{4.3}$$

Here, the number of data points per measurement S_{single} is systematically reduced to 1 in the image reconstruction step, where only the amplitude of the Fourier transform is used.

In addition, in order to reduce the error due to contact impedance effects, the TDM based excitation strategy requires dead time between successive excitations [Dupré, 2017], when selecting another pair of excitation electrodes.

4.2.2. Data from FPGA based ONE-SHOT method

On the other hand, the association of FDM with the appropriate FPGA firmware strategy allows to keep only the Fourier magnitudes of interest. The FPGA based FFT permits an online spectral analysis over 16 channels at the rate of 1 MS/s.

The FFT is computed from a P-point voltage measurement sequence $\{V_n^{meas}(p)\}$ with p the discrete time and $0 \;\leq\; p \;\leq\; P$. The data points are the magnitudes of the Fourier coefficients in the n-electrode channel, i.e.:

$$M_n(k) \;=\; \frac{1}{P}\left|\sum_{p=0}^{P-1} V_n^{meas}(p)e^{\mathrm{i}k\beta_p}\right|, \tag{4.4}$$

with $\beta_p \;=\; 2\pi p/P$, $\mathrm{i}=\sqrt{-1}$ and a synchronous sampling is assumed.

Each 32-bits magnitude data point $M_n(k)$ is assigned with the corresponding 16-bits Fourier coefficient and 16-bits n-electrode address as:

$$M_n(k) \;=\; \underbrace{16\text{ bits}}_{k}+\underbrace{16\text{ bits}}_{n}+\underbrace{32\text{ bits}}_{M}. \tag{4.5}$$

The data format of each element is then a `U64`. Theoretically, for 16 electrodes, it could be possible to reduce the data size by considering only 8-bits for the Fourier coefficients

and 4-bits for the electrode address. The number of bits allocated to the FFT magnitude must take into account the precision of the FFT reconstruction, which depends on the FFT integration time. The 16+16+32 bits data format is considered in this chapter for future developments of the ONE-SHOT method for 32 electrodes.

The 16 magnitudes measured on the 16 electrodes for a given Fourier coefficient k gives a data vector:

$$\{M_n(k)\} = \begin{pmatrix} M_1(k) & M_2(k) & M_3(k) & ... & M_{16}(k) \end{pmatrix}, \tag{4.6}$$

where the $M_n(k)$ are `U64` elements as in (4.5). A data matrix $\boldsymbol{D}$ then concatenates the set of magnitude vectors for the N Fourier coefficients corresponding to the N generated frequencies, i.e.:

$$\boldsymbol{D} = \begin{pmatrix} \{M_n(1)\} \\ \{M_n(2)\} \\ \{M_n(3)\} \\ \vdots \\ \{M_n(120)\} \end{pmatrix}, \tag{4.7}$$

which constitutes a data frame. In this case, by analogy with (4.3) the data size is given by:

$$S_{FDM} = Nn_e = \frac{n_e^2(n_e-1)}{2}, \tag{4.8}$$

where only the magnitudes of the Fourier transform are output, which reduces the data size by the factor of S_{single} in comparison with the TDM.

The FFT is computed at a frequency f_1 from P data points, resulting in P Fourier coefficients at the output. The generated signals are of frequency f_k with $1 \leq k \leq N$, and are defined as harmonics of f_1. Therefore, each coefficient k is associated with a specific frequency value f_k. In this setting, the data frame rate is f_1 and the resolution in the Fourier space is $\Delta f = f_{k+1} - f_k = f_1$. Considering the N independent pairs of electrodes for the excitations, the N^{th} harmonic of f_1 is imposed below the Nyquist limit f_{Nyq} as discussed in Section 4.1.1. One solution consists in generating the firsts N harmonics of f_1, giving $f_k = kf_1$, for $k = 1, ..., N$.

In addition, among all P Fourier coefficients, only the coefficients corresponding to the N generated signals are of interest. The magnitudes associated to a Fourier coefficient that are not related to a generated frequency are discarded.

Finally, one data frame $\boldsymbol{D}$ of the ONE-SHOT method is represented in Figure 4.4. With its elements in the format of (4.5), $\boldsymbol{D}$ contains 123 kB of information. By comparison with TDM EIT systems, the benefits of the ONE-SHOT method associated with the FPGA implementation strategy is more data frames for an equivalent total data size.

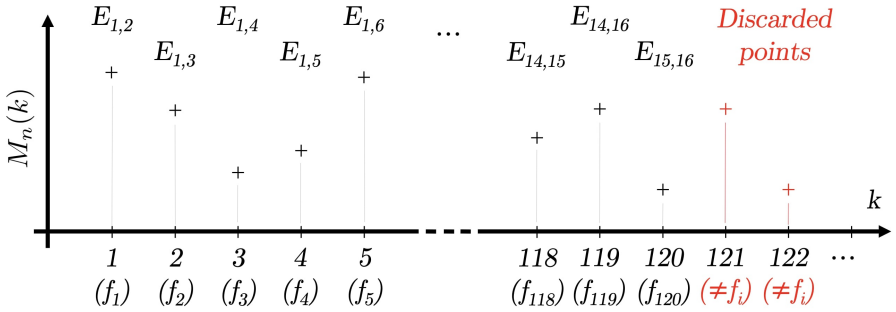

Figure 4.4. – Representation of the 120 data points considered in the ONE-SHOT method current measurement on a given electrode. All other magnitudes for any other Fourier coefficient k are discarded.

4.2.3. Sign of the signal magnitudes

The phase shift ϕ_n between the excitation signal and the measured signal at the n^{th} electrode depends on the frequency, the physical properties and material distribution of the probed medium. We consider the two following possibilities:

Case $|\phi_n| < \pi/2$

The sign of the measured magnitude can be determined from the sign of $\sin(\phi_n)$ with:

$$\phi_n \;=\; \arctan\left(\frac{-\sum_{p=0}^{P-1} V_n^{meas}(p)\sin(k\beta_p)}{\sum_{p=0}^{P-1} V_n^{meas}(p)\cos(k\beta_p)}\right), \tag{4.9}$$

and we can define the signed data matrix $\widetilde{\boldsymbol{D}}$ with its elements given by:

$$\widetilde{D}_n^k \;=\; \frac{\sin(\phi_n)}{|\sin(\phi_n)|} D_n^k. \tag{4.10}$$

where D_n^k denotes the elements of $\boldsymbol{D}$, defined in (4.7).

Case $|\phi_n| \geq \pi/2$

The dependency on the frequency or on the distance between the electrodes affects the sign. In this case, experimental parameters affects drastically the images associated with a given flow pattern. A solution is proposed with the introduction of the sign matrix $\boldsymbol{\Sigma}_{n_e}$ for n_e electrodes to affect an arbitrary sign to the signals.

The sign of the magnitude on a given electrode is arbitrarily chosen as the sign of the same magnitude for an electrostatic excitation in a homogeneous medium. In other words, the opposite sign of the closest excitation electrode. In the particular case of a measurement electrode at equal distance between two excitation electrodes, the amplitude is found experimentally to be of order $O(10^{-7})$ A which is a negligible contribution to

the data. To summarise, the $n_e \times N = 16 \times 120$ sign matrix is defined as follows:

$$\boldsymbol{\Sigma}_{16} = \begin{pmatrix} \oplus \ominus + + + + + + + - - - - - - - \\ \oplus - \ominus + + + + + + + - - - - - - \\ \oplus - + \ominus + + + + + + - - - - - - \\ \oplus - - + \ominus + + + + + - - - - - \\ \oplus - - + + \ominus + + + + - - - - - \\ \vdots \\ + + + + + + + - - - - - - \oplus - \ominus \\ + + + + + + + - - - - - - - \oplus \ominus \end{pmatrix}, \tag{4.11}$$

with the $+$ and $-$ symbols representing respectively the numbers $+1$ and -1. The symbols $\oplus$ and $\ominus$ denotes respectively the source and the drain.

Finally, for a large phase shift, $\widetilde{\boldsymbol{D}}$ contains the arbitrarily signed amplitudes of the 120 excitation patterns for the 16 electrodes where the element corresponding to the k^{th} Fourier coefficient and the n^{th} electrode is:

$$\widetilde{D}_n^k \;=\; \Sigma_n^k D_n^k, \tag{4.12}$$

similar to (4.10).

4.2.4. Spectral analysis of the impedance

The experimental datasets presented in Section 4.4 contain different magnitudes for the same excitation amplitude of all signals. The reason is that the impedance Z of a material depends on the frequency of the electrical excitation $Z = Z(f)$. We setup an experiment to measure the water impedance dependency on the frequency to explain the trend in the data from MF excitations.

In the following work, opposite electrodes (E_1 and E_9) are selected as the source and drain of an imposed alternative electrical potential. The magnitudes and phase responses measured from several NaCl solutions at various conductivities and excitation frequencies are investigated.

Impedance magnitude

As in Figure 4.5, the impedance in the low frequency domain ($f \leq 10^2$ Hz) is influenced by the electrode-electrolyte interface [Dupré et al., 2017b]. The response to an electric potential is the formation of a double ion layer, essentially acting as a dielectric. One layer of ions are formed by the electrons that are absorbed or emitted by the electrode. The ions of the other layer are attracted to the surface due to the Coulomb force. This double layer formation disappears when the frequency increases.

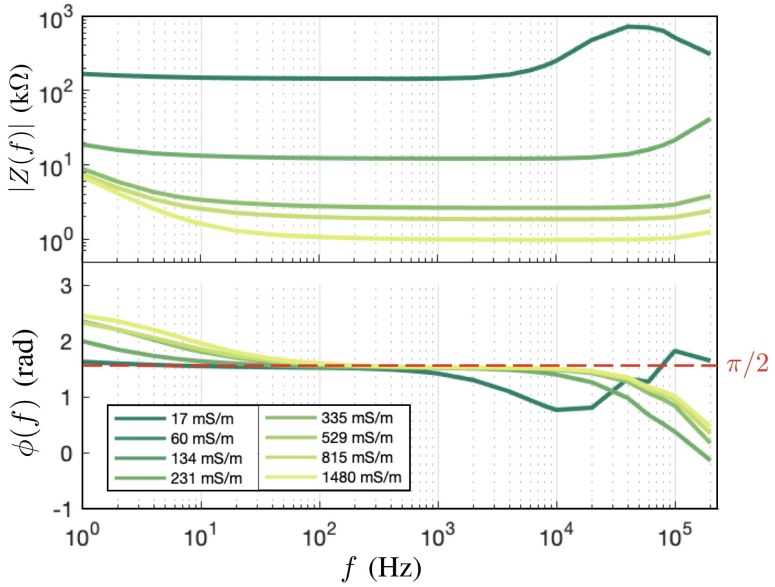

Figure 4.5. – Bode diagram of homogeneous NaCl solutions of different electrical conductivities. The impedance on the top and the phase on the bottom are represented as functions of the imposed signal frequency

At the medium frequencies (10^2 Hz $\leq f \leq 10^4$ Hz), the impedance seems independent to the frequency. In the frame of the ONE-SHOT method, the generation of a full set of signal frequencies within this range can be a solution to obtain a homogeneous magnitude response. However, the data frame acquisition rate is significantly reduced in this situation.

At higher frequencies ($f \geq 10^4$ Hz) the impedance shows an increasing dependency on frequency. This results in a weaker response in amplitude in the high harmonic range for the same conductivity change in the system.

Phase shift

Concerning the phase shift, the results in Figure 4.5 shows that $|\phi_n| \gtrsim \pi/2$ on most of the spectral domain. As discussed in Section 4.2.3, the sign of the magnitude data points cannot be ascertained from (4.10). For this reason, the usage of the sign matrix as given in (4.12) is justified.

4.3. The ONE-SHOT method software

The ONE-SHOT method depends heavily on a well functioning hardware and software integration with a precise and fast acting code to handle the many signals involved during generation, transmission and the capture of their respective responses at designated electrodes. I have completely developed the ONE-SHOT method software during the first and second years of my PhD. The development was a tremendous work and necessitated

numerous iterations with the `LabVIEW` support team to push the hardware device at the maximum of its capacities.

The software (Figure 4.6) is operated by `LabVIEW`, a graphical coding software. For this reason, the detailed explanation of the structure of the code must be based on screen-shots of the code itself. These screen-shots and the explanations can be found in the user guide of Appendix V.

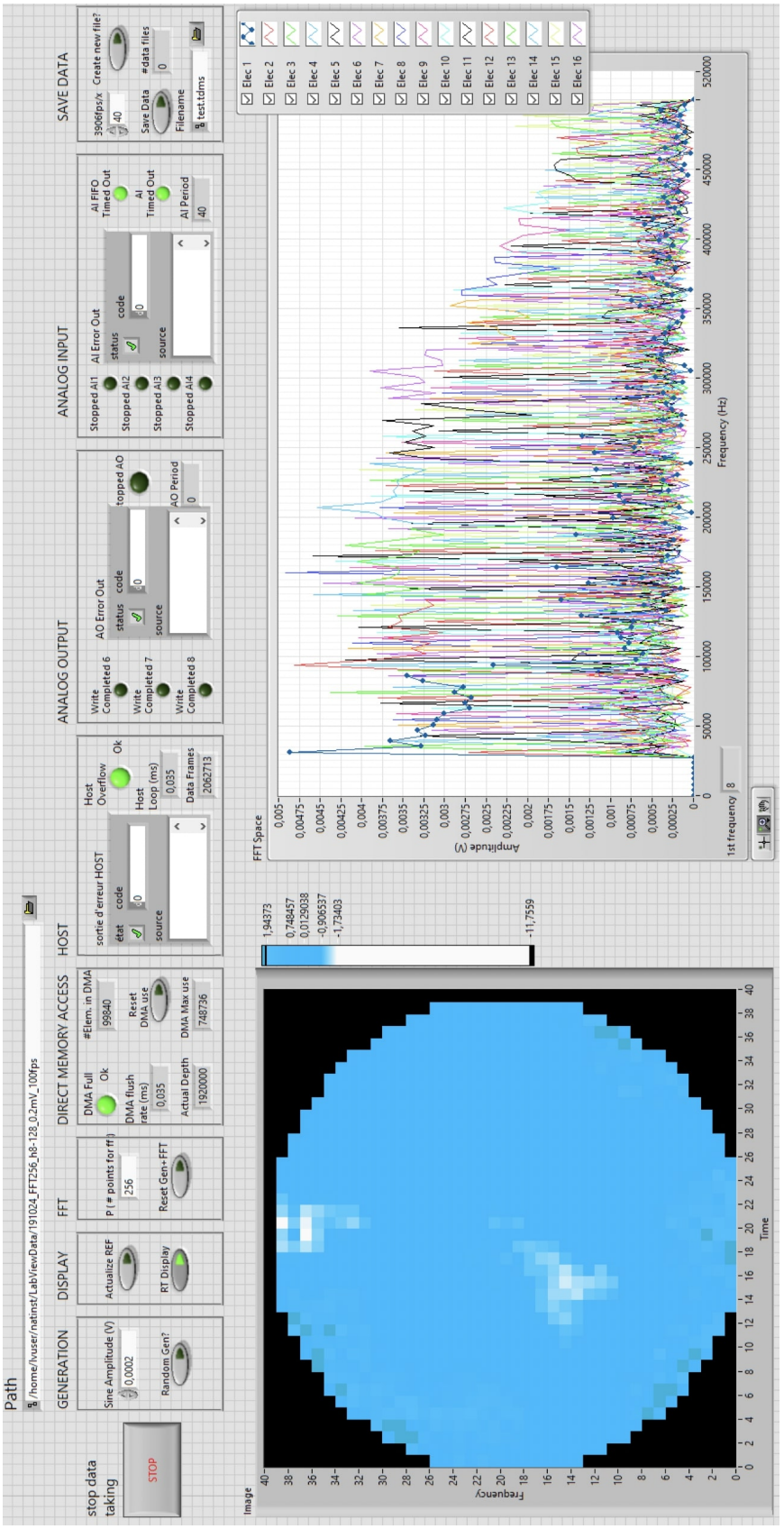

Figure 4.6. – Front panel of `ONE-SHOT v3.2`.

4.4. Experimental results with static flows

The full implementation of the ONE-SHOT method is assessed on static experiments. The excitation software, the measurement software and the data format are these described in Section 4.1 and Section 4.2. The following introduces the measured data of two homogeneous and inhomogeneous static mediums in Section 4.4.1 and Section 4.4.2, respectively. Finally, the Section 4.4.3 introduces a model of the contact impedance and the hypothesis for the validity of this model.

4.4.1. Static homogeneous medium

An experiment is set up to measure the system response from a homogeneous medium. The test section is filled with water of conductivity $\sigma = 635\ \mu\text{S}\cdot\text{m}^{-1}$ and a data frame is acquired. The data frame, with the same representation as in Figure 4.4 for the 120 magnitudes data points measured on the 16 electrodes is shown in Figure 4.7. The magnitudes are voltages measured over resistances on the PCB. The figure represents the measured current in Ampere, obtained from $M_n(k)/R$ with $R = 200\ \Omega$.

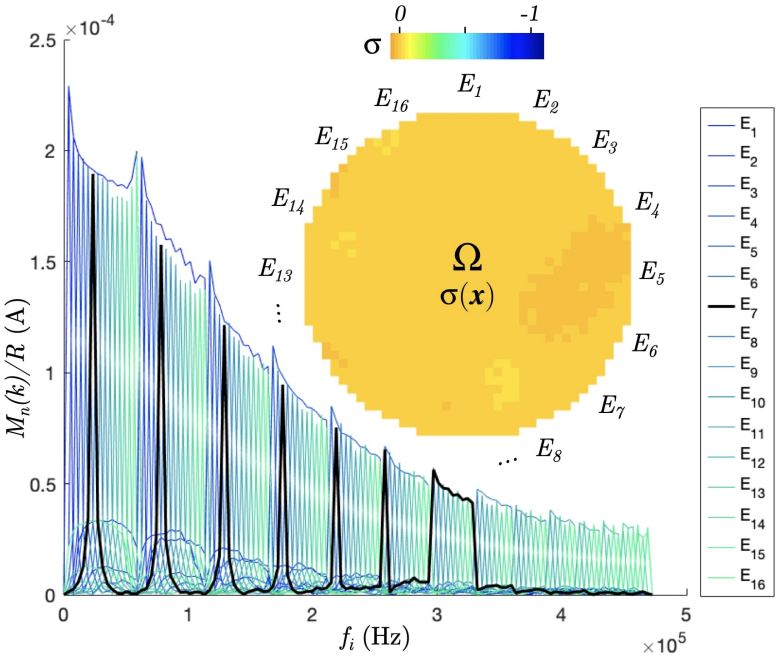

Figure 4.7. – Raw data from all of the 16 electrodes of a homogeneous water medium of conductivity $\sigma = 635\ \mu\text{S}\cdot\text{m}^{-1}$. The data from the electrode E_7 are shown in black for comparison purposes with the next figure. In the upper-right corner, the image of the reconstructed electrical conductivity $\sigma(\boldsymbol{x})$ with the arbitrary values $0 \leq \sigma \leq 1$ is shown.

The generated signals frequencies f_k are chosen so as to maximise the image refresh rate. This is obtained by considering the FFT to be computed over $P = 256$ data points at $f_{DAQ} = 1$ MS/s, with $f_1 = (256\ \mu\text{s})^{-1} = 3906$ Hz. Considering 16 electrodes, then $N = 120$ and the highest frequency is $Nf_1 = 468.7$ kHz, which respects the Nyquist

limit $f_{Nyq} = f_{DAQ}/2 = 500$ kHz. In this setting, the image refresh rate is maximised at 3906 fps with a full set of 1920 measurements per frame. It is important to point out that maximising the image refresh rate is at the price of a large bandwidth, i.e. a large difference between the lowest frequency f_1 and the largest frequency f_{120}.

We observe that the signal magnitudes are well discriminated from one another. The magnitudes decreases at higher frequencies giving a lower sensitivity at the region of the image excited with high frequency signals.

4.4.2. Static inhomogeneous medium

The dataset of an inhomogeneous medium is shown Figure 4.8. In this experiment, the test section is filled with the same water but includes a non-conducting PMMA rods of diameter 10 mm close to the electrode E_7, as shown in Figure 3.3.

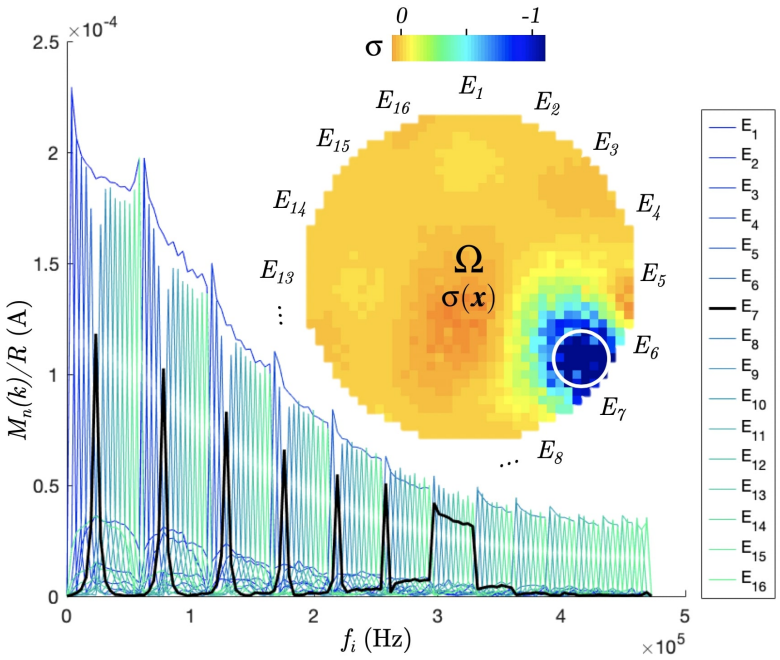

Figure 4.8. – Raw data for an inhomogeneous medium. The data from the electrode E_7 are shown in black for comparison purposes with the Figure 4.7. In the upper-right corner, the image of the reconstructed electrical conductivity $\sigma(x)$ with the arbitrary values $0 \leq \sigma \leq 1$ identifies the inclusion, shown with the white circle.

The comparison of Figure 4.7 and Figure 4.8 using the measured data from the electrode E_7 shows the system response for different frequencies. I observe signals of lower magnitudes close to the inclusion on the electrode E_7 and its neighbouring electrodes.

As an example, two images are reconstructed from the homogeneous and inhomogeneous data. The one-step least-squares iterative reconstruction method [Yorkey et al., 1987, Kim et al., 2001] is implemented, and the results are shown in the upper-right corner of Figure 4.7 and Figure 4.8.

The images show the non-dimensional normalised variation to a reference image of the electrical conductivity $\sigma(\boldsymbol{x})$ with $\boldsymbol{x} \in \Omega$, where Ω is the system representing the two dimensional median cross section of the 3D EIT sensor.

The variations in the conductivities are $\sigma_{\max}(\boldsymbol{x}) = 0.027$ for the homogeneous medium (Figure 4.7) and $\sigma_{\max}(\boldsymbol{x}) = -1$ for the inhomogeneous medium (Figure 4.8), in the close neighbourhood of electrode E_7.

Another set of images of one and two plastic rods inserted in a static water flow are obtained with `ONE-SHOT v3.2` and shown in Figure 4.9.

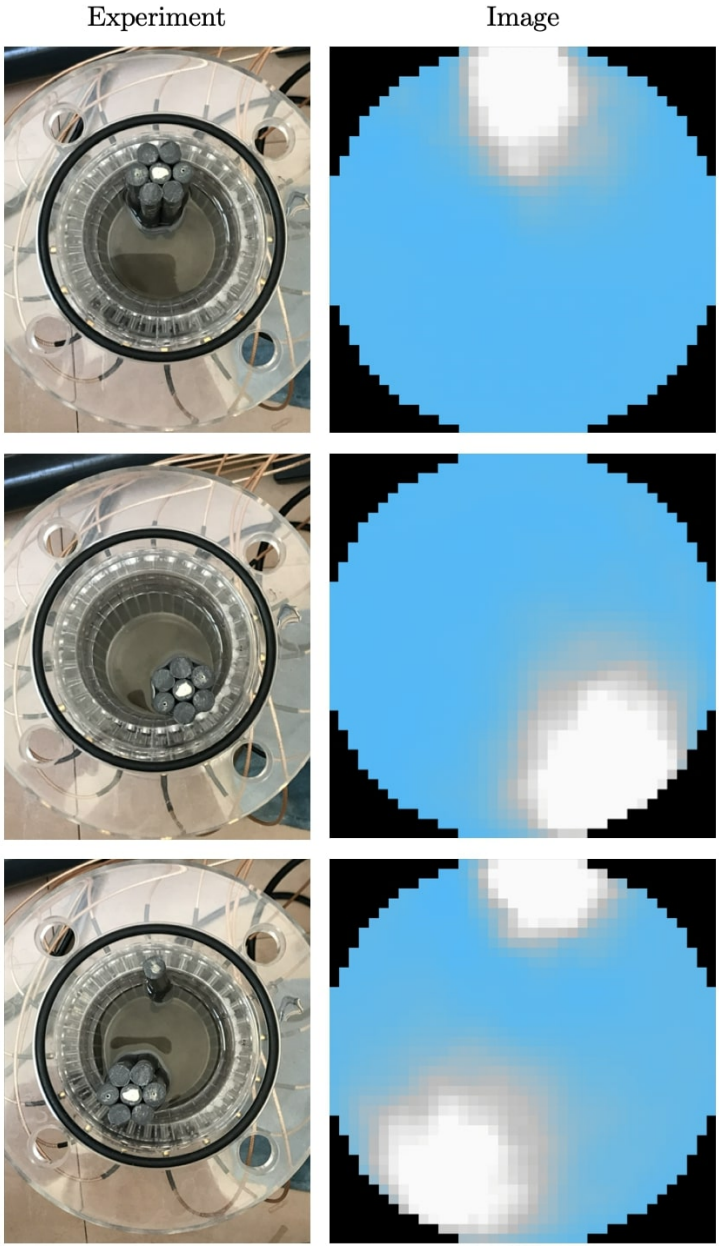

Figure 4.9. – Three images of static flows obtained with the ONE-SHOT method software.

4.4.3. Contact impedance

In TDM based EIT, the effects of contact impedance can be neglected by assuming the current in the measurement channel to be negligible. In practice, this is true since the data obtained from the pair of excitation electrodes are always discarded. Under these assumptions, the ideal circuit model is used for the ensuing calculations.

On the other hand, in the ONE-SHOT method each measurement channel is subject to the full set of simultaneous excitations. It is on an a priori basis impossible to use the ideal circuit model since every measurement electrode is used for excitation at the same time. The demodulation process occurs in different frequency bands, it ensures that a specific measurement associated with a specific channel with the associated frequency band is free from contact impedance effects due to currents at frequencies not in the bandwidth of the actual measurement channel.

A more accurate definition of the problem follows. The effects of the contact impedance from a frequency band to another can be investigated based on the electrode model described in [Wang et al., 2005, Khan et al., 2013]. The equivalent circuit shown in Figure 4.10 neglects the contribution of the diffusion layer impedance. The combination of the charge transfer resistance R_e and the double layer capacitance C_e contributes to the capacitive effects. It results in a phase shift between the applied current and the electrode potential.

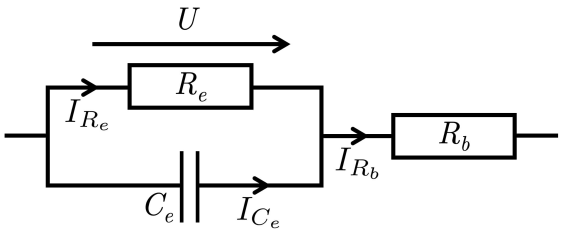

Figure 4.10. – Electrode model composed of a charge transfer resistance R_e, a double layer capacitance C_e and a bulk resistance R_b.

The total impedance according to the electrode model is:

$$Z(\omega) = \left(\frac{1}{R_e} + i\omega\ C_e\right)^{-1} + R_b \tag{4.13}$$

$$= \left(\frac{R_e}{1 + (\omega\ C_e R_e)^2} + R_b\right) - i\frac{\omega\ C_e R_e}{1 + (\omega\ C_e R_e)^2}. \tag{4.14}$$

With the time constant associated with the electrode, $\tau_0 = R_e C_e$, when the angular frequency $\omega \sim \omega_0 = 1/\tau_0$, i.e. $\omega R_e C_e \sim 1$, the phase shift between the applied current

and the electrode voltage is significant ($\sim \pi/4$) for $R_e \gg R_b$. The currents follows:

$$\begin{cases} I_{C_e} &= C_e \ dU/dt, \\ I_{R_e} &= U/R_e, \\ I_{R_b} &= I_{R_e} + I_{C_e} = I. \end{cases} \tag{4.15}$$

By applying a MF AC current of the form:

$$\widetilde{I} = I_0 \sum_{k=1}^{n_e-1} \sin(2\pi f_k t) \tag{4.16}$$

The total impedance becomes a function of the form:

$$\widetilde{Z}(\omega, f_1, f_2, ..., f_{n_e-1}) = \sum_{k=1}^{n_e-1} \widetilde{Z}(\omega, f_k) + \widetilde{\zeta}(\omega, f_1, f_2, ..., f_{n_e-1}) \tag{4.17}$$

where $\widetilde{\zeta}(\omega, f_1, f_2, ..., f_{n_e-1})$ is a cross-frequency term. In my model, I make the hypothesis that $\widetilde{\zeta}(\omega, f_1, f_2, ..., f_{n_e-1}) \ll \widetilde{Z}(\omega, f_k)$ for any $1 \ll k \ll n_e - 1$ and $k \in \mathbb{N}$. The quality of the images reconstructed by the ONE-SHOT method is an indicator that the hypothesis is valid in the scope of our applications.

Prospects and indication for further work

The following prospects are proposed for future developments. The prospects that are estimated as most interesting/important are given at the top of the list. The proposition written in **bold** is of top priority.

- The ONE-SHOT method software does not provides the verification that no data is lost during full rate operations. An important improvement of the code consists in **verifying that the real time is respected and no data frames are lost during the DAQ process.** To do so, each frame can be labelled with an integer N_i that indicates the loop iteration i. If $N_{i+1} - N_i > 1$, it means that a data frame is lost.
- Implementation an online reconstruction algorithm on the FPGA as proposed in [Zhou and Li, 2017]. The image reconstruction algorithm can be handled very fastly by the FPGA. If the FPGA code provides an online image reconstruction at 3906 fps, the images can be directly saved, reducing the data size.
- We have seen that due to the impedance dependancy to the frequency given by the Bode diagram, the image contrast is larger for low frequency excitation. In the current distribution of the excitation frequencies, the low frequencies are located in the same region, resulting in a higher contrast. I propose to improvement the CASE1 to distribute the frequencies with an optimal pattern.

- Quantify the cross-frequency impedance term $\widetilde{\zeta}(\omega, f_1, f_2, ..., f_{n_e-1})$ compared to the impedance $\widetilde{Z}(\omega, f_k)$ in the analysis of contact impedance with MF current excitations.
- New hardware system for 32 electrodes ONE-SHOT method. The corresponding full implementation requires the simultaneous excitation and measurement of 992 signals at 496 frequencies. The implementation of a 32 electrodes EIT with simultaneous excitations will be discussed in Chapter 6

- "Help! My husband is unconscious! Are you a doctor?"
- "Yes, but I am a doctor in physics. I am not sure I can help..."
- "Please he is dying!"
- "Ok, but first I need a cylindrical man in the vacuum."

5

Application to accidental scenarios in nuclear power-plants

EIT is considered for flow measurements in the primary circuit of Pressurised Water Reactors (PWR) due to the electrical conductivity difference between water phases and also for its non-intrusiveness, robustness, and relative low-cost in comparison with other tomographic techniques. The subject of special interest is the physics in the hot leg, as flow directions can change or even counter current flow conditions can occur [Jeong, 2002, Vallée et al., 2012, Querol et al., 2015].

The highest data frame rate in standard EIT based on TDM is not fast enough to image the quickly evolving flows of accidental conditions in the hot leg. Furthermore, the data obtained from this strategy is altered due to the contact impedance at the electrode electrolyte interface. For this reason, I am interested in applying the ONE-SHOT method for its advantages, in particular the high frame rate. Furthermore, the errors due to the contact impedance are canceled with the continuous excitations...

Contents

5.1 The Lost Of Coolant Accident (LOCA) in the hot leg 177
5.1.1 Accidental scenarios and design of nuclear power-plants 177
5.1.2 The Large LOCA Break (LBLOCA) scenario 180
5.1.3 Electrical conductivity in the hot leg during LOCA 180
5.1.4 Simulation of EIT measurements of accidental flows 182
5.2 Fastly evolving flows experiment 184
5.2.1 Experimental setup 184
5.2.2 Modelling of Small LOCA break (SBLOCA) 185
5.2.3 Modelling of Large LOCA break (LBLOCA) 189
5.2.4 Flow patterns experiments 189
5.3 High pressure and high temperature flows experiment 192
5.3.1 Primary circuit modelling flow rigs 192
5.3.2 The EIT sensor for high pressure and high temperature measurements 194
5.3.3 Dimensional variations due to temperature and pressure 199
5.3.4 EIT measurements on the Benson loop 200

This chapter discusses the application of EIT to measure the flow patterns in several accidental scenarios in the primary circuit of PWRs. These scenarios are introduced in Section 5.1, with a discussion of the applicability of EIT in a particular region of the primary circuit. The Section 5.2 relates the experimental results of measurements of fastly evolving two-phase flows in a horizontal pipe using the ONE-SHOT method. In a second experiment, introduced in Section 5.3, the ONE-SHOT method is tested on a high pressure and high temperature hydraulic loop.

5.1. The Lost Of Coolant Accident (LOCA) in the hot leg

The design of nuclear power-plants is required to anticipate various operational occurrences, including accidental scenarios. One of the basis scenario for PWR concerns the failure of a pipe element in the primary side, leading to the Lost Of Coolant Accident (LOCA). Although a major loss of coolant, fission product decay heat generated in the fuel would raise its temperature in absence of water coolant. In such context, it is required to avoid fuel melting and dispersal in order to minimise radiological consequences to the public.

The Section 5.1.1 briefly overviews the main accidental scenarios in a PWR. Then the Section 5.1.2 focuses on a particular accident that creates harsh flow patterns. The electrical conductivity in the hot leg for several phases is discussed in Section 5.1.3. Finally, Section 5.1.4 contains the simulation of EIT images of a particular flow, expected in this accidental scenario.

5.1.1. Accidental scenarios and design of nuclear power-plants

For accidental conditions, several criteria must be fulfilled to validate the design of a nuclear reactor. The main criterion being to cancel or impose drastic limits on the radiological effects onto the public. However, regarding this objective, numerous criteria are required on safety subsystems of the reactor, based on anticipating every risks and their probabilities to occur (Table 5.1). As an illustration, it was already generally accepted from the late sixties that in order to minimise radiological consequences to the public, it is mandatory to avoid core melting and fuel dispersal. Therefore, it became necessary to design the Emergency Core Cooling System (ECCS) to prevent this risk during all phases of a design basis accident. Introducing this element naturally led to the criterion that the fuel must be maintained under a coolable geometry during the whole LOCA sequence.

A loss of coolant can occur from the thinnest aperture to a large gap between pipe elements. The origin of the LOCA scenario is generally a pipe break but it can also be originated from the failure of any isolation valve connecting to the primary circuit. Depending to the size of the broken element, the scenario will be called Small LOCA Break (SBLOCA), Intermediate (IBLOCA) or large (LBLOCA). The phenomenology is expected to be specific to each kind of LOCA. In the following, I have focused on the two extreme scenarios.

Category	Description	1/Reac. year
1 : *Normal*	Conditions that occurs regularly in normal operation (*e.g.: Bringing the reactor to full power*)	~ 10
2 : *Expected*	Occurrences expected to occur at least once during the lifetime of a facility but which, in view of appropriate design provision, do not cause any significant damage to items important to safety or lead to accident conditions. (*e.g.: Loss of reactor coolant pump*)	~ 1
3 : *Possible*	Occurrences not expected to occur during the lifetime of a facility : Anticipated infrequent events requiring safety response (*e.g.: Small LOCA : Valves open*)	$\sim 10^{-2}$
4 : *Unlikely*	Improbable occurences, not expected in nuclear reactor operations but provided for in the design (*e.g.: Large LOCA : main steam line break*)	$\sim 10^{-4}$
5 : *Remote*	Extremely improbable scenarios, not anticipated in the design of the plant (*e.g.: LOCA without ECCS, total loss of site power*)	$\sim 10^{-6}$

Table 5.1. – Classification of occurrences and frequency of incident per reactor classified into five categories.

In SBLOCA, the broken pipe has an area in the range of 1% to 6% the area of the cross-section of the pipe. These two limits are obviously questionable. During the SBLOCA, the leakage through the break results in drop of primary system pressure due to loss of energy and water inventory from the break. After the pressure drop, steam bubble appears inside the circuit.

In LBLOCA, the main primary pipe is expected to break in double-guillotine: an equivalent break area of 200% the area of the cross-section of the pipe. As a result, a quick depressurisation occurs with the apparition of two-phase flows.

In order to anticipate these accidents and design a nuclear power-plant able to withstand these scenarios, it is fundamental to asses precisely the phenomenology. The subject of special interest is the physics in the hot leg, as fastly evolving flows including counter current flow conditions can occur [Jeong, 2002, Vallée et al., 2012, Querol et al., 2015]. The safety and licensing analyses of nuclear power-plants are performed with best-estimate thermal-hydraulic system codes. These codes are also used in the design of advance reactors. The evaluation of these codes and the estimation of the accurateness and performance must be accomplished by comparing the code predictions to actual experimental data, obtained on different test facilities [Aksan, 2008].

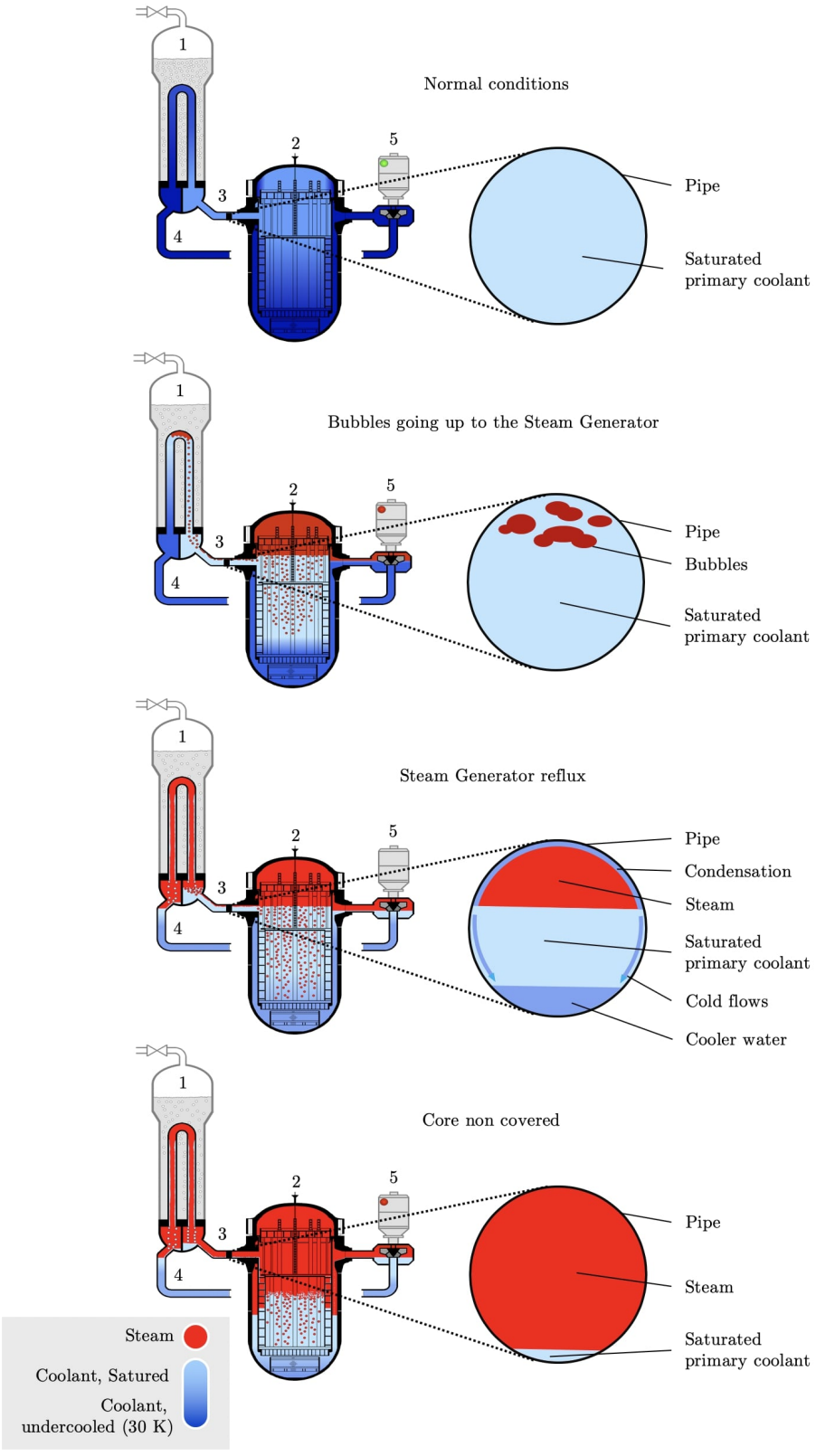

Figure 5.1. – Main steps of the LBLOCA scenario in a PWR. The right shows the cross section of the flows in the hot leg. The main elements of the primary circuit are shown. 1. Steam Generator 2. Reactor pressure vessel 3. Hot leg 4. Cold leg 5. Reactor coolant pump.

5.1.2. The Large LOCA Break (LBLOCA) scenario

Since the gas flux is tiny in SBLOCA, it mostly results in two-phase flows of well known flow regime. On the other hand, the LBLOCA results in extremely complex thermo-hydraulic phenomena. The LBLOCA impacts all the main elements in the primary circuit (Figure 5.1).

The steam generator acts as a steam source. The water evaporates with the flow in the U-tubes with a possible plate-out of boric acid inside the U-tubes. In addition, the steam generator constitutes an additional flow resistance and to steam binding. In the reactor pressure vessel, the high flow resistances induces swell-level depression. The reactor coolant pump impeller is at standstill and constitutes a large pressure drop in the loop. Below the reactor coolant pump forms two-phase flow mixtures with the constitution of additional head losses.

Finally in the hot leg, the pressure in the pipe is expected to be 40 bar. The temperature of the water in the hot leg is generally around 300°C. During a LBLOCA in the hot leg, the water inventory in the primary circuit will be reduced and different two-phase flow patterns can occur. The entrainment of water mixes with the steam flow and potentially with boric acid.

5.1.3. Electrical conductivity in the hot leg during LOCA

In this work, I have focused on EIT to measure the flow patterns in the hot leg since it provides an opportunity for non-intrusive measurement potentially applicable at high temperature and pressure. Such measurement techniques are considered for hydraulic loops since they do not disturb the flow pattern and would be operational in accidental conditions provided that the electrodes are robust enough to withstand the fluid properties under such circumstances.

The EIT image is an estimation of the variation of electrical conductivity σ to a reference image, measured on a homogeneous flow before the accident begins. The conductivity within the pipe depends on three main components : The phase of the water, its temperature and the concentration of boron. These three parameters and their effects on the electrical conductivity are discussed in the following.

Conductivity of the different phases of water

The phase of the water within the pipe is responsible of the main variation of the conductivity. The last were calculated [Marshall, 1987] for a supercritical liquid water at $T \sim 300$°C to be $\sigma = 3.5$ μS/cm for $P = 100$ bar.

Steam is, as all gases in general, a very poor electrical conductor. Usually, a gas conducts electricity when the voltage is high enough to ionize its atoms. However at this point, it becomes no longer correct to consider a gas, but a plasma. The ionization of water with an electrical potential is called electrolysis. In EIT, the voltage between two electrodes is typically around 1 V so the electrolysis reaction does not occur. In these

conditions, the conductivity of the steam is $< 10^{-5}$ μS/cm and is generally approximated to zero.

Conductivity variations with temperature

The temperature gradient from $T \sim 300$°C to $T \sim 250$°C that appears in the liquid phase during the accident is responsible for the second main variation of the conductivity.

From Figure 5.2, experimental results shows that the electrical conductivity of water at low pressure in this range varies between $\sigma = 3.0$ μS/cm and $\sigma = 3.5$ μS/cm. Furthermore, the thermal conductivity λ of the water at $T \sim 300$°C and $P = 150$ bar is [Kretzschmar and Wagner, 2009] $\lambda = 0.55$ Wm^{-1}.K^{-1}.

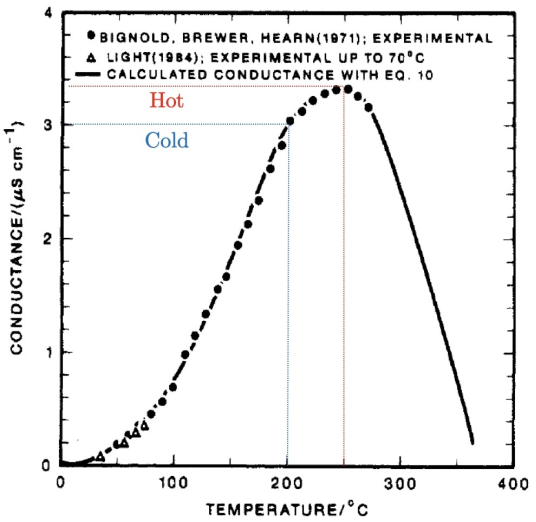

Figure 5.2. – Comparison of the experimental values of water conductance of [Bignold et al., 1971] from 50°C to 271°C and [Light, 1984] from 50°C to 271°C with the values calculated in [Marshall, 1987].

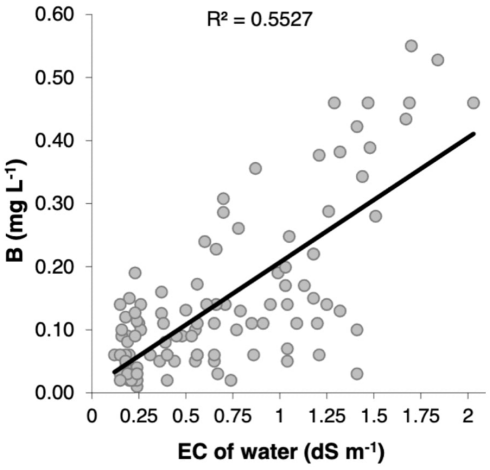

Figure 5.3. – Relationship of electrical conductivity (EC) and boron (B) concentration of canal water samples collected from different locations in Southern Punjab, Pakistan during winter and summer months. [Niaz et al., 2018]

Conductivity variations with boron concentration

Boron is used as a neutron poison because of its neutron absorbing properties. Absorbing neutrons is important to control the excess reactivity of a reactor core due to having more mass at beginning of life than needed for criticality.

The concentration of the Boron in the pipe is the third factor affecting the conductivity. Consisting of two stable isotopes ^{11}B (80.1%) and ^{10}B (19.9%), the Boron is commonly used as a neutron absorber due to the high cross-section between thermal neutrons n and Boron 10 isotopes. The main reaction is :

$$^{10}\mathrm{B} + n \rightarrow {}^{7}\mathrm{Li} + \alpha, \tag{5.1}$$

with the production of a ^{7}Li Lithium atom associated with an α particle. The electrical conductivity of the Boron is $\sigma_B = 5.10^{-6}$ S.m^{-1}.

The concentration of boron in water affects its conductivity as shown in Figure 5.3. In order to maintain a negative coefficient, the boron concentration in the primary coolant must be less than about 1000 ppm [British Electricity International, 1992]. In practice, the boron concentration drops to zero after few hundreds of effective full power days. For this reason, the estimation of the effects of boron concentration on the conductivity in an accidental scenario must take into account the operation context of the reactor.

To conclude, the gradient of the conductivity results in large contrast for changes between water phases. By comparison, the electrical conductivity gradient to the variation of temperature and boron concentration is tinier in the range of variations expected in the hot leg.

5.1.4. Simulation of EIT measurements of accidental flows

During the LBLOCA in the hot leg, the level of water decreases leading to a stratification with water and steam (Figure 5.4a.). The condensation of the steam on the inner wall of the pipe creates a flow, which is cold by comparison with the temperature of the primary water. Furthermore, these cold flows are also poor in boron concentration since the boron does not evaporate in the steam.

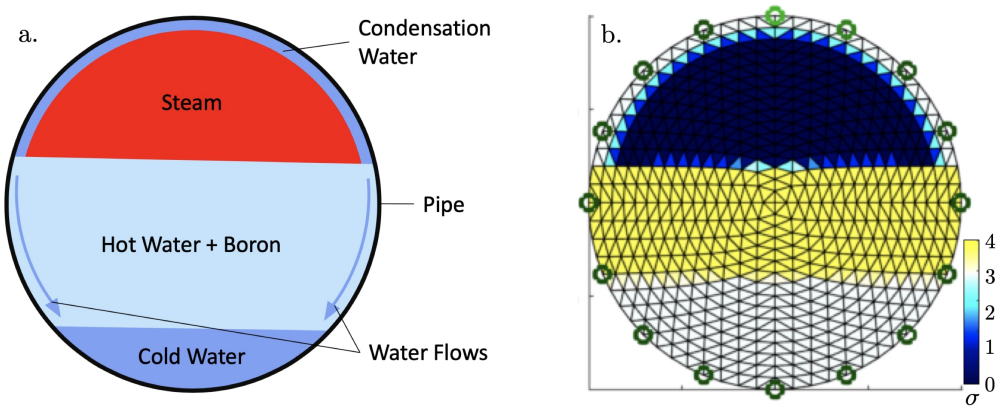

Figure 5.4. – a. Expected flow phenomena in the hot leg during LBLOCA. b. Modelling of the phenomena.

The simulation of this phenomena has been handled with `EIDORS` (Section 2.1.1). The Figure 5.4b. is the simulation domain, containing four regions:

- On the top, the condensation water has no boron and an arbitrary electrical conductivity of $\sigma = 3.0$ μS/cm has been set.
- The steam phase is modelled with a very low electrical conductivity of $\sigma = 10^{-5}$ μS/cm.

- The water with boron has a slightly higher electrical conductivity than pure water. It has been modelled with an electrical conductivity of $\sigma = 3.5$ μS/cm.
- Finally, at the bottom of the pipe, the "cold" water stratification is expected to have a temperature of $T \sim 250°$C. This stratification is modelled with an electrical conductivity of $\sigma = 3.0$ μS/cm since it provides from the condensation at the top of the pipe.

As it is difficult to estimate the temperature and the boron concentration drop between the two liquid phases at the bottom of the pipe, the two effects have been modelled together with a conductivity change of $\sim$20% of the conductivity of liquid water at $T \sim 300°$C and $P = 100$ bar.

The Figure 5.5 contains the reconstruction of this domain from EIT sensors containing different number of electrodes. In this particular situation, an EIT sensor containing more than 32 electrodes seems to give more accurate images.

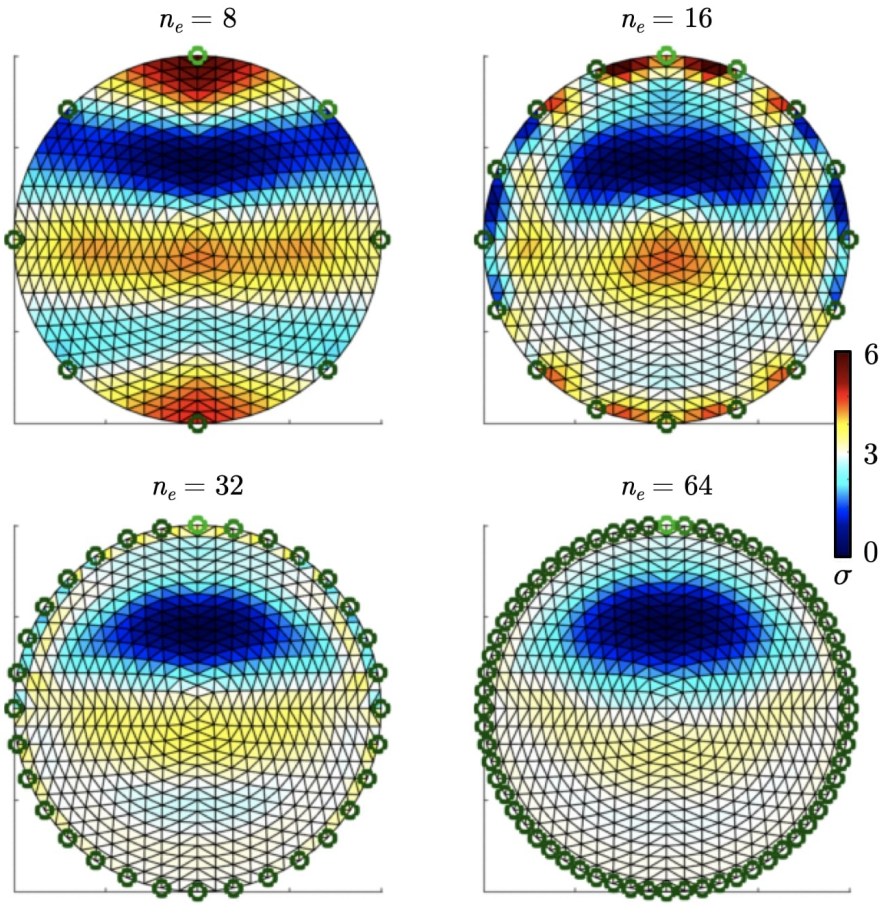

Figure 5.5. – Reconstructed image with several number of electrodes n_e of the expected flow in the hot leg during LBLOCA.

The EIT data acquisition system must be extremely accurate to measure temperature or boron concentration variations in two phase flows. For this reason in what follows and

as a first step, I only consider two phase flows measurement. In future development, it could be an interesting topic to measure temperature and boron concentration gradients in two phase flows, measured with EIT.

5.2. Fastly evolving flows experiment

An experiment were set up on a horizontal water/air two-phase flow rig to test the performances of the ONE-SHOT method in the context of fastly evolving two-phase flows. The experimental campaign were performed between October 14^{th} and October 25^{th}, 2019 at the University College of South-eastern Norway (USN), campus Porsgrunn.

The setup used along the experiment is introduced in Section 5.2.1. In a first time, two LOCA scenarios were considered in this experiment. In Section 5.2.2 the SBLOCA is modelled with a low air rate introduced in water flows of several velocities. Then in Section 5.2.3, the LBLOCA is modelled by suddently increasing the air rate in the pipe filled with a water flow. In a second time, the measurement of 80 different flow patterns were performed as discussed in Section 5.2.4.

5.2.1. Experimental setup

The two-phase flow experiments have been carried out at the multiphase flow rig at USN, schematised in Figure 5.6. The flow rig enables the mixture of air, water and oil on a horizontal pipe. Each medium flowing into the pipe section is monitored independently using dedicated flow meters. The following experiment considers only air/water mixture to reproduce the flows in PWRs.

The input mass flow rates are accurately controlled and monitored by Coriolis flow meters. One can select water mass flow rates up to 150 kg/min and air mass flow rates up to 5 kg/min. The pipe inner diameter is 56 mm and its length is 15 m long so the flow is fully developed in the measurement section at its end.

Three independent flow measurement systems are placed in cascade : the EIT sensor, the ECT sensor and the Gamma ray Densitometry (GD) sensor.

ECT sensor

The dual-plane 12-electrodes ECT sensor (Section 1.2.4) operates at a frequency of 1 MHz and is able to reconstruct 100 images per seconds on two layers.

EIT sensor

The DAQ controller and the PCB are connected to an EIT sensor of diameter 51 mm which contains a set of 16 electrodes of surface 1 cm × 0.5 cm. The excitation strategy uses the ONE-SHOT method which is operated by the `ONE-SHOT v3.2` software. Each of the 120 positive and negative excitation signals has an amplitude of 0.2 mV. Their frequencies vary from 31 kHz to 499 kHz. The FFT in each electrode channel is computed

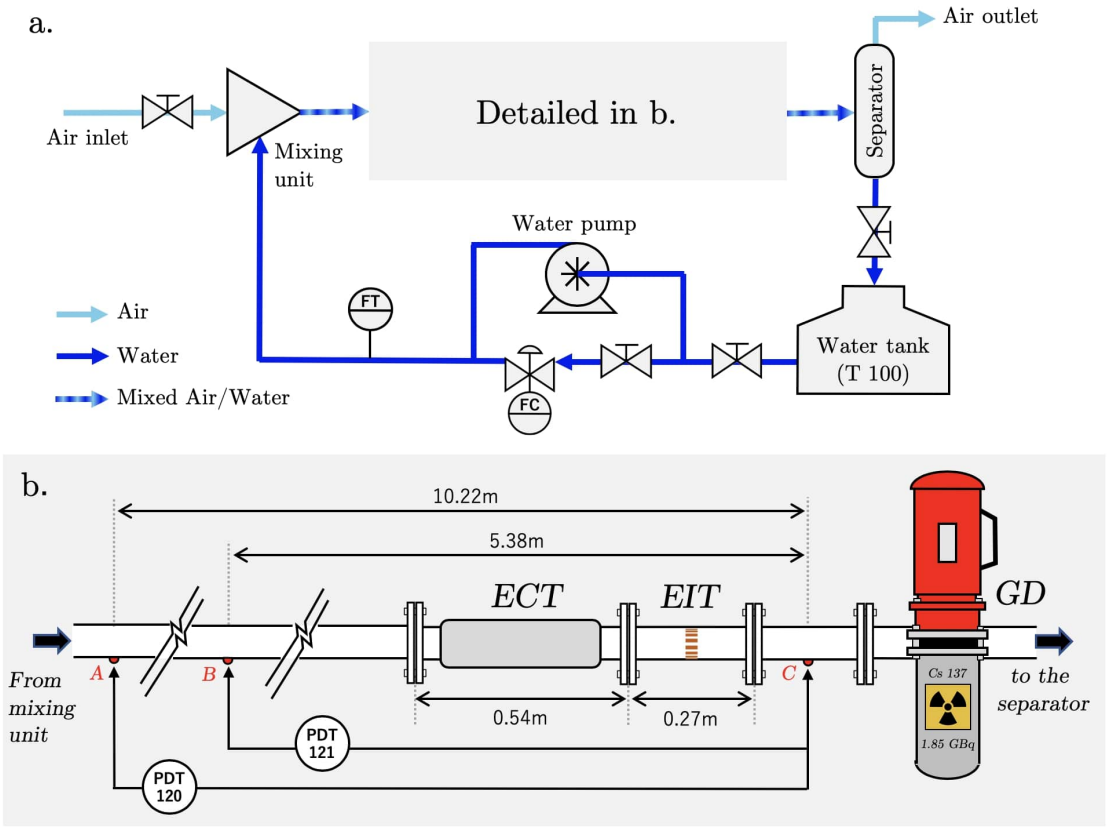

Figure 5.6. – a. Schematic diagram of air/water flow rig with sensors and actuators. FT: Coriolis mass flowmeter, PDT: Differential Pressure. b. Detail of the ECT, EIT and GD sensors region.

over 256 data points at the rate $f_{DAQ} = 1$ MS/s. Therefore, each data frame contains 1920 measurement data points. The frames are recorded at the rate of 3906 fps.

Gamma ray Densitometry (GD) sensor

The S-Tec Density Transmitter DT-9300 [S-TEC Sensor Technology, 2019] is a microprocessor based precision instrument for the measurement of density of liquids and suspensions. It is associated to a source holder SH-79XX which includes a 1.85 GBq (50 mC) radioactive ^{137}Cs source. The source holder SH-79XX and the Density Transmitter DT-9300 are clamped to the process pipe. The Density Transmitter DT-9300 contains a plastic scintillator to measure the absorption of the gamma rays passing through the region of interest.

5.2.2. Modelling of Small LOCA break (SBLOCA)

SBLOCA are characterised by long periods (tens of minutes to hours) during which the core of the reactor remain covered and assure a relatively high pressure. A SBLOCA can result in tiny bubbles flowing quickly in the pipe.

Figure 5.7a. illustrates the EIT sensor plugged in the multiphase rig in USN. The experiment consists in a water flow mass of 60 kg/min flowing in a pipe of diameter 51 mm. A tiny air flow of 0.01 kg/min is introduced in the pipe, resulting in small bubbles flowing at the velocity of about 1 m/s.

A series of images (Figure 5.7b. and c.) are reconstructed from the inhomogeneous dynamic flows with the one-step least-squares iterative reconstruction method, introduced in Section 1.3.4. The ONE-SHOT method successfully measured 156 frames of the bubble passing the cross-section of the electrodes in 40 ms. This series of experiments shows for the first time EIT images at nearly 4 000 fps. With the new ONE-SHOT method, it becomes possible to measure very fast processes with EIT.

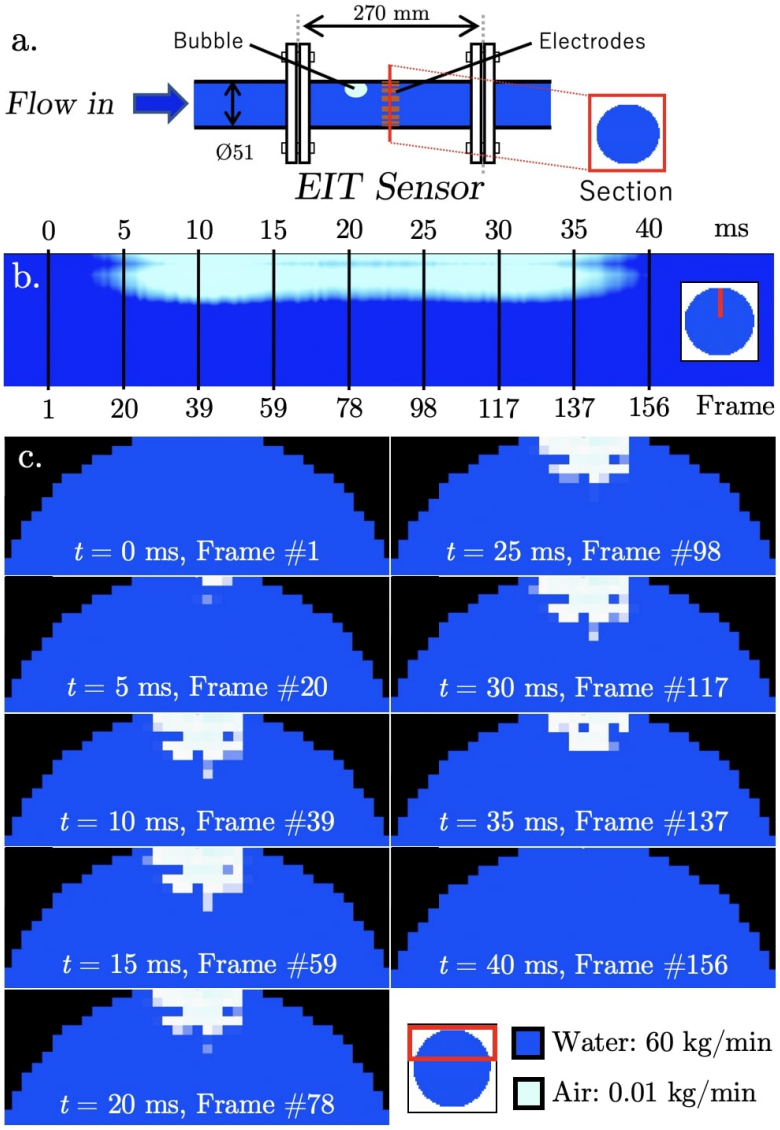

Figure 5.7. – a. Layout of the dynamic experiment. b. Longituginal representation of the 156 reconstructed EIT images of an air bubble passing through the pipe section with the electrodes in 40 ms. The pixels at the vertical radius of the pipe cross section are shown for each image. c. Transverse representation of 9 of the 156 reconstructed EIT images of the air bubble. The state of the bubble at different instances is clearly seen in the nine tomograms.

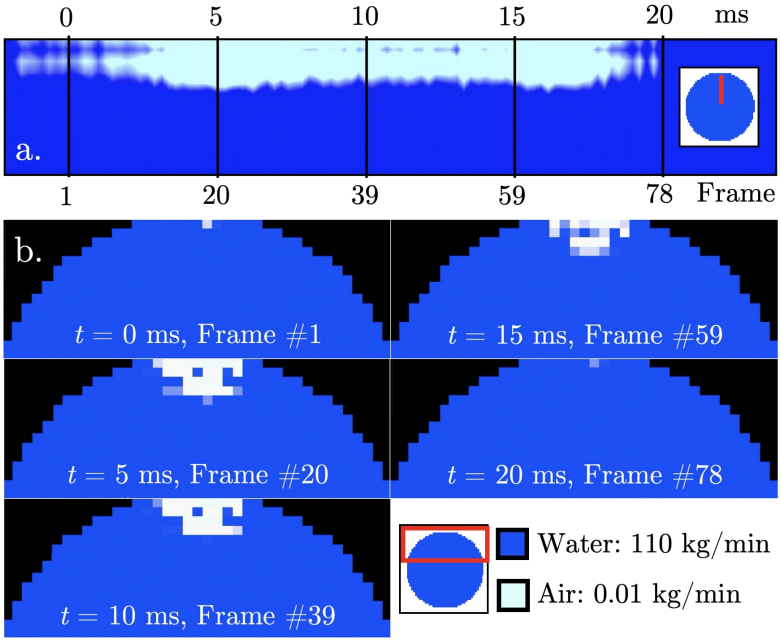

Figure 5.8. – Reconstructed images of an air bubble passing through the plan of the electrodes in ∼20 ms. a. Visualisation in the vertical line of pixels. b. 5 of the ∼80 reconstructed EIT images.

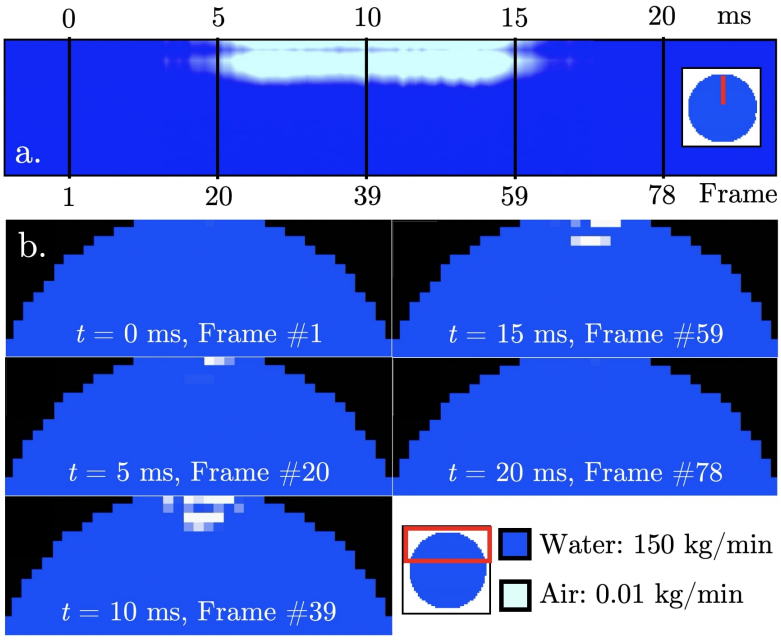

Figure 5.9. – Reconstructed images of an air bubble passing through the plan of the electrodes in ∼10 ms. a. Visualisation in the vertical line of pixels. b. 5 of the ∼80 reconstructed EIT images.

The other equipment, ECT sensor and gamma ray densitometry sensor, were not able to measure the bubbles.

A real time operation of the ONE-SHOT method associated to a void fraction estimation algorithm such as [Dang et al., 2019] is a powerful tool to detect fastly traveling bubbles. An appropriate triggering allows to detect and record variations with a measurement every 256 μs with the ONE-SHOT method operated at nearly 4 000 fps.

5.2.3. Modelling of Large LOCA break (LBLOCA)

The main difference between a SBLOCA and a LBLOCA are the rates of coolant discharge and pressure variation with time. This implies the domination of gravity effects in small breaks compared to inertial domination effects in large breaks.

LBLOCA were modelled with the following process. Firstly I closed the air valve and activate the water pump with several flow rates for several experiments. The water flow rate were set to 60, 80, 120 and 140 kg/min. Secondly, the air flow rate were set to a tiny value, while keeping the valve closed, in order to increase slowly the pressure. Thirdly, the air valve were open creating a fast transient from homogenous flow to slug flow. The first slug for each water flow rate is recorded with the EIT, ECT and GD sensors.

As a result, the ECT sensor and GD sensor both failed in measuring accurately the transient since the data appears as a step function. The first 300 ONE-SHOT method EIT data frames of the first slug for the four water flow rates are shown in Figure 5.10. The representation of the data is the center pixel column of the images.

The NOSER image reconstruction algorithm is chosen for its rapidity and simplicity to implement online. Other reconstruction algorithms with better accurateness could be implemented from these data. However, I consider this work as a separated study and keep the focus on high EIT data frame acquisition rate.

5.2.4. Flow patterns experiments

In the horizontal configuration, stratified smooth, stratified wavy, annular, plug and slug flows can also be generated by selecting the water and air mass flow rates. Only the dispersed bubble flow cannot be generated because of the limitations of water mass flow rates.

In addition to the LOCA modelling, a series of 80 flows have been created by changing the air and water flow rates (Figure 5.11 and Figure 5.12). The list of flows is available in Table 5.2 and Table 5.3.

The data from the ECT, the GD and the `ONE-SHOT v3.2` of these flow experiments have been used in two independent studies. Firstly in a flow regime identification algorithm based on deep learning in [Poverud, 2019]. Secondly in a work on eigenvalue analysis in [REF Chunhui]. In the last, the correlation between GD and ONE-SHOT method measurement shows an agreement between the two measurement techniques.

Table 5.2. – Details of the air and water flow rates for the first 40 flow pattern experiments

#	**Water flow** kg/min	**Air flow** kg/min	**Regime**	**Comments**
1	79.43	0.10	Plug	
2	79.43	0.16	Slug	Border transition
3	79.43	0.25	Slug	
4	79.43	0.40	Slug	
5	63.10	0.10	Plug	
6	63.10	0.16	Slug	
7	63.10	0.25	Slug	
8	63.10	0.40	Slug	
9	63.10	0.63	Slug	
10	63.10	1.00	Slug	
11	60.10	0.10	Plug	
12	55.35	0.10	Plug	
13	50.10	0.16	Plug	
14	45.58	0.10	Plug	
15	43.10	0.16	Plug	
16	39.81	0.10	Plug	
17	39.81	0.16	Plug	
18	39.81	0.25	Slug	4-5s per slug response or longer, up to 7
19	39.81	0.40	Slug	9s per slug response
20	39.81	0.63	Slug	
21	39.81	1.00	Slug	
22	39.81	1.58	Slug	Slug flow type, transition phase between slug and annular
23	25.12	0.16	Wavy	Pipe filled with water, small waves
24	25.12	0.25	Slug	
25	25.12	0.40	Slug	Can take up to 31 seconds to get slugs, made sure the buildup + slugs are present in the measurement.
26	25.12	0.63	Slug	
27	25.12	1.00	Slug	
28	25.12	1.58	Slug	
29	25.12	2.51	Annular	
30	15.85	0.16	Wavy	
31	15.85	0.25	Wavy	
32	15.85	0.40	Wavy	Smooth waves
33	15.85	0.63	Slug	Rare strong slugs and some slight waves
34	15.85	1.00	Slug	Rough waves with intermittent slug like waves (not filling pipe)
35	15.85	1.58	Wavy	Rough uneven waves
36	15.85	2.51	Annular	
37	15.85	3.98	Annular	Strong annular flow top pipe wet
38	10.00	0.10	Stratified smooth	
39	10.00	0.16	Stratified smooth	
40	10.00	0.25	Stratified	

Table 5.3. – Details of the air and water flow rates for the remaining 40 flow pattern experiments

#	**Water flow** kg/min	**Air flow** kg/min	**Regime**	**Comments**
41	10.00	0.40	Stratified	
42	10.00	0.63	Wavy	
43	10.00	1.00	Wavy	
44	10.00	1.58	Wavy	
45	10.00	2.51	Annular	Very close to wavy
46	10.00	3.98	Annular	
47	10.00	5.01	Annular	
48	6.31	0.10	Stratified	
49	6.31	0.25	Stratified	
50	6.31	0.40	Stratified	
51	6.31	0.63	Stratified	
52	6.31	1.00	Wavy	
53	6.31	1.58	Wavy	
54	6.31	2.51	Wavy	
55	6.31	3.98	Annular	
56	6.31	5.01	Annular	
57	3.98	0.10	Stratified	
58	3.98	0.16	Stratified	
59	3.98	0.25	Stratified	
60	3.98	0.40	Stratified	
61	3.98	0.63	Stratified	
62	3.98	1.00	Stratified	Very close to wavy
63	3.98	1.58	Wavy	
64	3.98	2.51	Wavy	
65	3.98	3.98	Annular	
66	3.98	5.01	Annular	
67	2.51	0.10	Stratified smooth	
68	2.51	0.63	Stratified	Slightly rough surface
69	2.51	1.00	Stratified	Very close to wavy
70	2.51	1.58	Wavy	
71	2.51	2.51	Wavy	
72	2.51	3.98	Annular	
73	2.51	5.01	Annular	
74	1.58	0.10	Stratified smooth	Almost no water in pipe
75	1.58	0.25	Stratified	
76	1.58	1.00	Stratified	Very close to wavy
77	1.58	1.58	Wavy	
78	1.58	2.51	Wavy	
79	1.58	3.98	Annular	
80	1.58	5.01	Annular	

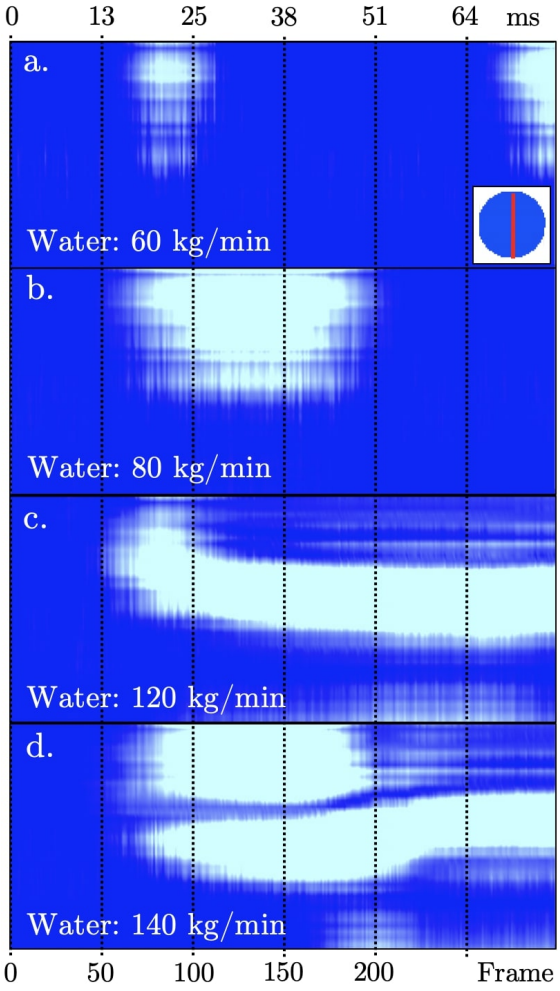

Figure 5.10. – First 300 reconstructed images of slugs flows in the electrodes plan for four different water flow rates. The images are visualised in the vertical line of pixels.

5.3. High pressure and high temperature flows experiment

The applicability of EIT to measure flow patterns in the hot leg necessitates to validate the technique in a high pressure and high temperature environment. The Section 5.3.1 introduces two thermo-hydraulic experiments to model accidental scenarios in the hot leg of a PWR. The load specifications and design of the EIT sensor to perform measurements in these loops are discussed in Section 5.3.2. The deformation of the material in the EIT sensor and the effects on the measurement is quantified based on a numerical simulation in Section 5.3.3. Finally, the early results of a first EIT measurement series in high pressure and high temperature conditions are presented in Section 5.3.4.

5.3.1. Primary circuit modelling flow rigs

The frame of this experimental work it to assess the usability of EIT to measure flow patterns in the hot leg of PWRs during a LOCA. The idea is to plug an EIT sensor into

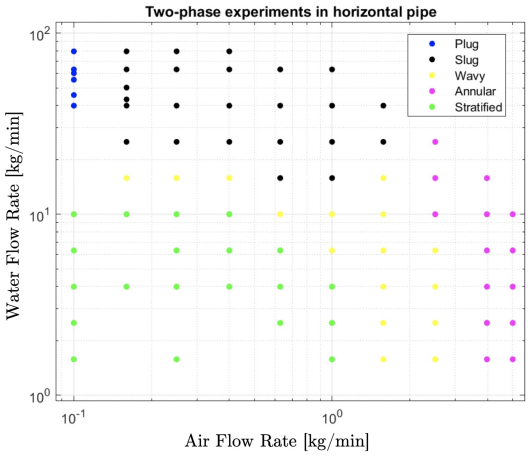

Figure 5.11. – Flow pattern experiments at USN.

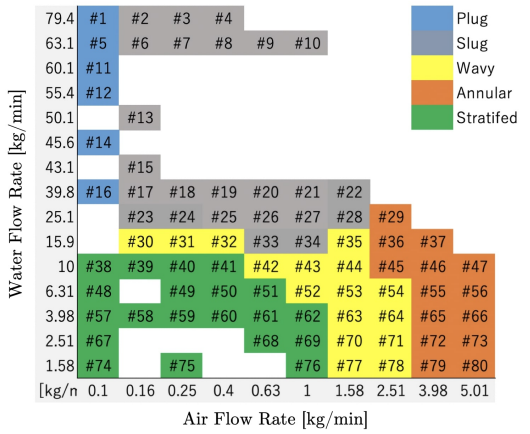

Figure 5.12. – Flow pattern experiments as listed in Table 5.2 and Table 5.3.

a high pressure and high temperature thermo-hydraulic flow rig such as the PKL test facility. In a first step, prior to operate the very large PKL facility, it was necessary to validate the EIT measurement in primary conditions on the Benson loop, a tinier thermo-hydraulic flow rig.

The PKL test facility

The necessity to analyse thermal-hydraulic related accidental scenarios led to the conception of reactor flow modelling experiments. In the seventies, reactor safety researches were focused on the experimental and theoretical analysis of the LOCA scenario in order to verify the effectiveness of the ECCS. In 1977, the German Ministry of Research and Technology supported Siemens/KWU to place in service the large-scaled test facility PKL (from the german abbreviation for *PrimärKreisLauf*, i.e. *primary circulation*) at the Framatome research center of Erlangen, Germany. The PKL experiment performed various experiments through numerous upgrades for over fifty years. The results have significantly contributed in understanding highly complex hydraulics behaviours involved in various accidental scenarios, improving the control, the safety as well as thermal hydraulics computer codes.

The four-loops facility (Figure 5.13) models completely the primary circuit of a nuclear power-plant plus the boiler of the secondary side. The design (Table 5.4) is a 1:1 scale model in heights of a PWR of the 1,300 MW class and was outlined with the Philippsburg 2 nuclear power-plant as reference [T. Mull, 2004]. Volumes are modelled with a scaling factor 1:145 of a typical 1,300 MW nuclear power-plant, corresponding to a hydraulic reduction of 1:12. The core is modelled with a set of 314 electrically heated rods, supplied with a power of 2.5 MW corresponding to 10% of the nominal power at scale.

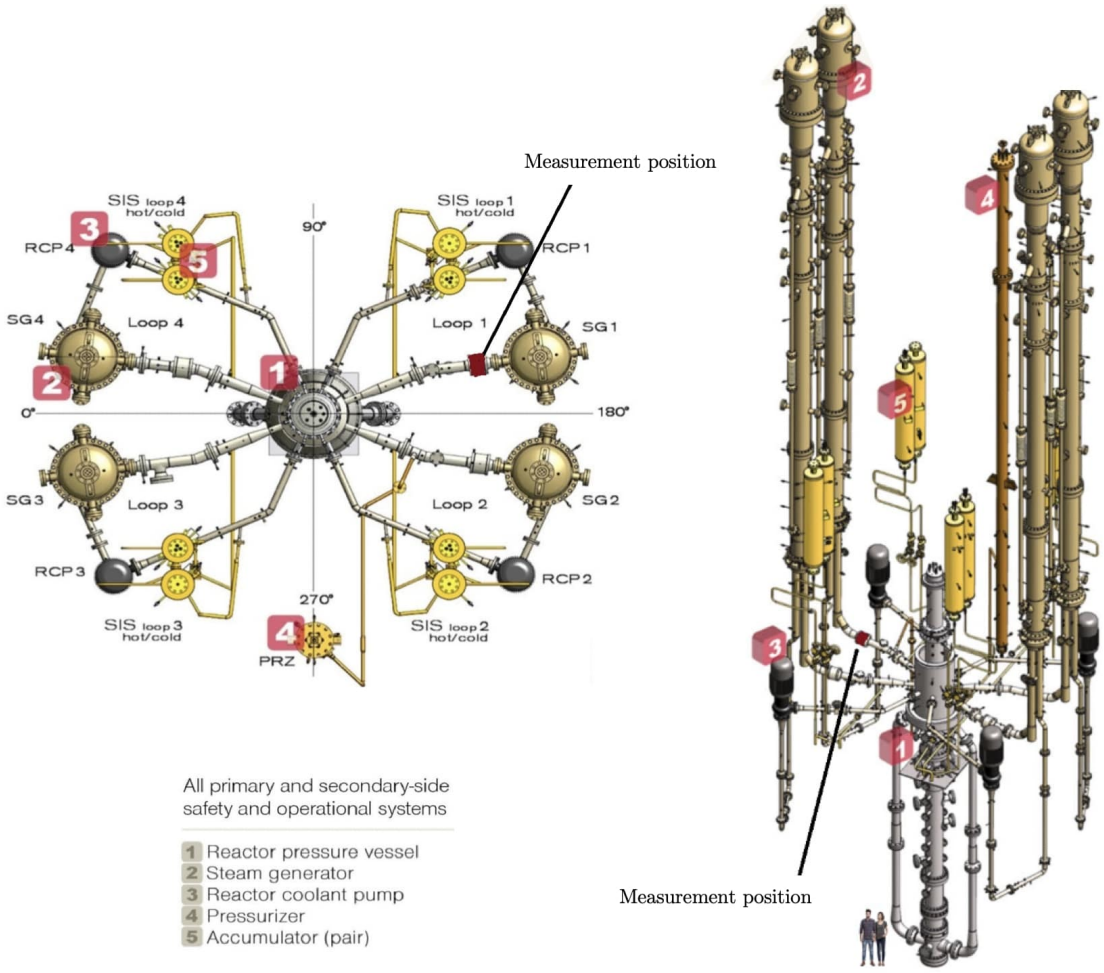

Figure 5.13. – Layout of the PKL Test Facility. The figure contains the measurement position, between the steam generator and the reactor pressure vessel, to plug the EIT sensor.

The Benson loop

The Benson loop is another high temperature high pressure boiling test facility located in the same area as PKL at the Framatome research center of Erlangen in Germany. The Figure 5.14 shows the scheme of the Benson loop. The pressure in the loop can reach up to 330 bar, the heating capacity is 2000 kW, the maximum temperature is 600°C, and the maximum mass flow rate is 28 kg/s.

5.3.2. The EIT sensor for high pressure and high temperature measurements

The design of the EIT sensor is imposed by the specifications of the available measurement region in PKL. However, according to the results of Chapter 2, if the measurement region size changes, it is preferable to have a region that is longer than the diameter of the pipe. The dimensions of the test section at the benson loop have been chosen to be

Table 5.4. – Specifications of the PKL thermo-hydraulic experiment

Scales	Elevations	1:1
	Volumes	1:145
Power	Max. core power	2.5MW
Flow	Flow rates	35 kg/s
Max. Pressure	Primary	45 bar
	Secondary	60 bar
Temperatures	Primary fluid	300° C
	Sec. fluid	300° C
	Max. rod cladding	750° C

the same as in PKL to use the same EIT sensor.

As discussed in Section 2.3, the remaining specifications concerns the electrodes. Since the electric potential is imposed during measurements, the image reconstruction quality of the images is optimised for the largest area of the electrodes. The *angular size* is maximised, limited by technical constraints with a gap of approximately 1 mm. The *axial size* affects the leakage of current that spreads the energy outside the sensitive region. From the results of the simulation in Section 2.3, a maximum of energy were found in the sensitive region for electrodes axial length of 84% of the distance between those conductive pipes. This ratio is verified for any length and any diameter of the measurement section. The symmetry of the stratified flow in PKL and the expected reduction of the noise from Ohm's law are good arguments to choose long electrodes in order to maximise the sensitive area. The summary of the requirements on the design that are expected to optimise the image reconstruction quality is presented in Table 5.5.

Table 5.5. – Load specifications of the EIT sensor for high pressure and high temperature experiments in the PKL and Benson thermo-hydraulical loops.

EIT sensor	Inner diameter $\mathcal{D}$	128.20 mm
	Outer diameter	286 mm
	Length $\mathcal{L}_{EIT}$	170 mm
Electrodes	Number of rings	1
	Number of electrodes n_e	64
	Angular size	5.3 mm
	Gap	1 mm
	Length $\mathcal{L}_E$	142.8 mm

The Figure 5.15 contains the schematic of the design of a sensor that contains the characteristics discussed above, and that can fit in the PKL and Benson thermo-hydraulical loops. Some dimensions (Width of the plates, the wire, and space between electrodes) are only limited with technical constraints since there is no particular need except the insulation between the electrodes and with the pipes up and down-stream. The final EIT sensor, build by Framatome GmbH from these load specifications, is shown in Figure 5.16.

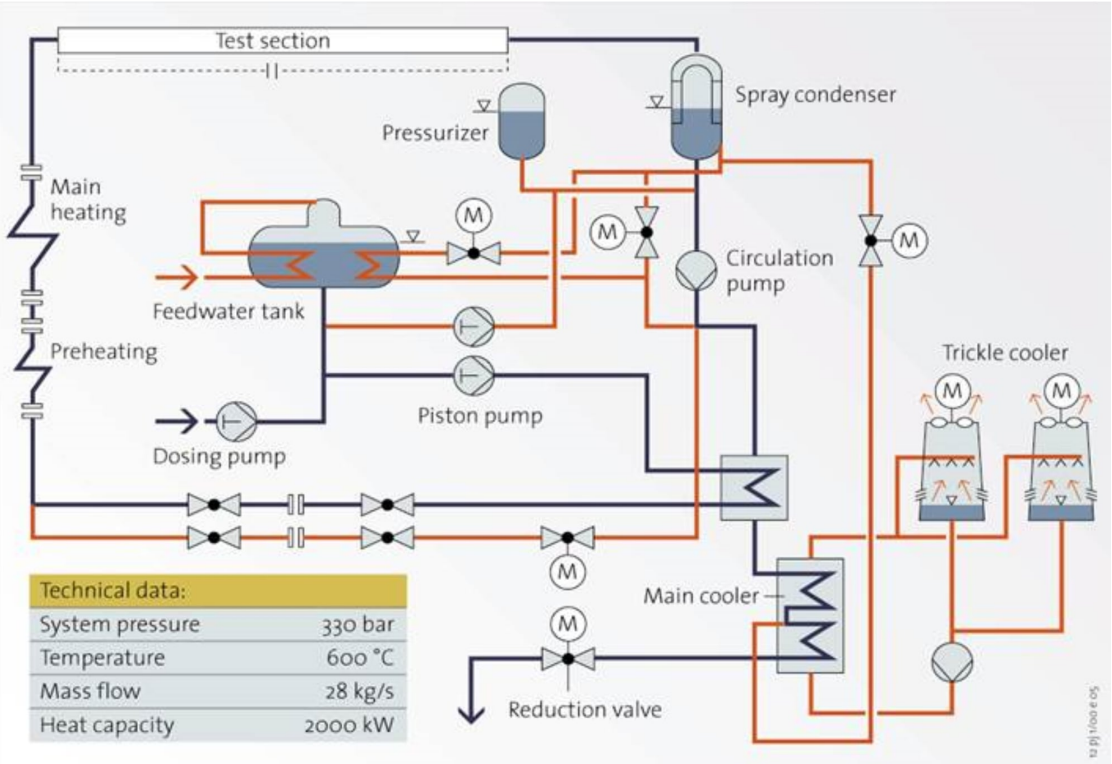

Figure 5.14. – Schematic of the Benson thermo-hydraulic loop. The EIT sensor is connected at the top left of the figure.

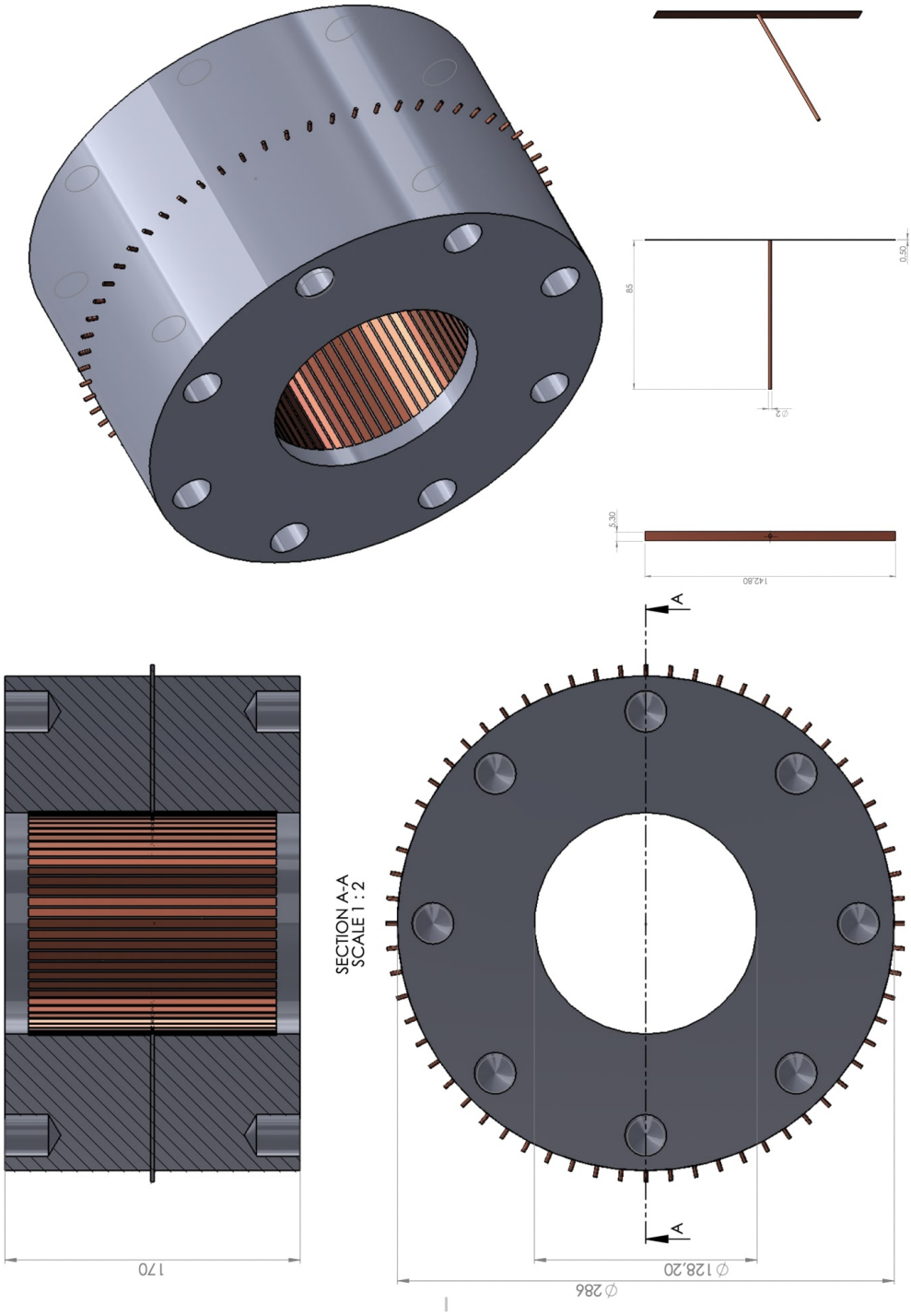

Figure 5.15. – Schematic of the proposed detector design for the PKL and Benson thermo-hydraulical loops

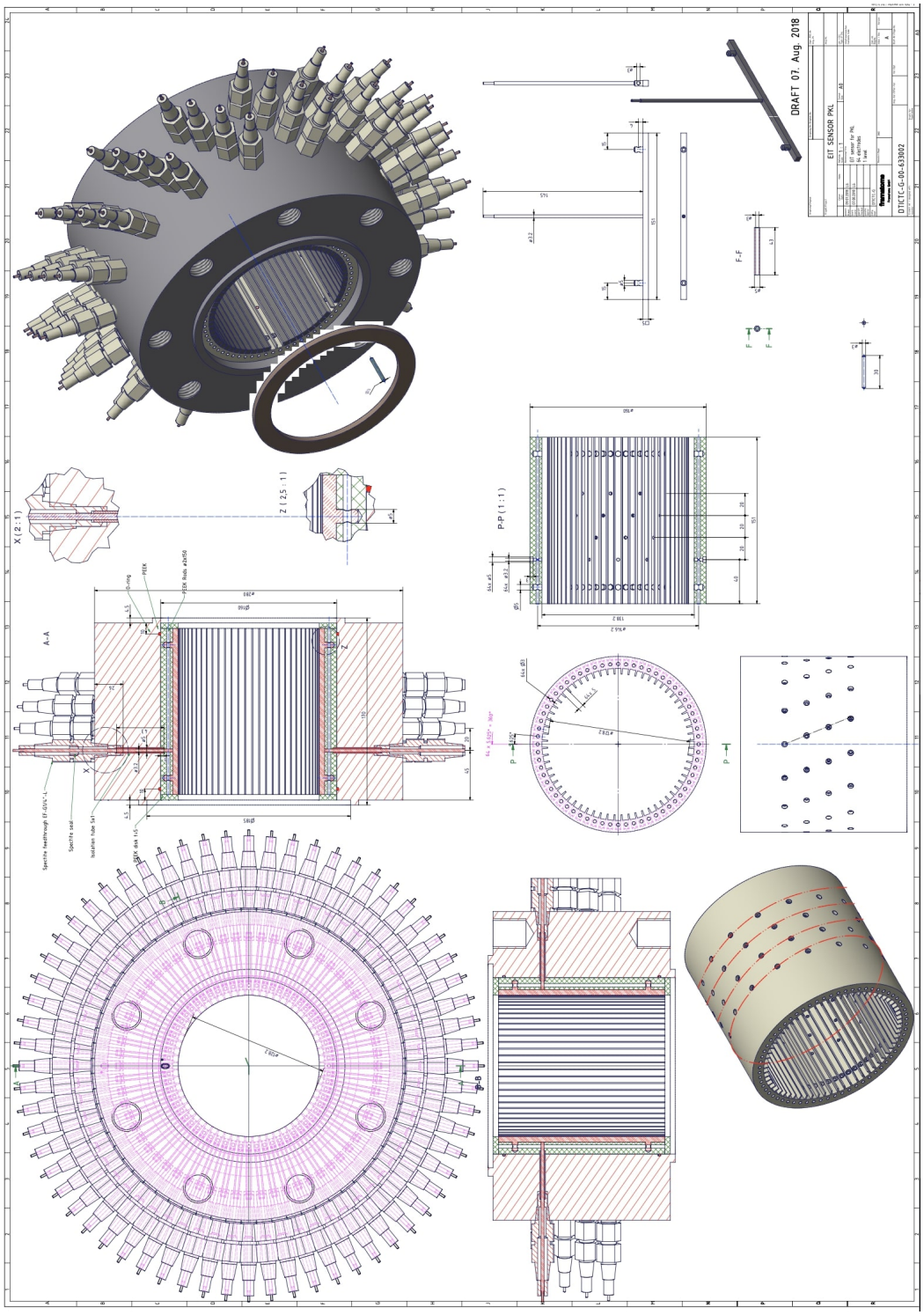

Figure 5.16. – Schematic of the final EIT sensor for PKL and Benson thermo-hydraulical loops.

5.3.3. Dimensional variations due to temperature and pressure

The final design of Figure 5.16 has an inner insulated layer made in PEEK. Contrary to stainless steel, peek can be significantly deformed by high temperatures. This deformation can create a gap (Figure 5.17), filled with water and making an external circuit for the current between the electrodes. Another effect is the current leaking through the stainless steal that surround the peek layer in which the electrodes are plugged. These effects were quantified prior to manufacture the EIT sensor.

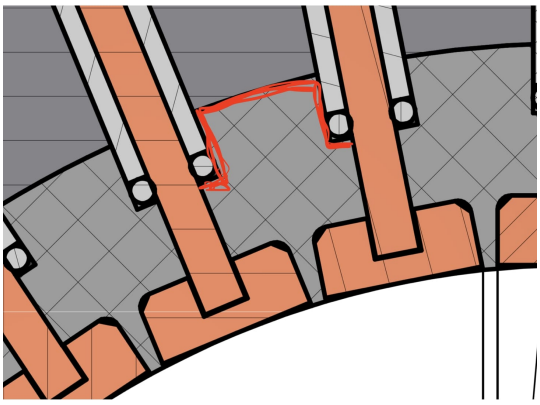

Figure 5.17. – Leaking current inside the EIT sensor due to the apparition of a gap (in red) between the electrodes.

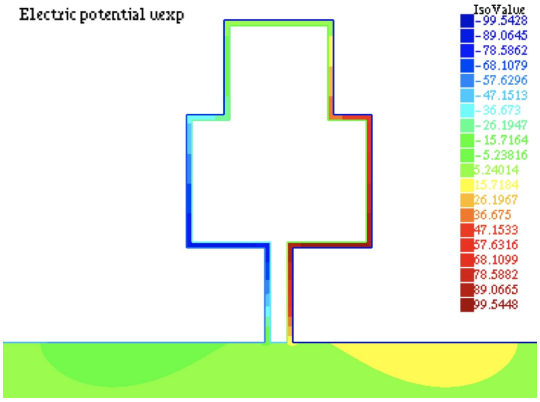

Figure 5.18. – Iso potential regions in the simulation domain.

In order to assess the effects on the measurement, a simulation (Figure 5.18) were developed with `FreeFEM++` to estimate the energy involved in the inner circuit: If the last is tiny compared to the energy within the pipe, the related measurement error is expected to be tiny. The simulation were based on the following assumptions:

- The simulation is in 2D. The case in 3D is expected to give a tinier leaking energy compared to the energy inside the pipe. This is explained by the fact that the volume created by the pipe is bounded in the $z-$axis by the electrodes length, as contrary to the energy inside the pipe that is spread in the water.
- The detector leaking current were simulated for an excitation between adjacent electrodes. If the related energy is tiny, the leaking energy between distant electrodes is expected to be tiny as well, as the circuit created by the gap increases more than the distance between the electrodes.
- The pipes were considered with an infinitely large diameter. For the sake of simplicity, the electrodes surfaces are considered coplanar.

The boundary conditions are the following: On the electrodes, and their stems, a current of $\pm$ 1 A is imposed. On the insulated borders, the current is 0 A. On the conductive stainless steal pipe, the potential is imposed to be 0 V. Finally, the borders on the left, right and bottom of the electrodes (within the pipe) are taken sufficiently far so the current density goes to zero on their surfaces.

The simulation considered a gap δ opened between the peek material and the electrodes and the same gap between the peek material and the stainless steel pipe element. Several values of δ were considered between 0.05 to 0.95 mm. In real conditions, the space will not be constantly opened around the peek material, but the worth case is considered here. If the result predicts a low leaking current, then any other situations will be favourable.

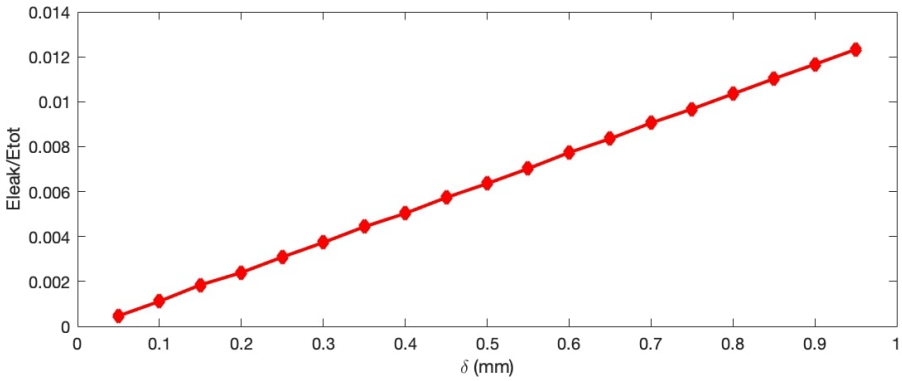

Figure 5.19. – Energy of the leaking current between adjacent electrodes, normalised to the total energy for different gap sizes.

For a gap of 0.95mm, which is very large, the leaking energy component (Figure 5.19) is estimated to be 1.2% of the total energy in the system. During the LOCA scenario, steam can fill the gap, making an insulated layer that drops the leaking energy to zero. Depending on the thickness of the gap, an uncertainty of about 1% can be expected.

The case considered here between adjacent excitation is the largest effect of the leaking energy. All other independent measurements are expected to have an even lower effect on the measurement. The alteration of the total dataset of all measurements will be low and the effect of leaking energy can be neglected.

5.3.4. EIT measurements on the Benson loop

The tests on the Benson loop have been proceed from July 18^{th} to 20^{th}, 2019. The EIT sensor is placed horizontally on a pipe of length of 3 m, at 30 cm upstream of the outlet.

Test procedure

The phase fraction α of saturated water-steam can be estimated from the mass flow rate $S = dm/dt$ and the steam quality χ, correlated to the heating power. Through monitoring S and the heating power, different volumetric void fractions could be obtained at certain pressures, as shown in Figure 5.20.

The preliminary plan is to perform three series of tests at 5 bar, 20 bar, 40 bar, separately. Three different mass flow rate are used at each pressure, that is, 0.15 kg/s, 0.4 kg/s, 1.0 kg/s. For each mass flow rate, 11 data points are selected with different values of χ.

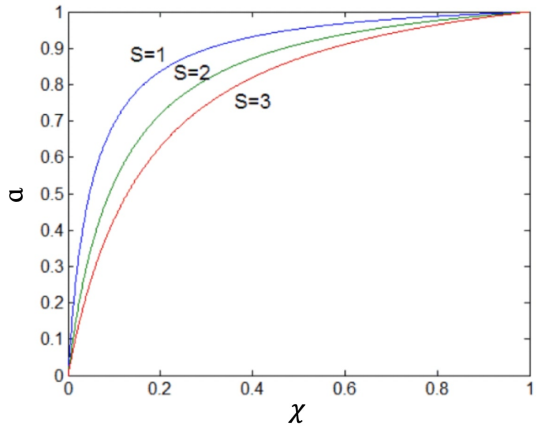

Figure 5.20. – Correlation between the flow rate, the steam quality and the phase fraction. This figure is used for illustration purpose and does not contain any actual data.

In the first stage of the experiment, only the test series at 20 bars have been considered. The investigated mass flow rates are 0.22 kg/s, 0.4 kg/s and 1.0 kg/s. At each flow rate, the EIT system is employed to take measurements at 11 different values of steam quality. It has to be mentioned that only stratified flow is obtained during the test due to the restriction of the facility.

Experimental results

During the tests in BENSON loop, the real-time imaging shows poor result, the images between neighbour frames change greatly and the stratified configuration can hardly be distinguished. The high electromagnetic noise in the laboratory due to the water heating process results in a high noise level in the data: the EIT sensor necessitates a proper shielding for future tests. However from the data, not shown in this thesis, we can barely assess a stratification level which is an encouraging result.

Prospects and indication for further work

The following prospects are proposed for future developments. The prospects that are estimated as most interesting/important are given at the top of the list.

- We have seen that EIT can be potentially applicable for temperature and boron concentration gradients measurement. However the electrical conductivity is less altered than in two-phase flows. The measurement of temperature and boron concentration in two-phase flows necessitates a high precision EIT data with low noise.
- The PKL experiment is a very large facility that is operated less than once a year. Therefore, the EIT measurements at PKL to measure the thermo-hydraulic phenomenons during a LOCA necessitates a perfect coordination between Framatome GmbH and the CEA. I hope such experiments will be possible in a close future.

"Coltrane, you can't play everything at once!" *Miles Davis*

6
The COLTRANE method

In the ONE-SHOT method, all linearly independent pairs of electrodes are considered to create a strategy of simultaneous excitations and measurement. As introduced in Section 1.3.1, there are only $(n_e - 1)$ linearly independent excitation patterns for a system containing n_e electrodes. The Fourier basis functions are a natural choice to describe the linearly independent patterns:

$$\frac{1}{\sqrt{2\pi}} e^{in\theta}.$$

Starting from the ONE-SHOT method, it is possible to consider a full set of simultaneous trigonometric excitations, leading to a higher image rate. In this chapter, the concretisation of this idea follows, with the Continuous Overlapping operations with Linear Trigonometric Response ANalysis for EIT (COLTRANE) method...

Contents

6.1 Excitation strategy and software implementation 205
6.1.1 General Spatial trigonometric excitation pattern 205
6.1.2 General simultaneous trigonometric excitation pattern 206
6.1.3 Practical implementation 206
6.2 Measurement and output data format 207
6.2.1 Measurement with FDM 207
6.2.2 Practical excitation and measurement strategy 208
6.2.3 Data format 209
6.2.4 Sign of the signal magnitudes 210
6.2.5 Experimental results from the COLTRANE method 211
6.3 Implementation of the COLTRANE method for 32 electrodes 213
6.3.1 Evolution of the hardware 214
6.3.2 Excitation setting and data format 216
6.3.3 Implementation and execution issues 217

The simultaneous trigonometric excitation strategy is discussed in Section 6.1, with the presentation of its software implementation. The measurement strategy and the output data format of the COLTRANE method are presented in Section 6.2, including experimental results. Finally, Section 6.3 discusses the preliminary work to develop the COLTRANE method for 32 electrodes.

6.1. Excitation strategy and software implementation

The set of simultaneous excitation is decomposed in *spatial oscillations* describing the Fourier basis of (6) and *time oscillations* with different frequencies to discriminate the trigonometric patterns with FDM.

In the following, the generated simultaneous trigonometric signals are defined in Section 6.1.1 and Section 6.1.2. The practical implementation of this excitation pattern based on a new structure is discussed in Section 6.1.3.

6.1.1. General Spatial trigonometric excitation pattern

Trigonometric strategy was proposed as an optimal excitation pattern to maximise the ability of the EIT to distinguish materials with similar conductivities. In each stimulation pattern, a static set of voltages $\{V_n^{sta}\}$ is imposed at the electrodes $\{E_n\}$ and forms a set of cosine and sinusoidal signal functions with different spatial frequencies m (Figure 6.1).

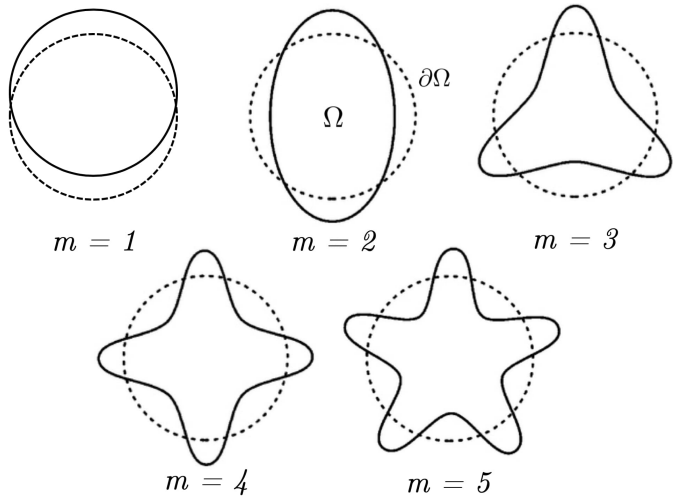

Figure 6.1. – Spatial cosine patterns for $m = 1$ to $m = 5$. The sinusoidal signal patterns are not shown in this figure. The boundary $\partial\Omega$ of the system Ω contains the electrodes and is shown with the dashed line. The solid line represents the excitation potential imposed on the electrodes.

Given an arbitrary number n_e of electrodes, one defines the static potential $V_{n,m}^{sta}$ imposed on the electrode E_n with:

$$V_{n,m}^{sta} \;=\; A\left[\delta_m^{\mathbb{O}}\cos(m\theta_n) + \delta_m^{\mathbb{E}}\sin(m\theta_n/2)\right], \tag{6.1}$$

where

- $n \in 1, ..., n_e$ the index of electrode,
- $m \in 1, ..., (n_e - 1)$ the spatial frequency,
- $\mathbb{O} = \{2k + 1 : k \in \mathbb{N}\}$ the set of odd integers,
- $\mathbb{E} = \{2k : k \in \mathbb{N}^*\}$ the set of non-zero even integers,
- δ the Kronecker symbol with $\delta_m^{\mathbb{O}} = 1$ if $m \in \mathbb{O}$ and $\delta_m^{\mathbb{O}} = 0$ otherwise,
- $\theta_n = 2\pi n/n_e$ the angular coordinate of the electrode E_n,
- A is the amplitude of imposed voltage.

For a given set of n_e electrodes, all independent excitation patterns are fully described with $(n_e - 1)$ different spatial frequencies.

6.1.2. General simultaneous trigonometric excitation pattern

In the COLTRANE method, each spatial frequency m in (6.1) is associated to a time frequency f_m and simultaneously imposed on every electrodes.

Each simultaneous excitation potential V_n^{exc} contains a superposition of $(n_e - 1)$ trigonometric patterns, each of which oscillating with a particular frequency f_m:

$$V_n^{exc}(t) = \sum_{m=1}^{n_e} \cos(2\pi f_m t) V_{n,m}^{sta} \tag{6.2}$$

$$= A \sum_{m=1}^{n_e} \cos(2\pi f_m t) \left[\delta_m^{\mathbb{O}} \cos(m\theta_n) + \delta_m^{\mathbb{E}} \sin(m\theta_n/2)\right]. \tag{6.3}$$

Here, the excitation pattern ensures that the sum of boundary voltages

$$\sum_{n=1}^{n_e} V_n^{exc}(t) = 0, \tag{6.4}$$

at any time in order to set a constant ground value.

Finally, the COLTRANE method consists in imposing simultaneously the set of potentials $\{V_n^{exc}(t)\}$ over the set of electrodes $\{E_n\}$.

6.1.3. Practical implementation

The COLTRANE method is implemented with `LabVIEW`. The code is an adaptation of `ONE-SHOT v3.2` with the new trigonometric excitation pattern, also based on two levels: HOST and FPGA. While the HOST sends continuously the frequencies and amplitude parameters to the FPGA, the latter takes the data points 16 by 16 in a loop cadenced at the high rate of 1 MS/s to create 16 analog signals.

Since `LabVIEW` is a graphical coding software, the detailed explanation of the structure of the code must be based on screen-shots of the code itself. These screen-shots and the explanations of the main differences with the ONE-SHOT method software can be found in the user guide of Appendix VI.

6.2. Measurement and output data format

This section presents the COLTRANE method measurement strategy, configuration and data format. In Section 6.2.1, the measurement based on FDM is presented. The practical setting of the measurement and FFT parameters are discussed in Section 6.2.2. The data format from the COLTRANE method is presented in Section 6.2.3. Finally, the sign matrix for the COLTRANE method data is computed in Section 6.2.4.

6.2.1. Measurement with FDM

In the COLTRANE method software, the host computer controls the FPGA to provide a fast generation of 16 arbitrary signals, detailed in Section 6.1. The 16 signals are transformed from 1 MS/s digital to analog signals using the NI-9262 modules and sent with coaxial cables to the electrodes. The excitation circuit at the electrode E_n contains a resistance R as shown in Figure 6.2. The Dirichlet boundary conditions are imposed with V_n^{exc} as in (6.11) one side of the resistance. The other side is connected to the electrode.

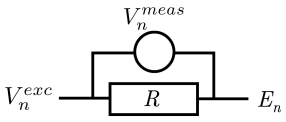

Figure 6.2. – Layout of the excitation and measurement circuit in the COLTRANE method. V_n^{exc} excitation voltage, V_n^{meas} measurement voltage, R resistance.

The Neumann boundary condition at E_n is the current I_n passing through the excitation circuit. It is obtained from voltage measurements $V_n^{meas} = RI_n$ over the resistance. As in (6.11), this signal is a sum of trigonometric functions. Their discrimination is obtained in the Fourier space.

The Fourier transform of the measured signal is computed from a P-point current measurement sequence $\{I_n(p)\}$ with p the discrete time and $0 \leq p \leq P$:

$$X_n(k) = \mathcal{F}[I_n(p)] = \frac{\theta}{R} \sum_{p=0}^{P-1} V_n^{meas}(p) e^{\mathrm{i}k\beta_p} \tag{6.5}$$

with $\beta_p = 2\pi p/P$, $\mathrm{i} = \sqrt{-1}$ and the normalisation factor $\theta = 1/P$. Let's consider the FFT to be computed at a frequency f_1, the rate at which P Fourier coefficients at the output.

The key to assure a discriminability consists in imposing the frequencies f_m of the generated signals (6.11) to be harmonics of f_1. Therefore, each coefficient k is associated with a specific frequency value f_m. In this setting, the data frame rate is f_1 and the resolution in the Fourier space is $\Delta f = f_{m+1} - f_m = f_1$. We note that the highest frequency is restricted below the Nyquist frequency $f_{Nyq} = 1/2\Delta p$ and Δp the sampling time.

The data points are the magnitudes of the Fourier coefficients in the n-electrode channel; i.e.

$$M_n(k) \;=\; \frac{1}{RP}\left|\sum_{p=0}^{P-1} V_n^{meas}(p)e^{\mathrm{i}k\beta_p}\right| \tag{6.6}$$

Each data point defines the current of one particular trigonometric pattern at one particular electrode. The set of the $\{M_n(k)\}$ for all n and all k is the EIT measurement data.

6.2.2. Practical excitation and measurement strategy

The practical implementation needs a detailed discussion on the signal frequencies and amplitudes.

Determination of the excitation frequencies

In this section, I suggest suitable values for the frequencies f_i based on the performances of the DAQ system, which is the same as used to implement the ONE-SHOT method (Section 3.3) with 16 electrodes.

A first remark is that the sampling frequency $f_{DAQ} = 1$ MS/s of the DAQ system imposes f_i to be below the Nyquist limit: $f_{Nyq} = f_{DAQ}/2 = 500$ kHz. Secondly, continuous signals must be provided to keep the advantage on low error from the residual voltage resulting from the energy stored in the electrode-electrolyte contact impedance [Wang et al., 2005, Wilkinson et al., 2005, Dupré et al., 2017a, Dupré et al., 2020, Darnajou et al., 2020]. As in the COLTRANE method, the solution to generate continuous signals at different frequencies is to chose the signals to be harmonics of the lowest generated signal frequency f_1.

The COLTRANE method for 16 electrodes consists in a set of excitation signals at 15 frequencies. Considering the sampling rate of 1 MS/s of the DAQ system, one solution for these frequencies consists of $f_i = if_0$ for $1 \leq i \leq 15$ where f_0 is the fundamental frequency.

Furthermore, the the fastest DFT computation can be chosen to be over $P = 32$ points since I consider only the positive outputs. It results in a data frame acquisition rate of 1×10^6 / 32 = 31 250 fps. This choice implies the lowest sinusoidal signal frequency f_1 to be the same as the DFT computation frequency. The highest frequency $f_{15} = 15 \times f_0$ is 468.875 kHz, below the Nyquist limit of 500 kHz for the considered system.

Determination of the excitation amplitudes

The voltage generation and acquisition modules are constrained within the range ±10 V. Considering the generation patterns given in Section 6.1.2, the amplitude A of the sinusoids must be much lower than the generated sum of sinusoids due to constructive interferences between them. On the other hand, the signal amplitude must remain as large as possible in order to reduce the SNR.

Another limit is the maximum variation allowed between two successive generated voltages. A real-time control in the DAQ system allowed to set the adequate value of $A = 0.15$ V, giving resonance peaks at ± 2.25 V. The fast transition between negative and positive signal values cancels the apparition of electrolytic effects [Dupré et al., 2017a, Dupré and Mylvaganam, 2018].

6.2.3. Data format

In my example for 16 electrodes, the measurement precision of the NI-9223 AI modules suggests the fixed-point data format with 20 bits allocated to the number including 5 precision digits. The electrode index $n \in [1, 16]$ Fourier coefficient $k \in [1, 15]$ can be described by 4-bits binary numbers.

Considering the next upgrade of the COLTRANE method for 32 electrodes (Section 6.3), each magnitude data point $M_n(k)$ is assigned with the corresponding Fourier coefficient and n-electrode address as:

$$M_n(k) = \underbrace{\langle +, 8, 0\rangle}_{k} + \underbrace{\langle +, 8, 0\rangle}_{n} + \underbrace{\langle \pm, 16, 11\rangle}_{M}, \tag{6.7}$$

where the fixed-point format $\langle s, b, p\rangle$ is used with s: signed/unsigned, b: number of allocated bits, p: number of precision bits. The data elements of (6.7) are of the format `U32`.

The n_e magnitudes measured on the n_e electrodes for a given Fourier coefficient k, i.e. a given frequency f_m, gives a data vector:

$$\{M_n(k)\} = \begin{pmatrix} M_1(k) & M_2(k) & M_3(k) & \dots & M_{n_e}(k) \end{pmatrix} \tag{6.8}$$

where the $M_n(k)$ are `U32` integers as in (6.7). A data matrix $\boldsymbol{D}$ then concatenates the set of magnitude vectors for the $n_e - 1$ Fourier coefficients corresponding to the $n_e - 1$ generated frequencies, i.e.:

$$\boldsymbol{D} = \begin{pmatrix} \{M_n(1)\} \\ \{M_n(2)\} \\ \{M_n(3)\} \\ \vdots \\ \{M_n(n_e - 1)\} \end{pmatrix} \tag{6.9}$$

which constitutes a data frame. In this case, the data size is:

$$S = n_e(n_e - 1) \tag{6.10}$$

where only the magnitudes of the Fourier transform are output.

According to (6.10), the size of one data frame is $S \times 32$ bits $= 4.0$ kB. By comparison, the same number of electrodes under the ONE-SHOT method gives a data frame size of 127 kB without any additional information on the boundary conditions. Furthermore,

the equivalent dataset for EIT based on TDM is of order 10 to 100 larger [Darnajou et al., 2019].

To conclude, apart from the higher data frame acquisition rate, an important advantage of the COLTRANE method is to reduce the data size by a factor $n_e/2$ by comparison with the data from the ONE-SHOT method [Darnajou et al., 2020].

6.2.4. Sign of the signal magnitudes

The FFT returns the magnitude and the phase. The sign of each datapoint is estimated from the phase. From (6.11), let us consider the excitation signal:

$$V_{n,m}^{exc}(t) \;=\; A\cos(2\pi f_m t)\left[\delta_m^{\mathbb{O}}\cos(m\theta_n)+\delta_m^{\mathbb{E}}\sin(m\theta_n/2)\right], \tag{6.11}$$

imposed on electrode n at a given frequency f_m. Its phase is given [Max and Lacoume, 2004] by:

$$\phi_n^V(k) \;=\; \arctan\left(\frac{-\sum_{p=0}^{P-1} V_{n,m}^{meas}(p)\sin(k\beta_p)}{\sum_{p=0}^{P-1} V_{n,m}^{meas}(p)\cos(k\beta_p)}\right) \tag{6.12}$$

The phase $\phi_n^I(k)$ of the current $I_l^{meas}(t)$ measured on electrode l at frequency f_m is:

$$\phi_l^I(k) \;=\; \arctan\left(\frac{-\sum_{p=0}^{P-1} I_l^{meas}(p)\sin(k\beta_p)}{\sum_{p=0}^{P-1} I_l^{meas}(p)\cos(k\beta_p)}\right) \tag{6.13}$$

Assuming a synchronous sampling between AO and AI, the phase shift $\Phi_{n,l}$ between the excitation voltage and the measured current is:

$$\Phi_{n,l}(k) = \phi_n^I(k) - \phi_l^V(k). \tag{6.14}$$

Which can be obtained from the arctangent subtraction formula:

$$\arctan x - \arctan y \;=\; \arctan\left(\frac{x-y}{1-xy}\right). \tag{6.15}$$

The phase shift depends on the design of the EIT sensor and the nature of the flow. If the phase shift is large, wrapping effects makes impossible to reconstruct the sign of the data. In [Darnajou et al., 2020], two cases were identified: $|\Phi_{n,l}(k)| < \pi/2$ and $|\Phi_{n,l}(k)| \geq \pi/2$.

In the former case, the sign of the datapoint is computed from (6.14) and (6.15). Therefore the signed data matrix $\widetilde{\boldsymbol{D}}$ is given by:

$$\widetilde{D}_n^m \;=\; \frac{\sin(\Phi_{n,l}(k))}{|\sin(\Phi_{n,l}(k))|} D_n^m. \tag{6.16}$$

where D_n^m denotes the elements of $\boldsymbol{D}$.

On the other hand, if $|\Phi_{n,l}(k)| \geq \pi/2$ the wrapping is too important to estimate the sign of D_n^k from (6.14). The solution I propose consists in introducing the sign matrix

$\mathbf{\Sigma}_{n_e}$ for n_e electrodes to allocate an arbitrary sign to the data.

The sign matrix $\mathbf{\Sigma}_{n_e}$ is estimated from the sign of the excitation signal at $t = 0$ for a given harmonics at a given electrode with the introduction of the signum function:

$$\Sigma_{n,m} = \begin{cases} 1 & \text{if } V_{n,m}^{meas} > 0, \\ 0 & \text{if } V_{n,m}^{meas} = 0, \\ -1 & \text{if } V_{n,m}^{meas} < 0, \end{cases} \tag{6.17}$$

where $V_{n,m}^{meas}$ is given by (6.1).

The `MATLAB` script used to compute the trigonometric sign matrix for the COLTRANE method can be found in Appendix IV.3

In the current set-up with $n_e = 16$, the sign matrix is defined as:

$$\mathbf{\Sigma}_{16} = \left(\begin{array}{c} \textit{Pattern Number} \\ \textit{(1 to 15)} \end{array} \right. \begin{array}{c} \textit{Electrode Number} \\ \textit{(1 to 16)} \end{array} \left. \right) \tag{6.18}$$

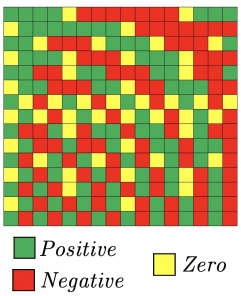

Finally, for a large phase shift, $\widetilde{\boldsymbol{D}}$ contains the arbitrarily signed amplitudes of the $n_e - 1$ excitation patterns for the n_e electrodes where the element corresponding to the k^{th} Fourier coefficient and the n^{th} electrode is:

$$\widetilde{D}_n^m = \Sigma_n^m D_n^m \tag{6.19}$$

similar to (6.16).

6.2.5. Experimental results from the COLTRANE method

The full implementation of the COLTRANE method is assessed on static experiments. The excitation strategy is described in Section 6.1, the measurement strategy and output data is discussed in Section 6.2.

An experiment is set up to measure the system response from a homogenous medium. The test section is filled with water of conductivity $\sigma = 635\ \mu\text{S}\cdot\text{m}^{-1}$ and a data frame is acquired. The data frame for the 15 magnitudes data points measured on the electrodes is shown in Figure 6.3.

The generated signals frequencies f_k are chosen so as to maximise the image refresh rate for the current set of 16 electrodes. This is obtained by considering the FFT to be computed over $P = 32$ data points at $f_{DAQ} = 1$ MS/s, with $f_1 = (32\ \mu\text{s})^{-1} = 33.250$ kHz.

Considering 16 electrodes, there is 15 different frequencies and the highest frequency is $(n_e - 1)\ f_1 = 468.875$ kHz, which respects the Nyquist limit $f_{Nyq} = f_{DAQ}/2 = 500$ kHz. In this setting, the image refresh rate is maximised at 33 250 fps with a full set of 15 trigonometric measurements per frame.

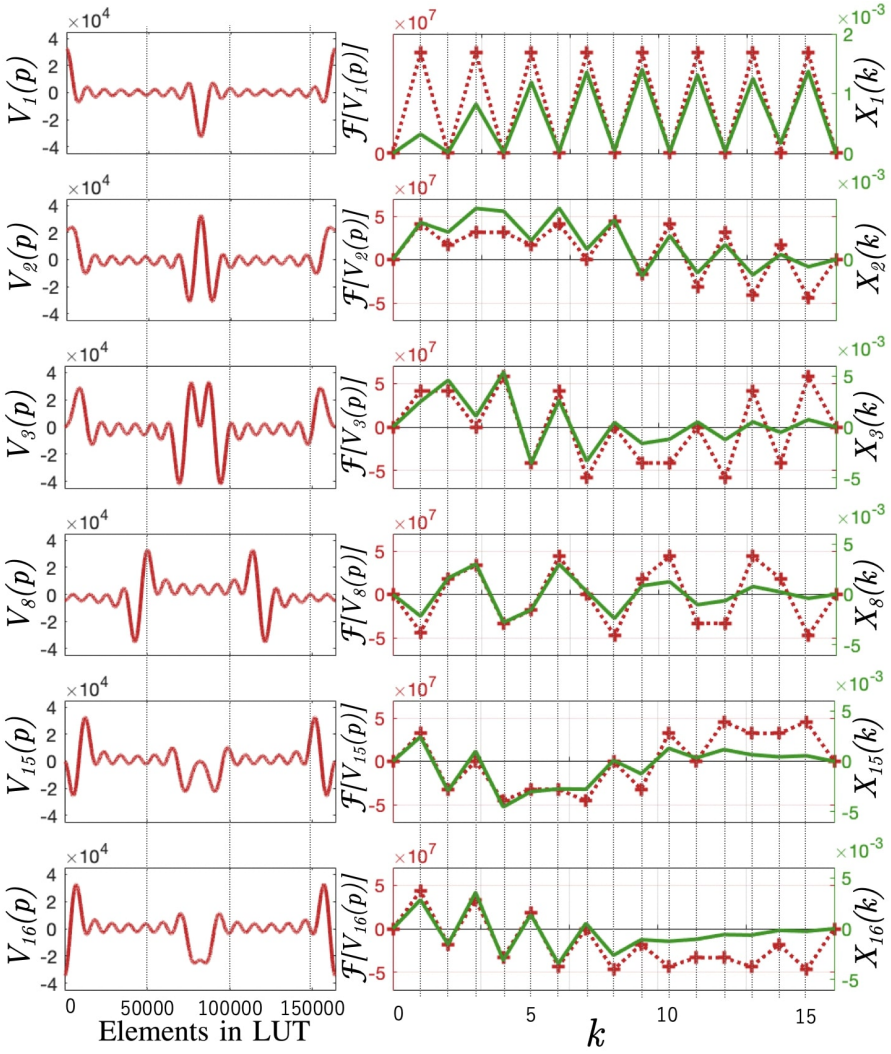

Figure 6.3. – On the left, data stored on the LUTs for 6 of the 16 electrodes. Each curve is computed by the VI of Figure VI.7 and contains a sum of 15 sinusoidal signals as suggested by the excitation pattern of the COLTRANE method.
On the right, two curves are plotted in the equivalent Fourier space. The red dashed curve is the Fourier transform of the generated voltage. The green curves are the magnitudes of the voltages measured over resistances on the PCB. The figure represents the measured current in Ampere, obtained from $M_n(k)/R$ with $R = 200\ \Omega$.

It is important to point out that maximising the image refresh rate is at the price of a large bandwidth, i.e. a large difference between the lowest frequency f_1 and the largest frequency f_{120}. As discussed in Section 4.2.4, the impedance shows an increasing dependency on frequency at higher range ($f \geq 10^4$ Hz). This results is observed in

Figure 6.3 with a weaker response in amplitude in the high harmonic range for the same conductivity change in the system.

We observe that the signal magnitudes are well discriminated from one another. The magnitudes decreases at higher frequencies.

6.3. Implementation of the COLTRANE method for 32 electrodes

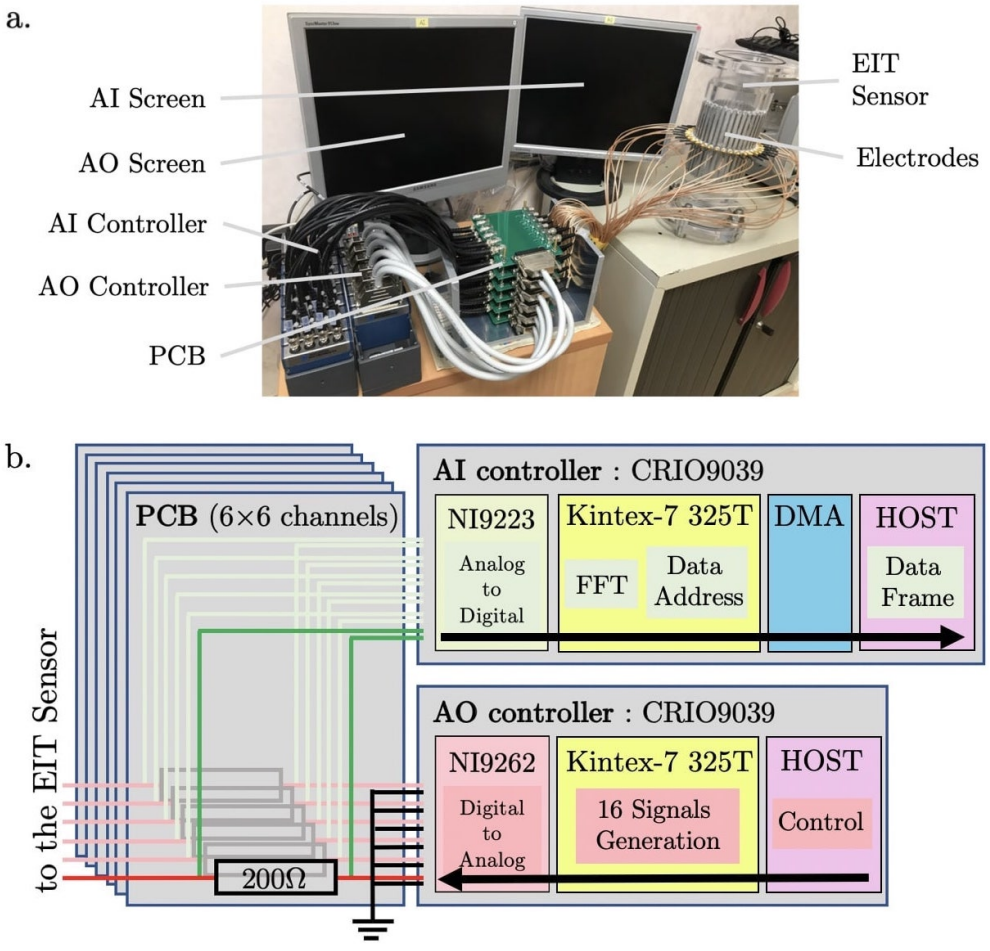

Figure 6.4. – a. The system implementing the COLTRANE method as used for static experiment. The EIT sensor is filled with water and a plastic rod of low conductivity is inserted to mimic non-conductive inclusions.
b. Layout of the DAQ system. On the left, details of the 6 PCBs. Each of which includes six independent circuits for voltage measurements over 100 Ω resistors. On the right, two FPGA-based CRIO-9039, containing six NI-9262 modules for the AO controller and eight NI-9223 modules in addition to the DMA buffer for the AI controller. The two controllers are operated by `Linux`. In red, the excitation circuit. In green, the measurement circuit.

In practical EIT, the number of electrodes is an important parameter since it allows more measurements and a better conditioning of the inverse problem, especially in the application discussed in Chapter 5. This motivated the application of the COLTRANE method on an EIT sensor containing 32 electrodes. I am interested in developing the COLTRANE method for twice the number of electrodes as described above. The current configuration does not support more analog input and outputs channels. We propose to duplicate the hardware and control the AO and the AI independently. This brings the benefit to have one DAQ module for AO that works independently and continuously. The other DAQ controller for AI is specially used to manage the data acquisition which simplifies the firmware architecture.

In Section 6.3.1, the evolution of the hardware system and the new configuration of each part is detailed. The practical excitation and measurement configuration for 32 electrodes is discussed in Section 6.3.2. Finally, Section 6.3.3 presents the implementation and discusses the issues appearing with this configuration.

6.3.1. Evolution of the hardware

The development of the COLTRANE method for 32 electrodes needed several changes that are detailed in the following. The complete system is shown in Figure 6.4a. and the hardware logics is illustrated in Figure 6.4b.

The Printed Circuit Board (PCB) for simultaneous excitation and sensing

A two-layer PCB (Figure 6.5) was designed to manage the voltage excitations and current measurements in parallel. The current is reconstructed from voltage measurement over 100 Ω resistors on the PCB. One PCB contains 6 channels. In my setup, a total of 6 PCBs are piled-up in a Faraday cage and provide the 32 channels. Coaxial connectors ensure the signal shielding with an interconnected ground connection,

The AO Controller

The AO controller is required to perform 32 voltage excitations at high rate with great accuracy. Apart from the performance requirements, the AO controller must be robust and light weight for transportation purposes in future prospects of experiments on several hydraulic loops. It also has to be controllable at a distance for an application to high pressure and high temperature flow experiments.

A suitable device for the AO controller is the National Instruments CRIO-9039 [NI-9039 Documentation, 2016], which includes a 1.91-GHz Quad-Core CPU, 2 GB of DRAM, and the Xilinx's FPGA Kintex-7 325T [Xilinx325T Documentation, 2019]. The FPGA includes 326,080 logic cells, 840 digital signal processing slices, and 16,020 block RAM elements. The CRIO-9039 AO controller includes a Linux host computer that operates the COLTRANE method with LabView 2017 Real-Time and FPGA. In addition, the CRIO-9039 provides 8 slots in which AO modules are connected.

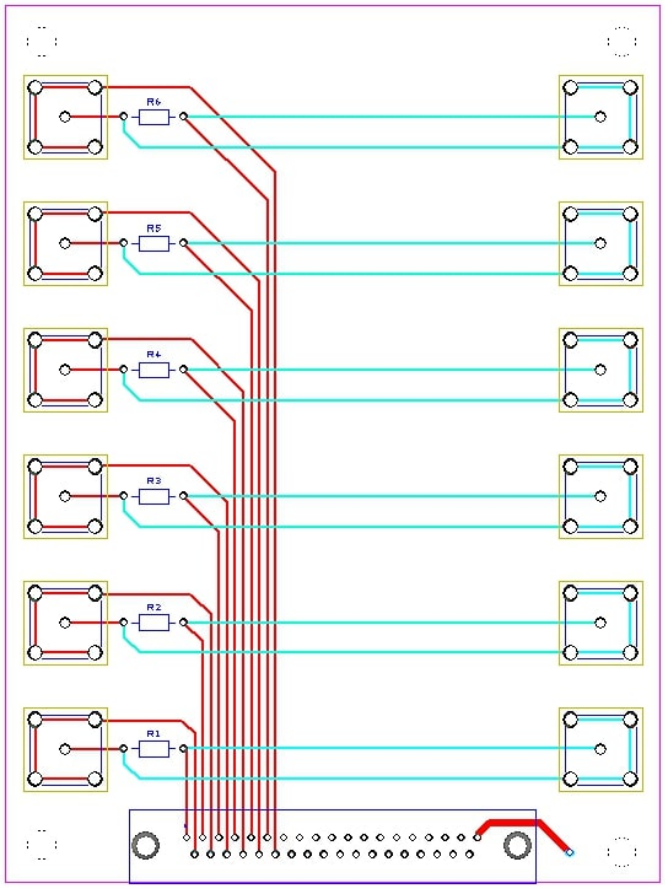

Figure 6.5. – Layout of the two-layer PCB design including 6 independent circuits for voltage excitation in red and current measurements in blue/green. The BNC connectors on the left send the excitation signal to the electrodes, the circuit assures a shielding of the coax cables. The BNC connectors on the right are differential measurements over the R1to R6 100 Ω resistors and connected to the NI-9223 modules. On the bottom, a DSUB connector for the excitation signals. A total of 6 of these PCBs have been piled up together to complete the needed 32 channels as shown in Figure 6.4a. The common ground is connected between these boards and a surrounding Faraday cage to assure the same ground reference for all the modules.

Regarding the necessity for fast and accurate operations, the AO is managed with the NI-9262 module [NI-9262 Documentation, 2017] to provide the voltage outputs. The six-channel module has a typical output voltage range of ±10.742 V, including an internal noise of 150 μV RMS per channel. In the system, six NI-9262 modules are connected to the 32-output excitations.

The AI Controller

The AI controller is required to perform 32 voltage measurements in parallel also at high rate. The input configuration computes Fourier transforms online for each electrode signal at a high rate, based on the FFT algorithm. Moreover, the AI controller is required

to perform fast data storage.

The strict requirements of fast computations, including FFT, and large data manipulation for multiple channel suggest the use of a FPGA. The CRIO-9039 [NI-9039 Documentation, 2016] is also a suitable device for this task. The main advantage of the Kintex-7 325T [Xilinx325T Documentation, 2019] FPGA is that it includes a large number of logic cells and large block RAM. The adequate use of the FPGA allows Real Time (RT) computation of FFT for a minimal data frame size, which allows efficient data transfer and reduces storage.

The monitoring of the COLTRANE method results in a large amount of data over numerous channels. The fast data monitoring is based on DMA, a buffer to send the data to the host computer. The AI modules are connected to the 8 slots provided by the AI controller .

The NI-9223 module [NI-9223 Documentation, 2016] is suitable to provide voltage inputs. The NI-9223 includes four channels with a typical input voltage range of ± 10.6 V with a noise of 229 μV RMS per channel. A total of eight NI-9223 modules are required to connect the 32 input measurement channels.

6.3.2. Excitation setting and data format

In the COLTRANE method for $n_e = 32$ electrodes, the maximal frame rate is reached by taking the FFT over 64 data points. In this situation, we have $f_1 = 1/64\mu s^{-1} = 15\,625$ Hz. In particular, the 31^{th} harmonics is $f_{31} = 31 \times 15\,625 = 484\,375$ Hz, below the Nyquist limit. This setting results in a data frame rate of 15 625 fps.

The data frames contains 32×31 data points. As in the previous, each data point is U32 format, and includes the Fourier magnitude, the electrode label and the Fourier coefficient which brings information on the trigonometric pattern and the excitation frequency. By analogy with Section 6.2.4, the sign of the data points is estimated with the following sign matrix with $n_e = 32$:

$$\mathbf{\Sigma}_{32} = \left(\begin{array}{c} \\ \textit{Pattern Number (1 to 31)} \\ \\ \end{array} \right. \begin{array}{c} \textit{Electrode Number (1 to 32)} \\ \\ \textit{Positive} \quad \textit{Negative} \quad \textit{Zero} \end{array} \left. \begin{array}{c} \\ \\ \\ \end{array} \right) \tag{6.20}$$

6.3.3. Implementation and execution issues

As illustrated in Figure 6.3, each data point is associated to a Fourier coefficient and hence, to a particular frequency. In this figure, we cannot see the noise effects as it can only be shown in a video. If we could see this video, we would see the effects of the noise that makes the noisy data $\tilde{M}_n(k)$ to oscillate around a value with an amplitude RMS of $\sim 1\%$ of the data amplitude.

In Chapter 3, we have approximated the noisy data:

$$\tilde{M}_n(k) = \left[\left(\frac{1}{P} \sum_{p=0}^{P-1} (V_n^{meas}(p) + \delta(p)) \cos(k\beta_p) \right)^2 + \left(\frac{1}{P} \sum_{p=0}^{P-1} (V_n^{meas}(p) + \delta(p)) \sin(k\beta_p) \right)^2 \right]^{1/2}, \quad (6.21)$$

with the probability function, δ, of the Gaussian-distributed noise pattern reads:

$$\delta(p) = \frac{1}{s\sqrt{2\pi}} e^{-\frac{1}{2}(\frac{p}{s})^2}. \quad (6.22)$$

When executing the code of the COLTRANE method for 32 electrodes, the data shown an abnormally large oscillation with an amplitude RMS from $\sim 10\%$ to $\sim 100\%$ of the data amplitude, depending on the frequency. In higher frequencies, the oscillation of ~ 3 Hz shown higher amplitudes. If several signals are simultaneously generated, the observed oscillations are in phase and of same frequency.

Three possible origins for this problem have been identified on two levels: software and hardware. These origins will be investigated in the following.

Software origin investigation

A first possible origin for this problem could be that the loop generating the AO (Figure VI.1) does not respects exactly the requirement of 40 ticks [1] when extending it to 32 outputs. To verify this, the code were modified to stop the loop if its iterating rate is different from 40 ticks at any time. This verification gave no change in the code operation suggesting that the AO loop generates the data at the correct rate.

A second possible origin of the problem could be that the LUT is not read properly. Since there is no interpolation between two data points in the LUT, if the number of points stored on the LUT does not match the reading rate, the lack of interpolation can result in an imprecision on the generated frequency. This effect is possibly stronger on higher frequencies, explaining the phenomenon.

To verify this, I have compared the frequency of two signals: one with a single sinusoidal signal period 1P stored on a LUT and read 30 times and another one with 30 sinusoidal

1. The ticks are defined by the onboard clock at 40 MHz. The precise value of 40 ticks is required to generate and acquire the data synchronously at 1 MHz.

signals with the duration of 30P stored on another LUT read a single time. The LUT reading rate is adjusted so the two signals have the same frequency.

The test consisted in generating the two signals in the same VI. The signal 1P were generated by reading the LUT at 30×15 625 Hz. The signal 30P were generated by reading the LUT at 15 625 Hz. In both cases, the oscilloscope shown an equivalent signal. Furthermore, by associating these two signal to the FPGA AI and FPGA FFT reading codes, I observed the same effect of the large oscillation of the data magnitude, in phase and with the frequency of 2.9 Hz. This indicates that no elements are added or deleted by the interpolation when reading periodically the LUT.

Hardware origin investigation

A third possible origin is hardware. The issue could be coming from a bad synchronisation between the clocks of the two CompactRIOs. This explanation is privileged since it explains why this issue did not appear for the COLTRANE method for 16 electrodes since the AO and AI are all operated with a single CompactRIO.

A verification to this issue however is somewhat more difficult to implement since it requires the installation of an external module for synchronisation. With the addition of a synchronisation module, the chassis of the AI CompactRIO should be extended from 8 to 9 slots. Some CompactRIOs also provide synchronisation via ethernet network. For this reason, this verification as well as the implementation of the COLTRANE method for 32 electrodes is suggested for further work.

Prospects and indication for further work

The following prospects are proposed for future developments. The prospects that are estimated as most interesting/important are given at the top of the list. The propositions written in **bold** are of top priority.

- The raw data from the COLTRANE method can be theoretically be used to reconstruct images. **It is fundamental to reconstruct images to prove the COLTRANE method.**
- The main advantage of the COLTRANE method is the very high data frame rate. Once the images are reconstructed, it is important to **perform dynamic experiment to demonstrate the high imaging rate.**
- As seen in the ONE-SHOT method, it is difficult to assess the sigh of the measured currents. I suggest to determine the sign of the data close to zero for the sign matrices.
- The improvement of the COLTRANE method to 32 electrodes necessitates the synchronisation of two CompactRIOs. This task can be performed with synchronisation modules or by ethernet connection if supported by the CompactRIOs.

C

Conclusion

The application of EIT in the context of high-pressure and high-temperature flow rigs raised the problematic of developing a high imaging rate EIT system able to withstand these extreme conditions. In my work, the motivations for increasing the data frame rate of EIT led to the development of two innovative methods. The new EIT DAQ systems are based on the ONE-SHOT and COLTRANE novel methods with simultaneous MF excitation strategies and associated with FDM for measurement. The methods have been tested in various experiments, validating their ability for ultra high rate DAQ and opening EIT to new domains of application.

The focus of this work is the use of EIT in high-pressure and high-temperature hydraulic loops. In this context, one concern is the design of the detector itself. An EIT detector contains a set of non intrusive electrodes on the inner surface of the pipe, in contact with the flow. Due to the thermo-hydromechanical constraints, the experimental pipe is steel which is an electrical conductor, a leakage of current is expected. In the preliminary work, we have aimed at determining the physical length of the electrodes to maximise the measurement energy.

As in Chapter 2, the design of the EIT sensor is imposed by the specifications of the available measurement region in the primary circuit. The energy at the surface of measurement electrodes is greater for a detector longer than the diameter of the pipe. Concerning the electrodes, since the electric potential is imposed during measurements, the signal energy is optimised for the largest area of the electrodes. The *angular size* is maximised, with the limitation of technical constraints. The *axial size* affects the leakage of current that spreads the energy outside of the sensitive region. The maximum energy were found in the sensitive region for electrodes axial length that occupies 84% of the distance between those conductive pipes.

The sensitivity map of Chapter 2 contains a valley between the excitation and measurement electrodes. This result were numerically confirmed using an indirect computation method based on a point-by-point reconstruction. Furthermore, the sensitivity map were computed for one measurement with an arbitrary position of the electrodes. In real conditions, the EIT detector excites and measures all independent combination to reconstruct an image. The sensitivity map for such "full-scan" strategy were computed and discussion are ongoing on the adequate measurement strategy, regarding the corresponding sum of sensitivity maps.

Concerning the need to increase the DAQ rate of EIT, the feasibility of the method with simultaneous MF excitation strategies and associated with FDM for measurement is investigated. In Chapter 3, we have discussed the requirements for the hardware system based on the excitation strategy and measurement process, as well as the motivations to determine the number of electrodes. An efficient hardware solution for implementing the simultaneous EIT excitation strategy was proposed with an analysis of the error and noise propagation through the measurement process. An experiment proved the feasibility of 15 simultaneous MF excitations with discrimination on a single electrode in

the low and high harmonic ranges of the excitation signals. This proof were a milestone in the project of applying the novel ONE-SHOT method for high-speed EIT.

Thereupon, the complete implementation of simultaneous excitations and measurements using a MF strategy for high-speed EIT, based on the novel ONE-SHOT method is presented in Chapter 4 with the details of hardware and software using `LabVIEW` and NI-modules. In this full implementation of the ONE-SHOT method, the number of frequencies becomes 120, bringing several new challenges. Mainly, the limit imposed by the Nyquist frequency of 500 kHz for the current system associated with the resolution in the frequency space from the choice of the DFT computation time window results in a maximum number of harmonics. Adding more frequencies may impose a longer time window, directly impacting the data frame acquisition rate. However, considering frequencies in the very high harmonic range may drastically affect the SNR due to higher resistivity and noise peaks. Furthermore, the limited physical space in the FPGA restricts the number of sinusoidal signal generators. The DFT computed over measurements of $P = 256$ points have increase the data acquisition rate up to 3 906 fps, while keeping $f_{120} = 469$ kHz, below the Nyquist limit.

Table C.1 shows the performances of the ONE-SHOT method with a number of existing high-rate EIT systems. The description of the different hardware systems contains several characteristics that have to be considered in spite of the data frame rates, including the Number of Measurements per Second (NMS). Firstly, the AI sampling frequency directly affects the data frame rate. Secondly, the data size is an important factor to be maximised to improve the conditioning of the inverse problem. Thirdly, the noise also directly impacts the image quality. The noise is the value currently measured in a partially-shielded DAQ prototype.

The ONE-SHOT method and software have been tested in two experiments described in Chapter 5 to model accidental scenarios in nuclear reactors. A first experiment aimed at measuring fastly evolving two-phase flows in SBLOCA and LBLOCA scenarios. In the two scenarios, images of air in water flows were successfully produced at the high rate of 3906 fps. A second experiment demanded deeper work on the EIT sensor itself to apply it in high-pressure and high-temperature flow rigs. Preliminary results shown good robustness of the produces EIT sensor but noisy data, mainly due to the electromagnetic noise from the heaters of the flow-rig.

Finally, the COLTRANE method is introduced in Chapter 6. This novel method uses simultaneous trigonometric excitation patterns to increase the data acquisition rate of EIT. The software have been developed for a 16 electrodes EIT sensor and is able to produce data frames at the rate of 32 250 fps. The evolution to 32 electrodes brings an issue of synchronisation between the generation and the acquisition devices. Several solutions are proposed for future prospects. The performances of the COLTRANE method with a number of existing high-rate EIT systems are presented in Table C.1.

Table C.1. – Comparison of the performances of the novel ONE-SHOT and COLTRANE methods with three existing high-rate EIT systems based on TDM.

System	f_{acq} (MS/s)	n_e	Data size	NMS	Frame rate (fps)	Excitation frequency (kHz)	SNR (dB)
Phantom [Halter et al., 2008]	1	64	15 × 63	172 652	182.7	1 to 10 000	65.5 to 98.6
Phantom [Khan et al., 2015]	10	16	16 × 16	28 160	110	97.65	90
ProME-T [Dupré, 2017]	2	16	16 × 120	1 599 360	833	15	60
ONE-SHOT							
- *Preliminary* [Darnajou et al., 2019]	1	16	16 × 15	468,744	1 953.1	2 to 250	59.6 to 69.1
- $n_e = 16$ [Darnajou et al., 2020]	1	16	16 × 120	7 500 000	3 906.3	4 to 469	55.6 to 69.1
COLTRANE							
- $n_e = 16$, 2020	1	16	16 × 15	7 500 000	31 250	31 to 469	55.6 to 69.1
- $n_e = 32$ (*Prospects*)	1	32	32 × 31	15 500 000	15 625	15 to 484	-

C.1. Research prospects

The improvement of the imaging rate of EIT to thousands of images per seconds opens the technique to new domains of application. The following prospects are proposed for future research.

- The characterisation of velocity fields in a liquid flow is a problematic of numerous scientific and industrial applications. The current techniques of velocity field mapping are mainly based on optical techniques, in particular PIV and PTV (Particle Image Velocimetry and Particle Tracking Velocimetry), not applicable in an opaque medium flowing inside an opaque pipe. Under accident conditions with a loss of coolant in a sodium-cooled fast reactor, the sodium inventory will be reduced resulting in two phase flows. Based on the difference in electrical characteristics of the liquid sodium and gas phases, EIT provides an opportunity for non-intrusive measurement potentially applicable at high temperature. The deployment of the ONE-SHOT or COLTRANE methods in such environments could provide a high precision on the velocity thanks to the high imaging rate.
- The RUPTUBE experimental device (Figure C.1) has been designed by Tristan Julien in the frame of his PhD at the CEA of Cararache. The purpose is to test the tube failures, to estimate the breaking pressure and to measure the resulting vibratory effects. The failures are obtained by pressurising the water inside test tubes that initially contain a rift. The test parameters are adjusted in order to necessitate a breaking pressure lower than 70 bar. The measurement of the resulting vibratory effects can be measured with high rate EIT, by placing a ring of electrodes around the test tube, at the level of the rift. Furthermore, the RUPTUBE experimental device can be dipped in a water tank of homogeneous electrical conductivity and the water inside the test tube with salty water of different homogeneous electrical conductivity. The ONE-SHOT method for EIT provides an opportunity to measure high rate images of the rupture due to the electrical conductivity difference between the tube material (metal or plastic) and the water mediums.

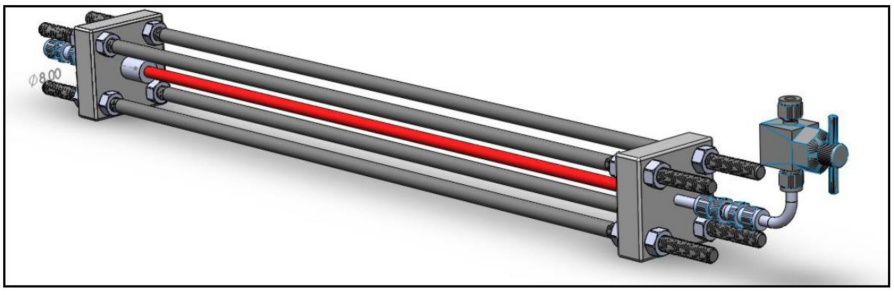

Figure C.1. – Layout of the RUPTUBE experimental device. The test tube is shown in red.

- In medical applications, EIT has the potential to expedite the differentiation of ischaemic or haemorrhagic stroke, one of the most important challenges in stroke

management and care [Goren et al., 2018]. This differentiation decreases the time to treatment. EIT attempts to exploit the contrast in the electrical impedance of healthy brain tissue, blood and ischaemic brain tissue. Contrary to conventional imaging methods, EIT has the potential to provide an inexpensive portable unit for use in ambulances or general practitioner surgeries which would revolutionise the management of stroke by providing imaging at the point of contact. The clinical scenario dictates that data must be collected at a single time point in the absence of a reference or 'pre-stroke' image, which prevents the use of conventional TDM algorithms for dynamic imaging [Lionheart, 2004,Malone et al., 2014]. It is therefore necessary to use frequency difference EIT algorithms, which use data collected at a single point in time and image changes across frequency. The ONE-SHOT method provides a large number of simultaneous excitations and a high timing resolution possibly applicable for medical imaging. Reducing the timing resolution of this method increases the available bandwidth to measure the reference and image data simultaneously.

- The internal structures of the vocal tract are difficult to measure without affecting their normal movement patterns [Stone, 1991]. Imaging techniques overcome that difficulty because they measure internal movement non-intrusively. Tongue and vocal tract researchers have employed X-ray tomography, MRI and ultrasound tomography techniques. However, MRI create low rate images only, ultrasound cannot image hard tissue and radiation exposure limits the duration of X-ray tomography. EIT can theoretically be applied since the difference between tissues and air electrical conductivity difference. The main advantage is the high timing resolution provided by EIT. In addition, EIT can be continuously operated without damaging the tissues.

List of Figures

1.1 a. CT scan with cover removed to show internal components. T: X-ray tube, D: X-ray detectors, X: X-ray beam, R: Gantry rotation. b. Sinogram (graphic representation) of the raw data obtained from a CT scan. [Jun and Yoon, 2017] c. Image sample of human brain, derived from the raw data. 49

1.2 a. Visual representation of the spin of a proton in a constant magnetic field B_0, then subject to a RF wave. The two colours represents two typical behaviours. b. Visualisation of the relaxation times T_1 and T_2. c. IRM machine in closed geometry. d. Spin-echo, T_1 weighted. MRI of the head measuring spin-lattice relaxation by using a short TR and TE. e. Spin-echo, T_2 weighted. Measuring spin-spin relaxation by using long TR and TE times. 53

1.3 The principle of magnetic induction tomography [Igney et al., 2005]. . 56

1.5 Illustration of the Adjacent excitation pattern (Left), the Opposite (Center) and the Full-Scan (Right) for 16 electrodes. The lines on the schematic are used to show the pairs of excitation electrodes and have no physical meaning. In the last, several colours were used for clarity to show the 120 patterns. 61

1.6 Illustration of four excitation patterns corresponding to a 16 electrode system [Mueller and Siltanen, 2012]. Theta is the angular coordinate of the electrodes. 63

1.7 The basic concept of multiplexing. The MUX combines the data from n channels, then the data is separated into n channels with the DEMUX. 72

1.8 Illustration of the TDM operation. the s_1, ... , s_n are packets of data that are send individually on the datalink. At any given time, the datalink transmit a single packet. 73

1.9 FDM multiplexing process. 75

1.10 FDM demultiplexing process 75

2.1 Image reconstruction using linear back projection from simulated data of bubbles in liquid for EIT detectors containing 8, 16, and 32 electrodes, represented with the green circles. On the left, one bubble of diameter 0.1 $\mathcal{D}$, with $\mathcal{D}$ being the diameter of the pipe. In the middle, two bubbles of the same diameter. On the right, stratified flow. The gas–liquid interface is shown with the purple line. 88

2.2 The function `MK_COMMON_MODEL` for different shapes and number of electrodes. 89

2.3 The image of a bubble (with conductivity 1×10^{-5} S.m^{-1}) of diameter $1/10\mathcal{D}$ in a medium of constant conductivity value 0.5 S.m^{-1}. 90

2.4 On the left, system with mesh size independent of the radius. On the right, mesh refinement on the edges, where the sensitivity is higher. . . 91

2.5 THD and SNR of signals on 16 measurement channels for 1 VAC 5 kHz excitation 92

2.6 4 levels of noises added to default bubble cases. The pink dashed circles show the position and size of the bubbles. 93

2.7 4 levels of noises added to 3 bubbles cases. The pink dashed circles show the position and size of the bubbles. 93

2.8 Layout of a 16 electrodes EIT detector, surrounded by grounded stainless pipes. 94

2.9 Illustration of the behaviour of the energy with the presence of leakage. This figure is only to report a general behaviour and do not contain any numerical data. 95

2.10 a. Illustration of the simulation domain in the plan of the two excitation electrodes. b. Scheme of the boundary conditions for the 2D leakage simulation. c. Iso-potential lined in the medium during an excitation. d. Current lines that let appear the leaking component from the electrodes to the ground surfaces. 99

2.11 Leakage of current versus the electrode length for EIT detectors containing $n_e = 4$, 8, 16, 32 or 64 electrodes. 100

2.12 Normalized utilisable energy versus the electrode length for EIT detectors containing $n_e = 4$, 8, 16, 32 or 64 electrodes.. The maximum of $\mathcal{U}(\alpha)$ is given at $\alpha = 0.84$. 101

2.13 Current leakage and Energy, varying with the Form Factor $\mathcal{F}$. The dependency is shown for several ratio of electrode lengths to the EIT detector length. 102

2.14 a. Contour and mesh for the simulation with arbitrary position of the excitation electrodes E_{exc_1}, E_{exc_2} and the measurement electrodes E_{meas_1}, E_{meas_2}. The mesh contains 14158 Triangles and 7234 Vertices. b. Iso-potential regions in the simulation domain for an excitation of ± 1 V between the excitation electrodes. c. Representation of the current vector filed fot the same excitation. d. The sensitivity map for a set of excitations and measurements on four electrodes with arbitrary position. 106
2.15 Log of the Sensitivity map normalised to $Max(\mathcal{S}) = 1$ for two pairs of excitation and measurement electrodes of width $\pi/20$. Each point $\boldsymbol{x}_0$ of the map is estimated from a small change over the area a centred at $\boldsymbol{x}_0$ of the electrical conductivity σ. 107
2.16 Log of the reconstructed sensitivity map normalised to $Max(\mathcal{S}) = 1$ for two pairs of excitation and measurement electrodes of width and positions as in Figure 2.15. The sensitivity is reconstructed for bubbles at positions (x, y). 108
2.17 Log of the sensitivity map average out from M excitations in the full-scan strategy. 110
2.18 The domain of the 3D simulation with the boundary conditions as in Figure 2.10. 113
2.19 Four representations in of the 3D simulations of a 4 electrode EIT sensor in the $x - y - z$ space and in the $x - z$, $y - z$ and $x - y$ plans for a. The iso-potential surfaces b. Log of the sensitivity c. Log of the sensitivity with the cylindrical boundary. 113
2.20 3D simulations of a 4 electrode EIT sensor with a cavity in the center of conductivity zero. a. The conductivity field on the mesh elements, the green lines are $\sigma = 0$ and the red lines are $\sigma = 1$. b. The iso-potential lines with the cavity c. The iso-potential lines of the potential field Δu. 114

3.1 a. Representation of two bubbles of different shapes passing through the cross section of the pipe. b. Simulated image of a bubble measured in a very short time Δt_1. c. Image of another bubble measured in a very short time Δt_2. d. Reconstructed image from the hybrid simulated data matrix. 120
3.2 a. Layout of a 6 electrodes EIT system: E_1 to E_4 are used for current excitation while the potential is measured between E_5 and E_6. b. Alternative excitation current between two excitation electrodes as used in the Adjacent, Opposite and Full-Scan Strategies. c. New MF excitation pattern between 4 electrodes. 121
3.3 The system implementing the ONE-SHOT method as used for static experiment. The EIT sensor is filled with water and a plastic rod of low conductivity is inserted to mimic non-conductive inclusions. The software provides a 2D real time image of the probed medium. 133

3.4 Scheme of the EIT sensor used for low pressure and low temperature tests. This sensor is composed of four parts: The body in Figure 3.5, the pipe connectors in Figure 3.6, the electrodes in Figure 3.7 and the SMA adaptors in Figure 3.8. 135
3.5 PMMA body of the EIT sensor. 135
3.6 PMMA pipes connector for inner diameter 80 and ISO standard pn10. 136
3.7 Stainless steal electrodes. 136
3.8 PEEK SMA connectors. 137
3.9 Layout of the PCB design including 18 independent circuits for voltage excitation and current measurements. The M1 to M18 BNC connectors are differential measurements over the R1 -R18 100Ω resistors and connected to the NI-9223 modules. The E1 to E18 BNC connectors send the excitation signal to the electrodes, the circuit assures a shielding of the coax cables. On the bottom, 3 DSUB connectors for the excitation signals, the common ground assures the same ground reference for the 3 NI-9262 modules. 138
3.10 Layout of the DAQ system. On the left, details of the PCB that includes 16 independent circuits for voltage measurements over 100 Ω resistors. On the right, the FPGA-based CRIO-9039 configuration containing four NI-9223 AI modules, three NI-9262 AO modules, and a DMA buffer all controlled by the host, operated by Linux. In red, the excitation circuit. In green, the measurement circuit. 140
3.11 The 15 excitation signals V_n^{exc} imposed on electrodes E_n of frequencies if_1^{exc} for $1 \leq i \leq 15$, and $f_1^{exc} = (512\ \mu s)^{-1}$. The drain excitation signal is shown in black on the left plot. 141
3.12 Simulation of the magnitudes of the 15 frequencies plus the drain at the 16 channels. On the right, rescaled zoom in the bottom part in the logarithmic scale of the DFT plot to show the tails of the peaks due to the discretisation onto 512 points. 142
3.13 Propagation of the Gaussian white noise through DFT computation for four generated frequencies. The Noise RMS was computed from 1000 Gaussian white noises and averaged out. The four curves follow the same linear interpolation: $y = 2.14 \times 10^{-4}\ x + 1.81 \times 10^{-4}$. . . . 143
3.14 Measured current, represented as the magnitude of the DFT of 16 voltages over resistances in the excitation circuit of the 16 electrodes. This result corresponds to excitations in the low harmonic domain. . . 145
3.15 Magnitudes of the DFT from excitations in the high harmonic domain. 145
3.16 Noise measured over the full spectrum available for the sampling rate of 1 MS/s. The results show five of the 16 electrode channels. The low, high, and very high harmonic ranges are also shown. 146

3.17 Electrical conductivity indicator function. Two non-conductive rods of diameter 20 and 30 mm, shown with black circles, are inserted in the test section filled with salt water. a. A 30-mm rod at the center. b. A 20-mm rod half way to the edge. c. A 20-mm rod on the edge. d. Two rods on the edge. 147

4.1 Layout of AO Logic. The colours of the boxes and arrows indicate respectively the nature of the VIs used and the formats of the data transfer. 156

4.2 Layout of AI Logic representing the HOST software, shared with the AO and the FPGA firmware including two loops operating in parallel at 1 MHz. The colours of the boxes and arrows indicate respectively the nature of the functions used and the formats of the data transfer. . 158

4.3 Representation of a full dataset for the standard TDM EIT acquisition process for 16 electrodes. The full dataset contains 120 single measurements, and here, only three are shown. The dead time dedicated to multiplexing is usually longer than the above representation. 160

4.4 Representation of the 120 data points considered in the ONE-SHOT method current measurement on a given electrode. All other magnitudes for any other Fourier coefficient k are discarded. 163

4.5 Bode diagram of homogeneous NaCl solutions of different electrical conductivities. The impedance on the top and the phase on the bottom are represented as functions of the imposed signal frequency 165

4.6 Front panel of `ONE-SHOT v3.2`. 167

4.7 Raw data from all of the 16 electrodes of a homogeneous water medium of conductivity $\sigma = 635\ \mu\text{S}\cdot\text{m}^{-1}$. The data from the electrode E_7 are shown in black for comparison purposes with the next figure. In the upper-right corner, the image of the reconstructed electrical conductivity $\sigma(\boldsymbol{x})$ with the arbitrary values $0 \leq \sigma \leq 1$ is shown. . . 168

4.8 Raw data for an inhomogeneous medium. The data from the electrode E_7 are shown in black for comparison purposes with the Figure 4.7. In the upper-right corner, the image of the reconstructed electrical conductivity $\sigma(\ x)$ with the arbitrary values $0 \leq \sigma \leq 1$ identifies the inclusion, shown with the white circle. 169

4.9 Three images of static flows obtained with the ONE-SHOT method software. 170

4.10 Electrode model composed of a charge transfer resistance R_e, a double layer capacitance C_e and a bulk resistance R_b. 171

5.1 Main steps of the LBLOCA scenario in a PWR. The right shows the cross section of the flows in the hot leg. The main elements of the primary circuit are shown. 1. Steam Generator 2. Reactor pressure vessel 3. Hot leg 4. Cold leg 5. Reactor coolant pump. 179

5.2 Comparison of the experimental values of water conductance of [Bignold et al., 1971] from 50°C to 271°C and [Light, 1984] from 50°C to 271°C with the values calculated in [Marshall, 1987]. 181
5.3 Relationship of electrical conductivity (EC) and boron (B) concentration of canal water samples collected from different locations in Southern Punjab, Pakistan during winter and summer months. [Niaz et al., 2018] 181
5.4 a. Expected flow phenomena in the hot leg during LBLOCA. b. Modelling of the phenomena. 182
5.5 Reconstructed image with several number of electrodes n_e of the expected flow in the hot leg during LBLOCA. 183
5.6 a. Schematic diagram of air/water flow rig with sensors and actuators. FT: Coriolis mass flowmeter, PDT: Differential Pressure. b. Detail of the ECT, EIT and GD sensors region. 185
5.7 a. Layout of the dynamic experiment. b. Longituginal representation of the 156 reconstructed EIT images of an air bubble passing through the pipe section with the electrodes in 40 ms. The pixels at the vertical radius of the pipe cross section are shown for each image. c. Transverse representation of 9 of the 156 reconstructed EIT images of the air bubble. The state of the bubble at different instances is clearly seen in the nine tomograms. 187
5.8 Reconstructed images of an air bubble passing through the plan of the electrodes in ∼20 ms. a. Visualisation in the vertical line of pixels. b. 5 of the ∼80 reconstructed EIT images. 188
5.9 Reconstructed images of an air bubble passing through the plan of the electrodes in ∼10 ms. a. Visualisation in the vertical line of pixels. b. 5 of the ∼80 reconstructed EIT images. 188
5.10 First 300 reconstructed images of slugs flows in the electrodes plan for four different water flow rates. The images are visualised in the vertical line of pixels. 192
5.11 Flow pattern experiments at USN. 193
5.12 Flow pattern experiments as listed in Table 5.2 and Table 5.3. 193
5.13 Layout of the PKL Test Facility. The figure contains the measurement position, between the steam generator and the reactor pressure vessel, to plug the EIT sensor. 194
5.14 Schematic of the Benson thermo-hydraulic loop. The EIT sensor is connected at the top left of the figure. 196
5.15 Schematic of the proposed detector design for the PKL and Benson thermo-hydraulical loops 197
5.16 Schematic of the final EIT sensor for PKL and Benson thermo-hydraulical loops. 198

5.17 Leaking current inside the EIT sensor due to the apparition of a gap (in red) between the electrodes. 199

5.18 Iso potential regions in the simulation domain. 199

5.19 Energy of the leaking current between adjacent electrodes, normalised to the total energy for different gap sizes. 200

5.20 Correlation between the flow rate, the steam quality and the phase fraction. This figure is used for illustration purpose and does not contain any actual data. 201

6.1 Spatial cosine patterns for $m = 1$ to $m = 5$. The sinusoidal signal patterns are not shown in this figure. The boundary $\partial\Omega$ of the system Ω contains the electrodes and is shown with the dashed line. The solid line represents the excitation potential imposed on the electrodes. . . . 205

6.2 Layout of the excitation and measurement circuit in the COLTRANE method. V_n^{exc} excitation voltage, V_n^{meas} measurement voltage, R resistance. 207

6.3 On the left, data stored on the LUTs for 6 of the 16 electrodes. Each curve is computed by the VI of Figure VI.7 and contains a sum of 15 sinusoidal signals as suggested by the excitation pattern of the COLTRANE method. On the right, two curves are plotted in the equivalent Fourier space. The red dashed curve is the Fourier transform of the generated voltage. The green curves are the magnitudes of the voltages measured over resistances on the PCB. The figure represents the measured current in Ampere, obtained from $M_n(k)/R$ with $R = 200\ \Omega$. 212

6.4 a. The system implementing the COLTRANE method as used for static experiment. The EIT sensor is filled with water and a plastic rod of low conductivity is inserted to mimic non-conductive inclusions. b. Layout of the DAQ system. On the left, details of the 6 PCBs. Each of which includes six independent circuits for voltage measurements over 100 Ω resistors. On the right, two FPGA-based CRIO-9039, containing six NI-9262 modules for the AO controller and eight NI-9223 modules in addition to the DMA buffer for the AI controller. The two controllers are operated by `Linux`. In red, the excitation circuit. In green, the measurement circuit. 213

6.5 Layout of the two-layer PCB design including 6 independent circuits for voltage excitation in red and current measurements in blue/green. The BNC connectors on the left send the excitation signal to the electrodes, the circuit assures a shielding of the coax cables. The BNC connectors on the right are differential measurements over the R1to R6 100 Ω resistors and connected to the NI-9223 modules. On the bottom, a DSUB connector for the excitation signals. A total of 6 of these PCBs have been piled up together to complete the needed 32 channels as shown in Figure 6.4a. The common ground is connected between these boards and a surrounding Faraday cage to assure the same ground reference for all the modules. . . . 215
C.1 Layout of the RUPTUBE experimental device. The test tube is shown in red. . . . 225

I.1 First four eigenstates of the periodic functions $f(\theta)$ (black lines) defined on the edge of the domain $\partial\Omega$ (dashed circles) . . . 244

V.1 Structure of the HOST VI . . . 282
V.2 HOST 1 . . . 284
V.3 CASE 1 . . . 285
V.4 *Harmonic Index* sub-VI . . . 285
V.5 *Generate Sines* sub-VI . . . 285
V.6 *Calculate FPGA Parameters* sub-VI . . . 286
V.7 *Extract Accumulator Value 2 Loops* sub-VI . . . 286
V.8 HOST 2 . . . 287
V.9 HOST 3 . . . 288
V.10 CASE 2 . . . 289
V.11 CASE 3 . . . 290
V.12 CASE 4 . . . 290
V.13 CASE 5 . . . 290
V.14 *Image Reco* sub-VI . . . 291
V.15 CASE 6 . . . 292
V.16 CASE 7 . . . 292
V.17 *Sort Data* sub-VI . . . 295
V.18 Structure of the FPGA AO VI . . . 296
V.19 FPGA AO 1 . . . 297
V.20 FPGA AO 2 . . . 298
V.21 CASE 8 . . . 298
V.22 FPGA AO 3 . . . 299
V.23 FPGA AO 4 . . . 300
V.24 FPGA AO 5 . . . 301
V.25 *DDS Sine Gen x10 2loops* sub-VI . . . 302
V.26 Representation of the intricate values for AO . . . 303

V.27 *SinGen 14bits LUT* sub-VI . . . 303
V.28 CASE 9 . . . 303
V.29 *120 freq40T* sub-VI . . . 304
V.30 *Add 15freq* sub-VI . . . 305
V.31 CASE 10 . . . 305
V.32 Structure of the FPGA AI VI . . . 306
V.33 FPGA AI 1 . . . 307
V.34 FPGA AI 2 . . . 308
V.35 FPGA AI 3 . . . 309
V.36 FPGA AI 4 . . . 310
V.37 CASE 11 . . . 311
V.38 CASE 12 . . . 311
V.39 Structure of the FPGA FFT VI . . . 312
V.40 FPGA FFT 1 . . . 313
V.41 CASE 13 . . . 314
V.42 CASE 14 . . . 314
V.43 CASE 15 . . . 314
V.44 Timing diagram outside the SCTL . . . 315
V.45 CASE 16 . . . 315
V.46 CASE 17 . . . 315
V.47 FPGA FFT 2 . . . 316
V.48 FPGA FFT 3 . . . 317

VI.1 FPGA AO VI for the COLTRANE method . . . 324
VI.2 CASE A . . . 325
VI.3 CASE B . . . 325
VI.4 CASE C . . . 325
VI.5 CASE D . . . 326
VI.6 *SinGen 14bits LUT* sub-VI . . . 326
VI.7 LUT initialisation . . . 327

List of Tables

1.1 Number of measurement and time for one frame under several excitation strategies and number of electrodes. 64

2.1 List of function inputs and the resulting output for the mesh generation. 89
2.2 Number of lines of code for the full-scan simulation of the sensitivity for different number of electrodes. 110

5.1 Classification of occurrences and frequency of incident per reactor classified into five categories. 178
5.2 Details of the air and water flow rates for the first 40 flow pattern experiments 190
5.3 Details of the air and water flow rates for the remaining 40 flow pattern experiments 191
5.4 Specifications of the PKL thermo-hydraulic experiment 195
5.5 Load specifications of the EIT sensor for high pressure and high temperature experiments in the PKL and Benson thermo-hydraulical loops. 195

C.1 Comparison of the performances of the novel ONE-SHOT and COLTRANE methods with three existing high-rate EIT systems based on TDM. . . 224

V.1 History of the versions of the ONE-SHOT method software. 283
V.2 Details of compilation times 319
V.3 Compilation timing for each compilation steps 320
V.4 Device utilisation after compilation 320
V.5 Clock timing results after compilation 320

VI.1 Details of compilation times of the COLTRANE method software . . . 328
VI.2 Compilation timing for each compilation steps of the COLTRANE method software 329

VI.3 Device utilisation after compilation of the COLTRANE method software 329
VI.4 Clock timing results after compilation of the COLTRANE method software 329

A

Appendix

I

Functional and Fourier Spaces

Contents

I.1 Functional spaces 243
I.2 Fourier spaces 244

I.1. Functional spaces

The definition of the functional spaces over the region Ω gives information on the behaviour of the functions. The wide use of such spaces in numerous mathematical applications makes the general definition far from the application considered here. The idea in the following list is not to give a strict mathematical definition of each domain, but to understand the relation with the physical behaviour of the functions and variables.

- L^∞ indicates the functions that are bounded above. The L^2 domain is defined relatively to a norm and a scalar product: every function $f \in L^2(\Omega)$ satisfies the following

$$||f||_{L^2(\Omega)} = \left(\int_\Omega |f|^2 dx \right)^{1/2} < +\infty \tag{I.1.1}$$

  In physics, a finite squared quantity means a finite energy. The set of functions f defined as above corresponds therefore to a set of functions of finite energy.

- C^∞ gives information on how smooth a function is. Furthermore, $C^\infty(\bar{\Omega})$ indicates that the function defined on the closure $\bar{\Omega}$ is infinitely derivable (smooth curve). This implies that there is no corner on the closure.

- H^1 is the Sobolev space which is a subspaces of L^2. Similarly to L^2, it indicates a bounded norm for the potential and the intensity $e = \nabla u$. In EIT, it fixes a bound

for a function f and its gradient ∇f under the following relation :

$$||f||_{H^1(\Omega)} = \left(\int_\Omega (|f|^2 + |\nabla f|^2)dx\right)^{1/2} < +\infty \tag{I.1.2}$$

The space of traces (i.e. : on the boundary) is given by the trace operator $\gamma_D : H^s(\Omega) \to H^{s-1/2}(\partial\Omega)$. Therefore in the EIT problem, $u|_{\partial\Omega} \in H^{1/2}(\partial\Omega)$, the space of traces of functions with finite energy and $\nabla u|_{\partial\Omega} \in H^{-1/2}(\partial\Omega)$.

The constraints given by the domains listed above makes the EIT problem simpler.

The assumption that Ω is a C^∞ domain requires the potential and the current to be smooth functions (forbidding angles and discontinuities) over the closure $\bar{\Omega}$. Therefore, the potential $u(\boldsymbol{x}) \in \bar{\Omega}$ and the current $\boldsymbol{j}(\boldsymbol{x}) = -\gamma(\boldsymbol{x}, \omega)\nabla u(\boldsymbol{x}, \omega) \in \bar{\Omega}$ are periodic functions. The definition of $\boldsymbol{j}(\boldsymbol{x})$ here is given by the Ohm's law.

I.2. Fourier spaces

Fourier analysis gives a complete orthonormal basis $B = \{e_j\}_{j\in\mathbb{N}}$ with

$$e_j(x) = e^{i2\pi\frac{j}{T}x} \tag{I.2.3}$$

and $T \in \mathbb{R}^{+*}$, for any periodic functions $g \in L^2(\Omega)$ that are decomposed over the eigenvectors with respect to the following :

$$g(x) = \sum_{j=1}^{+\infty} g_j e_j(x) \tag{I.2.4}$$

$$\text{with} \quad g_j \equiv \langle g, e_j\rangle = \int_\Omega g(x)e_j(x)dx. \tag{I.2.5}$$

Here, $\langle a, b\rangle$ denotes the L^2 inner product of a and b and the eigenfunctions g_j are the trigonometric functions on the unit circle. In Figure I.1 is illustrated the firsts coefficients for

$$f(\theta) \sim \cos(j\theta). \tag{I.2.6}$$

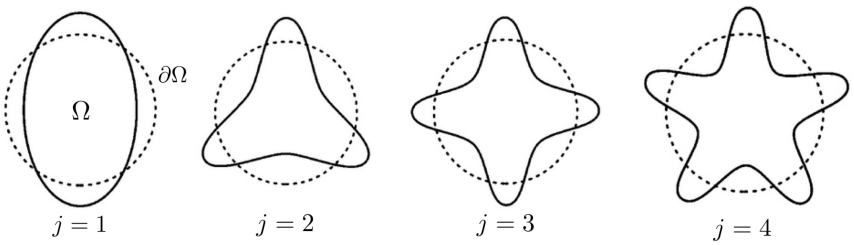

Figure I.1. – First four eigenstates of the periodic functions $f(\theta)$ (black lines) defined on the edge of the domain $\partial\Omega$ (dashed circles)

II

EIDORS Script

Contents

II.1 EIDORS V.3 features 247
II.2 Script to simulate EIT measurements 248

II.1. EIDORS V.3 features

The last version, EIDORS V.3 [Adler and Lionheart, 2006], provides the following features:

- *Generalized model formats* to use the software for general configurations of the electrodes. Additionally, several functions are available to create common electrode and stimulation configurations, specifying the electrode positions, contact impedances, and stimulation and measurement patterns. The data depending on all these configurations can be used to reconstruct images.
- *Multiple algorithm support* to provide access of the algorithms from [Adler and Guardo, 1996, Vauhkonen et al., 2001, Polydorides and Lionheart, 2002, Asfaw and Adler, 2005, Soleimani et al., 2006].
- *Interface software for common EIT systems* provides the ability to load from a variety of EIT hardware storage formats into the EIT data format.
- *Usage examples* are included from basic usage for the new user to more complex examples with various image reconstruction algorithms and combinaison of these.
- *Test suite* which includes a series of regression test scripts to allow automatic testing of code modifications. For instance an automatic validation function to calculate the Jacobian against an approximation of the Jacobian using the perturbation method.

- *Open source licence* under the GNU General Public Licence. Users are free to use, modify and distribute their modifications.
- *Sourceforge hosting* allows the collaborative development while proposing a read-only access to everyone.
- *Language independance* to support multiple mathematical software packages. `EIDORS` can be implemented on `MATLAB` and `OCTAVE` [Eaton, 2008] to provide a full open source platform.
- *Pluggable code base* with function pointers to allow adding new modules and controlling which parts of functions are executed.
- *Automatic matrix caching* to offer the ability to automatically detect and reuse the objects that have already been stored in the previous computation. This is particularly utilisable to increase the performances of the image reconstruction software since it uses computationally expensive variables such as the Jacobian and image priors.
- *Enhanced finite element model and graphical output* are provided with functions for image presentation using the `MATLAB` graphic features.

II.2. Script to simulate EIT measurements

The following script is an example to simulate EIT measurements with `EIDORS`. The code is run with `MATLAB`.

```
% clear all; clc;
run('C:\Users\cd252075\Desktop\Reconstruction_20180306\EIDORS_Software\eidors\
    startup.m')
nelec= 16; nrings= 1; heigth=270; ring_vert_pos = [heigth/2.,]; conduct = 1;

%% Direct problem - Reference medium
%%ng_mk_cyl_models(cyl_shape, elec_pos, ...elec_shape, extra_ng_code);
%%cyl_shape= {height, [radius, [maxsz]]}; elec_shape=[radius, 0, maxsz ];
%%maxsz (OPT) -> max size of mesh elems (default = coarse mesh)
fmdl_ref= ng_mk_cyl_models([270,25.5,5],[nelec,ring_vert_pos],[4,154.,2.]);
fmdl_ref.stimulation = tool_Full_Scan_Stimulation(nelec,nrings,1);
img_ref = mk_image( fmdl_ref, conduct );
% h1= subplot(121);
show_fem(img_ref);
v_ref = fwd_solve(img_ref); v_ref.nodes=fmdl_ref.nodes; v_ref.elems=fmdl_ref.
    elems;

%% Reconstruction with EIDORS default
imdl=mk_common_model('a2C',16);
imdl.fwd_model = fmdl_ref; clear fmdl_ref ; save('imdl','imdl','-v7.3')

J = calc_jacobian( calc_jacobian_bkgnd( imdl) ); save('J','J','-v7.3')
```

```
21 iRtR = inv(prior_noser( imdl )); save('iRtR','iRtR','-v7.3'); clear imdl;%
       rearrange the matrix
22 hp = 0.10; iRN = hp^2 * speye(size(J,1)); % generate a sparse identity matrix
23 B=(J*iRtR*J' + iRN); %save('B','B','-v7.3'); clear iRN;
24 A=iRtR*J'; %save('A','A','-v7.3'); clear J;
25 RM=A/B; save('RM','RM','-v7.3'); clear iRN J A B;
26
27 %% for the calculation of v_im numerically for L curve analysis (temp?)
28 % x_cyl='00';y_cyl='00';R_cyl='20';
29 % extra={'ball',horzcat(['solid ball = cylinder(',x_cyl,',',y_cyl,',0;',x_cyl
       ,',',...
30 % y_cyl,',200;',R_cyl,') and orthobrick(-50,-50,0;50,50,190) -maxh=1;'])};
31 % fmdl_im = ng_mk_cyl_models([heigth,50,5],[nelec,ring_vert_pos],[0.5,0,0.020],
       extra);
32 % fmdl_im.stimulation = tool_Full_Scan_Stimulation(nelec,nrings,1);
33 % figure; show_3d_slices(img, [95]); view (0,90); colorbar;
```

III

FreeFEM++ scripts

Contents

III.1 FreeFEM++ features 251
III.2 Script for leakage simulation and energy estimation 253
III.3 Script for generalisation with the form factor 257
III.4 Script to estimate the sensitivity map of a single EIT measurement 262
III.5 Script for the hand reconstruction of the sensitivity map 264
III.6 Script for 3D simulations 268

This annexe contains the scripts used in the simulations presented in Chapter 2. The first script (Sec. III) is used for modelling the electrodes in a grounded environment to estimate the leaking current and quantify the energy in the sensitive region.

III.1. FreeFEM++ features

The characteristics of FreeFEM++ are the following:

- *Problem description* from their variational formulations, with access to the internal vectors and matrices if needed.
- *multi-equations of multi-variables* handing,
- *linear or non-linear* coupled systems,
- *Two- and three-dimensional* problems
- *Static or time dependant*
- *Automatic mesh generator* with metric-based anisotropic adaptive mesh, based on the Delaunay-Voronoi algorithm. The inner point density is proportional to the density of points on the boundaries [George, 1996]

- *Easy geometric input* by analytic description of boundaries by pieces.
- *Vector formulations* of the geometries
- *Parallelisation* of the computation
- *A large variety of triangular finite elements* : linear, quadratic Lagrangian elements and more, discontinuous P1 and Raviart-Thomas elements, elements of a non-scalar type, the mini-element,. . . (but no quadrangles).
- *Automatic interpolation* of data over multiple finite element meshes with a large variety of triangular finite elements.
- *Tools* to define Galerkin finite element formulations `P0`, `P1dc`, `P2dc` and keywords: `jump`, `mean`, `intalledges`.
- *A large variety of solvers* for direct or iterative and eigenvalue or eigenvector.
- *Near optimal execution speed* (compared with compiled `C++` implementations programmed directly).
- *Online graphics*, generation of ,.txt,.eps,.gnu, mesh files for further manipulations of input and output data.
- *Many examples and tutorials*: elliptic, parabolic and hyperbolic problems, Navier-Stokes flows, elasticity, Fluid structure interactions, Schwarz's domain decomposition method, eigenvalue problem, residual error indicator, ...
- *A parallel version* using `mpi`.

In (2.11), P_1 refers to the behavior of the continuous functions at the edge of the triangles:

- `P0` piecewise constant,
- `P1` continuous piecewise linear,
- `P2` continuous piecewise quadratic,
- `P3` continuous piecewise cubic,
- `RT0` Raviart-Thomas piecewise constant,
- `RT1` Raviart-Thomas degree 1 piecewise constant
- `BDM1` Brezzi-Douglas-Marini degree 1 piecewise constant
- `RT0Ortho Nedelec` type 1 degree 0 piecewise constant
- `RT1Ortho Nedelec` type 1 degree 1 piecewise constant
- `BDM1Ortho` Brezzi-Douglas-Marini degree 1 piecewise constant
- `P1nc` piecewise linear non-conforming,
- `P1dc` piecewise linear discontinuous,
- `P2dc` piecewise quadratic discontinuous,
- `P2h` quadratic homogene continuous (without P1)
- `P3dc` piecewise cubic discontinuous,

- `P4dc` piecewise quartic discontinuous,
- `P1b` piecewise linear continuous plus bubble,
- `P2b` piecewise quadratic continuous plus bubble.
- Morley Morley finite element
- `HCT` Hsieh-Clough-Tocher C
- 1 finite element
- `P2BR` P2 Bernardi-Raugel finite element
- `P0edge` a finite element constant per edge
- `P1edge` to `P5edge` a finite element polynomial on edge
- ...

`FreeFEM++` provides a wide variety of functions. For more information, please refer to [Hecht, 2012].

III.2. Script for leakage simulation and energy estimation

```
////////////////////////////////////////////////////////////////////
// EIT simulation in a square domain //
//Computation of one source/receiver config. with grounded edges //
////////////////////////////////////////////////////////////////////

string Name="LeakageCurrent";
{
        int DATE = 180418 ;
        int D=2;



////
// Parameters
////

real gamma=1. ; // Conductivity field
real Uimpup=1. ; // Value up of imposed current
real Uimpdown=-1. ; // Value down of imposed current

// Remark: we are required to have that the integral of the imposed current is zero.

real A = D*128.; //diameter of the pipe
real b=400. ;  // test section width (GRD ISO ELEC ISO GRD)

real c=170. ;  // Detector width (ISO ELEC ISO) c < b
real e=(b-c)/2; // Ground layer width
real g=5; //electrodes width

```

```
int Nelec = 64;
int N=100 ; // Number of nodes on whole contour

ofstream file(DATE + "_" + Name + "_Nelec"+Nelec+ "_b"+b+ "_c"+c+"_N"+N+ "D_"+
    D+".txt");

real theta = 2*pi/Nelec;//angle between two electrodes
real[int] Dist(Nelec/2);
real[int] Norm(Nelec/2);
cout << "Angle entre les electrodes : " << theta/pi << "pi RAD."<< endl;

if(2*pi/Nelec <= 2*g/A)
{
        cout << "ERROR : electrodes are touching! " << endl;
}

for (int j=0;j<Nelec/2;j++){
        Dist[j]= sqrt(((A/2)-(A/2)*cos(((j+1)*theta)-2*g/A))^2+((A/2)*sin(((j+1)*theta)
            -2*g/A))^2);
        cout<<"Distance BTWN Electrodes 1 and " << j+2 <<" : " << Dist[j]<<endl;
        }

for (int ii=2;ii<(c)/5;ii++)//Loop over the length of the electrodes
        { real d=5*ii;
//for (int ii=150;ii<c-1;ii++)//Loop over the width of the electrodes for thin ISO
// { real d=ii;
                real f=(b-2*e-d)/2; // isolation (ISO) width

for (int i=0;i<Nelec/2;i++)// boucle over the distance between two electrodes
        { real a=Dist[i];


////
// Geometry and Finite Elements
////

border CGRDleftdown(t=0,1)  {x=e*t;  y=0;}
border CIsoleftdownG(t=0,1)  {x=e+(f/2)*t;   y=0;}
border CIsoleftdownE(t=0,1)  {x=e+f/2+(f/2)*t;  y=0;}
border CElecdown(t=0,1)  {x=e+f+d*t;  y=0;}
border CIsorightdownE(t=0,1)  {x=e+f+d+(f/2)*t; y=0;}
border CIsorightdownG(t=0,1)  {x=e+f+d+f/2+(f/2)*t; y=0;}
border CGRDrightdown(t=0,1)  {x=e+2*f+d+e*t; y=0;}

border CEdgeright(t=0,1)  {x=2*e+2*f+d; y=a*t;}

border CGRDrightup(t=1,0)  {x=e+2*f+d+e*t; y=a;}
border CIsorightupG(t=1,0)  {x=e+f+d+f/2+(f/2)*t; y=a;}
```

```
75  border CIsorightupE(t=1,0)  {x=e+f+d+(f/2)*t; y=a;}
76  border CElecup(t=1,0)   {x=e+f+d*t; y=a;}
77  border CIsoleftupE(t=1,0)  {x=e+f/2+(f/2)*t; y=a;}
78  border CIsoleftupG(t=1,0)  {x=e+(f/2)*t;  y=a;}
79  border CGRDleftup(t=1,0)  {x=e*t;  y=a;}
80
81  border CEdgeleft(t=1,0)  {x=0;  y=a*t;}
82
83  border CGRDISOleftdown(t=0,1)  {x=e;  y=-10*t;}
84
85  // Number of nodes by section of the border to have a uniform mesh
86  int NElec = 3*N*d/(b+a) ;
87  int NGRD = 3*N*e/(b+a) ;
88  int NIso  = N*f/(b+a) ;
89  int Nedge  = N*a/(b+a) ;
90
91  if(NElec <= 5){NElec = 5;};
92  if(NGRD <= 5){NGRD = 5;};
93  if(NIso <= 5){NIso = 5;};
94  if(Nedge <= 5){Nedge = 5;};
95
96
97  /*plot( CGRDleftdown(NGRD)+CIsoleftdownG(NIso/2)+CIsoleftdownE(NIso/2)+CElecdown
        (NElec)+CIsorightdownE(NIso/2)+CIsorightdownG(NIso/2)+CGRDrightdown(NGRD)
98          +CEdgeright(Nedge)
99          +CGRDrightup(NGRD)+CIsorightupG(NIso/2)+CIsorightupE(NIso/2)+CElecup(
                NElec)+CIsoleftupE(NIso/2)+CIsoleftupG(NIso/2)+CGRDleftup(NGRD)
100         +CEdgeleft(Nedge), wait=1,cmm="Domain");
101 */
102
103 mesh Th = buildmesh(
104                     CGRDleftdown(NGRD)+CIsoleftdownG(NIso/2)+CIsoleftdownE(NIso/2)+
                            CElecdown(NElec)+CIsorightdownE(NIso/2)+CIsorightdownG(NIso/2)+
                            CGRDrightdown(NGRD)
105                    +CEdgeright(Nedge)
106                    +CGRDrightup(NGRD)+CIsorightupG(NIso/2)+CIsorightupE(NIso/2)+
                           CElecup(NElec)+CIsoleftupE(NIso/2)+CIsoleftupG(NIso/2)+
                           CGRDleftup(NGRD)
107                    +CEdgeleft(Nedge)
108                        );
109 //plot(Th, wait=1,cmm="Mesh");
110
111 // Finite element space
112 fespace Vh(Th,P2) ;
113 Vh uexp,vtest,jx,jy ; // Define F.E. fields
114
115
116 //////
```

```
117 // Simulation of experiment with IMPOSED CURRENT on CElecup and CElecdown
118 // Dielectric edges
119 //////
120
121 // Colormap for plotting potential maps
122 real[int] colorhsv=[
123                         239./360. , 1. , 0.56,
124                         238./360. , 1. , 1 ,
125                         179./360. , 1. , 1,
126                         59./360. , 1 , 1,
127                         0. , 1 , 1. ,
128                         0. , 1. , 0.5
129                         ];
130
131 int NbIso=50 ;
132
133 solve conductivity1(uexp,vtest,solver=LU) =
134 int2d(Th)( gamma*( dx( uexp)*dx(vtest) + dy(uexp)*dy(vtest) ) )
135 + on(CElecup,uexp=Uimpup)+on(CElecdown,uexp=Uimpdown)
136 + on(CGRDleftdown,uexp=0)+on(CGRDrightdown,uexp=0)
137 + on(CGRDleftup,uexp=0)+on(CGRDrightup,uexp=0);
138
139 // Compute current field j=gamma*grad(uexp)
140 jx=gamma*dx(uexp) ; jy=gamma*dy(uexp) ;
141
142 // Show potential
143 plot(uexp,wait=1,fill=1,cmm="Electric potential uexp",nbiso=NbIso,hsv=colorhsv,value=true);
144
145 plot(uexp,wait=1,cmm="Isolines of electric potential uexp",nbiso=NbIso,hsv=colorhsv,value=
        true);
146
147 plot([jx,jy],wait=0,cmm="Current field\n for a = "+a+" and for d"+d+" with N = "+N+"
        Main: "+ii+"/"+(c-20)/5+" loc: "+i+"/"+Nelec/2 ,hsv=colorhsv,value=true) ;
148
149
150 //////
151 // STORE DATA
152 //////
153
154 //calcul Leakage
155 real Aele = g*d;
156 real Agnd = 2.*pi*e;
157
158 real Jleak = (abs(int1d(Th,CGRDrightup)(jy))+abs(int1d(Th,CIsorightupG)(jy))+abs(int1d(
        Th,CIsoleftupG)(jy))+abs(int1d(Th,CGRDleftup)(jy))
159                 +abs(int1d(Th,CGRDrightdown)(jy))+abs(int1d(Th,CIsorightdownG)(jy))+
                    abs(int1d(Th,CIsoleftdownG)(jy))+abs(int1d(Th,CGRDleftdown)(jy)))/
```

```
                    Agnd;
real Jsensor = (abs(int1d(Th,CIsorightupE)(jy))+abs(int1d(Th,CElecup)(jy))+abs(int1d(Th,
    CIsoleftupE)(jy))
        +abs(int1d(Th,CIsorightdownE)(jy))+abs(int1d(Th,CElecdown)(jy))+abs(int1d(Th,
            CIsoleftdownE)(jy)))/Aele;

real JlonJs = Jleak/Jsensor;

//energy computation
real Stot = a*b;
real Aeele = d*a;

Vh Eregion = 0*(x<(b/2.-d/2.))*(x>(b/2.+d/2.))+1.*(x>(b/2.-d/2.))*(x<(b/2.+d/2.));
real Etot = (int2d(Th)(gamma*(dx(uexp)*dx(uexp)+dy(uexp)*dy(uexp))))/Stot ;
real Eele = (int2d(Th)(Eregion*gamma*(dx(uexp)*dx(uexp)+dy(uexp)*dy(uexp))))/Aeele ;

cout << "Etot : " << Etot << " Eele : " << Eele << endl << endl << endl;

file << f << ","<< a << ","<< JlonJs << ","<< Etot << ","<< Eele <<endl;

//plot(Eregion,wait=1,cmm="Eregion",hsv=colorhsv,value=true) ;

//cout << "Electrode width: " << d << " mm."<<endl<<endl;
cout << "Distance BTWN Electrodes: " << a << " mm."<<endl;
}
file << endl;

}
cout <<endl<< DATE + "_" + Name + "_Nelec"+Nelec+ "_b"+b+ "_c"+c+"_N"+N+ ".
    txt Saved OK."<<endl;
}
```

III.3. Script for generalisation with the form factor

```
//////////////////////////////////////////////////////////////////
// EIT simulation in a square domain //
//Computation of one source/receiver config. with grounded edges //
//////////////////////////////////////////////////////////////////

string Name="FormFactor";
{
        int DATE = 180420 ;



////
// Parameters
```

```
////

real gamma=1. ; // Conductivity field
real Uimpup=1. ; // Value up of imposed current
real Uimpdown=-1. ; // Value down of imposed current

// Remark: we are required to have that the integral of the imposed current is zero.

real A = 100.; //pipe diameter
real b=600. ;  // test section width (GRD ISO ELEC ISO GRD)
real d=10;
real c=100. ;  // Detector width (ISO ELEC ISO) c < b
real e=(b-c)/2; // Ground layer width
real f=(b-2*e-d)/2; // isolation width
real g=5; //electrodes width

int Nelec = 64;

int N=100 ; // Number of nodes on whole contour

//for (int iii=1;iii<3;iii++)//Loop over the electrode widths
        { d= 84;
        f=(b-2*e-d)/2; // isolation width

ofstream file(DATE + "_" + Name + "_b"+b+ "_d"+d+"_Nconstant.txt");

real theta = 2*pi/Nelec;//angle between two electrodes
real[int] Dist(Nelec/2);
real[int] Norm(Nelec/2);
cout << "Angle entre les electrodes : " << theta/pi << "pi RAD."<< endl;

if(2*pi/Nelec <= 2*g/A)
{
        cout << "ERROR : electrodes are touching! " << endl;
}

for (int ii=1;ii<61;ii++)//Loop over the form factor
        {
A = ii*0.05*c;

real F = A/c;

for (int j=0;j<Nelec/2;j++){
        Dist[j]= sqrt(((A/2)-(A/2)*cos(((j+1)*theta)-2*g/A))^2+((A/2)*sin(((j+1)*theta)
            -2*g/A))^2);
        cout<<"Distance BTWN Electrodes 1 and " << j+2 <<" : " << Dist[j]<<endl;
        }

```

```
60  for (int i=0;i<Nelec/2;i++)// boucle sur la distance entre les electrodes
61          { real a=Dist[i];
62
63
64  ////
65  // Geometry and Finite Elements
66  ////
67
68  border CGRDleftdown(t=0,1)  {x=e*t;  y=0;}
69  border CIsoleftdownG(t=0,1)  {x=e+(f/2)*t;   y=0;}
70  border CIsoleftdownE(t=0,1)  {x=e+f/2+(f/2)*t;  y=0;}
71  border CElecdown(t=0,1)  {x=e+f+d*t;  y=0;}
72  border CIsorightdownE(t=0,1)  {x=e+f+d+(f/2)*t; y=0;}
73  border CIsorightdownG(t=0,1)  {x=e+f+d+f/2+(f/2)*t; y=0;}
74  border CGRDrightdown(t=0,1)  {x=e+2*f+d+e*t; y=0;}
75
76  border CEdgeright(t=0,1)  {x=2*e+2*f+d; y=a*t;}
77
78  border CGRDrightup(t=1,0)  {x=e+2*f+d+e*t; y=a;}
79  border CIsorightupG(t=1,0)  {x=e+f+d+f/2+(f/2)*t; y=a;}
80  border CIsorightupE(t=1,0)  {x=e+f+d+(f/2)*t; y=a;}
81  border CElecup(t=1,0)   {x=e+f+d*t; y=a;}
82  border CIsoleftupE(t=1,0)  {x=e+f/2+(f/2)*t; y=a;}
83  border CIsoleftupG(t=1,0)  {x=e+(f/2)*t;  y=a;}
84  border CGRDleftup(t=1,0)  {x=e*t;  y=a;}
85
86  border CEdgeleft(t=1,0)  {x=0;  y=a*t;}
87
88  border CGRDISOleftdown(t=0,1)  {x=e;  y=-10*t;}
89
90  // Number of nodes by section of the border to have a uniform mesh
91  int NElec = 3.*d/10 ;
92  int NGRD = 3.*e/10 ;
93  int NIso  = f/10 ;
94  int Nedge  = a/10 ;
95
96  if(NElec <= 5){NElec = 5;};
97  if(NGRD <= 5){NGRD = 5;};
98  if(NIso <= 5){NIso = 5;};
99  if(Nedge <= 5){Nedge = 5;};
100
101 /*plot( CGRDleftdown(NGRD)+CIsoleftdownG(NIso/2)+CIsoleftdownE(NIso/2)+CElecdown
        (NElec)+CIsorightdownE(NIso/2)+CIsorightdownG(NIso/2)+CGRDrightdown(NGRD)
102         +CEdgeright(Nedge)
103         +CGRDrightup(NGRD)+CIsorightupG(NIso/2)+CIsorightupE(NIso/2)+CElecup(
                NElec)+CIsoleftupE(NIso/2)+CIsoleftupG(NIso/2)+CGRDleftup(NGRD)
104         +CEdgeleft(Nedge), wait=1,cmm="Domain");
105 */
```

```
106
107 mesh Th = buildmesh(
108                       CGRDleftdown(NGRD)+CIsoleftdownG(NIso/2)+CIsoleftdownE(NIso/2)+
                              CElecdown(NElec)+CIsorightdownE(NIso/2)+CIsorightdownG(NIso/2)+
                              CGRDrightdown(NGRD)
109                     +CEdgeright(Nedge)
110                     +CGRDrightup(NGRD)+CIsorightupG(NIso/2)+CIsorightupE(NIso/2)+
                            CElecup(NElec)+CIsoleftupE(NIso/2)+CIsoleftupG(NIso/2)+
                            CGRDleftup(NGRD)
111                     +CEdgeleft(Nedge)
112                         );
113
114 //plot(Th, wait=1,cmm="Mesh");
115
116 // Finite element space
117 fespace Vh(Th,P2) ;
118 Vh uexp,vtest,jx,jy ; // Define F.E. fields
119
120
121 //////
122 // Simulation of experiment with IMPOSED CURRENT on CElecup and CElecdown
123 // Dielectric edges
124 //////
125
126 // Colormap for plotting potential maps
127 real[int] colorhsv=[
128                         239./360. , 1. , 0.56,
129                         238./360. , 1. , 1 ,
130                         179./360. , 1. , 1,
131                         59./360. , 1 , 1,
132                         0. , 1 , 1. ,
133                         0. , 1. , 0.5
134                         ];
135
136 int NbIso=50 ;
137
138 solve conductivity1(uexp,vtest,solver=LU) =
139 int2d(Th)( gamma*( dx( uexp)*dx(vtest) + dy(uexp)*dy(vtest) ) )
140 + on(CElecup,uexp=Uimpup)+on(CElecdown,uexp=Uimpdown)
141 + on(CGRDleftdown,uexp=0)+on(CGRDrightdown,uexp=0)
142 + on(CGRDleftup,uexp=0)+on(CGRDrightup,uexp=0);
143
144 // Compute current field j=gamma*grad(uexp)
145 jx=gamma*dx(uexp) ; jy=gamma*dy(uexp) ;
146
147 // Show potential
148 //plot(uexp,wait=1,fill=1,cmm="Electric potential uexp",nbiso=NbIso,hsv=colorhsv,value=
        true);
```

```
149
150 //plot(uexp,wait=1,cmm="Isolines of electric potential uexp",nbiso=NbIso,hsv=colorhsv,value
        =true);
151
152 plot([jx,jy],wait=0,cmm="Current field\n for F = "+F+" and for d"+d+" with N = "+N+"
        Main: "+ii+"/"+(c-20)/5+" loc: "+i+"/"+Nelec/2 ,hsv=colorhsv,value=true) ;
153
154
155 //////
156 // STORE DATA
157 //////
158
159 //calcul Leakage
160 real Aele = g*d;
161 real Agnd = 2.*pi*e;
162
163 real Jleak = (abs(int1d(Th,CGRDrightup)(jy))+abs(int1d(Th,CIsorightupG)(jy))+abs(int1d(
        Th,CIsoleftupG)(jy))+abs(int1d(Th,CGRDleftup)(jy))
164                     +abs(int1d(Th,CGRDrightdown)(jy))+abs(int1d(Th,CIsorightdownG)(jy))+
                            abs(int1d(Th,CIsoleftdownG)(jy))+abs(int1d(Th,CGRDleftdown)(jy))))/
                            Agnd;
165 real Jsensor = (abs(int1d(Th,CIsorightupE)(jy))+abs(int1d(Th,CElecup)(jy))+abs(int1d(Th,
        CIsoleftupE)(jy))
166             +abs(int1d(Th,CIsorightdownE)(jy))+abs(int1d(Th,CElecdown)(jy))+abs(int1d(Th,
                    CIsoleftdownE)(jy)))/Aele;
167
168 real JlonJs = Jleak/Jsensor;
169
170 //Calcul energie
171 real Stot = a*b;
172 real Aeele = d*a;
173
174 Vh Eregion = 0*(x<(b/2.-d/2.))*(x>(b/2.+d/2.))+1.*(x>(b/2.-d/2.))*(x<(b/2.+d/2.));
175 real Etot = (int2d(Th)(gamma*(dx(uexp)*dx(uexp)+dy(uexp)*dy(uexp))))/Stot ;
176 real Eele = (int2d(Th)(Eregion*gamma*(dx(uexp)*dx(uexp)+dy(uexp)*dy(uexp))))/Aeele ;
177
178 cout << "Etot : " << Etot << " Eele : " << Eele << endl << endl << endl;
179
180 file << F << ","<< JlonJs << ","<< Etot << ","<< Eele <<endl;
181
182 //plot(Eregion,wait=1,cmm="Eregion",hsv=colorhsv,value=true) ;
183
184 //cout << "Electrode width: " << d << " mm."<<endl<<endl;
185 cout << "Distance BTWN Electrodes: " << a << " mm."<<endl;
186
187 }
188 file << endl;
189 }
```

```
cout <<endl<< DATE + "_" + Name + "_Nelec"+Nelec+ "_b"+b+ "_c"+c+"_N"+N+ "
    F02-3.txt Saved OK."<<endl;
}}
```

III.4. Script to estimate the sensitivity map of a single EIT measurement

```
//////////////////////////////////////////////////////////////////////
// EIT simulation in a circular domain //
// Computation of sensitivity map for one source/receiver config. //
// which is a four electrodes model //
//////////////////////////////////////////////////////////////////////


////
//// MAP FOR 4 ELECTRODES
////

int Nelec = 4;

// Colormap for plotting potential maps

real[int] colorhsv=[
                        239./360. , 1. , 0.56,
                        238./360. , 1. , 1 ,
                        179./360. , 1. , 1,
                        59./360. , 1 , 1,
                        0. , 1 , 1. ,
                        0. , 1. , 0.5
                        ];

int NbIso=40 ;


////
// Parameters
////

real gamma=1. ; // Conductivity field

real Uimp1=1. ; // Value 1 of imposed current
real Uimp2=-1. ; // Value 2 of imposed current
// Remark: we are required to have that the integral of the imposed current is zero.

real DistBtwnElec = 2*pi/Nelec;
real ElecSize=pi/20. ; // Angular size of the eletrodes
```

```
40
41 int N=100*pi ; // Number of nodes on whole contour
42
43
44 ////
45 // Geometry and Finite Elements
46 ////
47
48 // The domain is circular.
49 // Electrodes are defined as portion of the boundary of angular size given by the parameter
       ElecSize
50 // Electrodes are placed arbitrarily on the boundary
51
52 border CElec1(t=DistBtwnElec+ElecSize/2,DistBtwnElec-ElecSize/2){x=cos(t); y=sin(t);}
53 border C1(t=DistBtwnElec-ElecSize/2,ElecSize/2){x=cos(t); y=sin(t);}
54
55 border CElec2(t=ElecSize/2,-ElecSize/2){x=cos(t); y=sin(t);}
56 border C2(t=-ElecSize/2,-DistBtwnElec+ElecSize/2){x=cos(t); y=sin(t);}
57
58 border CElec3(t=-DistBtwnElec+ElecSize/2,-DistBtwnElec-ElecSize/2){x=cos(t); y=sin(t)
       ;}
59 border C3(t=-DistBtwnElec-ElecSize/2,-2*DistBtwnElec+ElecSize/2){x=cos(t); y=sin(t);}
60
61 border CElec4(t=2*DistBtwnElec+ElecSize/2,2*DistBtwnElec-ElecSize/2){x=cos(t); y=sin(t)
       ;}
62 border C4(t=2*DistBtwnElec-ElecSize/2,DistBtwnElec+ElecSize/2){x=cos(t); y=sin(t);}
63
64 // Number of nodes by section of the border to have a uniform mesh
65 int NonElec=N*ElecSize/(2.*pi) ;
66 int NonBorder=N*(DistBtwnElec-ElecSize)/(2.*pi);
67
68 // Show total contour
69 //plot(CElec1(NonElec)+C1(NonBorder)+CElec2(NonElec)+C2(NonBorder)+CElec3(
       NonElec)+C3(NonBorder)+CElec4(NonElec)+C4(NonBorder),wait=1,cmm="Domain",ps
       ="test.ps") ;
70
71 // Build the mesh
72 mesh Th = buildmesh(CElec1(-NonElec)+C1(-NonBorder)+CElec2(-NonElec)+C2(-
       NonBorder)+CElec3(-NonElec)+C3(-NonBorder)+CElec4(-NonElec)+C4(-NonBorder
       ));
73 //plot(Th,wait=1,cmm="Mesh") ;
74
75 // Finite element space
76 fespace Vh(Th,P1) ;
77 Vh vtest ; // Define F.E. fields
78 Vh Sensitivity ;
79
80
```

```
//////
// Simulation of experiment with IMPOSED P0TENTIAL on sensor 1 and 2
//////
Vh phiexc12, phimeas1234 ;
// Potential field for excitation electrodes (solution of Laplace problem)

solve potentialExc12(phiexc12,vtest,solver=LU) =
int2d(Th)( dx(phiexc12)*dx(vtest) + dy(phiexc12)*dy(vtest) )
+ on(CElec1,phiexc12=Uimp1)+on(CElec2,phiexc12=Uimp2);

solve potentialMeas1234(phimeas1234,vtest,solver=LU) =
int2d(Th)( dx(phimeas1234)*dx(vtest) + dy(phimeas1234)*dy(vtest) )
+ on(CElec3,phimeas1234=Uimp1)+on(CElec4,phimeas1234=Uimp2);

Sensitivity = abs(dx(phiexc12)*dx(phimeas1234) + dy(phiexc12)*dy(phimeas1234)) ;

plot(Sensitivity,wait=1,fill=1,cmm="Log sensitivity map for full-scan excitation/measurement
    config for elecsize = pi/ "+pi*1/ElecSize+".",nbiso=NbIso,hsv=colorhsv,value=true, ps="
    sensivitymap4sensors"+pi*1/ElecSize+".ps");
```

III.5. Script for the hand reconstruction of the sensitivity map

```
////////////////////////////////////////////////////////////////////
// EIT simulation in a circular domain //
// Hand estimation of the sensitivity map for //
// a four electrodes model //
////////////////////////////////////////////////////////////////////

string Name="HandReconstruction";
{

int DATE = 181212 ;

// Colormap for plotting potential maps
real[int] colorhsv=[
                    239./360. , 1. , 0.56,
                    238./360. , 1. , 1 ,
                    179./360. , 1. , 1,
                    59./360. , 1 , 1,
                    0. , 1 , 1. ,
                    0. , 1. , 0.5
                    ];

int X = 30 ; //Nombre de pas en x
int Y = X ; //Nombre de pas en Y
int Y1=0; int Y2=X;//diviser le fichier output (default : Y1 = 0, Y2 = X)
```

```
25 real B = .05; //taille de la bulle
26 int n=50 ; int N=n*pi; // Number of nodes on whole contour
27
28 real[int] Coody(Y+1) ;
29 real[int] Coodx(X+1) ;
30
31 real[int] Coodybubble(Y+1) ;
32 real[int] Coodxbubble(X+1) ;
33
34 real refVmeas1 ;
35 real refVmeas2 ;
36 real Vmeas1 ;
37 real Vmeas2 ;
38 real deltaV ;
39 real refdeltaV ;
40 real deldeltaV ;
41 real Sensitivity ;
42
43 int NbIso=30 ;
44 ofstream file(DATE + "_" + Name + "_X"+X+"_N"+n+"pi_B"+B+"Y"+Y1+"-"+Y2+".txt
       ");
45
46
47 ////
48 // Parameters
49 ////
50
51 real Uimp1=1. ; // Value 1 of imposed current
52 real Uimp2=-1. ; // Value 2 of imposed current
53 // Remark: we are required to have that the integral of the imposed current is zero.
54
55 real PosElecExc1=pi/3. ; // Position excitation electrode 1
56 real PosElecMeas1=3.*pi/2. ; // Position measurement electrode 1
57 real ElecSize=pi/20. ; // Angular size of the eletrodes
58 real DistElec1=pi/1.5 ; // Distance between excitation electrodes
59 real DistElec2=pi/5 ; // Distance between measurement electrodes
60
61
62 ////
63 // Geometry and Finite Elements
64 ////
65
66 // The domain is circular.
67 // Electrodes are defined as portion of the boundary of angular size given by the parameter
       ElecSize
68 // Electrodes are placed arbitrarily on the boundary
69 border C1(t=0,PosElecExc1){x=cos(t); y=sin(t);}
70 border CElecEx1(t=PosElecExc1,PosElecExc1+ElecSize){x=cos(t); y=sin(t);}
```

```
71  border C2(t=PosElecExc1+ElecSize,PosElecExc1+ElecSize+DistElec1){x=cos(t); y=sin(t);}
72  border CElecMeas1(t=PosElecExc1+ElecSize+DistElec1,PosElecExc1+2.*ElecSize+DistElec1)
        {x=cos(t); y=sin(t);}
73  border C3(t=PosElecExc1+2.*ElecSize+DistElec1,PosElecMeas1){x=cos(t); y=sin(t);}
74  border CElecEx2(t=PosElecMeas1,PosElecMeas1+ElecSize){x=cos(t); y=sin(t);}
75  border C4(t=PosElecMeas1+ElecSize,PosElecMeas1+ElecSize+DistElec2){x=cos(t); y=sin(t);}

76  border CElecMeas2(t=PosElecMeas1+ElecSize+DistElec2,PosElecMeas1+2*ElecSize+
        DistElec2){x=cos(t); y=sin(t);}
77  border C5(t=PosElecMeas1+2*ElecSize+DistElec2,2.*pi){x=cos(t); y=sin(t);}
78
79  // Number of nodes by section of the border to have a uniform mesh
80  int NElec=N*ElecSize/(2.*pi) ;
81  int N1=N*PosElecExc1/(2.*pi) ; int N2=N*DistElec1/(2.*pi) ; int N3=N*(PosElecMeas1-(
        PosElecExc1+2.*ElecSize+DistElec1))/(2.*pi) ;
82  int N4=N*DistElec2/(2.*pi) ; int N5=N*(2.*pi-(PosElecMeas1+2*ElecSize+DistElec2))/(2.*
        pi) ;
83
84  // Show total contour
85  //plot(C1(N1)+CElecEx1(NElec)+C2(N2)+CElecEx2(NElec)+C3(N3)+CElecMeas1(NElec)+
        C4(N4)+CElecMeas2(NElec)+C5(N5),wait=1,cmm="Domain") ;
86
87  // Build the mesh
88  mesh Th = buildmesh( C1(N1)+CElecEx1(NElec)+C2(N2)+CElecEx2(NElec)+C3(N3)+
        CElecMeas1(NElec)+C4(N4)+CElecMeas2(NElec)+C5(N5) );
89  //plot(Th,wait=1,cmm="Mesh") ;
90
91  //Reference voltage
92  // Finite element space
93  fespace Vh(Th,P2) ;
94  Vh uexp,vtest,jx,jy ; // Define F.E. fields
95  Vh phiexc,phimeas ;
96
97  solve conductivity1(uexp,vtest,solver=LU) =
98  int2d(Th)( 100*( dx(uexp)*dx(vtest) + dy(uexp)*dy(vtest) ) )
99  + on(CElecEx1,uexp=Uimp1)+on(CElecEx2,uexp=Uimp2);
100
101 refVmeas1 = int1d(Th,CElecMeas1)(uexp);
102 refVmeas2 = int1d(Th,CElecMeas2)(uexp);
103 refdeltaV = refVmeas1 - refVmeas2;
104
105
106 //////
107 // X and Y coordinates of the bubble
108 //////
109
110 for (int i=Y1;i<=Y2;i++){
111         for (int j=0;j<=X;j++){
```

```
112                     Coody[i] = 1.-2.*i/Y ;
113                     Coodx[j] = -1.+2.*j/X ;
114                             real r = sqrt(Coody[i]^2+Coodx[j]^2);
115                             if(r<=1.)
116                             { Coodybubble[i] = Coody[i] ;
117                                     Coodxbubble[j] = Coodx[j] ;
118
119 // Finite element space
120 Vh uexp,vtest,jx,jy ; // Define F.E. fields
121 Vh phiexc,phimeas ;
122
123 Vh gammaBubble = 100-99.99*(x<(Coodxbubble[j]+B/2.))*(x>(Coodxbubble[j]-B/2.))*(y
        <(Coodybubble[i]+B/2.))*(y>(Coodybubble[i]-B/2.))*((Coodxbubble[j])^2+(
        Coodybubble[i])^2<1);
124 Vh areaBubble = 1*(x<(Coodxbubble[j]+B/2.))*(x>(Coodxbubble[j]-B/2.))*(y<(
        Coodybubble[i]+B/2.))*(y>(Coodybubble[i]-B/2.))*((Coodxbubble[j])^2+(Coodybubble[
        i])^2<1);
125
126 //cout << int2d(Th)(areaBubble) << endl;
127 //plot(areaBubble,wait=1,hsv=colorhsv,value=true) ;
128
129 //for (int iii=0;iii<1;iii++) {
130 //mesh aTh = adaptmesh(Th,gammaBubble);
131 //areaBubble = 1*(x<(Coodxbubble[j]+B/2.))*(x>(Coodxbubble[j]-B/2.))*(y<(
        Coodybubble[i]+B/2.))*(y>(Coodybubble[i]-B/2.))*((Coodxbubble[j])^2+(Coodybubble[
        i])^2<1);
132
133 //plot(areaBubble,wait=1,hsv=colorhsv,value=true) ;
134 //plot(aTh,gammaBubble,wait=1);
135
136 //cout << "yolo" << iii << endl;
137 //}
138
139
140 //////
141 // Simulation of experiment with IMPOSED CURRENT on CElecEx1 and CElecEx2
142 //////
143
144 solve conductivity1(uexp,vtest,solver=LU) =
145 int2d(Th)( gammaBubble*( dx(uexp)*dx(vtest) + dy(uexp)*dy(vtest) ) )
146 + on(CElecEx1,uexp=Uimp1)+on(CElecEx2,uexp=Uimp2);
147
148 //plot(uexp,wait=0,fill=1,cmm="Electric potential uexp",nbiso=NbIso,hsv=colorhsv,value=
        true);
149
150 Vmeas1 = int1d(Th,CElecMeas1)(uexp);
151 Vmeas2 = int1d(Th,CElecMeas2)(uexp);
152 deltaV = abs(Vmeas1 - Vmeas2);
```

```
153 deldeltaV = abs(deltaV - refdeltaV);
154
155 Sensitivity = deldeltaV * int2d(Th)(areaBubble)*100; //multiplied by the area of the region
        with deltaSigma different from zero, multiplied with 1/deltaSigma
156
157 file << Coodxbubble[j] << ","<< Coodybubble[i] <<"," << Sensitivity << endl;
158
159 /*
160 // Compute current field j=gamma*grad(uexp)
161 jx=gamma*dx(uexp) ; jy=gamma*dy(uexp) ;
162
163 // Show potential
164 plot(uexp,wait=1,cmm="Isolines of electric potential uexp",nbiso=NbIso,hsv=colorhsv,value=
        true);
165 //plot([jx,jy],wait=1,cmm="Current field",hsv=colorhsv,value=true) ;
166 */
167
168 }//condition within the domain
169
170 }//Loop over the x-coordinate of the bubble
171
172 cout<< "ligne from Y1 " << Y1 << " : " << i <<"/"<<Y2<<endl;
173
174 }//Loop over the y-coordinate of the bubble
175
176 //}
177 //}
178 //cout << DATE + "_" + Name + "_X"+X+"_N"+n+"pi_B"+B+"Y"+Y1+"-"+Y2+".txt
        =====> SAVED!\n" << endl;
179 }
```

III.6. Script for 3D simulations

```
1
2 ////////////////////////////////////////////////////////////////////////
3 // 3D EIT simulation in a circular domain //
4 // Computation of sensitivity kernel for one source/receiver configuration //
5 // which is a four electrodes model as in Kotre's paper //
6 ////////////////////////////////////////////////////////////////////////
7
8 load "msh3"
9 load "tetgen"
10 load "medit"
11
12         int DATE = 180403 ;
13
```

```
14 // Remark: we are required to have that the integral of the imposed current is zero.
15 real A = 128.; //Diameter of the pipe
16 real b=400. ;  // test section width (GRD ISO ELEC ISO GRD)
17
18 real c=170. ;  // Detector width (ISO ELEC ISO) c < b
19 real d=100. ;  // electrods lenght (ELEC) d < c < b
20 real e=(b-c)/2; // Ground layer width
21 real f=(b-2*e-d)/2; // isolation width
22 real g=5; //electrodes width
23
24 load "msh3"// buildlayer
25 load "medit"// buildlayer
26
27
28 ////
29 //// MAP FOR 4 ELECTRODES
30 ////
31
32 int Nelec = 4;
33
34 // Colormap for plotting potential maps
35 real[int] colorhsv=[
36                         239./360. , 1. , 0.56,
37                         238./360. , 1. , 1 ,
38                         179./360. , 1. , 1,
39                         59./360. , 1 , 1,
40                         0. , 1 , 1. ,
41                         0. , 1. , 0.5
42                         ];
43
44 int NbIso=40 ;
45
46
47 ////
48 // Parameters
49 ////
50
51 real gamma=1. ; // Conductivity field
52
53 real Uimp1=1. ; // Value 1 of imposed current
54 real Uimp2=-1. ; // Value 2 of imposed current
55 // Remark: we are required to have that the integral of the imposed current is zero.
56
57 real DistBtwnElec = 2*pi/Nelec;
58 real ElecSize=pi/20. ; // Angular size of the eletrodes
59
60 int N=20*pi ; // Number of nodes on whole contour
61 int Nz=15 ; // Number of Layers in z direction
```

```
62
63 int NElec = 4;
64
65 //int NElec = Nz*d/b ;
66 int NGRD = Nz*e/b ;
67 int NIso  = Nz*f/b ;
68
69
70 ////
71 // Geometry and Finite Elements
72 ////
73
74 // The domain is circular.
75 // Electrodes are defined as portion of the boundary of angular size given by the parameter
       ElecSize
76 // Electrodes are placed arbitrarily on the boundary
77 border CElec1(t=DistBtwnElec+ElecSize/2,DistBtwnElec-ElecSize/2){x=A*cos(t); y=A*sin(
       t);label=1;}
78 border C1(t=DistBtwnElec-ElecSize/2,ElecSize/2){x=A*cos(t); y=A*sin(t);label=11;}
79
80 border CElec2(t=ElecSize/2,-ElecSize/2){x=A*cos(t); y=A*sin(t);label=2;}
81 border C2(t=-ElecSize/2,-DistBtwnElec+ElecSize/2){x=A*cos(t); y=A*sin(t);label=21;}
82
83 border CElec3(t=-DistBtwnElec+ElecSize/2,-DistBtwnElec-ElecSize/2){x=A*cos(t); y=A*
       sin(t);label=3;}
84 border C3(t=-DistBtwnElec-ElecSize/2,-2*DistBtwnElec+ElecSize/2){x=A*cos(t); y=A*
       sin(t);label=31;}
85
86 border CElec4(t=2*DistBtwnElec+ElecSize/2,2*DistBtwnElec-ElecSize/2){x=A*cos(t); y=A*
       sin(t);label=4;}
87 border C4(t=2*DistBtwnElec-ElecSize/2,DistBtwnElec+ElecSize/2){x=A*cos(t); y=A*sin(t);
       label=41;}
88
89 // Number of nodes by section of the border to have a uniform mesh
90 int NonElec=N*ElecSize/(2.*pi) ;
91 int NonBorder=N*(DistBtwnElec-ElecSize)/(2.*pi);
92
93 // Show total contour
94 //plot(CElec1(NonElec)+C1(NonBorder)+CElec2(NonElec)+C2(NonBorder)+CElec3(
       NonElec)+C3(NonBorder)+CElec4(NonElec)+C4(NonBorder),wait=1,cmm="Domain",ps
       ="test.ps") ;
95
96 // Build the mesh
97 mesh Elec = buildmesh(CElec1(-NonElec)+C1(-NonBorder)+CElec2(-NonElec)+C2(-
       NonBorder)+CElec3(-NonElec)+C3(-NonBorder)+CElec4(-NonElec)+C4(-NonBorder
       ));
98 //plot(Elec,wait=1,cmm="Mesh") ;
99
```

```
100 // Build ELEC
101 int[int] rupelec=[0,0], rdownelec=[0,0], rmidelec=[1,10 , 11,5, 2,20 ,21,5 , 3,30 , 31,5 , 4,40 ,
        41,5];
102 real zminelec= -d/2;
103 real zmaxelec= d/2;
104
105 mesh3 Thelec=buildlayers(Elec,NElec,
106   coef= 1.,
107   zbound=[zminelec,zmaxelec],
108   labelmid=rmidelec,
109   reffaceup = rupelec,
110   reffacelow = rdownelec);
111
112 // Build ISOLATION
113 int[int] rupiso=[0,0], rdowniso=[0,0], rmidiso=[1,6 , 11,6, 2,6 ,21,6 , 3,6 , 31,6 , 4,6 , 41,6];
114 real zminisoup= d/2;
115 real zmaxisoup= d/2+f;
116
117 mesh3 Thisoup=buildlayers(Elec,NIso,
118   coef= 1.,
119   zbound=[zminisoup,zmaxisoup],
120   labelmid=rmidiso,
121   reffaceup = rupiso,
122   reffacelow = rdowniso);
123
124 real zminisodown= -d/2-f;
125 real zmaxisodown= -d/2;
126
127 mesh3 Thisodown=buildlayers(Elec,NIso,
128   coef= 1.,
129   zbound=[zminisodown,zmaxisodown],
130   labelmid=rmidiso,
131   reffaceup = rupiso,
132   reffacelow = rdowniso);
133
134 // Build GROUND
135
136 int[int] rupgnd=[0,0], rdowngnd=[0,0], rmidgnd=[1,7 , 11,7 , 2,7 ,21,7 , 3,7 , 31,7 , 4,7 , 41,7];
137 real zmingndup= d/2+f;
138 real zmaxgndup= d/2+f+e;
139
140 mesh3 Thgndup=buildlayers(Elec,NGRD,
141   coef= 1.,
142   zbound=[zmingndup,zmaxgndup],
143   labelmid=rmidgnd,
144   reffaceup = rupgnd,
145   reffacelow = rdowngnd);
146
```

```
147 real zmingnddown= -d/2-f-e;
148 real zmaxgnddown= -d/2-f;
149
150 mesh3 Thgnddown=buildlayers(Elec,NGRD,
151   coef= 1.,
152   zbound=[zmingnddown,zmaxgnddown],
153   labelmid=rmidgnd,
154   reffaceup = rupgnd,
155   reffacelow = rdowngnd);
156
157 mesh3 Th = Thelec + Thisoup + Thisodown + Thgndup + Thgnddown;
158
159 // medit("Cyl",Th,wait=1);
160 // FFCS: testing 3d plots
161 //plot(Th,cmm="Test section, 4 electrodes");
162
163 // Finite element space
164 fespace Vh(Th,P13d) ;
165 Vh uexp, vtest, jx, jy, jz ;
166
167
168 //////
169 // Simulation of experiment with IMPOSED POTENTIAL on CElecEx1 and CElecEx2
170 //////
171 solve conductivity1(uexp,vtest,solver=LU) =
172         int3d(Th)( gamma*(dx(uexp)*dx(vtest) + dy(uexp)*dy(vtest)+ dz(uexp)*dz(vtest) ) )
173         +on(10,uexp=Uimp1)+on(20,uexp=Uimp2)
174         +on(7,uexp=0);
175
176 // Compute current field j=gamma*grad(uexp)
177 int nn=100;
178 jx=nn*gamma*dx(uexp) ; jy=nn*gamma*dy(uexp) ; jz=nn*gamma*dz(uexp) ;
179
180 plot(uexp,wait=1,fill=1,cmm="Electric potential uexp",nbiso=NbIso,hsv=colorhsv,value=true);
181 plot(uexp,wait=1,cmm="Isolines of electric potential uexp",nbiso=NbIso,hsv=colorhsv,value=
      true);
182 plot([jx,jy,jz],wait=1,cmm="Current field",hsv=colorhsv,value=true) ;
183
184
185 //////
186 // Computation of sensitivity map as in [Kotre, 1989] and [Breckon & Pidcock, 1987] papers.
187 //////
188
189 Vh phiexc, phimeas ;
190 Vh Sensitivity ;
191
```

```
192 // Potential field for excitation electrodes (solution of Laplace problem)
193 solve potentialExc(phiexc,vtest,solver=LU) =
194         int3d(Th)( dx(phiexc)*dx(vtest) + dy(phiexc)*dy(vtest) + dz(phiexc)*dz(vtest))
195         +on(10,phiexc=Uimp1)+on(20,phiexc=Uimp2)
196 // +on(7,phiexc=0)
197                 ;
198
199 // Potential field for measurement electrodes (solution of Laplace problem)
200 solve potentialMeas(phimeas,vtest,solver=LU) =
201         int3d(Th)( dx(phimeas)*dx(vtest) + dy(phimeas)*dy(vtest) + dz(phimeas)*dz(vtest))
202         +on(30,phimeas=Uimp1)+on(40,phimeas=Uimp2)
203 // +on(7,phimeas=0)
204                 ;
205
206 // Compute sensitivity
207 Sensitivity = (abs(dx(phiexc)*dx(phimeas) + dy(phiexc)*dy(phimeas)+ dz(phiexc)*dz(
        phimeas))) ;
208 //Sensitivity = dx(phiexc)*dx(phimeas) + dy(phiexc)*dy(phimeas) ;
209 //plot(Sensitivity,wait=1,fill=1,cmm="Sensitivity for excitation/measurement config.",nbiso
        =2*NbIso,hsv=colorhsv,value=true);
210
211 //Vh LogSensitivity = log(abs(dx(phiexc)*dx(phimeas) + dy(phiexc)*dy(phimeas)+ dz(phiexc
        )*dz(phimeas))) ;
212 //plot(LogSensitivity,wait=1,fill=1,cmm="Log sensitivity for excitation/measurement config.",
        nbiso=2*NbIso,hsv=colorhsv,value=true);
213
214 medit("Cyl", Th, Sensitivity,wait=1,save=DATE+"Sensititivy_EIT_4elec3D.solb");
```

IV

MATLAB scripts

Contents

IV.1 Computation of the ONE-SHOT method excitation pattern coefficients . . 275
IV.2 Script for image reconstruction inputs 276
IV.3 Computation of the COLTRANE method sign matrix 278

IV.1. Computation of the ONE-SHOT method excitation pattern coefficients

The validation of (3.38) is made with the following MATLAB script:

```
clear all;
ne = 16;

for k=1:1:ne
   for i=1:ne-1
      lmin = (k-1)*ne-k*(k-1)/2+1;
      lmax = k*ne-k*(k+1)/2;
      if i>=k&&lmin<=lmax
      V(k,i) = lmin + i - k;
      elseif i<=k
      V(k,i) = -V(i,k-1);
      else
      V(k,i) = 0; %error
      end
   end
end
```

With $n_e = 16$, the code returns the following matrix

$$\texttt{(k,i)} = \begin{pmatrix}
1 & 2 & 3 & 4 & 5 & 6 & 7 & 8 & 9 & 10 & 11 & 12 & 13 & 14 & 15 \\
-1 & 16 & 17 & 18 & 19 & 20 & 21 & 22 & 23 & 24 & 25 & 26 & 27 & 28 & 29 \\
-2 & -16 & 30 & 31 & 32 & 33 & 34 & 35 & 36 & 37 & 38 & 39 & 40 & 41 & 42 \\
-3 & -17 & -30 & 43 & 44 & 45 & 46 & 47 & 48 & 49 & 50 & 51 & 52 & 53 & 54 \\
-4 & -18 & -31 & -43 & 55 & 56 & 57 & 58 & 59 & 60 & 61 & 62 & 63 & 64 & 65 \\
-5 & -19 & -32 & -44 & -55 & 66 & 67 & 68 & 69 & 70 & 71 & 72 & 73 & 74 & 75 \\
-6 & -20 & -33 & -45 & -56 & -66 & 76 & 77 & 78 & 79 & 80 & 81 & 82 & 83 & 84 \\
-7 & -21 & -34 & -46 & -57 & -67 & -76 & 85 & 86 & 87 & 88 & 89 & 90 & 91 & 92 \\
-8 & -22 & -35 & -47 & -58 & -68 & -77 & -85 & 93 & 94 & 95 & 96 & 97 & 98 & 99 \\
-9 & -23 & -36 & -48 & -59 & -69 & -78 & -86 & -93 & 100 & 101 & 102 & 103 & 104 & 105 \\
-10 & -24 & -37 & -49 & -60 & -70 & -79 & -87 & -94 & -100 & 106 & 107 & 108 & 109 & 110 \\
-11 & -25 & -38 & -50 & -61 & -71 & -80 & -88 & -95 & -101 & -106 & 111 & 112 & 113 & 114 \\
-12 & -26 & -39 & -51 & -62 & -72 & -81 & -89 & -96 & -102 & -107 & -111 & 115 & 116 & 117 \\
-13 & -27 & -40 & -52 & -63 & -73 & -82 & -90 & -97 & -103 & -108 & -112 & -115 & 118 & 119 \\
-14 & -28 & -41 & -53 & -64 & -74 & -83 & -91 & -98 & -104 & -109 & -113 & -116 & -118 & 120 \\
-15 & -29 & -42 & -54 & -65 & -75 & -84 & -92 & -99 & -105 & -110 & -114 & -117 & -119 & -120
\end{pmatrix} \tag{IV.1.1}$$

which corresponds to the indices of the excitation pattern for 16 electrodes. The code works for any n_e.

IV.2. Script for image reconstruction inputs

The following `MATLAB` script calls `EIDORS` to compute the input matrix `New_RM`, and vectors `x` and `y` used for the image reconstruction. The code is written with the configuration of the PMMA EIT sensor described in Section 3.3.2 and used for low temperature and low pressure experiments.

```
%% Building the 2D sensitivity matrix by averaging the RM matrix
% load('imdl.mat');
% load('RM.mat');

%% prepare parameters
Ltot = 336; %Total length of the test section
Diam = 80; %Inner Diameter of the pipe
Lelec = 150; %Length of the electrodes
Welec = 6; %Width of the electrodes
Npix = 39; %Number of pixel in x and y
Zmax= Lelec + 10; %Length considered in the reconstruction

delta= Diam/(Npix +1);
x_pixel=[-(Diam/2-delta):delta:(Diam/2-delta)];
y_pixel=[-(Diam/2-delta):delta:(Diam/2-delta)];
x_fine=[-delta 0.0 delta]; y_fine=[-delta 0.0 delta]; z_fine=[Ltot/2-Zmax:10:
    Ltot/2+Zmax];
N=length(x_pixel)*length(y_pixel)*pi/4*length(x_fine)*length(y_fine)*length(
    z_fine) % should take roughly 16 h
elems=imdl.fwd_model.elems; N_elems=length(elems);% 4 nodes form a tetrahedron
    element
nodes=imdl.fwd_model.nodes; N_nodes=length(nodes);% 1 node is a position in x,y,z
     coordinate
% RM=imdl.solve_use_matrix.RM;

sensitivity=cell(39,39);
```

```
count=0;
for x_p=x_pixel
   for y_p=y_pixel
      if sqrt(x_p^2+y_p^2)> Diam/2
      else
         sensitivity{int64(1+(x_p+(Diam/2-delta))*(Npix-1)/(Diam-2*delta)),int64
             (1+(y_p+(Diam/2-delta))*(Npix-1)/(Diam-2*delta))}=zeros(1,1920);
         for z_p=z_fine
            distance=[];
            for node=[1:N_nodes]
               distance(node)=sqrt((nodes(node,1)-x_p)^2+(nodes(node,2)-y_p)^2+(
                   nodes(node,3)-z_p)^2);
            end
            index1=find(distance==min(distance));
            distance(index1)=9999;
            index2=find(distance==min(distance));
            distance(index2)=9999;
            index3=find(distance==min(distance));
            distance(index3)=9999;
            index4=find(distance==min(distance));
            for elem=[1:N_elems]
               if and(any(index1(1)-elems(elem,:)==0),any(index2(1)-elems(elem
                   ,:)==0))
                  if and(any(index3(1)-elems(elem,:)==0),any(index4(1)-elems(
                      elem,:)==0))
                     sensitivity{int64(1+(x_p+24.225)*38/48.45),int64(1+(y_p
                         +24.225)*38/48.45)}=sensitivity{int64(1+(x_p+24.225)
                         *38/48.45),int64(1+(y_p+24.225)*38/48.45)}+RM(elem,:);
                     break
                  end
               end
            end
         end

         save('sensitivity_refine.mat', 'sensitivity');
         count=count+1
      end
   end
end
%
%% building the new RM matrix
load('sensitivity_refine.mat');
count=0;
sensitivity=sensitivity.';
for i=[1:size(sensitivity,1)]
   for j=[1:size(sensitivity,2)]
      if length(sensitivity{i,j})==1920
         count=count+1;
```

```
        new_RM(count,:)=sensitivity{i,j};
        x(count)=i;
        y(count)=j;
      end
   end
end
save('new_RM.mat','new_RM');
```

IV.3. Computation of the COLTRANE method sign matrix

The following MATLAB script is used to compute the trigonometric sign matrix for the COLTRANE method with any number of electrode:

```
ne= 16 ; %Number of electrodes
n= 0:1:ne-1; %Electrodes index
Theta= n.*2.*pi./ne; %Electrodes radian cordinates
Sigma= zeros(1,ne); %initialize Sigma

for h= 1:1:ne/2 %h for harmonics
    C= cos(h*Theta); %Cosine spatial pattern
    Sigma= [Sigma ; C] ; %fill Sigma
    S= sin(h*Theta) ; %Sine spatial pattern
    Sigma= [Sigma ; S]; %fill Sigma
end

Sigma([1,ne+1],:)= [];%Remove first and last lines
Sigma(abs(Sigma)<1e-10)= 0;%approximate to zero

Sigma= sign(Sigma);%Keep only the sign
```

V

User guide of the ONE-SHOT method
LabVIEW software

Contents

V.1 Details of the HOST VI 282
V.2 Details of the FPGA AO 296
V.3 Details of the FPGA AI 306
V.4 Details of the FPGA FFT 312
V.5 Compilation of the FPGA VI 318

The software version presented in this work is `ONE-SHOT v3.2`. An history of the previous versions can be found in Table V.1. During the development, many tests concerned the cadency of the AO and AI at 40 clock ticks, i.e. the generation and acquisition at 1 MHz for a 40 MHz clock.

The following will overview the `LabVIEW` code of the last version of the ONE-SHOT method software: `ONE-SHOT v3.2`. In the `LabVIEW` jargon, a page of code is referred as a Virtual Instrument (VI).

The `ONE-SHOT v3.2` is decomposed in two VIs, the HOST VI in Section V.1 and the FPGA VI. The FPGA VI is decomposed into three parts: the FPGA AO in Section V.2, the FPGA AI in Section V.3 and the FPGA FFT in Section V.4. These three parts are all compiled together on the same FPGA chip. The compilation process and compilation results are presented in Section V.5. Along this section, the reader is invited to make the parallel with the schematic representation of the AO and AI logics in Figure 4.1 and Figure 4.2, respectively.

V.1. Details of the HOST VI

The HOST VI is decomposed in three screen-shots, as illustrated in Figure V.1. The HOST 1 calls four functions, called *sub-VI*, to prepare the data and inject it into the FPGA. The HOST 2 is an independent loop for online control. The HOST 3 is the data acquisition and data process loop. This loop is also used for data saving and image reconstruction in a sub-VI.

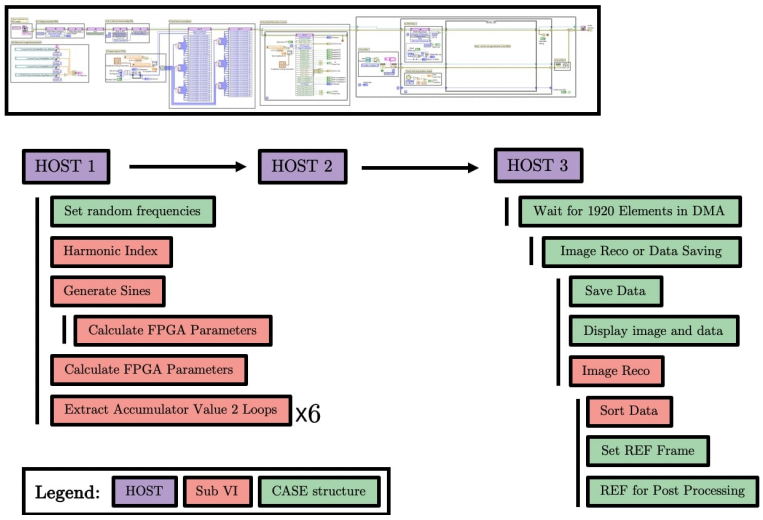

Figure V.1. – Structure of the HOST VI. The top image is a global view of the VI as decomposed into the three screen-shots HOST 1, HOST 2 and HOST 3. The bottom of the image shows the tree-structure details on the case structures and sub-VIs.
HOST 1 (Figure V.2) contains one case structure: CASE 1 **Set random frequencies** (Figure V.3), and four sub-VIs: **Harmonic Index** (Figure V.4), **Generate Sines** (Figure V.5), **Calculate FPGA Parameters** (Figure V.6) and **Extract Accumulator Value 2 Loops** (Figure V.7).
HOST 2 is shown in Figure V.8.
HOST 3 (Figure V.9) contains six case structures: CASE 2 **Wait for 1920 Elements in DMA** (Figure V.10), CASE 3 **Image Reco or Data Saving** (Figure V.11), CASE 4 **Save Data** (Figure V.12), Case 5 **Display Image and Data** (Figure V.13), Case 6 **Set REF Frame** (Figure V.15) and CASE 7 **REF for Post Processing** (Figure V.16), and two sub-VIs: **Image Reco** (Figure V.14) and **Sort Data** (Figure V.17).

Table V.1. – History of the versions of the ONE-SHOT method software.

Date	Version	Comments
2018/08/21	`v0.1`	First test for Read and Write in FPGA.
2018/09/12	`v0.2`	Excitation and FDM with 3 frequencies.
2018/08/19	`v0.3`	Test data transfer with FIFO.
2018/09/20	`v0.4`	Parallel computing of 512 points FFTs on 12 channels with 15 excitation frequencies.
2018/09/25	`v0.5`	Validation 1 AO channel at 40 ticks.
2018/09/27	`v0.6`	Extract voltage value from FFT peak.
2018/09/28	`v0.7`	Debug
2018/10/01	`v0.8`	Debug
2018/11/08	`v0.9`	Debug
2018/11/16	`v0.10`	Debug
2018/12/03	`v0.11`	Debug
2018/12/05	`v0.12`	Debug
2018/12/06	`v1.0`	First successful discrimination of 7 simultaneous signals on a single electrode.
2018/12/10	`v1.1`	Adress data in FPGA.
2018/12/10	`v1.2`	Test with Single Cycle Timed Loop (SCTL) to force generation at 40 ticks.
2019/01/28	`v2.0`	Rotating drain with 8 simultaneous signals. 8 parallel FFTs on FPGA and data send to the HOST.
2019/02/07	`v2.1`	Evolution to 16 electrodes.
2019/02/21	`v2.1.1`	Tests for AO at 40 ticks.
2019/02/21	`v2.2`	First generation of 120 frequencies.
2019/02/21	`v2.2.1`	Online image reconstruction with 120 frequencies.
2019/02/25	`v2.3`	Tests AO and AI both at 40 ticks.
2019/03/07	`v2.4`	Calibration tool to force the flat response of the impedance to the frequency. This tool is not used anymore.
2019/03/07	`v2.5`	Tests for two, three and four parallel read for a single LUT. The maximum of parallel read is two.
2019/04/04	`v3.0`	First implementation of the fully operated ONE-SHOT method.
2019/06/18	`v3.1`	New version for experiments on high pressure and high temperature flow rig at Erlangen, Germany.
2019/10/15	`v3.2`	New version for experiment on two- and three-phase flow rig at University College of South-eastern Norway.

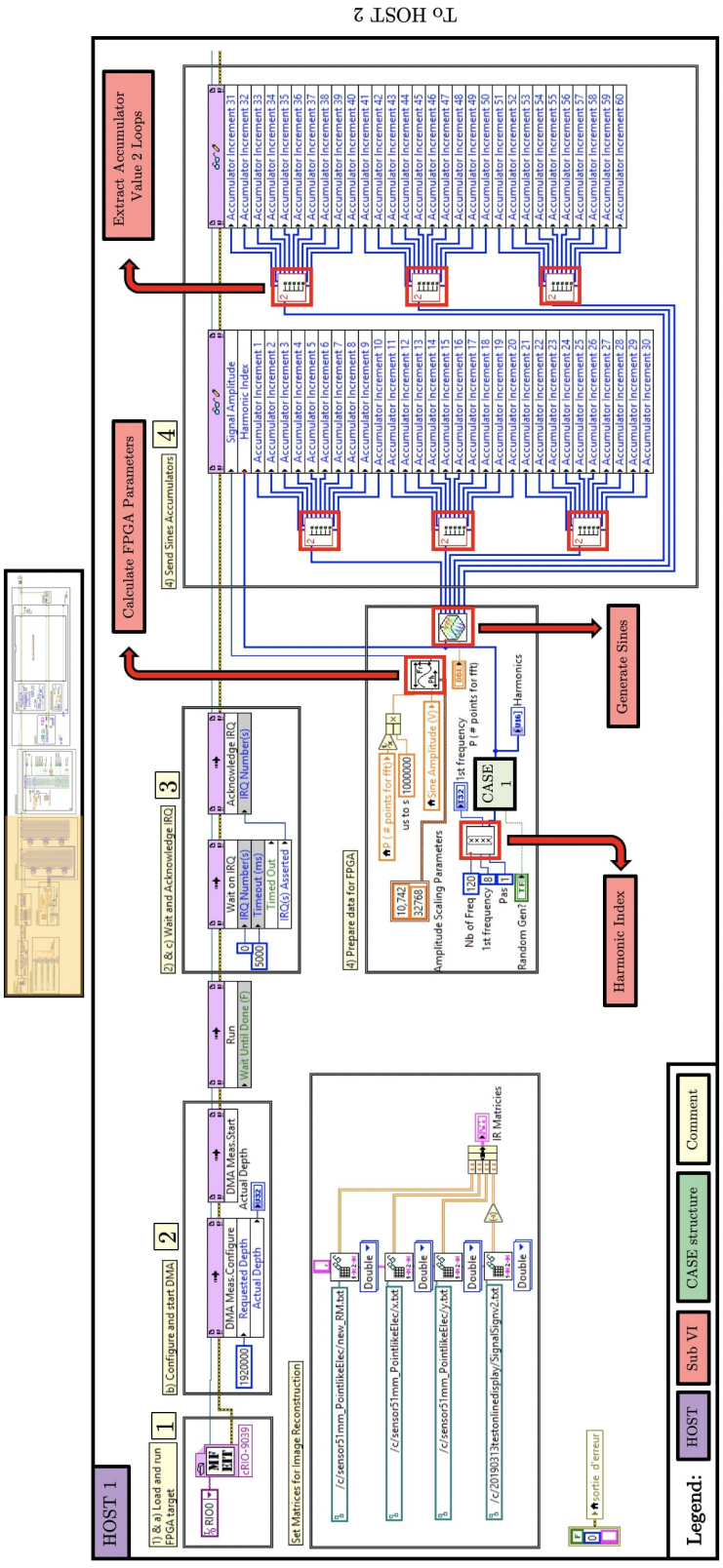

Figure V.2. – The HOST 1 contains the points ①, ② and ④ from Figure 4.1 and points ⓐ, ⓑ and ⓒ from Figure 4.2. This is the initialisation step of the HOST. All functions are used for preparing the FPGA and the data for output and input. The six main steps are squared and the role of each step is described with the comment in yellow. The main elements of the logical sequence are the following:
1. Open an FPGA VI reference to the *User-Controlled I/O Sampling* FPGA VI. It is configured to automatically run the FPGA VI.
2. Configure the FIFO depth such that it will hold a little more than 2ms worth of data. Then, start the DMA FIFO.
3. Wait for the FPGA VI to send an interrupt signaling its readiness and acknowledge that interrupt. This handshake is necessary to ensure that the FPGA VI is ready to begin acquiring data and the HOST VI has started the DMA FIFO.
4. Set the accumulator value for the 120 frequencies. Signal the FPGA VI that the HOST is ready to start the operation. The accumulator values could be placed in a single vector containing 120 elements. This impossible as explained in the FPGA AO Section V.2.

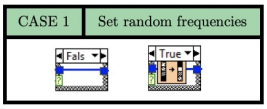

Figure V.3. – The CASE 1 is an option that is manually activated by the user. Is consists in randomly mixing the sequential ordering of the generated harmonics. This option has been implemented because of the non homogeneous response of the impedance to the frequency (See Section 4.2.4). Without mixing, the low frequencies are located in the low-number labeled electrode region (E_n with $n \lesssim 5$) and the high frequencies in the high-number labeled electrode region (E_n with $n \gtrsim 11$). The result without mixing is a higher sensitivity in the low numbering electrode region. The mixed frequencies are automatically reordered at the DAQ level by the *Sort Data* sub-VI (Figure V.17). The CASE 1 option is an interesting development for homogenisation of the sensitivity of the ONE-SHOT method. However it needs a development with a well established distribution of the frequencies instead of a random distribution.

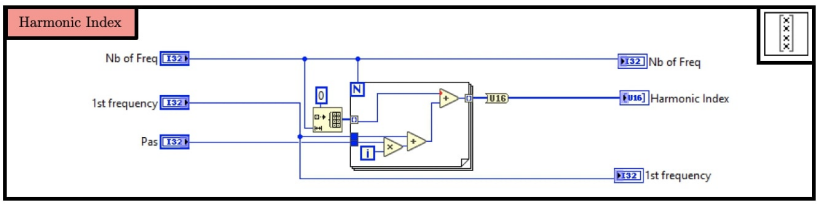

Figure V.4. – The *Harmonic Index* sub-VI is used to generate a vector of Fourier coefficients. In general, it is used to generate the first 120 coefficients. An improvement of this sub-VI could consist in generating only the prime numbers. However in this situation, the highest Fourier coefficient is large and the corresponding frequency may be above the Nyquist limit. This suggestion is for the development of a low noise ONE-SHOT method instead of high speed.

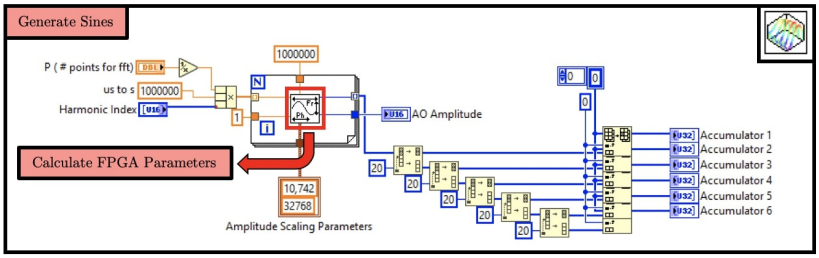

Figure V.5. – The accumulators gives the information to the FPGA to assess at what speed the LUT must be read. The *Generate Sines* sub-VI contains a `for` loop to generate 6 vectors of 20 accumulator value each. A total of 120 values corresponds to the generated frequencies. At each iteration of the `for` loop, the *Generate Sines* calls the *Calculate FPGA Parameters* sub-VI.

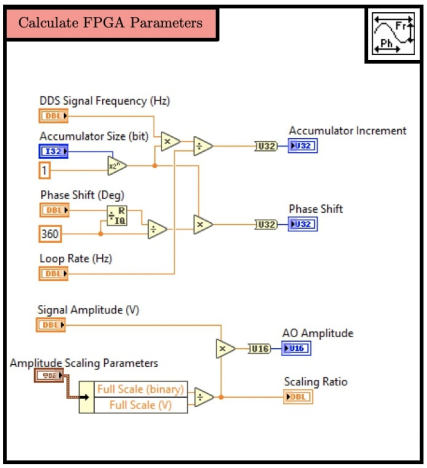

Figure V.6. – The *Calculate FPGA Parameters* sub-VI takes the signal and hardware characteristic values (frequency, phase shift, number of points for FFT computation, output AO voltage and calibration) to translate them into binary numbers of the size of the accumulator for fast processing into the FPGA.

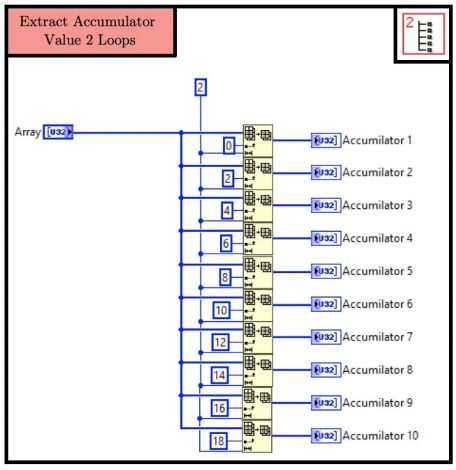

Figure V.7. – The FPGA cannot deal with long sized vectors. For optimisation, the *Extract Accumulator Value 2 Loops* sub-VI takes the values of from the 6 vectors from the *Generate Sines* sub-VI and associates them two-by-two. We will see that these two element vectors will be used in parallel in the FPGA to optimise the execution rate.

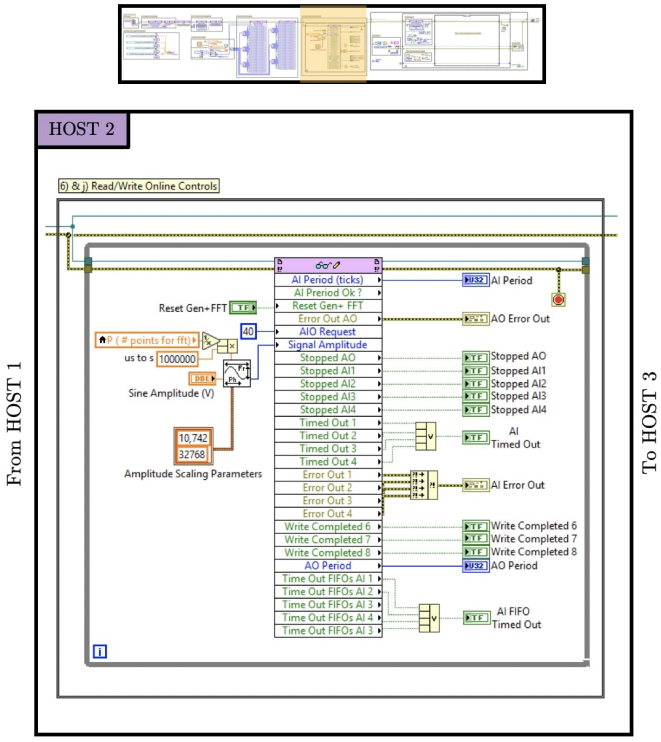

Figure V.8. – The HOST 2 contains the point (6) from Figure 4.1 and point (j) from Figure 4.2. It is composed of an independent `while` loop to read and write online commands and controls. It stops when the software is stopped. It reports errors at all levels of the FPGA. Some additional values are provided by the FPGA and can be added to this function without recompiling it.

In a previous version of the software, this loop were merged with the data processing loop of HOST 3. However, the loop of HOST 3 is required to iterate very fastly in order to flush the DMA faster than it is written. With the increasing data rate in the implementation of the ONE-SHOT method with 120 frequencies, it became impossible for the HOST 3 loop to read the data and online controls simultaneously in the previous version. The advantage of this new structure is that the HOST 2 loop is not cadenced and is free to iterate at its convenient speed.

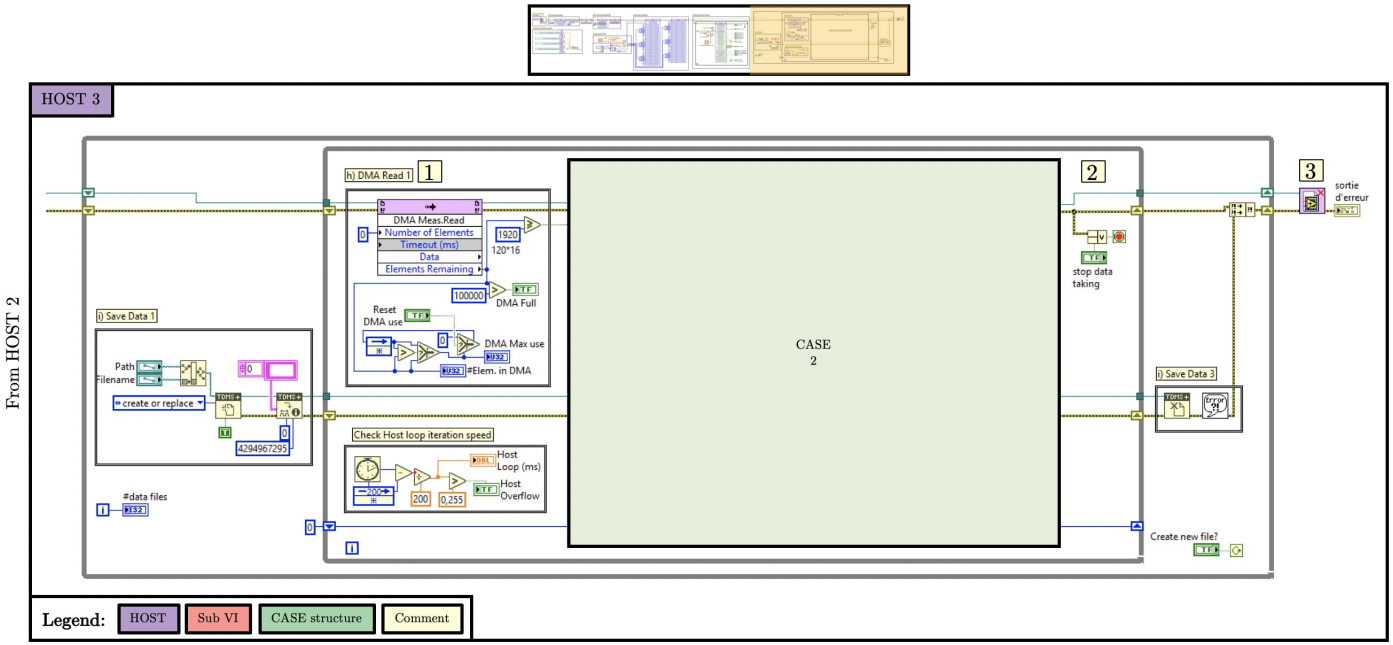

Figure V.9. – The HOST 3 contains the points (h) and (i) from Figure 4.2. It is composed of two nested `while` loops. The exterior one is used to create a new `.tdms` binary file for data saving. Once the file is created, the inner `while` loop operates the DAQ from the DMA. Once this inner loop is stopped, the `.tdms` binary file is closed and a new one is created while the user continues the experiment. The HOST 3 contains a function to check the HOST loop iteration speed, averaged over 200 iterations. The iteration speed must be faster than the data frame rate of 3906 fps. If not, the DMA fills until it saturates. For verification, another function reports the number of elements in the DMA and an error in case of saturation of the DMA. The main elements of the logical sequence are the following:

1. Check if the number of elements in the FIFO is greater than 1920 to form a full data frame. This function controls CASE 2 to read or not the data points from the FPGA VI, and add the data to a pre-allocated array to avoid additional memory operations during acquisition.
2. If the FPGA loop has stopped acquiring, stop the RT HOST acquisition loop. Stopping this loop also stops the control loop of HOST 2.
3. Retrieve error and status information from the FPGA VI and display it on the front panel. Close the FPGA VI reference and reset the FPGA.

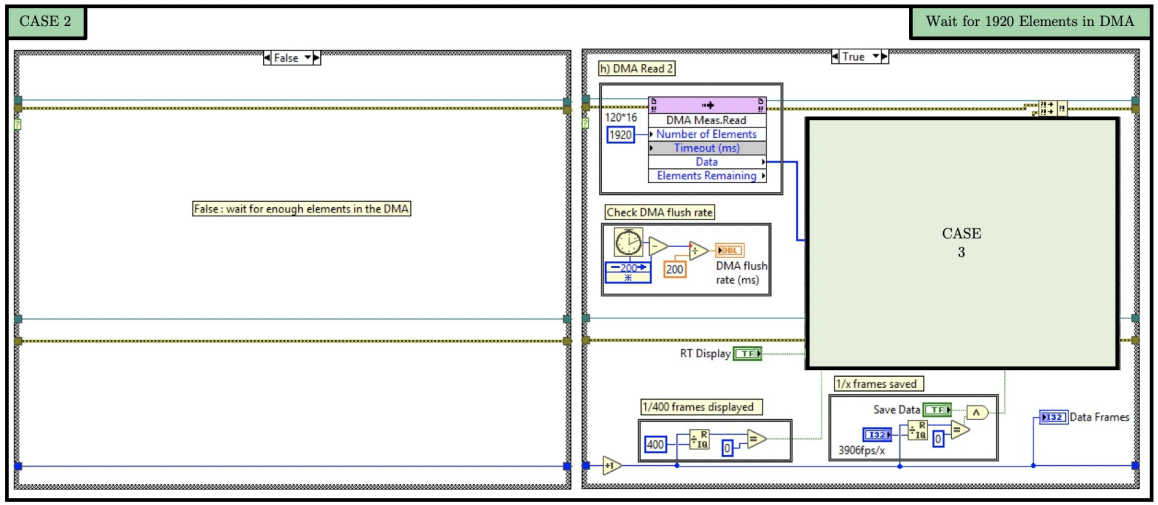

Figure V.10. – The CASE 2 is automatically controlled by the function called "h) DMA Read 2" in the comments of Figure V.3. The function questions the DMA if there is enough elements to create a full frame of data. In our situation, the DMA is required to contain at least 120 (frequencies) $\times$ 16 (electrodes) = 1920 elements. If no, the CASE 2 is empty to wait the DMA to fill until the next iteration. If yes, 1920 elements are taken out from the DMA and send to the CASE 3. This structure is fundamental to create data frames without empty elements. At the bottom of the true case, two functions are provided for controlling the only display rate and data saving rate.

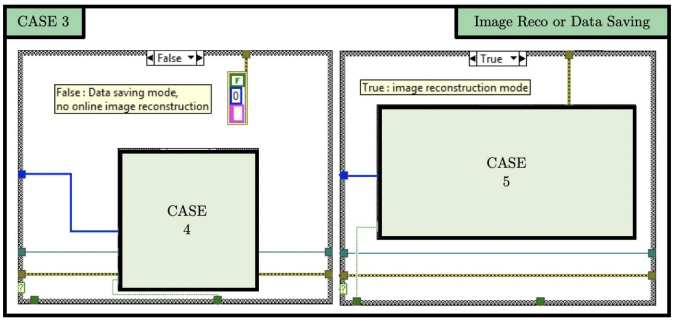

Figure V.11. – The CASE 3 is manually activated by the user to select between two modes. False: Data saving mode and True: image reconstruction mode.

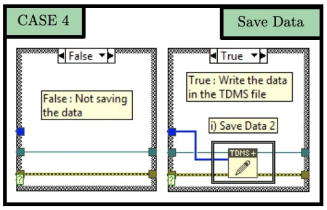

Figure V.12. – The CASE 4 is used to activate the data writing function. This function is called at a rate chosen by the user, for a maximum rate of 3906 fps, the maximal acquisition rate of `ONE-SHOT v3.2`. Once this function is called, a line is added in the `.tdms` binary file. This line contains a full data frame of 1920 elements where each element is of the form given by (4.5).

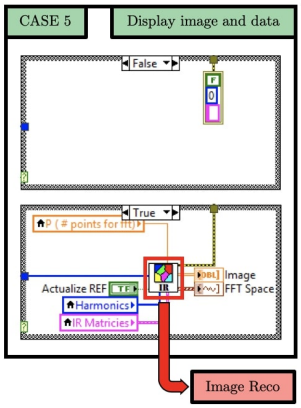

Figure V.13. – The algorithms for online image reconstruction and plot the raw data are computationally heavy. The CASE 5 is an automatically activated case to plot one data frame and one image from this data frame at a rate significantly lower than the real data frame acquisition rate. This slower rate can be controlled by the user. If it is too low, the online images appears jerky. On the other hand, if the rate of online image reconstruction is too high, the loop that flushes the DMA iterates too slowly and the DMA gets full, resulting in a loss of data. In the present version of the software, only about one over 400 images can be reconstructed this way.

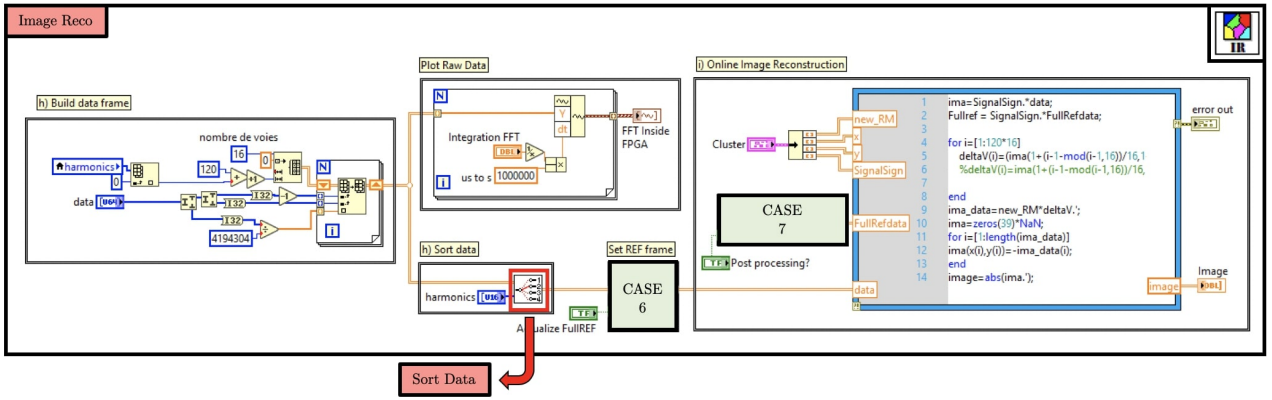

Figure V.14. – The *Image Reco* sub-VI contains the points (h) and (i) from Figure 4.2. On the left, the raw data is decomposed and the address of each element (4.5) is used for the x and y coordinates of a 16×120 data matrix. The matrices are both used to plot the raw data and for image reconstruction. In the second case, the data is ordered thanks to the *Sort Data* sub-VI and send to the image reconstruction algorithm. The CASE 6 provides the saving of a reference data frame.

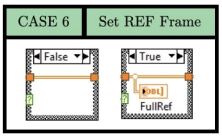

Figure V.15. – The CASE 6 must be called by the user at the beginning of the experiment to save a reference frame. This reference frame is a single data matrix containing 16 × 120 data elements. The reference data frame is typically saved from a homogeneous flow. The user can update this frame anytime. In the current version (`ONE-SHOT v3.2`), a reference data frame must be taken at the beginning of each experiment.

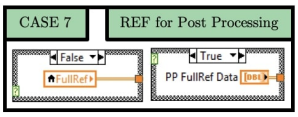

Figure V.16. – The CASE 7 can be called by the user to save a reference frame for post processing. The `ONE-SHOT v3.2` software provides a tool for post process the data. This tool is similar to the *Image Reco* sub-VI, in a `for` loop that reads the saved `.tdms` binary files. The post processing tool is not described in this work.

The algorithm for the image reconstruction uses a `MATLAB` script as shown in Figure V.14. For the sake of optimising the image reconstruction speed, the mesh elements of the image are squared pixels. The number of nodes should not be too large with respect to the number of independent measurements to avoid the inverse-problem becoming ill-posed. On the other hand, the number of nodes should not be small since the image would lose information. In our case, the number of nodes should be around 1920.

In this thesis, I focus on high speed data taking and not optimal image reconstruction which is a topic considered in [Dang, 2020]. By taking a round image with 39 × 39 square pixels, the number of nodes is 1253, the same order of the number of independent measurements.

The code calls six inputs:

- `x`: Vector of length 1253 containing the x-coordinate of every node.
- `y`: Idem for the y-coordinate.
- `new_RM`: This matrix is the Jacobian function $\mathcal{J}$ as defined in 1.81. It contains 1253 × 1920 elements and is computed from information on the geometry of the sensor (Electrode number, electrode size, pipe diameter, ...). The `new_RM` matrix as well as the `x` and `y` vectors are computed with `EIDORS`. The script to obtain these values is given in Appendix IV.2.
- `SignalSign`: This is the Sign Matrix as defined in (4.11).
- `data`: A data frame is a matrix containing 16 × 120 elements and is renewed at each iteration of the loop.

- `FullRefdata`: The reference data frame is saved by the user when using the CASE 6 (Figure V.15).

The first four inputs are loaded by HOST 1 when the VI initialises. The two last inputs are online variables. From these inputs, the image reconstruction algorithm can be implemented online in a MathScript RT module engine operated by `LabVIEW`. The MathScript node is shown in Figure V.14 and contains the following in a `MATLAB` script.

```
1  ima=SignalSign.*data;
2  Fullref = SignalSign.*FullRefdata;
3
4  for i=[1:120*16]
5      deltaV(i)=(ima(1+(i-1-mod(i-1,16))/16,1+mod(i,16))-ima(1+(i-1-mod(i
           -1,16))/16,1+mod(i-1,16)) )-(Fullref(1+(i-1-mod(i-1,16))/16,1+mod
           (i,16))-Fullref(1+(i-1-mod(i-1,16))/16,1+mod(i-1,16)));
6  end
7
8  ima_data=new_RM*deltaV.';
9  ima=zeros(39)*NaN;
10
11 for i=[1:length(ima_data)]
12         ima(x(i),y(i))=-ima_data(i);
13 end
14
15 image=abs(ima.');
```

Here, the line `5` has two tasks: Firstly to compute `deltaV`, the difference between the measured data and the reference data. Secondly to create a vector of length 1920 from the data matrix to multiply to the Jacobian matrix in line `5`.

Let be $\boldsymbol{V}$ the data matrix that contains the set of voltages $\{V_n^{meas}\}$ at the boundary of the domain Ω for the N linearly independent measurements. Regarding the measurement circuit configuration (Figure 3.10), $\boldsymbol{V}$ is related by Kirchhoff's law to two sets of voltages. Firstly, to the reference voltages $\boldsymbol{V}^{ref}$ with its elements V_n^{ref} measured over the boundaries of the $R = 100\ \Omega$ resistor connected to the the n-th electrode. Secondly, to the excitation voltages $\boldsymbol{V}_n^{exc}$ imposed on the resistor. The relation follows:

$$V_n = [(V_n^{exc} - V_n^{ref}) - (V_m^{exc} - V_m^{ref})]. \tag{V.1.1}$$

The voltage variations $\Delta\boldsymbol{V}$ are obtained from a set of reference voltages measured over the resistor:

$$\boldsymbol{V}^{ref} \rightarrow \boldsymbol{V}^{ref}, \tag{V.1.2}$$

and image voltages:

$$\boldsymbol{V}^{ref} \rightarrow \boldsymbol{V}^{im}. \tag{V.1.3}$$

The voltage variation between electrodes n and m follows:

$$\Delta V_{n,m} = [(V_n^{exc} - V_n^{ref}) - (V_m^{exc} - V_m^{ref})] - [(V_n^{exc} - V_n^{im}) - (V_m^{exc} - V_m^{im})] \quad \text{(V.1.4)}$$
$$= [V_m^{ref} - V_m^{ref}] - [V_n^{im} - V_m^{im}] \quad \text{(V.1.5)}$$
$$= \Delta V^{ref} - \Delta V^{im}, \quad \text{(V.1.6)}$$

where the excitation voltages cancelled. The outputs of this code are an error message and a round image of 39 $\times$ 39 pixels. The image is displayed on the front panel (Figure 4.6) and is updated online if the case 3 (Figure V.11) is set on true.

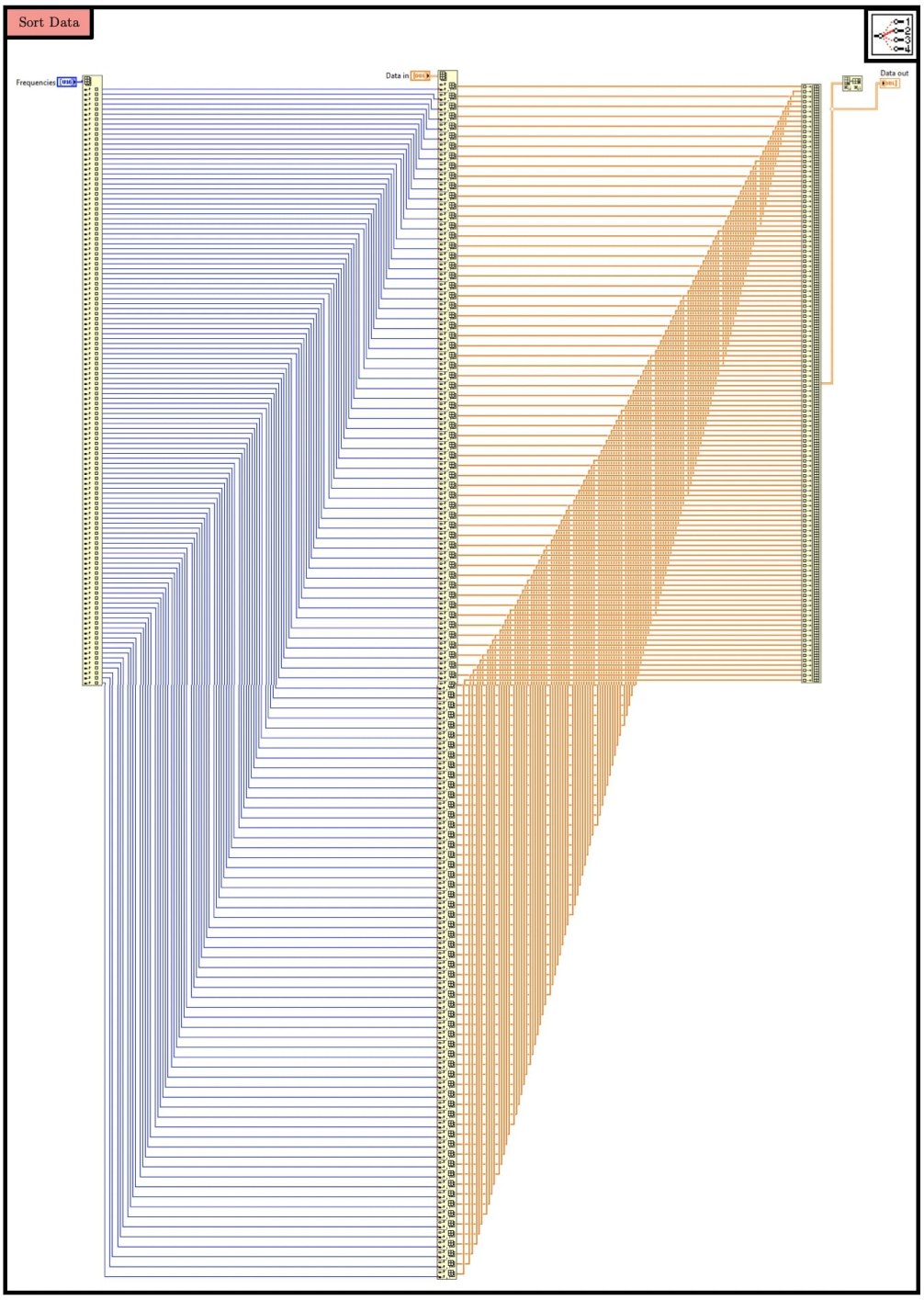

Figure V.17. – The *Sort Data* sub-VI is very useful in the case where the generated frequencies skips some Fourier coefficients, for instance to avoid harmonic effects. In this situation, the data matrix line corresponding to the address of the missing Fourier coefficient is empty. The output data is then corrupted with lines of zeros that increase its size, with no additional information. Moreover, in a post processing step, the matrices containing lines of zeros can be used only if the user knows the Fourier coefficient of each of the 120 generated frequencies. Thanks to the *Sort Data* sub-VI, the output data matrix deletes the lines of zero, for any distribution of the harmonic index vector. This is also useful when using the *Set random frequencies* sub-VI (Figure V.3) since the frequencies are always ordered in output, whatever the order at the input.

V.2. Details of the FPGA AO

The logic of the FPGA AO VI is shown in Figure 4.1. It is decomposed in five screen-shots as illustrated in Figure V.18. The FPGA AO 1 pre-initialises the three modules for signal generation. The FPGA AO 2 and FPGA AO 3 initialises each of the three modules for data generation. These functions assure the correct cadency at 40 clock ticks (40 μs) of the AO. The FPGA AO 4 and FPGA AO 5 contains the LUT to generate 120 signals. The signals are summed into 16 output channels and send to a digital-to-analog converter in the NI-9262 AO modules.

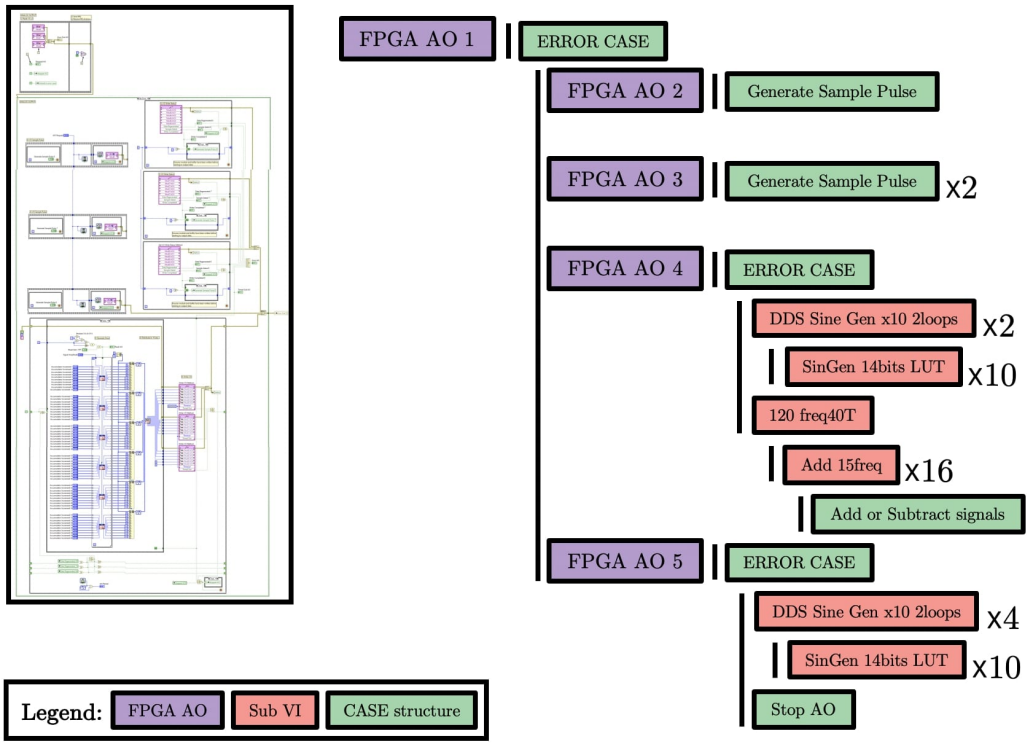

Figure V.18. – Structure of the FPGA AO VI. The left image is a global view of the VI as decomposed into the five screen-shots FPGA AO 1, FPGA AO 2, FPGA AO 3, FPGA AO 4 and FPGA AO 5, shown in Figure V.19, Figure V.20, Figure V.22, Figure V.23 and Figure V.24, respectively. The right image shows the tree-structure details on the case structures and sub-VIs.
FPGA AO VI contains four case structures: CASE 8 **Generate Sample Pulse** (Figure V.21), CASE 9 **Stop AO** (Figure V.28), CASE 10 **Add or Subtract signals** (Figure V.31), in addition, the ERROR CASE reports an error when activated.
Besides, FPGA AO VI also contains four sub-VIs: **DDS Sine Gen x10 2loops** (Figure V.25), **SinGen 14bits LUT** (Figure V.27), **120 freq40T** (Figure V.29) and **Add 15freq** (Figure V.30).

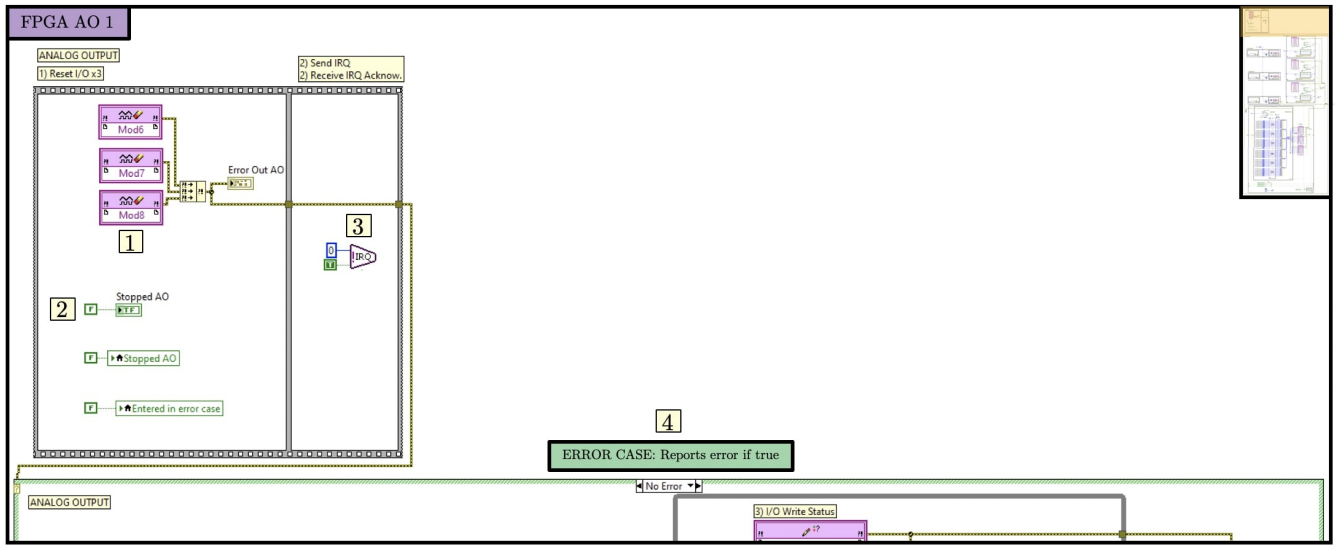

Figure V.19. – The FPGA AO 1 contains the points ① and ② from Figure 4.1. It is composed of three steps for a pre-initialisation of the NI-9262 AO modules:

1. Call the *Reset I/O* function. When this call completes the module is ready to perform an acquisition using the *User-Controlled I/O Sampling* functions. The *Reset I/O* function must be called first to prepare the NI-9262 AO module to use the other *User-Controlled I/O Sampling* functions.
2. Set the *Stopped* boolean to false. This boolean provides synchronisation between the while loops in the last sequence frame. If any loop stops it will cause the others to stop as well.
3. Use an interrupt to signal the HOST that the FPGA is ready to begin writing data and wait to start the operation until the HOST acknowledges it. This is necessary to ensure that the DMA FIFO has been started prior to acquiring data.
4. The pre-initialisation must complete successfully for the NI-9262 AO modules to start. In case of error, the other FPGA AO functions are not operated and the error message is reported.

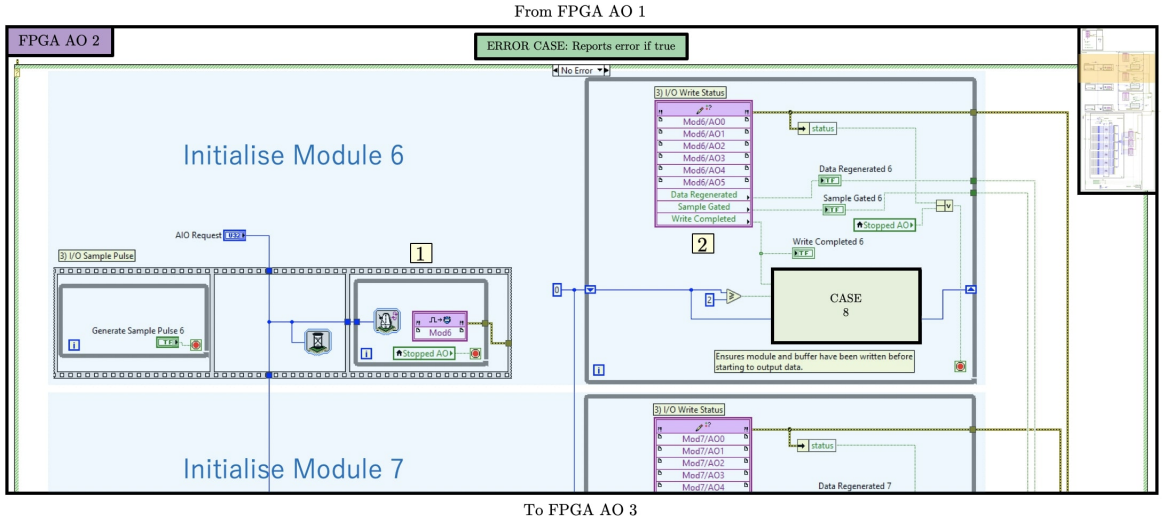

Figure V.20. – The FPGA AO 2 contains the point (3) from Figure 4.1. It is the initialisation step for the NI-9262 AO module 6:
1. Call the *Generate I/O Sample Pulse* method to begin acquiring data. The rate at which this function is called will determine the update rate for the operation so a loop timer is used to enforce the desired sample period.
2. Call the *Get I/O Write Status* method at the same rate as the *Generate I/O Sample Pulse* function is called. This will check the status of every sample we acquire. If a data regenerated or sample gated event occur, report the status to the HOST and stop the VI. Calling the *Get I/O Write Status* function is useful for development and debugging but is not strictly necessary for deployment if there is no variable timing in the application. In the above example, it is not possible to get a sample gated status unless the top loop's sample period is less than the minimum sample period supported by the module. However, this application could produce a data regenerate status if the DMA FIFO is not filled fast enough.

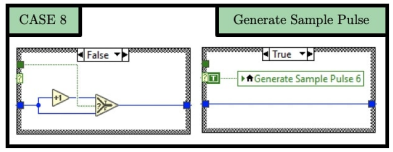

Figure V.21. – The CASE 8 is automatically controlled by the *Get I/O the Write Completed* boolean of the *Write Status* Method of FPGA AO 2. When the *Write Completed* boolean becomes true, it implements a rational number from 0. After two iterations with a true *Write Completed*, the CASE 8 becomes true and activates the *Generate Sample Pulse*. This structure is used to confirm that the NI-9262 AO module is ready to write samples before generating them.

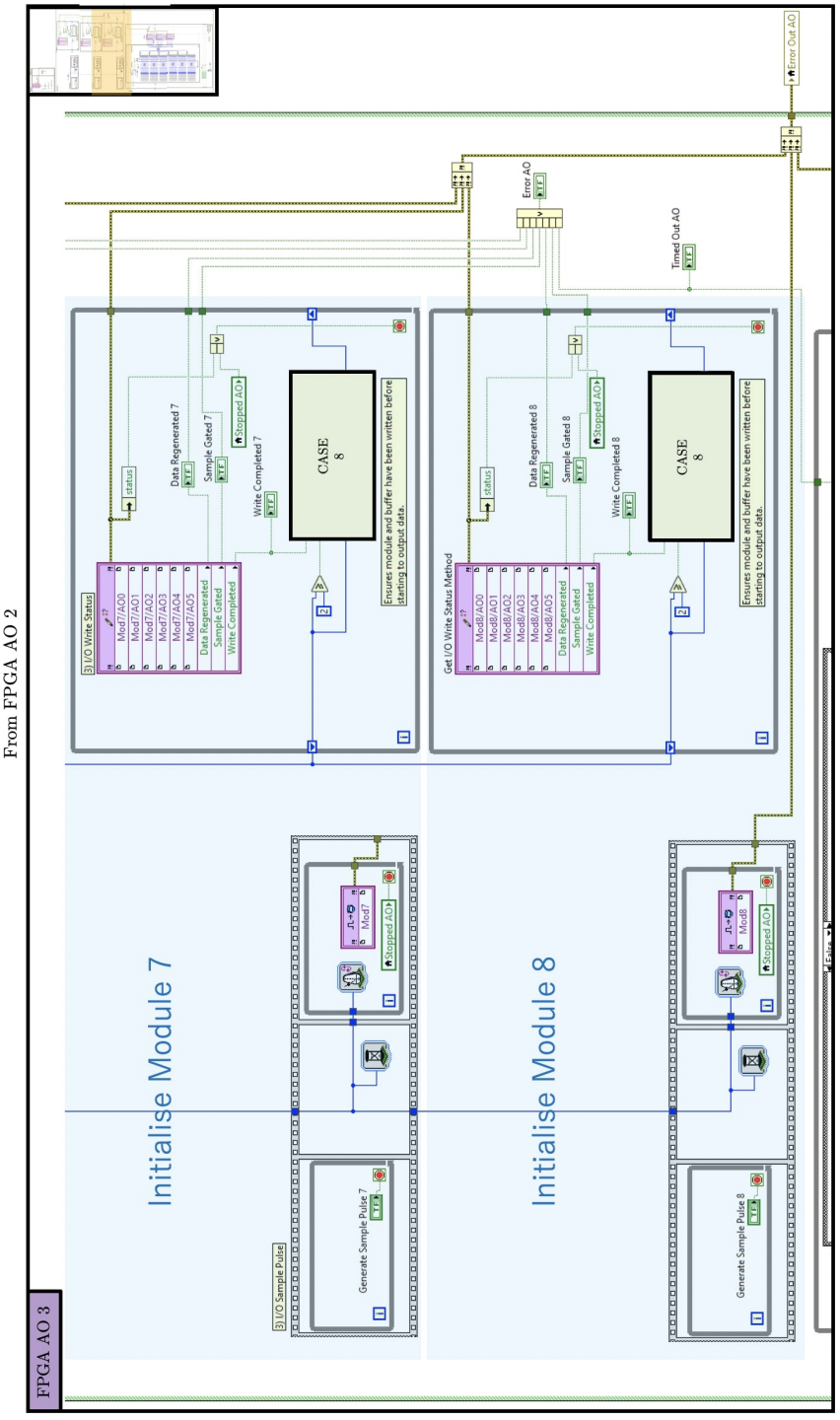

Figure V.22. – The FPGA AO 3 function contains the point ③ from Figure 4.1. It is the initialisation step for the NI-9262 AO modules 7 and 8. The initialisation process is the same as for the NI-9262 AO module 6 in Figure V.20. On the right of the figure, all the errors are merged and send together to the HOST.

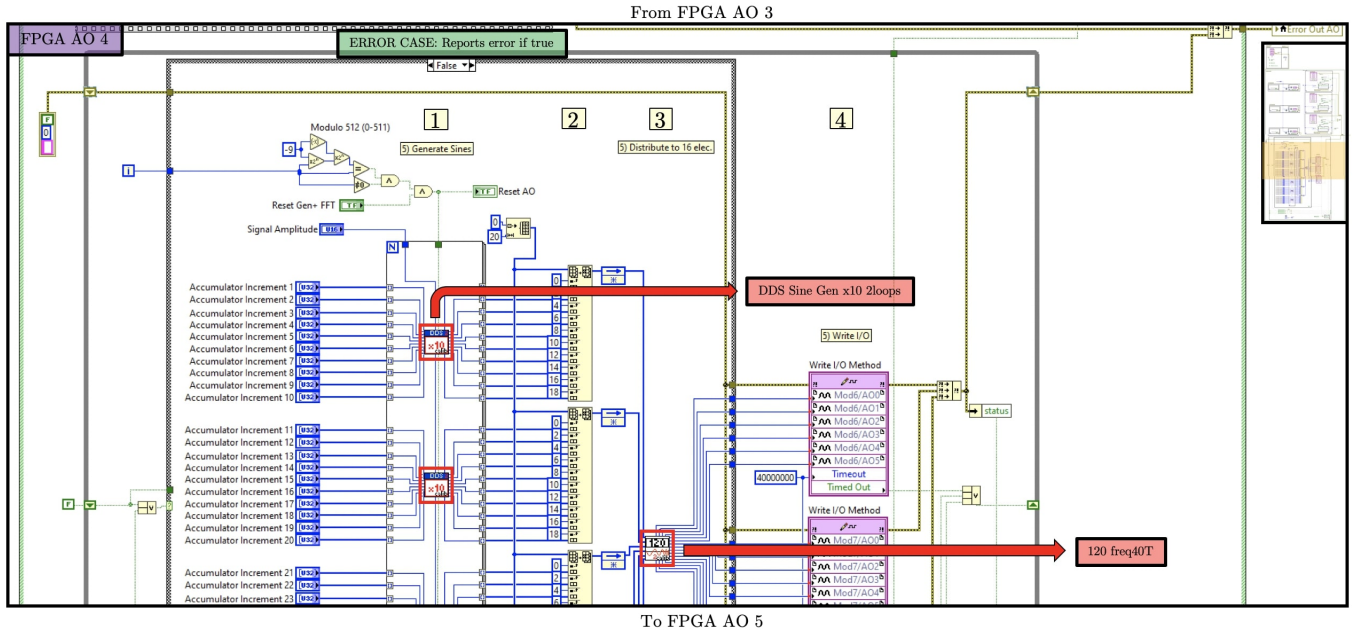

Figure V.23. – The FPGA AO 4 contains the point (5) from Figure 4.1. It prepares the data and send it into the 16 AO channels.

1. Compute the 120 sines at 120 different frequencies. In order to reduce the BRAM on the FPGA, two accumulators are send in parallel to the same LUT in a `while` loop iterating at least at the rate of 2 MHz.
2. Merge all the data into 6 vectors. Each vector contains 20 signal values at a given time. The size of these vectors is a balance between the maximal size of vectors accepted by the FPGA and the maximal number of inputs in the *120 freq40T* sub-VI inputs.
3. Sum positive and negative signal values to create 16 arbitrary functions that are send to the 16 electrodes.
4. Call the *Write I/O* method to write data to the module. This function is configured to write a single sample to each channel on the module. Since this function waits for write buffer to become available, a generous but non-infinite timeout is provided. In the case of default 40 MHz top level clock, the timeout is one second. The acquisition loop is pipelined in order to complete each iteration quickly enough to keep up with the 1 MS/s maximum rate of the NI-9262 AO module. For this reason, the data write that is computed in the previous functions is immediately passed into a shift register and written to the respective channels in the next iteration.

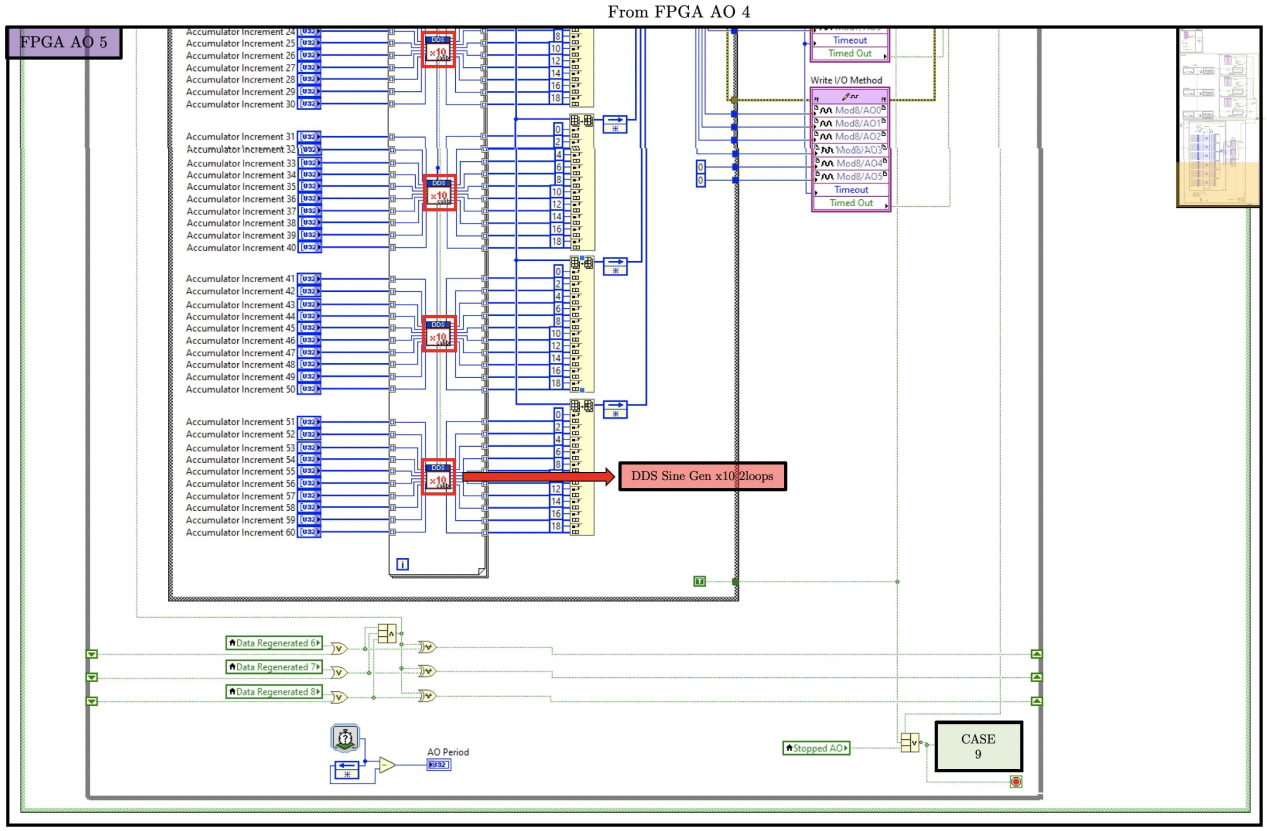

Figure V.24. – The FPGA AO 5 contains the bottom of the logic explained in Figure V.23. The bottom of FPGA AO 5 contains three functions, firstly the *Data Generated* status checks that the data have been generated in all three modules. If not, the ERROR CASE is activated. Secondly, a clock to confirm that the rate of 40 ticks is respected. Thirdly, the CASE 9.

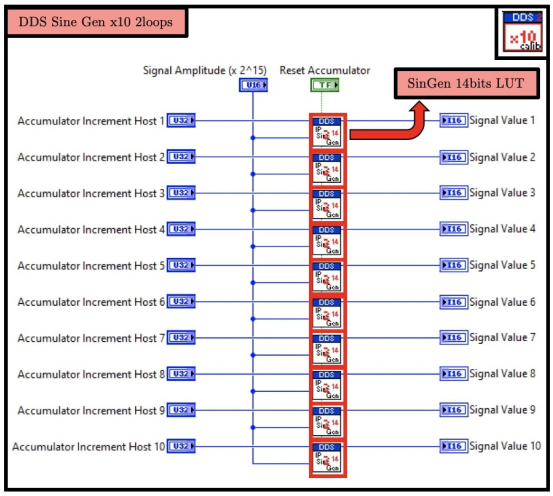

Figure V.25. – In the *DDS Sine Gen x10 2loops* sub-VI, the SinGen *SinGen 14bits LUT*14bits LUT sub-VI would normally be placed in a loop but a loop in `LabVIEW` FPGA adds overhead and each iteration adds two ticks (2 μs) to the amount of time for it to complete. In order to complete each iteration of the while loop quickly enough to keep up with the 1 MS/s maximum rate of the NI-9262 AO module, this example removes the overhead of an additional loop by using a sequence of sub-VIs.
The *DDS Sine Gen x10 2loops* sub-VI is called at twice the rate of the generation signal, i.e. 2 MHz. The sub-VI inputs are 10 accumulator values and the signal amplitude that are send in parallel to 10 LUTs. The output are 10 signal values that are actualised at the rate of 2 MHz. Each output signal value contains the information of two sinusoidal signal functions as illustrated in Figure V.26. This novel structure were developed to solve the problem of too large BRAM use on the FPGA.

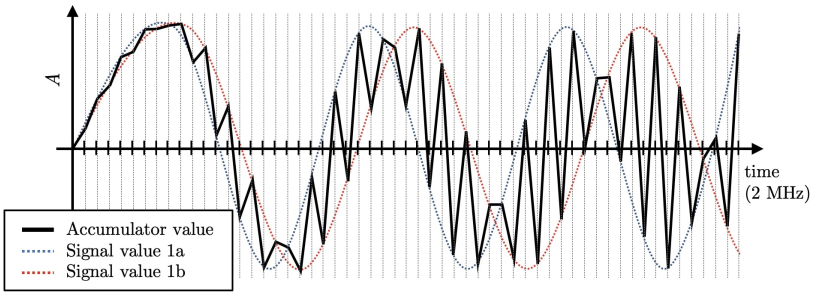

Figure V.26. – When the *DDS Sine Gen x10 2loops* sub-VI is called, it computes a signal value 1a at a given time. At the next iteration, the *DDS Sine Gen x10 2loops* sub-VI outputs another signal value 1b, corresponding to a sinusoidal signal at another frequency. Then, the next iteration gives again a signal value 1a and so on so forth. Since the *DDS Sine Gen x10 2loops* sub-VI is called in a `while` loop iterating at twice the frequency of the generation, it is possible to construct vectors containing two values, from the signal 1a and 1b. The `ONE-SHOT v2.5` (Table V.1) aim at testing this idea with three and four parallel reading for a single LUT, necessating an iteration rate of 3 MHz and 4 MHz, respectively. These tests have concluded that the maximum of parallel use of LUTs is two. The development of this strategy were the keystone to create the first fully operated ONE-SHOT method for 16 electrodes in `ONE-SHOT v3.0`.

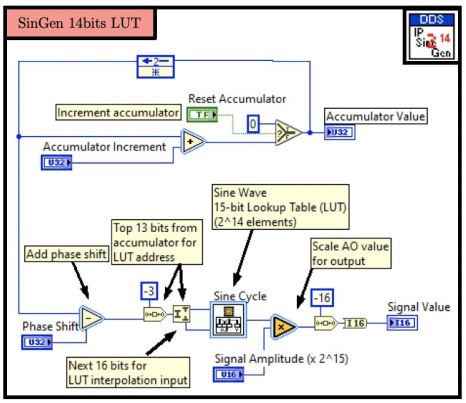

Figure V.27. – At a given iteration 1 the accumulator increment 1a is added to the accumulator value 1a. The top 13 bits of this value indicates the address of the element to read in the LUT. The element is then output, scaled to a given amplitude chosen by the user and then translated into to the `I16` format. The core of the strategy of concatenating two signal values 1a and 1b is located in the shift register at the top of the *SinGen 14bits LUT* sub-VI. This shift register waits two iterations to increment a given accumulator value 1a. Between the iterations, another accumulator value 1b is computed from another accumulator increment 1b as illustrated in Figure V.26.

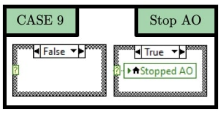

Figure V.28. – The CASE 9 is automatically activated if a timeout occurred either while waiting for data from the signal generating function or waiting to write the data to the module then report the timeout to the HOST and stop the VI. Otherwise stop for an error or if all required samples have been acquired and written into the module.

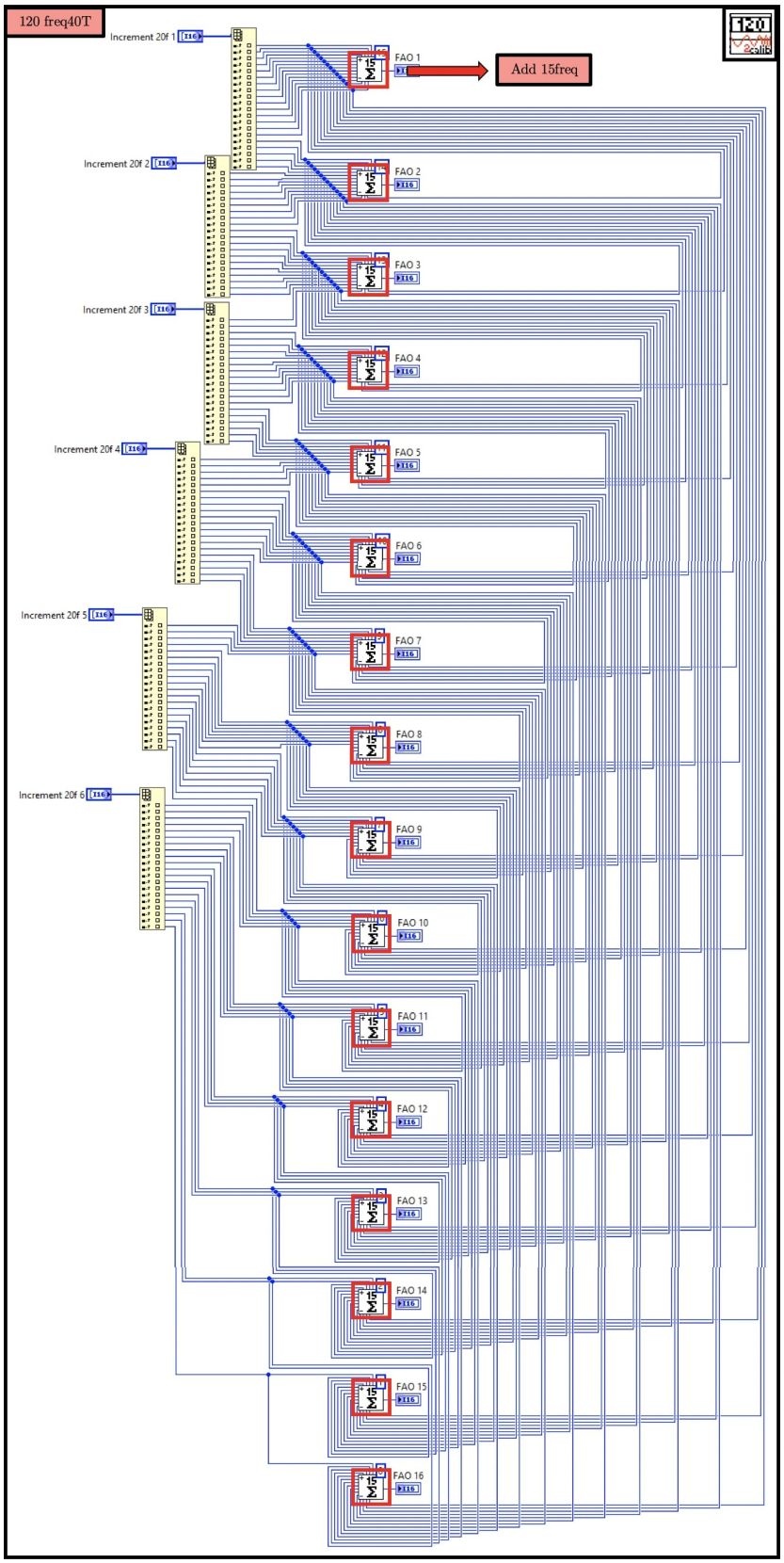

Figure V.29. – In the *120 freq40T* sub-VI, the 120 sinusoidal signals are distributed onto the 16 electrodes. Each signal is routed to a pair of electrodes to create a full-scan excitation pattern.

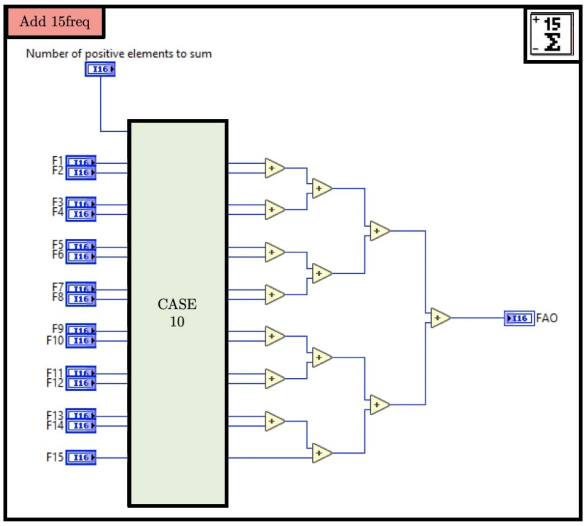

Figure V.30. – The *Add 15freq* sub-VI sums the 15 input elements to create an excitation signal. By calling the CASE 8, the *Add 15freq* sub-VI takes the negative of the signal routed to the highest labeled electrode to create a full-scan excitation pattern.

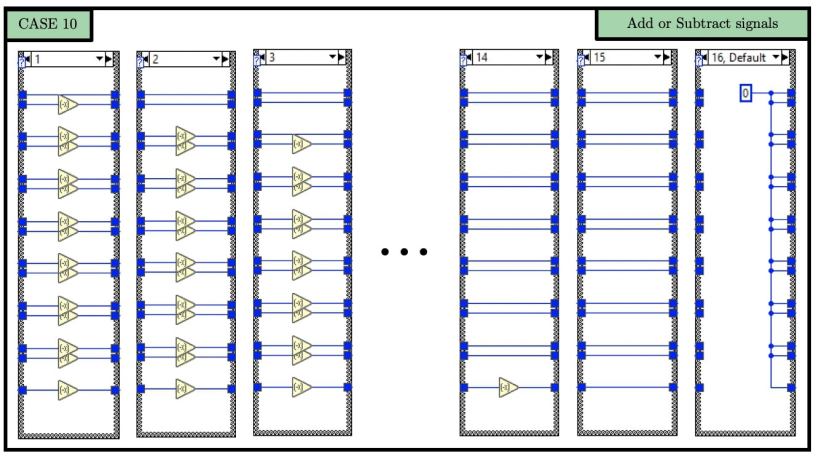

Figure V.31. – The CASE 10 has 15 data input values $F1, ..., F15$ at the format `I16`. Another input $n \in \mathbb{N}$ selects which case between 15 possibilities for $n = 1, ..., 15$ with an additional default possibility for $n \neq \{1, ..., 15\}$. Here, n is the number of positive elements to sum. In the case where the default case is selected, the corresponding excitation channel has no signal.

V.3. Details of the FPGA AI

The logic of the FPGA AI VI is shown in Figure 4.2. It is decomposed in five screen-shots as illustrated in Figure V.32. The FPGA AI 1, FPGA AI 2, FPGA AI 3 and FPGA AI 4 initialises and acquire data from the modules 1, 2, 3 and 4, respectively, for signal generation. These functions assure the correct cadency of the AI while digitalising the signals from 16 input channels and saving them into 16 FIFOs.

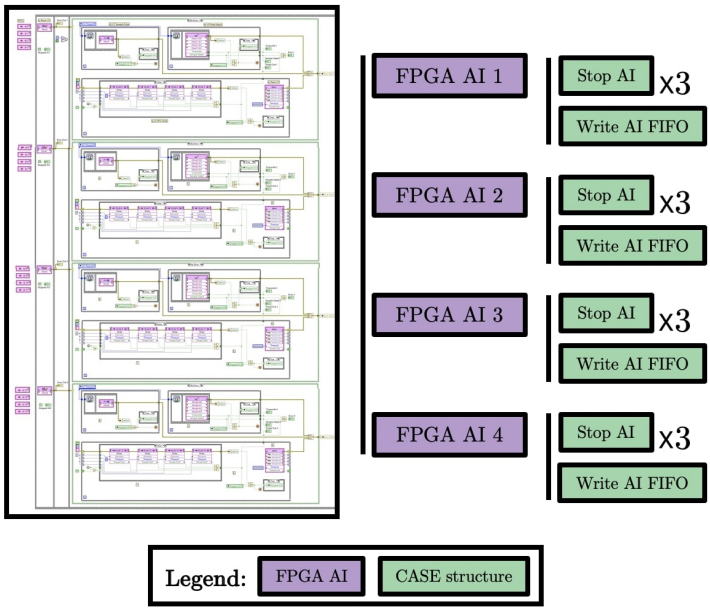

Figure V.32. – Structure of the FPGA AI VI. The left image is a global view of the VI as decomposed into the four screen-shots FPGA AI 1 (Figure V.33), FPGA AI 2 (Figure V.34), FPGA AI 3 (Figure V.35) and FPGA AI 4 (Figure V.36). The right image shows the tree-structure details on the case structures. Each of these function is used to initialise and operate and acquire data with the four NI-9223 AI modules.
The functions contain two case structures: CASE 11 **Stop AI** (Figure V.37), and CASE 12 **Write AI FIFO** (Figure V.38).

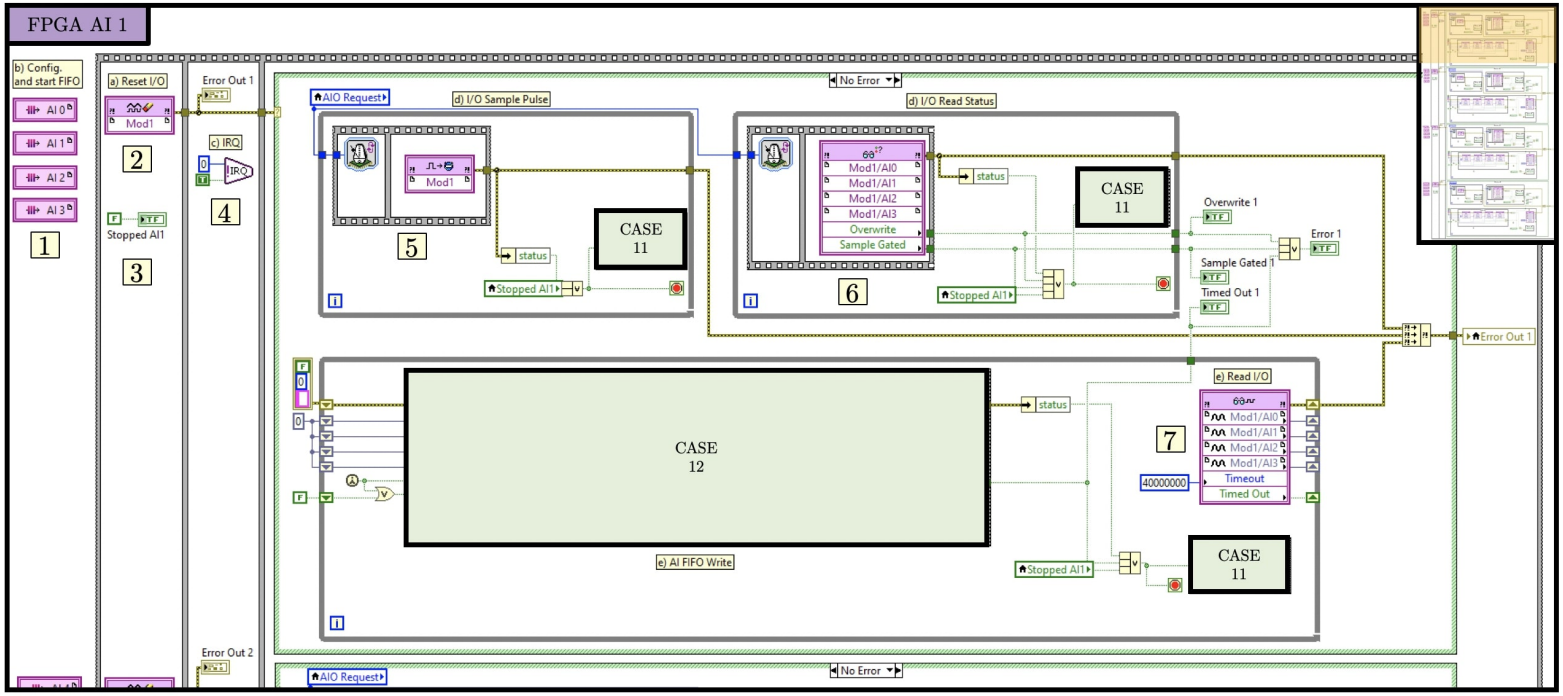

To FPGA AI 2

Figure V.33. – The FPGA AI 1 contains the points (a), (b), (c), (d) and (e) from Figure 4.2. There is one equivalent block of functions to initialise each of the four NI-9223 AI modules. In this caption, we describe the pre-initialisation steps:

1. Define the AI FIFOs configuration. There is one FIFO per channel, containing 1024 element implemented in block memory.
2. Call the *Reset I/O* function. When this call completes the module is ready to perform an acquisition using the *User-Controlled I/O Sampling* functions. The *Reset I/O* function must be called first to prepare the NI-9223 to use the other *User-Controlled I/O Sampling* functions.
3. Set the Stopped boolean to false. This boolean provides synchronisation between the while loops in the last sequence frame. If any loop stops it will cause the others to stop as well.
4. Use an interrupt to signal the HOST that the FPGA is ready to begin acquiring data and wait to start the acquisition until the HOST acknowledges it. This is necessary to ensure that the DMA and the 16 AI FIFOs of all modules has been started prior to acquiring data.

The next steps are described in the caption of Figure V.34.

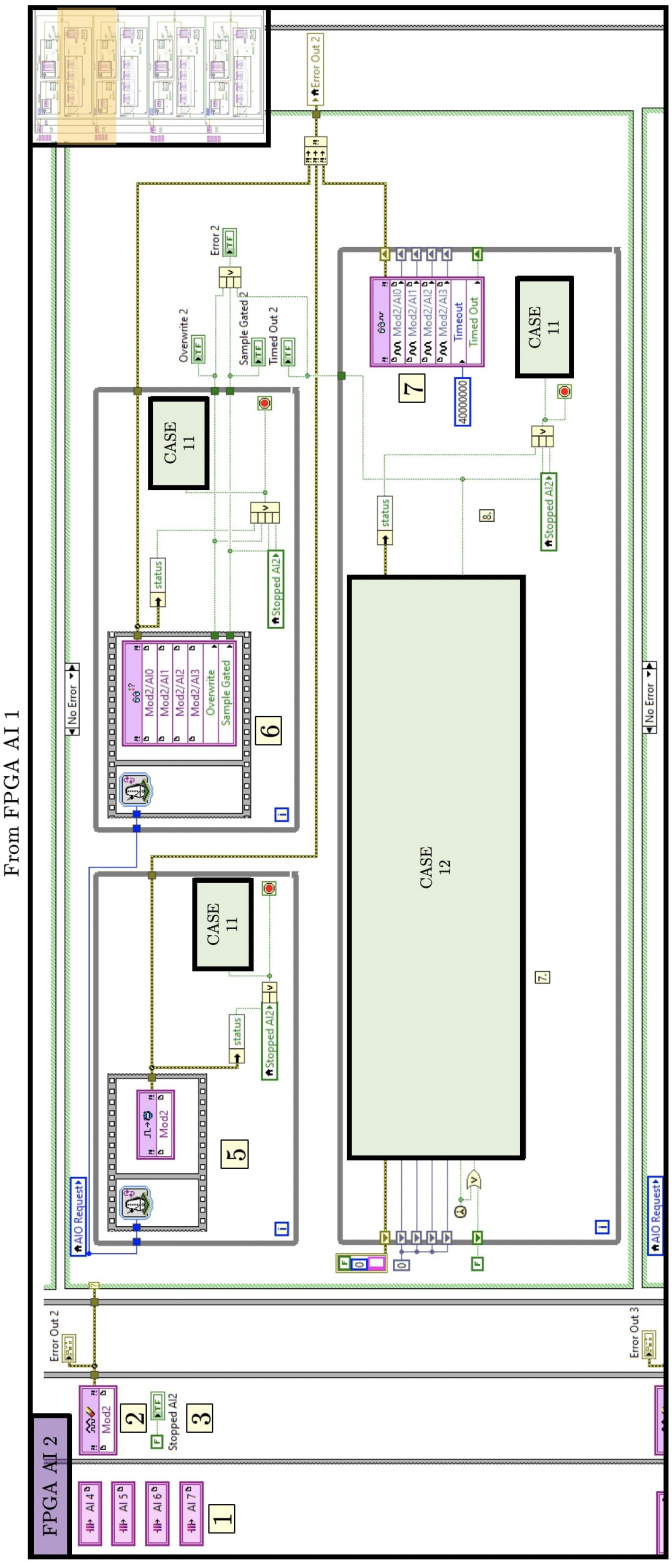

Figure V.34. – The FPGA AI 2 contains the points ⓐ, ⓑ, ⓒ, ⓓ and ⓔ from Figure 4.2. In this caption, we describe the *Generate I/O Sample Pulse* function:

5. Call the *Generate I/O Sample Pulse* function to begin acquiring data. The rate at which this function is called will determine the sample rate for the acquisition so a loop timer is used to enforce the desired sample period. The strategy is similar as for the FPGA AO VI since it is required for the generation and the acquisition to be precisely synchronous. It has been observed that a tiny delay of few nano-seconds in the synchronisation makes the data unusable. This issue will be detailed in the Chapter 6 with the use of two CompactRIOs to operate simultaneous excitations and measurements for 32 electrodes.

The next steps are described in the caption of Figure V.35.

From FPGA AI 2

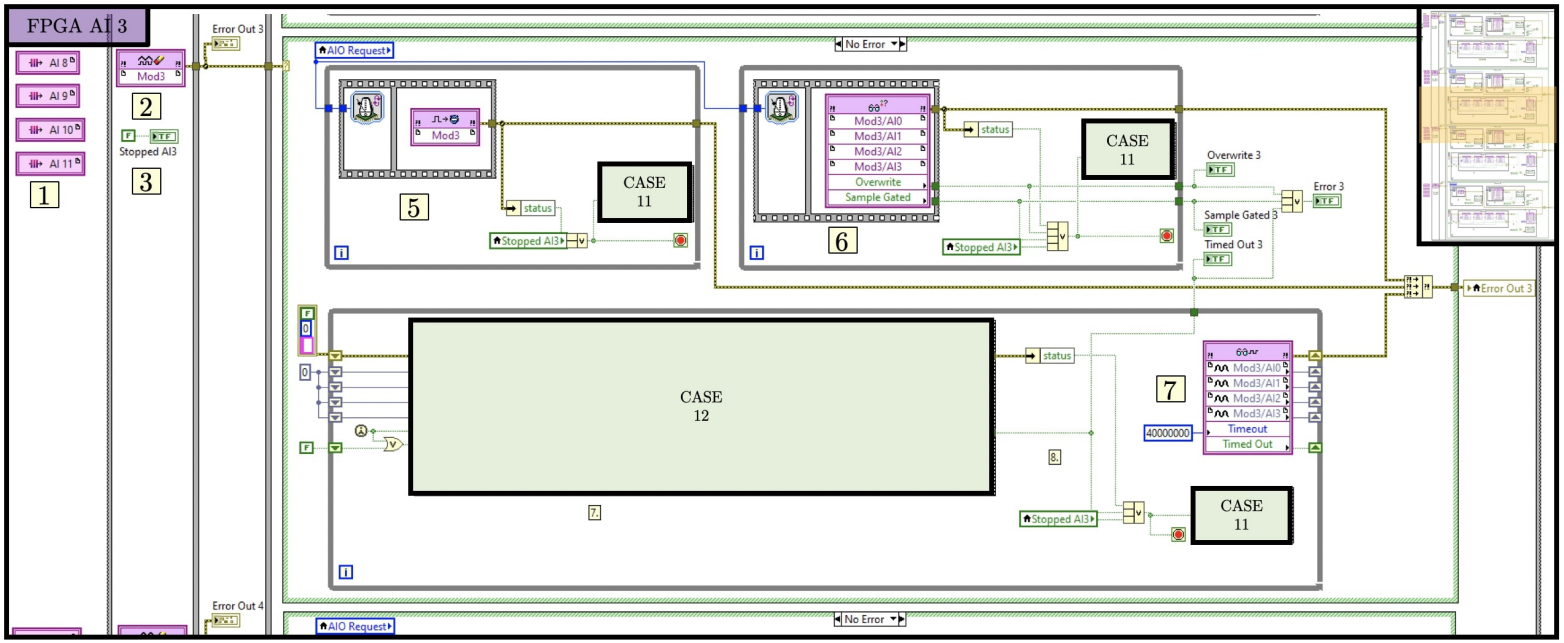

To FPGA AI 4

Figure V.35. – The FPGA AI 3 contains the points (a), (b), (c), (d) and (e) from Figure 4.2. In this caption, we describe the *Get I/O Read Status* function:

6. Call the *Get I/O Read Status* function at the same rate as we call the *Generate I/O Sample Pulse* function. This will check the status of every sample we acquire. If an overwrite or sample gated event occur, report the status to the HOST and stop the VI. As in the FPGA AO VI, calling the *Get I/O Read Status* function is useful for development and debugging but is not strictly necessary for deployment if there is no variable timing in the application. In the above example, it is not possible to get a sample gated status unless the top loop's sample period is less than the minimum sample period supported by the module. However, this application could produce an overwrite status if the HOST VI cannot read from the DMA FIFO fast enough.

The last step is described in the caption of Figure V.36.

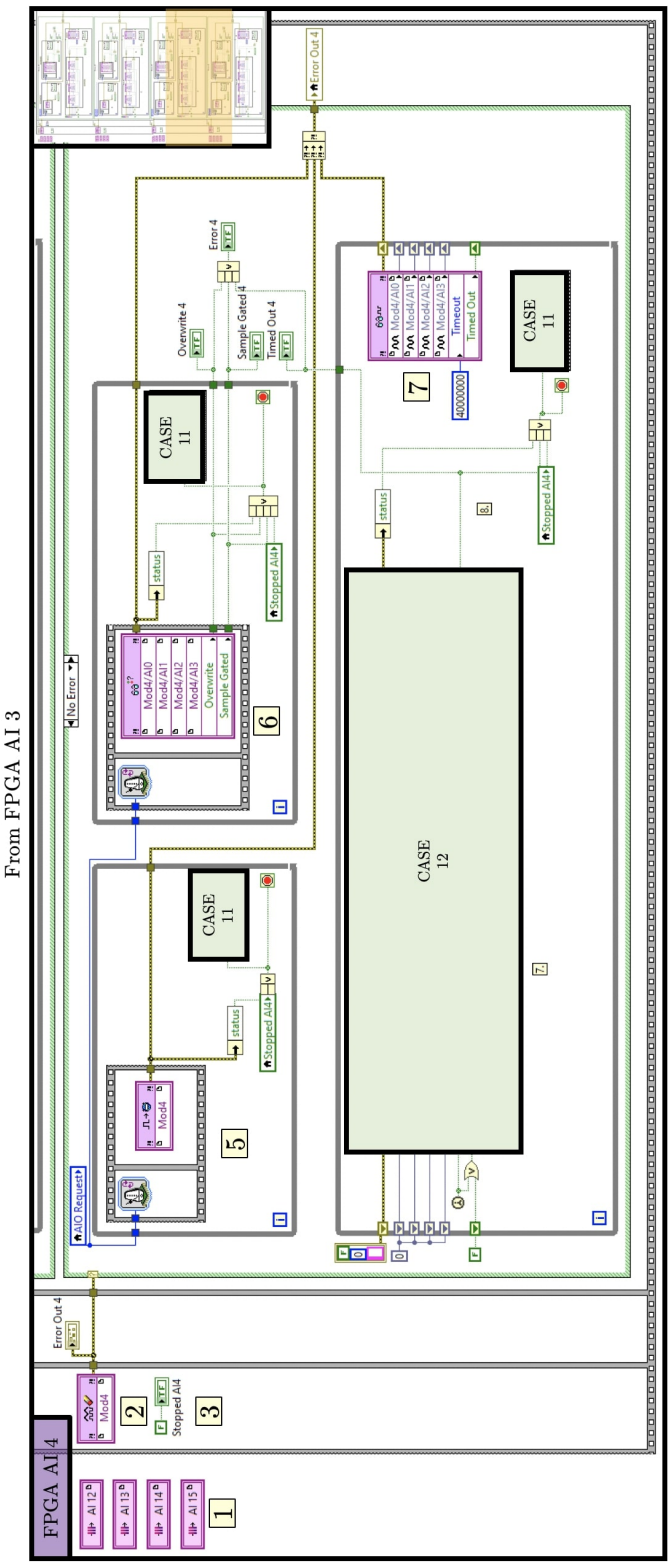

Figure V.36. – The FPGA AI 4 contains the points (a), (b), (c), (d) and (e) from Figure 4.2. In this caption, we describe the data acquisition steps:
7. Call the *Read I/O* function to read data acquired from the module. This function is configured to read a single sample from each channel on the module. Since this function waits for data to become available, a generous but non-infinite timeout is provided. In the case of default 40 MHz top level clock, the timeout is one second. The acquisition loop is pipelined in order to complete each iteration quickly enough to keep up with the 1 MS/s maximum rate of the NI-9223 AI module. For this reason, the data read in is immediately passed into a shift register and placed into the DMA FIFO the next iteration.

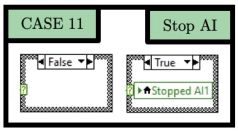

Figure V.37. – The CASE 11 is automatically activated in case of an error from three levels: *I/O Sample Pulse initialisation*, *I/O Read Status* control and *Read I/O* acquisition. If a timeout occurred either while waiting for data from the module or waiting to write the data to the AI FIFO in CASE 11 then report the timeout to the HOST and stop the VI. Otherwise stop for an error or if all requested samples have been acquired and placed into the AI FIFO.

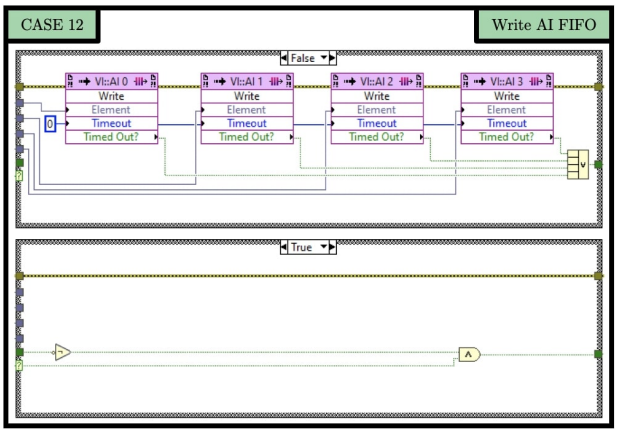

Figure V.38. – Write the acquired data from each channel into the AI FIFOs. The *FIFO Write* method would normally be placed in a loop but a loop in `LabVIEW` FPGA adds overhead and each iteration adds two ticks (2 μs) to the amount of time for it to complete. In order to complete each iteration of the while loop quickly enough to keep up with the 1 MS/s maximum rate of the NI-9223 AI module, this example removes the overhead of an additional loop by using a sequence of *FIFO Write* methods. The CASE 12 is automatically activated if one of the input is timed out. When it becomes true, it stops the data acquisition from all channels. The true case structure is made so it stays true once activated.

V.4. Details of the FPGA FFT

The last part of the FPGA VI contains the tools to extract the superposed signals in the AI channels. The logic of the FPGA FFT VI is shown in Figure 4.2. It is decomposed in three screen-shots as illustrated in Figure V.39. The FPGA FFT 1, FPGA FFT 2 and FPGA FFT 3 contains the parallel extraction of the superposed signals, filtering and data address for all AI channels. In addition, the FPGA FFT 1 contains the DMA *FIFO Write* method to send the data to the HOST.

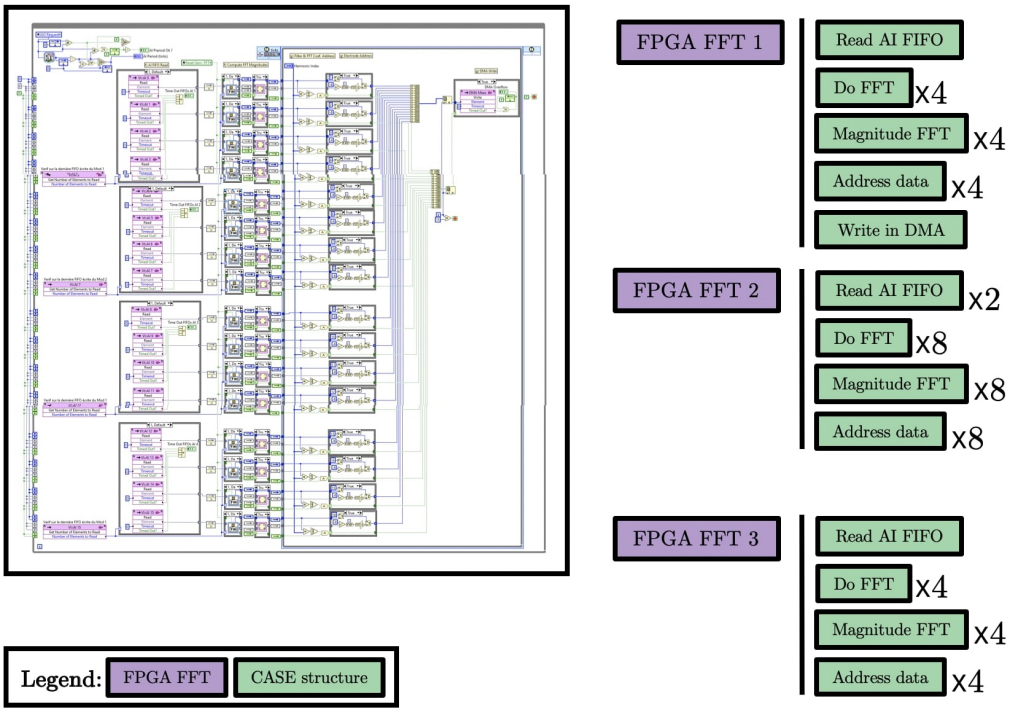

Figure V.39. – Structure of the FPGA FFT VI. The left image is a global view of the VI as decomposed into the three screen-shots FPGA FFT 1 (Figure V.40), FPGA FFT 2 (Figure V.47), and FPGA FFT 3 (Figure V.48). The right image shows the tree-structure details on the case structures.
The FPGA FFT VI contains five case structures: CASE 13 **Read AI FIFO** (Figure V.41), CASE 14 **Do FFT** (Figure V.42), CASE 15 **Magnitude FFT** (Figure V.43), CASE 16 **Address Data** (Figure V.45), and CASE 17 **Write in DMA** (Figure V.46).

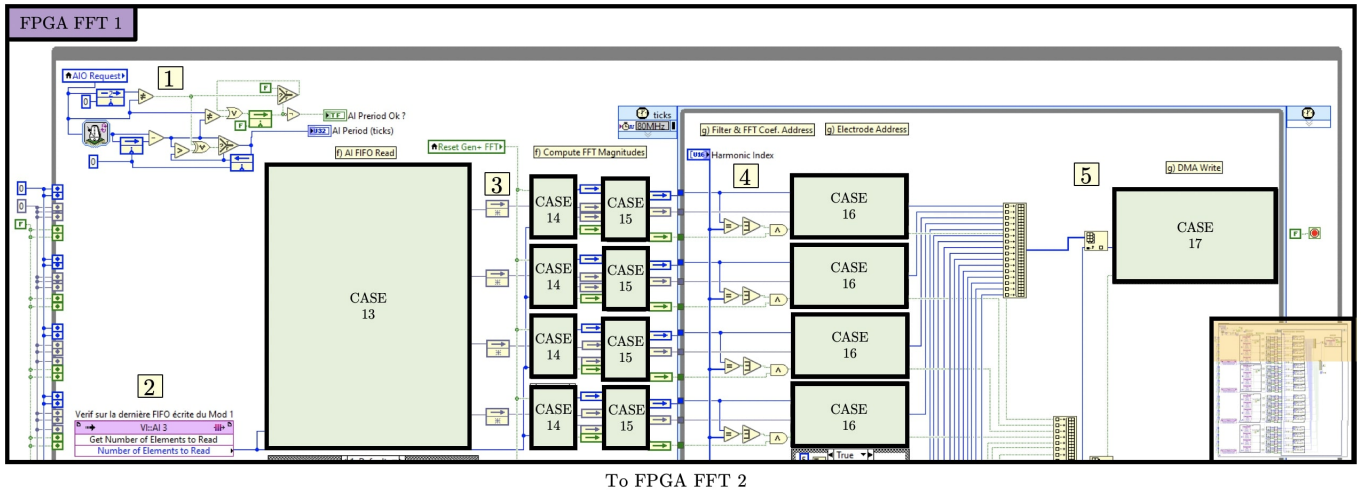

Figure V.40. – The FPGA FFT 1 contains the points (f) and (g) from Figure 4.2. It contains the FDM process for the four channels of module 1:

1. This clock verifies the time elapsed between two iterations of the FFT loop. An error is reported if it does not respect the imposed iteration rate of 40 ticks.
2. Verification that the last FIFO of the module (here, AI FIFO 3 of module 1) contains data to read. This verification step is not mandatory in the current version of the ONE-SHOT method software. It has been developed during the debug versions of the software in order to avoid empty data in the FFT.
3. The code structure contains shift registers between each steps to maximise the parallelisation of the computations. Each series of computation, i.e. between two shift registers, is restricted in time below 40 clock ticks (40 μs) to respect the synchronisation with the FPGA AO VI and the FPGA AI VI. These shift registers implies delays at each implementation. However at this step, since the nature of the FFT imposes a delay of at least twice the number of points P necessary for its computation, the delay imposed by the shift registers is tiny by comparison. The most important is to keep the same delay between all channels.
4. This step is to activate the CASE 16 if a particular Fourier coefficient match a generated frequency. This powerful point-by-point bandpass filter permits to consider only the data in the spectral domain that contains information. This step and the next are forced to iterate faster than the data acquisition rate with a SCTL operated by a derived clock at 80 MHz.
5. At each iteration of the FFT loop (at 1 MHz), the elements of a vector of length 16 is written in the DMA in CASE 17. Each element is a $M_n(k)$ as defined in (4.5).

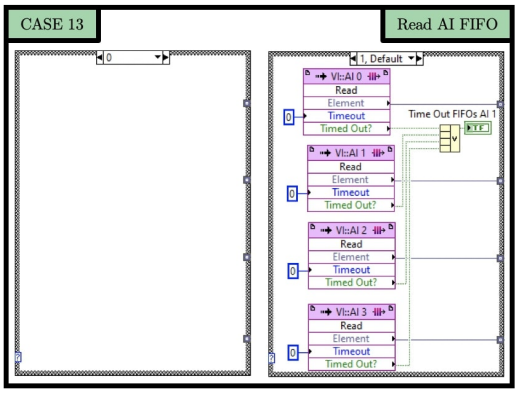

Figure V.41. – The CASE 13 is automatically activated with the verification that there is an element to read in the last written AI FIFO. When activated, it reads the new data from four AI FIFOs, corresponding to the four channels of a NI-9223 AI module. The *FIFO Read* method would normally be placed in a loop but a loop in `LabVIEW` FPGA adds overhead and each iteration adds two ticks to the amount of time for it to complete. In order to complete each iteration of the while loop quickly enough to keep up with the 1 MS/s maximum rate of the NI-9262 AO and NI-9223 AI modules, this example removes the overhead of an additional loop by using a sequence of *FIFO Read* methods.

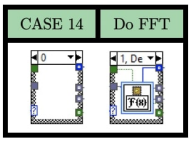

Figure V.42. – The CASE 14 is automatically activated with the verification that there is an element to read in the last written AI FIFO. Once activated, it computes the FFT point-by-point with the single channel, single sample input format (Figure V.44). The data acquisition rate of the ONE-SHOT method software is controlled by setting the number of points P to compute the FFT. According to the FFT algorithm, P must be a power of 2.
In the version used for experiments in Section 4.4 and Chapter 5, the FFTs are computed over 256 data points, defining the spectral band of the excitation signals from $f_1 = 3\ 906.25$ Hz to $f_{120} = 468\ 750$ Hz, and the DAQ rate of 3 906.25 fps. By setting $P = 512$ as considered in the preliminary studies of Chapter 3, the spectral band is half the bandwidth from $f_1 = 1\ 953.12$ kHz to $f_{120} = 234.375$ kHz, and the DAQ rate of 1 953.12 fps. The advantage of reducing the spectral band is to diminish the effects of impedance dependancy to the frequency (Section 4.2.4).

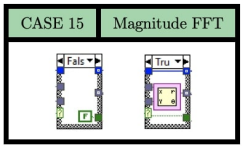

Figure V.43. – The CASE 15 is automatically activated if the output of the FFT is valid (Figure V.44). The function inside the true case converts cartesian coordinates into polar coordinates to extract the magnitude of the FFT outputs.

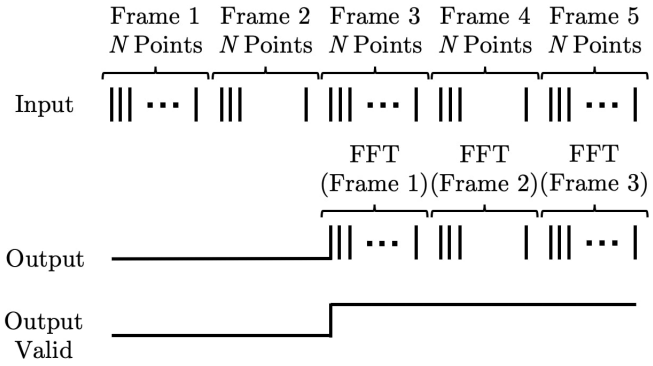

Figure V.44. – Timing diagram outside the SCTL, i.e. single channel, single sample input format.

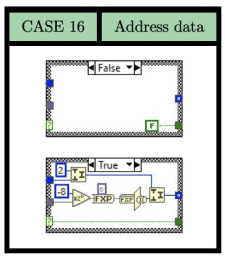

Figure V.45. – The CASE 16 is automatically activated if the output of the FFT is valid and if the Fourier coefficient it related to one of the 120 excitation frequencies. Once activated, the fixed-point data is translated into an integer `I32`. This integer is joined to the Fourier coefficient k integer `I16` and the electrode number n integer `I16` by creating an integer `I64` from the component bytes. This integer is $M_n(k)$ as defined in (4.5). In the true case of the above figure, the integer 2 refers to the electrode E_2. There is 16 different cases structures as the one presented here, each one corresponding to an electrode E_n with the corresponding integer.

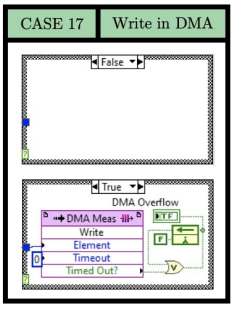

Figure V.46. – The CASE 17 is automatically activated if the FFT output from a given electrode is valid. Once activated, the acquired data is written into the DMA FIFO and send to the HOST.

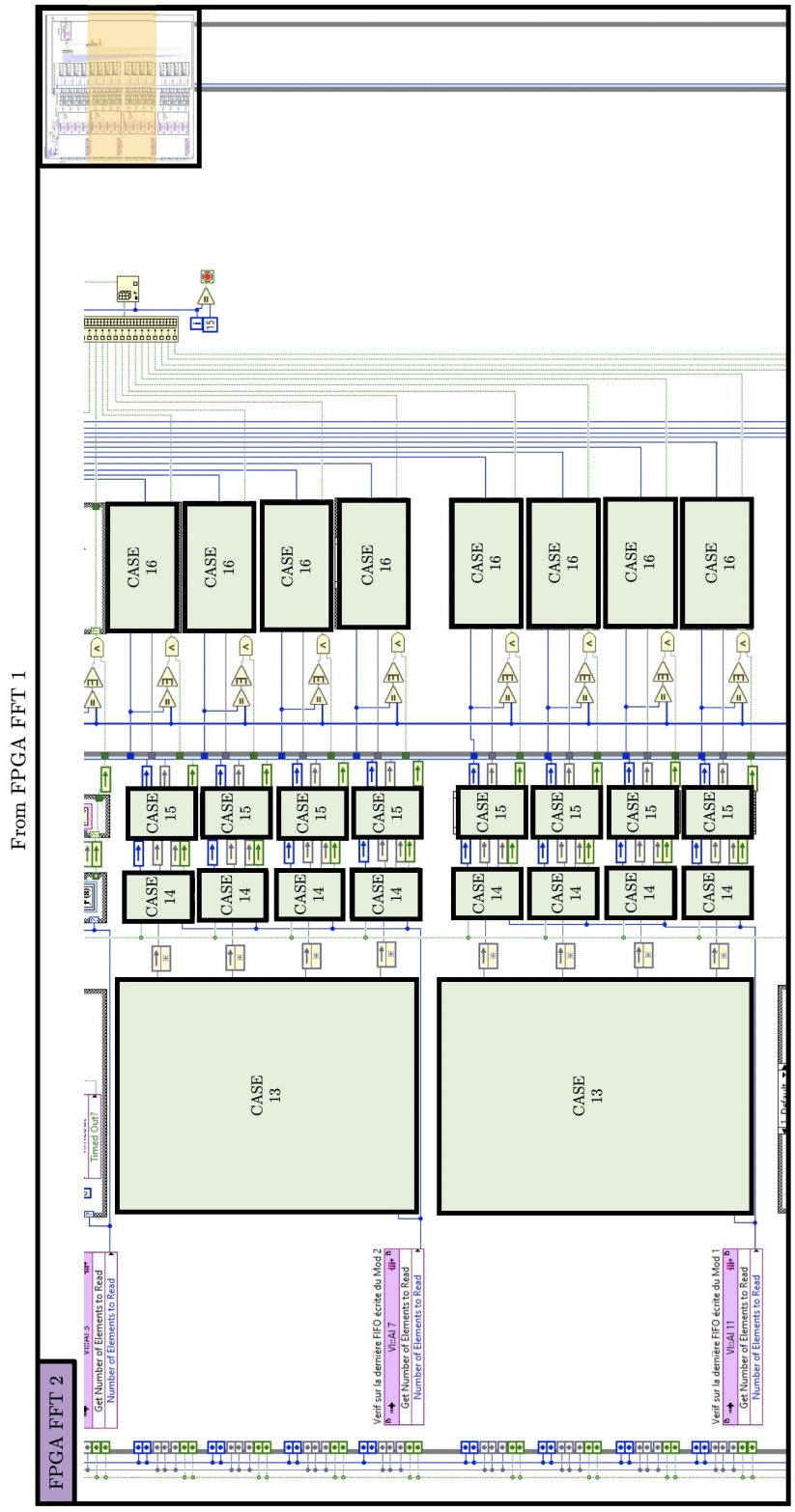

Figure V.47. – The FPGA FFT 2 contains the points ⓕ and ⓖ from Figure 4.2. It contains the FDM process for the eight channels of modules 2 and 3.

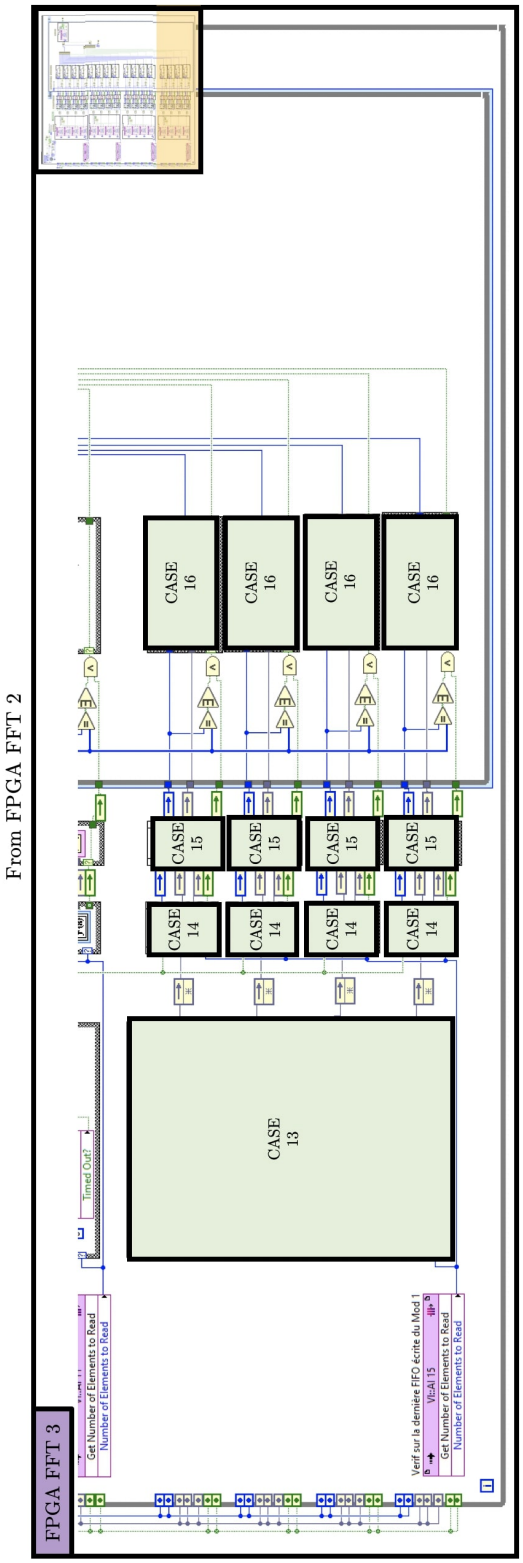

Figure V.48. – The FPGA FFT 3 contains the points ⓕ and ⓖ from Figure 4.2. It contains the FDM process for the four channels of module 4

V.5. Compilation of the FPGA VI

The process of running a user-defined application directly in silicon requires the application to be synthesised to a bitfile. FPGA programmers know that one difficulty with FPGA technology is overcoming the processor intensive task of compiling an FPGA design. To further compound this problem, Moore's law has held true over the last decade, resulting in larger and more complex designs.

The FPGA compiler is not one big monolithic algorithm. Instead, it is a collection of large, complex algorithms. The computational challenge takes the design through a flow that generates an optimised layout on a chip with millions of processing elements that can be configured in any way. The compiler uses synthesis to create a system of logical connections between processing elements. The compiler then maps, places, and routes in an iterative process to find the best solution and hooks everything up on the physical chip while attempting to stay within user constraints. Furthermore, the mathematics behind finding a globally optimised solution to a problem that has infinite possibilities is nontrivial. As a result, FPGA compiles can take hours or even longer with higher density silicon.

Compilation of the FPGA VI

The `LabVIEW` FPGA compile system contains three fundamental software components: the **module development environment**, the **compile server**, and the **compile worker**. There is three FPGA compilation options available that are used to offload the processor intensive process or even reduce compilation time by using compile systems based on `Linux`. For more sophisticated compile system structure such as the ONE-SHOT method software, the compile server and the compile worker are installed on another computer, the FPGA compile cloud service. This service offloads the FPGA compilations to a high-performance, high-reliability cloud server to reduce the compile time of the FPGA VIs.

- **Module development environment**: The first step in the compilation process is the generation of intermediate files. This step is run on the local computer to generate the intermediate files. For this compilation process, `LabVIEW` parses the block diagram and converts the code to a form that the `Xilinx` compiler can consume. A number of errors might occur during this step, causing the compile to fail. These errors usually involve an illegal VI or combination of VIs placed in SCTLs. After generation, the development computer sends the intermediate files through web services communication to the compile server.
- **Compile server**: The compile server accepts compile jobs from one or many `LabVIEW` FPGA development systems and looks for available compile workers to farm out compile jobs. If no compile workers are available, the compile server holds the compile job in a queue until a compile worker becomes available.

- **Compile worker**: The compile worker has the `Xilinx` compilation tools installed for FPGA design synthesis, mapping, placing, and routing. With these tools, a compile worker implements the design and generates a bitfile. The compile worker sends the bitfile back to the compile server, which, in turn, sends the bitfile back to the development computer.

The benefit of this compile system architecture is that it supports multiple compile workers and the automatic farming of compile jobs. The compile server handles the queuing and farming, and is fault-tolerant to compile workers dropping in and out. In fact, if a compile worker drops out during a compilation job, the compile server detects this and farms the compilation to another available compile worker. Although the compile job has to start over, it finishes without any action on user's part. Because the communication lines between the development environment and the compile server are all robust web services, the compile system is fault-tolerant to a number of development-side issues as well, like a development computer restart.

Compilation report of the `ONE-SHOT v3.2` FPGA VI

This section gives the latest compilation result of the FPGA VI detailed in Section 4.3. The VI were compiled on `LabVIEW` FPGA cloud compile service with the compilation tool `Xilinx Vivado 2015.4` (64-bit), and submitted the 20/04/2020 at 14:06 UTC+2.

All `Xilinx` options: implementation strategy, design optimisation directive, placement directive, physical design optimisation directive and routing directive have been selected to default as no particular specification is required. The job identifier is `IcOS7wn` and the working directory is `C:\NIFPGA\compilation\v19.04.04-V3.0_FPGATarget2_-190404MF-EITFPGA_2EKaUNODUsc` on the server.

The compilation successfully completed with the compilation timing given in Table V.2.

Table V.2. – Details of compilation times

Date submitted	20/04/2020 14:06 UTC+2
Date results were retrieved	20/04/2020 17:01 UTC+2
Time waiting in queue	08:48
Time compiling	02:46:49

The details on the compilation times for the compiling steps are given in Table V.3.

The device utilisation of the `Xilinx`'s FPGA `Kintex-7 325T` [Xilinx325T Documentation, 2019] given in Table V.4. Here, the DSP48 block is an arithmetic logic unit embedded into the fabric of the FPGA and is composed of a chain of three different blocks. The computational chain in the DSP48 contains an add/subtract unit connected to a multiplier connected to a final add/subtract/accumulate engine.

Table V.3. – Compilation timing for each compilation steps

Generate Xilinx IP	01:37:46
Synthesise - Vivado	37:01
Optimise Logic	04:05
Place	10:36
Optimise Timing	02:21
Route	09:42
Generate Programming File	04:32

Table V.4. – Device utilisation after compilation

Total Slices	64,5%	32863 out of 50950
Slice Registers	18,0%	73456 out of 407600
Slice LUTs	44,4%	90522 out of 203800
Block RAMs	30,8%	137 out of 445
DSP48s	53,2%	447 out of 840

Every VI or function placed in an FPGA VI takes a certain amount of time, known as logic delay, to execute. The top-level clock at 40 MHz on the FPGA target determines the execution time of the individual functions and VIs on the FPGA VI block diagram. In addition, the FPGA target in Figure V.40 uses a 80 MHz derived clock, created from a base clock. The compilation results on the timing precision is given in Table V.5.

Table V.5. – Clock timing results after compilation

40 MHz Onboard Clock	40,00 MHz	(Met MHz maximum)
80 MHz Derived Clock	80,00 MHz	(Met MHz maximum)

VI

User guide of the COLTRANE method

LabVIEW software

Contents

VI.1 Details of the FPGA AO 323
VI.2 Compilation of the COLTRANE method software FPGA VI 328

The practical implementation of this excitation pattern based on a new structure is discussed in Section VI.1 with a description of the software architecture for the generation of these signals. The Section VI.2 details the compilation of the new FPGA VI with a comparison with the compilation of `ONE-SHOT v3.2`.

VI.1. Details of the FPGA AO

The main difference with `ONE-SHOT v3.2` is located in the FPGA AO VI (Section V.2). More precisely, it is located in the `while` loop iterating at 1 MHz to generate the data points on the 16 output channels in Figure V.23 and Figure V.24. The new version to adapt the COLTRANE method is illustrated in Figure VI.1. With this new structure, the HOST VI is simplified since there is less data to prepare at the initialisation step, before execution.

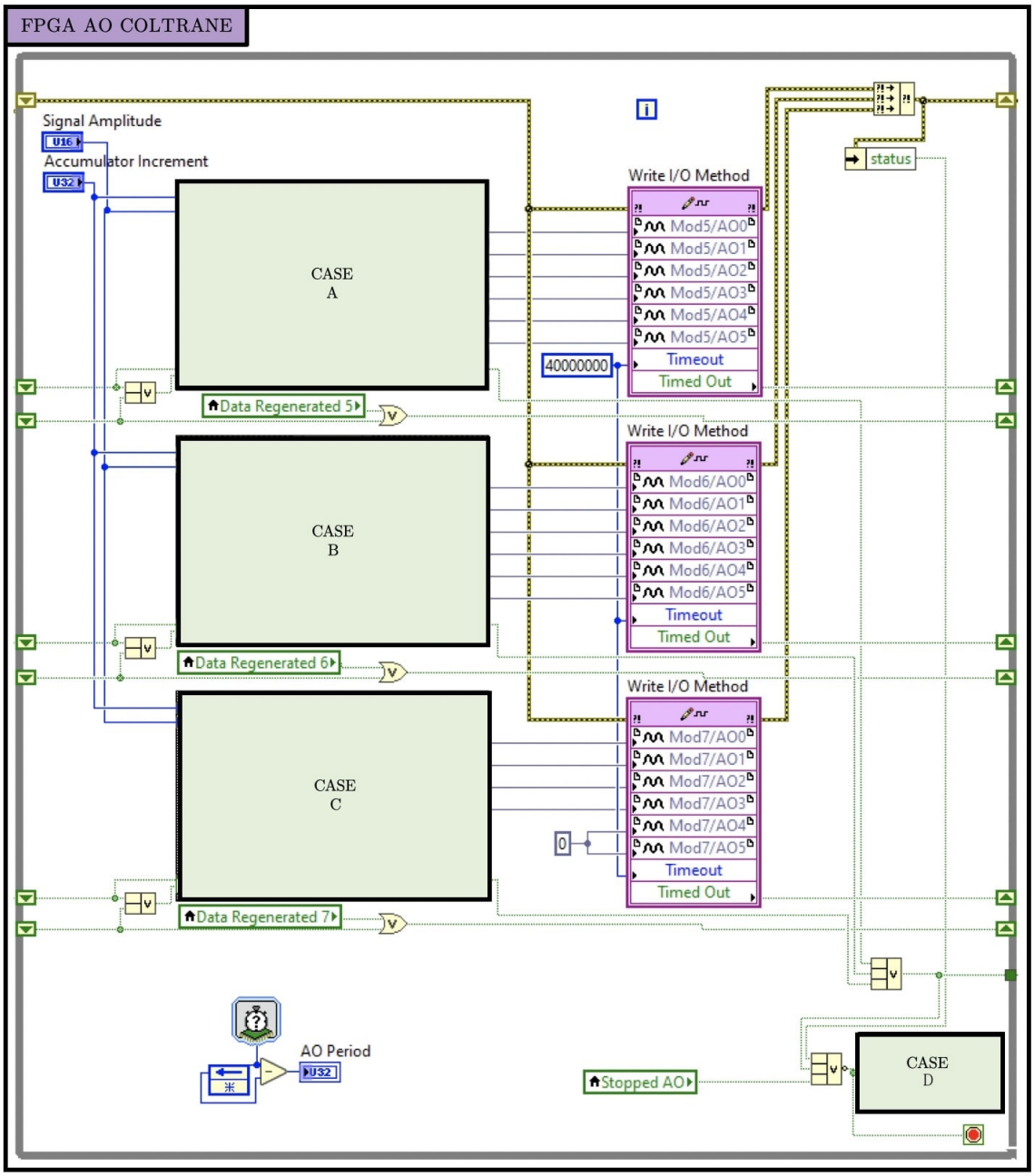

Figure VI.1. – The FPGA AO VI for the COLTRANE method contains new structure in the `while` loop that generates the data points. The CASE A, CASE B and CASE C are used to create 16 arbitrary functions, containing the full set of simultaneous trigonometric excitations. The data is output by calling the *Write I/O* method to write data to the module. This function is configured to write a single sample to each channel on the module. Since this function waits for write buffer to become available, a generous but non-infinite timeout is provided. In the case of default 40 MHz top level clock, the timeout is one second. The acquisition loop is pipelined in order to complete each iteration quickly enough to keep up with the 1 MS/s maximum rate of the NI-9262 AO module. The limited number of operations in this new structure provides the opportunity to read the data from the LUT and write it in the same loop iteration.

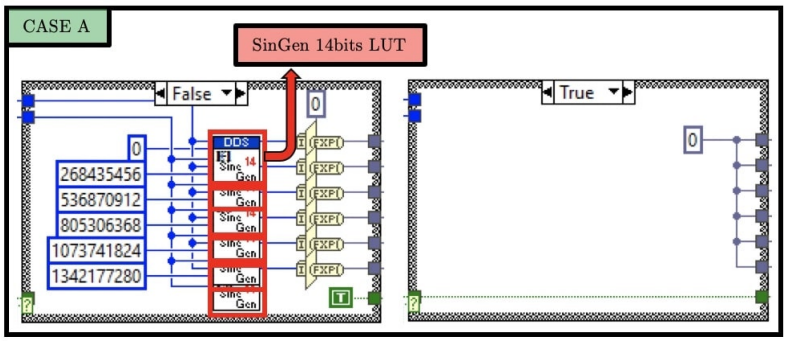

Figure VI.2. – The CASE A is an equivalent to the *DDS Sine Gen x10 2loops* sub-VI in `ONE-SHOT v3.2` (Figure V.25). However, each output is an arbitrary function, corresponding directly to the excitation signal at the electrodes E_1 to E_6. These 6 electrodes are joined together to complete the 6 outputs on a single NI-9262 module.
The `I16` values on the left are the polar coordinates $\{\theta_n\}$ of the electrodes $\{E_n\}$ in radian, directly converted into binary numbers of the size of the accumulator for fast processing into the FPGA.
The true case is automatically activated by the *Data Generated* status that checks that the data have been generated in the corresponding module.

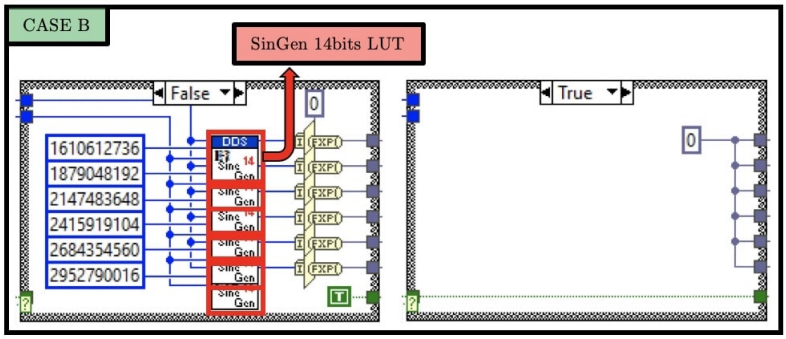

Figure VI.3. – The CASE B is similar to CASE A for electrodes E_7 to E_{12}.

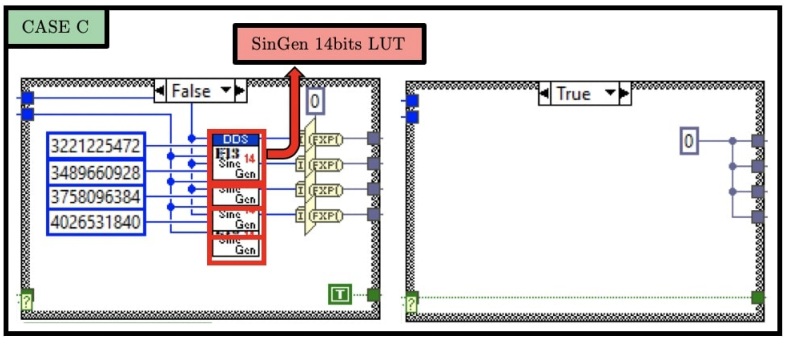

Figure VI.4. – The CASE C is similar to CASE A for electrodes E_{13} to E_{16}.

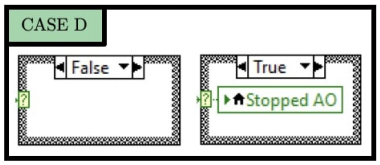

Figure VI.5. – The CASE D is automatically activated if a timeout occurred either while waiting for data from the signal generating function or waiting to write the data to the module then report the timeout to the HOST and stop the VI. Otherwise stop for an error or if all required samples have been acquired and written into the module.

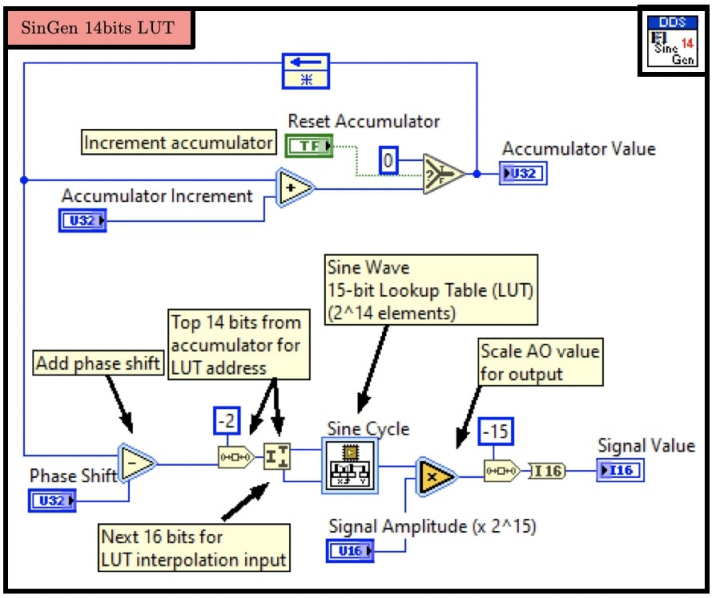

Figure VI.6. – The *SinGen 14bits LUT* sub-VI is a function from `ONE-SHOT v3.2` (Figure V.27). The simplification of the code in the implementation of the COLTRANE method consists in a reduced number of LUTs and hence, a reduced use of memory on the FPGA: It is not necessary in the new code to read at twice the generation rate of 1 MHz. In practice, the shift register at the top-left of the figure waits one single iteration to increment a given accumulator value instead of two.

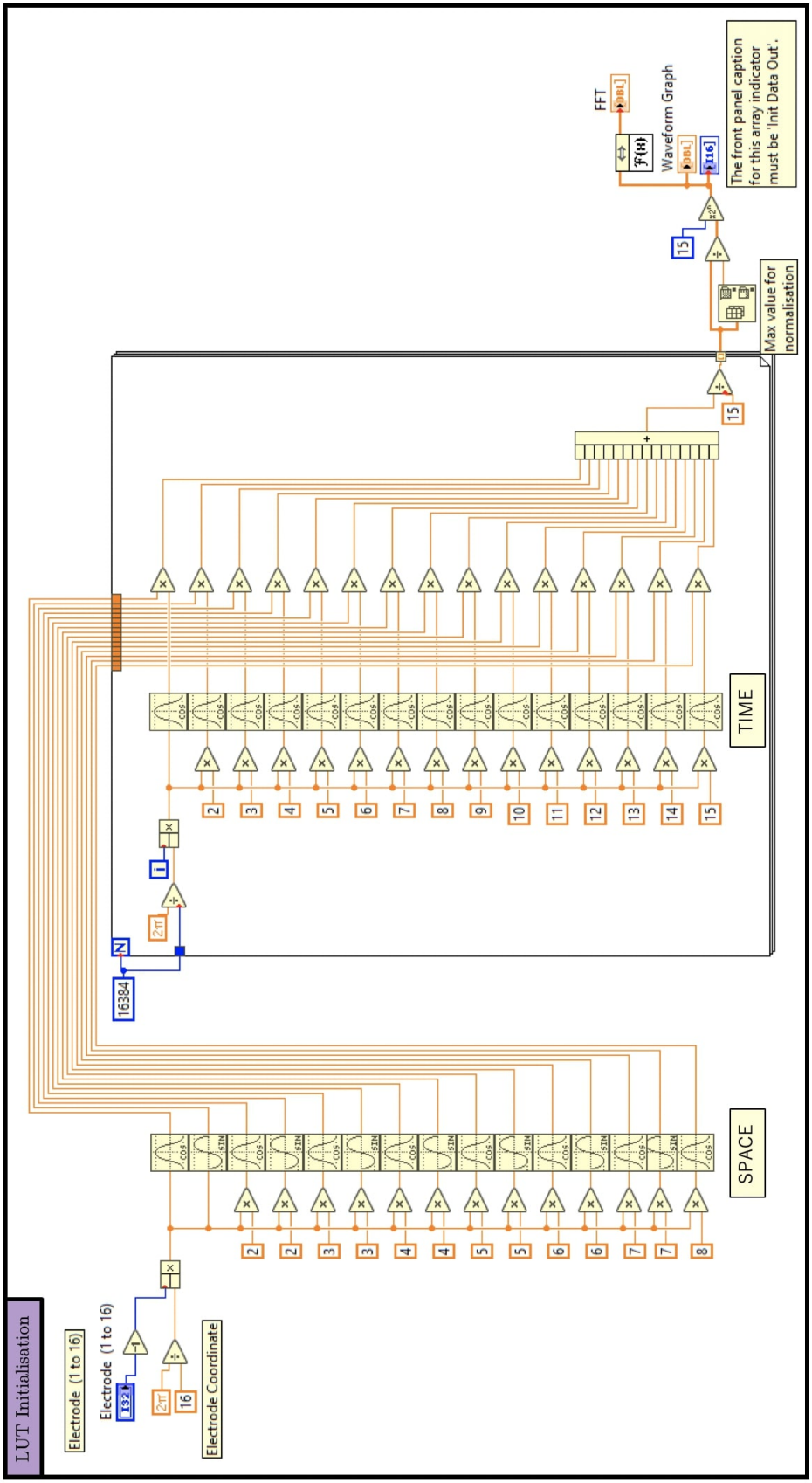

Figure VI.7. – Computation of the trigonometric excitation patterns for a given electrode, selected by the user on the top-left. According to (6.11), the general simultaneous trigonometric excitation pattern decomposes in space on a Fourier basis around the boundary $\partial\Omega$ and in time for the decomposition of the simultaneous signals for the FDM. The output vector contains a number of elements set by the user and is to be loaded in the corresponding LUT before compiling the FPGA VI.

VI.2. Compilation of the COLTRANE method software FPGA VI

This section gives the latest compilation result of the FPGA VI of the COLTRANE method software. I am interested in comparing the new AO structure compilation to the compilation of the FPGA VI of `ONE-SHOT v3.2` in Section V.5. The two FPGA VIs were compiled on the same `LabVIEW` FPGA cloud compile service with the same compilation tool `Xilinx Vivado 2015.4` (64-bit). The FPGA VI of the COLTRANE method software were submitted the 05/05/2020 at 13:21 UTC+2.

All `Xilinx` options: implementation strategy, design optimisation directive, placement directive, physical design optimisation directive and routing directive have been selected to default as no particular specification is required. The job identifier is `Vnr812v` and the working directory is `C:\NIFPGA\compilation\v19.04.04-V3.0_FPGATarget2_-191203TrigoEIT16_azxq5Bxq7nI` on the server.

The compilation successfully completed with the compilation timing given in Table VI.1.

Table VI.1. – Details of compilation times of the COLTRANE method software

		Comparison with `ONE-SHOT v3.2`
Date submitted	05/05/2020 13:21 UTC+2	N/A
Date results were retrieved	05/05/2020 15:46 UTC+2	N/A
Time waiting in queue	04:35	- 04:13
Time compiling	02:20:18	- 26:27

The details on the compilation times for the compiling steps are given in Table VI.2. The device utilisation of the `Xilinx`'s FPGA `Kintex-7 325T` [Xilinx325T Documentation, 2019] given in Table VI.3. Finally, the compilation results on the timing precision is given in Table VI.4.

Table VI.2. – Compilation timing for each compilation steps of the COLTRANE method software

		Comparison with `ONE-SHOT v3.2`
Generate Xilinx IP	01:44:10	+06:24
Synthesise - Vivado	17:37	- 19:24
Optimise Logic	02:08	- 01:57
Place	06:07	- 04:29
Optimise Timing	01:22	- 00:59
Route	04:39	- 05:03
Generate Programming File	03:15	- 01:17

Table VI.3. – Device utilisation after compilation of the COLTRANE method software

			Comparison with `ONE-SHOT v3.2`
Total Slices	39.6%	20179 out of 50950	- 24.9%
Slice Registers	9.7%	39726 out of 407600	- 8.3%
Slice LUTs	30.2%	61638 out of 203800	- 14.6%
Block RAMs	50.1%	223 out of 445	+19.3%
DSP48s	42.7%	359 out of 840	- 10.5%

Table VI.4. – Clock timing results after compilation of the COLTRANE method software

40 MHz Onboard Clock	40,00 MHz	(Met MHz maximum)
80 MHz Derived Clock	80,00 MHz	(Met MHz maximum)

B

Bibliography

Bibliography

[Abeida et al., 2013] Abeida, H., Zhang, Q., Li, J., and Merabtine, N. (2013). Iterative sparse asymptotic minimum variance based approaches for array processing. *IEEE Transactions on Signal Processing*, 61(4):933–944.

[Adler and Guardo, 1996] Adler, A. and Guardo, R. (1996). Electrical impedance tomography: regularized imaging and contrast detection. *IEEE Transactions on Medical Imaging*, 15(2):170–179.

[Adler and Lionheart, 2006] Adler, A. and Lionheart, W. R. B. (2006). Uses and abuses of EIDORS: an extensible software base for EIT. *Physiological Measurement*, 27(5):S25–S42.

[Aksan, 2008] Aksan, N. (2008). International Standard Problems and Small Break Loss-of-Coolant Accident (SBLOCA). *Science and Technology of Nuclear Installations*, 2008.

[Ammari et al., 2017] Ammari, H., Triki, F., and Tsou, C. H. (2017). Numerical determination of anomalies in multifrequency electrical impedance tomography. Research Report 2017-21, Seminar für Angewandte Mathematik, Eidgenössische Technische Hochschule, CH-8092 Zürich, Switzerland.

[Andersson and Holcombe, 2017] Andersson, P. and Holcombe, S. (2017). A computerized method (upprec) for quantitative analysis of irradiated nuclear fuel assemblies with gamma emission tomography at the halden reactor. *Annals of Nuclear Energy*, 110:88 – 97.

[Arakawa et al., 2018] Arakawa, M., Kanai, H., Ishikawa, K., Nagaoka, R., Kobayashi, K., and Saijo, Y. (2018). A method for the design of ultrasonic devices for scanning acoustic microscopy using impulsive signals. *Ultrasonics*, 84:172 – 179.

[Asfaw and Adler, 2005] Asfaw, Y. and Adler, A. (2005). Automatic detection of detached and erroneous electrodes in electrical impedance tomography. *Physiological Measurement*, 26(2):S175–S183.

[Banasiak and Soleimani, 2010] Banasiak, R. and Soleimani, M. (2010). Shape based reconstruction of experimental data in 3d electrical capacitance tomography. *NDT & E International*, 43(3):241 – 249.

[Barber and Brown, 1984] Barber, D. C. and Brown, B. H. (1984). Applied potential tomography. *Journal of Physics E: Scientific Instruments*, 17(9):723–733.

[Baumgartner et al., 1989] Baumgartner, R. N., Chumlea, W. C., and Roche, A. F. (1989). Estimation of body composition from bioelectric impedance of body segments. *The American Journal of Clinical Nutrition*, 50(2):221–226.

[Bellis et al., 2012] Bellis, C., Constantinescu, A., Coquet, T., Jaravel, T., and Lechleiter, A. (2012). A non-iterative sampling approach using noise subspace projection for EIT. *Inverse Problems*, 28(7):075015.

[Berrington de Gonzalez et al., 2009] Berrington de Gonzalez, A., Mahesh, M., Kim, K.-P., Bhargavan, M., Lewis, R., Mettler, F., and Land, C. (2009). Projected Cancer Risks From Computed Tomographic Scans Performed in the United States in 2007. *Archives of Internal Medicine*, 169(22):2071–2077.

[Betta et al., 2000] Betta, G., Liguori, C., and Pietrosanto, A. (2000). Propagation of uncertainty in a discrete fourier transform algorithm. *Measurement*, 27:231–239.

[Biard, 2013] Biard, B. (2013). Quantitative analysis of the fission product distribution in a damaged fuel assembly using gamma-spectrometry and computed tomography for the phébus fpt3 test. *Nuclear Engineering and Design*, 262:469 – 483.

[Bignold et al., 1971] Bignold, G. J., Brewer, A. D., and Hearn, B. (1971). Specific conductivity and ionic product of water between 50 and 271 °c. *Trans. Faraday Soc.*, 67:2419–2430.

[Binns et al., 2001] Binns, R., Lyons, A. R. A., Peyton, A. J., and Pritchard, W. D. N. (2001). Imaging molten steel flow profiles. *Measurement Science and Technology*, 12(8):1132–1138.

[Boas and Fleischmann, 2011] Boas, F. E. and Fleischmann, D. (2011). Evaluation of two iterative techniques for reducing metal artifacts in computed tomography. *Radiology*, 259(3):894–902. PMID: 21357521.

[Borcea, 2002] Borcea, L. (2002). Electrical impedance tomography. *Inverse Problems*, 18(6):R99–R136.

[Breckon and Pidcock, 1987] Breckon, W. R. and Pidcock, M. K. (1987). Mathematical aspects of impedance imaging. *Clinical Physics and Physiological Measurement*, 8(4A):77–84.

[British Electricity International, 1992] British Electricity International (1992). *Nuclear Power Generation (Third Edition)*. British Electricity International. Pergamon, Oxford, third edition edition.

[Brooks and Di Chiro, 1976] Brooks, R. and Di Chiro, G. (1976). Principles of computer assisted tomography (CAT) in radiographic and radioisotopic imaging. *Physics in Medicine and Biology*, 21(5):689–732.

[Brown et al., 1995] Brown, R., Venters, R., Tang, P., and Spicer, L. (1995). A test for scaler coupling between heteronuclei using gradient-enhanced proton-detected hmqc spectroscopy. *Journal of Magnetic Resonance, Series A*, 113(1):117 – 119.

[Buffiere and Maire, 2014] Buffiere, J. Y. and Maire, E. (2014). *Imagerie 3D en mecanique des materiaux.* Hermes science publications ed.

[Buxton, 2009] Buxton, R. B. (2009). *Introduction to Functional Magnetic Resonance Imaging: Principles and Techniques*. Cambridge University Press, 2 edition.

[Calderón, 2006] Calderón, A. P. (2006). On an inverse boundary value problem. *Computational & Applied Mathematics*, 25:133 – 138.

[Changhua et al., 2005] Changhua, M., Lihui, P., Danya, Y., and Deyun, X. (2005). Image reconstruction using a genetic algorithm for electrical capacitance tomography. *Tsinghua Science and Technology*, 10(5):587–592.

[Chavhan et al., 2009] Chavhan, G. B., Babyn, P. S., Thomas, B., Shroff, M. M., and Haacke, E. M. (2009). Principles, techniques, and applications of t2*-based mr imaging and its special applications. *RadioGraphics*, 29(5):1433–1449. PMID: 19755604.

[Cheney and Isaacson, 1992] Cheney, M. and Isaacson, D. (1992). Distinguishability in impedance imaging. *IEEE Transactions on Biomedical Engineering*, 39(8):852–860.

[Cheney and Isaacson, 1995] Cheney, M. and Isaacson, D. (1995). Issues in electrical impedance imaging. *IEEE Computational Science and Engineering*, 2(4):53–62.

[Cheney et al., 1999] Cheney, M., Isaacson, D., and Newell, J. (1999). Electrical impedance tomography. *SIAM Review*, 41(1):85–101.

[Cheney et al., 1990] Cheney, M., Isaacson, D., Newell, J. C., Simske, S., and Goble, J. (1990). Noser: An algorithm for solving the inverse conductivity problem. *International Journal of Imaging Systems and Technology*, 2(2):66–75.

[Cheng et al., 1989] Cheng, K.-S., Isaacson, D., Newell, J. C., and Gisser, D. G. (1989). Electrode models for electric current computed tomography. *IEEE Transactions on Biomedical Engineering*, 36(9):918–924.

[Cui et al., 2011] Cui, Z., Wang, H., Chen, Z., Xu, Y., and Yang, W. (2011). A high-performance digital system for electrical capacitance tomography. *Measurement Science and Technology*, 22:055503.

[Dalrymple et al., 2005] Dalrymple, N. C., Prasad, S. R., Freckleton, M. W., and Chintapalli, K. N. (2005). Introduction to the language of three-dimensional imaging with multidetector ct. *RadioGraphics*, 25(5):1409–1428. PMID: 16160120.

[Dang, 2020] Dang, C. (2020). *Two-Phase Flow Imaging and Fast Feature Extraction by Electrical Impedance Tomography*. Phd thesis, Ecole Centrale Marseille.

[Dang et al., 2019] Dang, C., Darnajou, M., Bellis, C., Ricciardi, G., Schmidt, H., and Bourennane, S. (2019). Numerical and experimental analysis of the correlation between EIT data eigenvalues and two-phase flow phase fraction. *Measurement Science and Technology*, 31(1):015302.

[D'Angelo et al., 1995] D'Angelo, P., Leroy, C., Pensotti, S., and Rancoita, P. (1995). High resolution silicon collimated photon imaging calorimeter for diagnostic in nuclear medicine. *Nuclear Physics B - Proceedings Supplements*, 44(1):719 – 728.

[Darnajou et al., 2017] Darnajou, M., Dang, C., Ricciardi, G., Bourennane, S., Bellis, C., and Schmidt, H. (2017). The design of electrical impedance tomography detectors in nuclear industry. In *Proceedings of the 9th World Congress on Industrial Process Tomography*, pages 457 – 465.

[Darnajou et al., 2019] Darnajou, M., Dupré, A., Dang, C., Ricciardi, G., Bourennane, S., and Bellis, C. (2019). On the implementation of simultaneous multi-frequency excitations and measurements for electrical impedance tomography. *Sensors*, 19(17).

[Darnajou et al., 2020] Darnajou, M., Dupré, A., Dang, C., Ricciardi, G., Bourennane, S., Bellis, C., and Mylvaganam, S. (2020). High Speed EIT with Multifrequency Excitation using FPGA and Response Analysis using FDM. *IEEE Sensors*.

[Donadio et al., 2008] Donadio, C., Halim, A. B., Caprio, F., Grassi, G., Khedr, B., and Mazzantini, M. (2008). Single- and multi-frequency bioelectrical impedance analyses to analyse body composition in maintenance haemodialysis patients: comparison with dual-energy x-ray absorptiometry. *Physiological Measurement*, 29(6):S517–S524.

[Dougall et al., 2004] Dougall, N., Bruggink, S., and Ebmeier, K. (2004). Systematic Review of the Diagnostic Accuracy of 99mTc-HMPAO-SPECT in Dementia. *American Journal of Geriatric Psychiatry*, 12(6):554?570.

[Dowrick and Holder, 2018] Dowrick, T. and Holder, D. (2018). Phase division multiplexed EIT for enhanced temporal resolution. *Physiological Measurement*, 39(3):034005.

[Dupré, 2017] Dupré, A. (2017). *Electrical impedance tomography for void fraction measurements of harsh two-phase flows : prototype development and reconstruction techniques*. Phd thesis, Ecole Centrale Marseille.

[Dupré et al., 2020] Dupré, A., Darnajou, M., Ricciardi, G., and Mylvaganam, S. (2020). Effects of Transients during Continuous and Simultaneous Excitation of Electrodes in Electrical Impedance Tomography (Submitted). *IEEE Sensors*.

[Dupré and Mylvaganam, 2018] Dupré, A. and Mylvaganam, S. (2018). A simultaneous and continuous excitation method for high-speed electrical impedance tomography with reduced transients and noise sensitivity. *Sensors*, 18(4).

[Dupré et al., 2017a] Dupré, A., Ricciardi, G., and Bourennane, S. (2017a). Novel approach for analysis and design of high-speed electrical impedance tomographic system for void fraction measurements in fast two-phase flows. *IEEE Sensors Journal*, 17(14):4472–4482.

[Dupré et al., 2017b] Dupré, A., Ricciardi, G., Bourennane, S., and Mylvaganam, S. (2017b). Electrical capacitance-based flow regimes identification: Multiphase experiments and sensor modeling. *IEEE Sensors Journal*, 17(24):8117–8128.

[Dupré, A. and Ricciardi, G. and Bourennane, S., 2016] Dupré, A. and Ricciardi, G. and Bourennane, S. (2016). Developement of a prototype device for imaging two-phase flows via electrical impedance tomography. *SWINTH*.

[Eaton, 2008] Eaton, J. (2008). *GNU Octave Manual*. Network Theory Ltd. Bristol, UK.

[Erasmus et al., 2004] Erasmus, L., Hurter, D., Naude, M., Kritzinger, H., and Acho, S. (2004). A short overview of mri artefacts. *South African Journal of Radiology*, 8(2):13.

[Evans et al., 2015] Evans, L., Margetts, L., Casalegno, V., Lever, L., Bushell, J., Lowe, T., Wallwork, A., Young, P., Lindemann, A., Schmidt, M., and Mummery, P. (2015). Transient thermal finite element analysis of cfc–cu iter monoblock using x-ray tomography data. *Fusion Engineering and Design*, 100:100 – 111.

[Fang, 2004] Fang, W. (2004). A nonlinear image reconstruction algorithm for electrical capacitance tomography. *Measurement Science and Technology*, 15(10):2124–2132.

[Fishman et al., 2006] Fishman, E. K., Ney, D. R., Heath, D. G., Corl, F. M., Horton, K. M., and Johnson, P. T. (2006). Volume rendering versus maximum intensity projection in ct angiography: What works best, when, and why. *RadioGraphics*, 26(3):905–922. PMID: 16702462.

[Flitton et al., 2013] Flitton, G., Breckon, T. P., and Megherbi, N. (2013). A comparison of 3d interest point descriptors with application to airport baggage object detection in complex ct imagery. *Pattern Recognition*, 46(9):2420 – 2436.

[Gamio, 2002] Gamio, J. C. (2002). A comparative analysis of single- and multiple-electrode excitation methods in electrical capacitance tomography. *Measurement Science and Technology*, 13(12):1799–1809.

[George et al., 2000] George, D., Torczynski, J., Shollenberger, K., O'Hern, T., and Ceccio, S. (2000). Validation of electrical-impedence tomography for measurements for material distribution in two-phase flows. *International Journal of Multiphase Flow*, 26:549–581.

[George, 1996] George, P. (1996). Automatic mesh generation and finite element computation. In *Finite Element Methods (Part 2), Numerical Methods for Solids (Part 2)*, volume 4 of *Handbook of Numerical Analysis*, pages 69 – 190. Elsevier.

[Giovannetti et al., 2016] Giovannetti, G., Guerrini, A., and Salvadori, P. A. (2016). Magnetic resonance spectroscopy and imaging for the study of fossils. *Magnetic Resonance Imaging*, 34(6):730 – 742.

[Gisser et al., 1990] Gisser, D., Isaacson, D., and Newell, J. (1990). Electric current computed tomography and eigenvalues. *SIAM Journal on Applied Mathematics*, 50(6):1623–1634.

[Gisser et al., 1988] Gisser, D. G., Isaacson, D., and Newell, J. C. (1988). Theory and performance of an adaptive current tomography system. *Clinical Physics and Physiological Measurement*, 9(4A):35–41.

[Goncharsky and Romanov, 2013] Goncharsky, A. V. and Romanov, S. Y. (2013). Supercomputer technologies in inverse problems of ultrasound tomography. *Inverse Problems*, 29(7):075004.

[Good et al., 1997] Good, I. J., Kotz, S., and Johnson, N. L. (1997). *Introduction to Cooley and Tukey (1965) An Algorithm for the Machine Calculation of Complex Fourier Series*, pages 201–216. Springer New York, New York, NY.

[Goren et al., 2018] Goren, N., Avery, J., Dowrick, T., Mackle, E., Witkowska-Wrobel, A., Werring, D., and Holder, D. (2018). Multi-frequency electrical impedance tomography and neuroimaging data in stroke patients. *Scientific Data*, 5(1):180112.

[Granot et al., 2007] Granot, Y., Ivorra, A., and Rubinsky, B. (2007). Frequency-division multiplexing for electrical impedance tomography in biomedical applications. *International Journal of Biomedical Imaging*, 2007:201 – 232.

[Green, 1990] Green, P. J. (1990). Bayesian reconstructions from emission tomography data using a modified em algorithm. *IEEE Transactions on Medical Imaging*, 9(1):84–93.

[Greenleaf and Bahn, 1981] Greenleaf, J. F. and Bahn, R. C. (1981). Clinical imaging with transmissive ultrasonic computerized tomography. *IEEE Transactions on Biomedical Engineering*, BME-28(2):177–185.

[Griffiths, 2001] Griffiths, H. (2001). Magnetic induction tomography. *Measurement Science and Technology*, 12(8):1126–1131.

[Halter et al., 2008] Halter, R. J., Hartov, A., and Paulsen, K. D. (2008). A broadband high-frequency electrical impedance tomography system for breast imaging. *IEEE Transactions on Biomedical Engineering*, 55(2):650–659.

[Hamidipour and Larachi, 2010] Hamidipour, M. and Larachi, F. (2010). Dynamics of filtration in monolith reactors using electrical capacitance tomography. *Chemical Engineering Science*, 65(1):504 – 510. 20th International Symposium in Chemical Reaction Engineering—Green Chemical Reaction Engineering for a Sustainable Future.

[Hanke and Bruhl, 2003] Hanke, M. and Bruhl, M. (2003). Recent progress in electrical impedance tomography. *Inverse Problems*, 19(6):S65–S90.

[Hecht, 2012] Hecht, F. (2012). New development in FreeFem++. *J. Numer. Math.*, 20(3-4):251–265.

[Hurd and John, 1991] Hurd, R. E. and John, B. K. (1991). Gradient-enhanced proton-detected heteronuclear multiple-quantum coherence spectroscopy. *Journal of Magnetic Resonance (1969)*, 91(3):648 – 653.

[Igney et al., 2005] Igney, C. H., Watson, S., Williams, R. J., Griffiths, H., and Dössel, O. (2005). Design and performance of a planar-array MIT system with normal sensor alignment. *Physiological Measurement*, 26(2):S263–S278.

[Isaacson, 1986] Isaacson, D. (1986). Distinguishability of conductivities by electric current computed tomography. *IEEE Transactions on Medical Imaging*, 5(2):91–95.

[Isaacson et al., 1991] Isaacson, D., Cheney, M., and Newell, J. (1991). Problems in impedance imaging. In Päivärinta, L. and Somersalo, E., editors, *Inverse Problems in Mathematical Physics*, pages 62–70, Berlin, Heidelberg. Springer Berlin Heidelberg.

[Isaacson and Cheny, 1991] Isaacson, D. and Cheny, M. (1991). Effects of measurement precision and finite numbers of electrodes on linear impedance imaging algorithms. *SIAM Journal on Applied Mathematics*, 51(6):1705–1731.

[Jacobs et al., 2008] Jacobs, S., Grunert, R., Mohr, F. W., and Falk, V. (2008). 3D-Imaging of cardiac structures using 3D heart models for planning in heart surgery: a preliminary study. *Interactive CardioVascular and Thoracic Surgery*, 7(1):6–9.

[Jang et al., 2006] Jang, J. D., Lee, S. H., Kim, K. Y., and Choi, B. Y. (2006). Modified iterative landweber method in electrical capacitance tomography. *Measurement Science and Technology*, 17(7):1909–1917.

[Jeong, 2002] Jeong, H. Y. (2002). Prediction of counter-current flow limitation at hot leg pipe during a small-break loca. *Annals of Nuclear Energy*, 29(5):571 – 583.

[Jha et al., 2014] Jha, D., Sarensen, H. O., Dobberschotz, S., Feidenhans'l, R., and Stipp, S. L. S. (2014). Adaptive center determination for effective suppression of ring artifacts in tomography images. *Applied Physics Letters*, 105(14):143107.

[Jun and Yoon, 2017] Jun, K. and Yoon, S. (2017). Alignment solution for ct image reconstruction using fixed point and virtual rotation axis. *Scientific Reports*, 7(1):41218.

[Kak and Slaney, 2001] Kak, A. C. and Slaney, M. (2001). *Principles of Computerized Tomographic Imaging*. Society for Industrial and Applied Mathematics.

[Kauppinen et al., 2006] Kauppinen, P., Hyttinen, J., and Malmivuo, J. (2006). Sensitivity distribution visualizations of impedance tomography measurement strategies. *International Journal of Bioelectromagnetism*, 8:VII/1 – VII/9.

[Kelloff et al., 2005] Kelloff, G. J., Hoffman, J. M., Johnson, B., Scher, H. I., Siegel, B. A., Cheng, E. Y., Cheson, B. D., O'Shaughnessy, J., Guyton, K. Z., Mankoff, D. A., Shankar, L., Larson, S. M., Sigman, C. C., Schilsky, R. L., and Sullivan, D. C. (2005). Progress and promise of fdg-pet imaging for cancer patient management and oncologic drug development. *Clinical Cancer Research*, 11(8):2785–2808.

[Kerrouche et al., 2001] Kerrouche, N., McLeod, C. N., and Lionheart, W. R. B. (2001). Time series of EIT chest images using singular value decomposition and fourier transform. *Physiological Measurement*, 22(1):147–157.

[Khan et al., 2013] Khan, S., Borsic, A., Manwaring, P., Hartov, A., and Halter, R. (2013). FPGA based high speed data acquisition system for electrical impedance tomography. *Journal of Physics: Conference Series*, 434:012081.

[Khan et al., 2015] Khan, S., Manwaring, P., Borsic, A., and Halter, R. (2015). Fpga-based voltage and current dual drive system for high frame rate electrical impedance tomography. *IEEE Transactions on Medical Imaging*, 34(4):888–901.

[Kharagpur, 2018] Kharagpur, I. (2018). *Data Communication Fundamentals, Module 2*. Version 2 CSE.

[Kidav et al., 2019] Kidav, J. U., Sivamangai, N. M., Pillai, M. P., and M, S. R. (2019). Architecture and fpga prototype of cycle stealing dma array signal processor for ultrasound sector imaging systems. *Microprocessors and Microsystems*, 64:53 – 72.

[Kim et al., 2001] Kim, M. C., Kim, S., Kim, K. Y., and Lee, Y. J. (2001). Regularization methods in electrical impedance tomography technique for the two-phase flow visualization. *International Communications in Heat and Mass Transfer*, 28(6):773 – 782.

[Korjenevsky et al., 2000] Korjenevsky, A., Cherepenin, V., and Sapetsky, S. (2000). Magnetic induction tomography: experimental realization. *Physiological Measurement*, 21(1):89–94.

[Kortschak et al., 2006] Kortschak, B., Wegleiter, H., and Brandstätter, B. (2006). Formulation of cost functionals for different measurement principles in nonlinear capacitance tomography. *Measurement Science and Technology*, 18(1):71–78.

[Kotre, 1989] Kotre, C. J. (1989). A sensitivity coefficient method for the reconstruction of electrical impedance tomograms. *Clinical Physics and Physiological Measurement*, 10(3):275–281.

[Kotre, 1993] Kotre, C. J. (1993). *Studies of image reconstruction methods for electrical impedance tomography*. Phd thesis, Newcastle University.

[Kretzschmar and Wagner, 2009] Kretzschmar, H.-J. and Wagner, W. (2009). *International Steam Tables*. Springer-Verlag GmbH Germany, 3 edition.

[Kryszyn et al., 2017] Kryszyn, J., Wráblewski, P., Stosio, M., Wanta, D., Olszewski, T., and Smolik, W. (2017). Architecture of evt4 data acquisition system for electrical capacitance tomography. *Measurement*, 101:28 – 39.

[Kuhl et al., 1999] Kuhl, D., Koeppe, R., Minoshima, S., Snyder, S., Ficaro, E., Foster, N., Frey, K., and Kilbourn, M. (1999). In vivo mapping of cerebral acetylcholinesterase activity in aging and alzheimer's disease. *Neurology*, 52(4):691–691.

[Landheer et al., 2020] Landheer, K., Schulte, R. F., Treacy, M. S., Swanberg, K. M., and Juchem, C. (2020). Theoretical description of modern 1h in vivo magnetic resonance spectroscopic pulse sequences. *Journal of Magnetic Resonance Imaging*, 51(4):1008–1029.

[Lei et al., 2011] Lei, J., Liu, S., Guo, H., Li, Z., Li, J., and Han, Z. (2011). An image reconstruction algorithm based on the semiparametric model for electrical capacitance tomography. *Computers and Mathematics with Applications*, 61(9):2843 – 2853.

[Lei et al., 2013] Lei, J., Liu, S., Wang, X., and Liu, Q. (2013). An image reconstruction algorithm for electrical capacitance tomography based on robust principle component analysis. *Sensors*, 13(2):2076–2092.

[Leroy and Rancoita, 2009] Leroy, C. and Rancoita, P.-G. (2009). *Principles of Radiation Interaction in Matter and Detection*. World Scientific, 2nd edition.

[Light, 1984] Light, T. S. (1984). Temperature dependence and measurement of resistivity of pure water. *Analytical Chemistry*, 56(7):1138–1142.

[Lionheart, 2004] Lionheart, W. R. B. (2004). EIT reconstruction algorithms: pitfalls, challenges and recent developments. *Physiological Measurement*, 25(1):125–142.

[Liu et al., 2007] Liu, C. H., Kim, Y. R., Ren, J. Q., Eichler, F., Rosen, B. R., and Liu, P. K. (2007). Imaging cerebral gene transcripts in live animals. *Journal of Neuroscience*, 27(3):713–722.

[Liu et al., 2008] Liu, S., Chen, Q., Xiong, X., Zhang, Z., and Lei, J. (2008). Preliminary study on ECT imaging of flames in porous media. *Measurement Science and Technology*, 19(9):094017.

[Lockstone, 1993] Lockstone, D. (1993). 20 - frequency division multiplexing. In Mazda, F., editor, *Telecommunications Engineer's Reference Book*, pages 20–1 – 20–22. Butterworth-Heinemann.

[Mager et al., 2008] Mager, J. R., Sibley, S. D., Beckman, T. R., Kellogg, T. A., and Earthman, C. P. (2008). Multifrequency bioelectrical impedance analysis and

bioimpedance spectroscopy for monitoring fluid and body cell mass changes after gastric bypass surgery. *Clinical Nutrition*, 27(6):832–841.

[Makkawi and Ocone, 2007] Makkawi, Y. and Ocone, R. (2007). Integration of ect measurements with hydrodynamic modelling of conventional gas–solid bubbling bed. *Chemical Engineering Science*, 62(16):4304 – 4315.

[Malone et al., 2014] Malone, E., dos Santos, G. S., Holder, D., and Arridge, S. (2014). Multifrequency electrical impedance tomography using spectral constraints. *IEEE Transactions on Medical Imaging*, 33(2):340–350.

[Mansfield and Grannell, 1975] Mansfield, P. and Grannell, P. K. (1975). "diffraction" and microscopy in solids and liquids by nmr. *Phys. Rev. B*, 12:3618–3634.

[Marshall, 1987] Marshall, W. (1987). Electrical conductance of liquid and supercritical water evaluated from 0/sup 0/c and 0. 1 mpa to high temperatures and pressures: Reduced-state relationships. *J. Chem. Eng. Data; (United States)*, 32(2).

[Masselli and Gualdi, 2012] Masselli, G. and Gualdi, G. (2012). Mr imaging of the small bowel. *Radiology*, 264(2):333–348. PMID: 22821694.

[Max and Lacoume, 2004] Max, J. and Lacoume, J. (2004). *Méthodes et techniques de traitement du signal - 5ème édition*. Sciences Sup, Dunod, Grenoble, France.

[Megherbi et al., 2010] Megherbi, N., Flitton, G. T., and Breckon, T. P. (2010). A classifier based approach for the detection of potential threats in ct based baggage screening. In *2010 IEEE International Conference on Image Processing*, pages 1833–1836.

[Miller and Roysam, 1991] Miller, M. I. and Roysam, B. (1991). Bayesian image reconstruction for emission tomography incorporating good's roughness prior on massively parallel processors. *Proceedings of the National Academy of Sciences*, 88(8):3223–3227.

[Miller and Snyder, 1987] Miller, M. I. and Snyder, D. L. (1987). The role of likelihood and entropy in incomplete-data problems: Applications to estimating point-process intensities and toeplitz constrained covariances. *Proceedings of the IEEE*, 75(7):892–907.

[Mita and Takiguchi, 2018] Mita, N. and Takiguchi, T. (2018). Principle of ultrasonic tomography for concrete structures and non-destructive inspection of concrete cover for reinforcement. *Pacific Journal of Mathematics for Industry*, 10(1):6.

[Monk, 2003] Monk, P. (2003). *Finite Element Methods for Maxwell's Equations*. Oxford University Press, New York.

[Morales et al., 2015] Morales, D., Lopez-Ruiz, N., Castillo, E., Garcia, A., and Martinez Olmos, A. (2015). Adaptative ECT System Based on Reconfigurable Electronics. *Measurement*, 74:238–245.

[Mueller and Siltanen, 2012] Mueller, J. L. and Siltanen, S. (2012). *Linear and Nonlinear Inverse Problems with Practical Applications*. Society for Industrial and Applied Mathematics, Philadelphia, PA, USA.

[Munk and Wunsch, 1979] Munk, W. and Wunsch, C. (1979). Ocean acoustic tomography: a scheme for large scale monitoring. *Deep Sea Research Part A. Oceanographic Research Papers*, 26(2):123 – 161.

[National Research Council, 1996] National Research Council (1996). *Mathematics and Physics of Emerging Biomedical Imaging*. The National Academies Press, Washington, DC.

[Necus et al., 2019] Necus, J., Sinha, N., Smith, F. E., Thelwall, P. E., Flowers, C. J., Taylor, P. N., Blamire, A. M., Cousins, D. A., and Wang, Y. (2019). White matter microstructural properties in bipolar disorder in relationship to the spatial distribution of lithium in the brain. *Journal of Affective Disorders*, 253:224 – 231.

[NI-9039 Documentation, 2016] NI-9039 Documentation (2016). *Embedded CompactRIO Controller with Real-Time Processor and Reconfigurable FPGA*.

[NI-9223 Documentation, 2016] NI-9223 Documentation (2016). *4 AI, ±10 V, 16 Bit, 1 MS/s/ch Simultaneous*.

[NI-9262 Documentation, 2017] NI-9262 Documentation (2017). *1 MS/s/ch Simultaneous, ±10 V, 6-Channel C Series Voltage Output Module*.

[Niaz et al., 2018] Niaz, A., Sultana, S., Aslam, A., and Kalsom, A. (2018). Boron concentration in irrigation water used for wheat-cotton cropping system in alkaline calcareous soils of southern punjab. *Sci Lett*, pages 6–12.

[Niedostatkiewicz et al., 2009] Niedostatkiewicz, M., Tejchman, J., Chaniecki, Z., and Grudzień, K. (2009). Determination of bulk solid concentration changes during granular flow in a model silo with ect sensors. *Chemical Engineering Science*, 64(1):20 – 30.

[Nieuwenhove et al., 2015] Nieuwenhove, V. V., Beenhouwer, J. D., Carlo, F. D., Mancini, L., Marone, F., and Sijbers, J. (2015). Dynamic intensity normalization using eigen flat fields in x-ray imaging. *Opt. Express*, 23(21):27975–27989.

[Oldendorf, 1978] Oldendorf, W. H. (1978). The quest for an image of brain. *Neurology*, 28(6):517–517.

[Ortiz-Aleman et al., 2004] Ortiz-Aleman, C., Martin, R., and Gamio, J. C. (2004). Reconstruction of permittivity images from capacitance tomography data by using very fast simulated annealing. *Measurement Science and Technology*, 15(7):1382–1390.

[Osterman et al., 2000] Osterman, K. S., Kerner, T. E., Williams, D. B., Hartov, A., Poplack, S. P., and Paulsen, K. D. (2000). Multifrequency electrical impedance imaging: preliminaryin vivoexperience in breast. *Physiological Measurement*, 21(1):99–109.

[Pacak et al., 2001] Pacak, K., Eisenhofer, G., Carrasquillo, J. A., Chen, C. C., Li, S.-T., and Goldstein, D. S. (2001). 6-[^{18}f]fluorodopamine positron emission tomographic (pet) scanning for diagnostic localization of pheochromocytoma. *Hypertension*, 38(1):6–8.

[Palle et al., 2016] Palle, S. S., Møllehave, L. T., Taheri-Kadkhoda, Z., Johansen, S., Larsen, L., Hansen, J. W., Jensen, N. K. G., Elingaard, A. O., Møller, A. H., Larsen, K., and Andersen, J. R. (2016). Multi-frequency bioelectrical impedance analysis

(bia) compared to magnetic resonance imaging (mri) for estimation of fat-free mass in colorectal cancer patients treated with chemotherapy. *Clinical Nutrition ESPEN*, 16:8–15.

[Payne, 2013] Payne, E. M. (2013). Imaging techniques in conservation. *Journal of Conservation and Museum Studies*, 10(2):17?29.

[Pessis et al., 2013] Pessis, E., Campagna, R., Sverzut, J.-M., Bach, F., Rodallec, M., Guerini, H., Feydy, A., and Drape, J.-L. (2013). Virtual monochromatic spectral imaging with fast kilovoltage switching: Reduction of metal artifacts at ct. *RadioGraphics*, 33(2):573–583. PMID: 23479714.

[Peyton et al., 1996] Peyton, A. J., Yu, Z. Z., Lyon, G., Al-Zeibak, S., Ferreira, J., Velez, J., Linhares, F., Borges, A. R., Xiong, H. L., Saunders, N. H., and Beck, M. S. (1996). An overview of electromagnetic inductance tomography: description of three different systems. *Measurement Science and Technology*, 7(3):261–271.

[Pollak, 1974] Pollak, V. (1974). An equivalent diagram for the interface impedance of metal needle electrodes. *Medical and biological engineering*, 12(4):454–459.

[Polydorides and Lionheart, 2002] Polydorides, N. and Lionheart, W. R. B. (2002). A matlab toolkit for three-dimensional electrical impedance tomography: a contribution to the electrical impedance and diffuse optical reconstruction software project. *Measurement Science and Technology*, 13(12):1871–1883.

[Poverud, 2019] Poverud, A. T. (2019). Flow-Analytics using Multiphase Flow Rig with Multimodal Sensor Suite with focus on Void Fraction, Water-Cut and Flow Regimes. Master's thesis, Faculty of Technology, University of South-Eastern Norway, Porsgrunn, Norway.

[Qi and Leahy, 2006] Qi, J. and Leahy, R. M. (2006). Iterative reconstruction techniques in emission computed tomography. *Physics in Medicine and Biology*, 51(15):R541–R578.

[Querol et al., 2015] Querol, A., Gallardo, S., and Verdú, G. (2015). Simulation of a sbloca in a hot leg. scaling considerations and application to a nuclear power plant. *Nuclear Engineering and Design*, 283:81 – 99. SI:NENE 2013.

[Quirás-Olozábal et al., 2016] Quirás-Olozábal, A., de-la Rosa, J. G., Cifredo-Chacán, M., and Sierra-Fernández, J. (2016). A novel FPGA-based system for real-time calculation of the Spectral Kurtosis: A prospective application to harmonic detection. *Measurement*, 86:101 – 113.

[Richmond, 2004] Richmond, C. (2004). Sir godfrey hounsfield. *BMJ*, 329(7467):687.

[Rimpilainen et al., 2012] Rimpilainen, V., Heikkinen, L. M., and Vauhkonen, M. (2012). Moisture distribution and hydrodynamics of wet granules during fluidized-bed drying characterized with volumetric electrical capacitance tomography. *Chemical Engineering Science*, 75:220 – 234.

[Rimpilainen et al., 2011] Rimpilainen, V., Poutiainen, S., Heikkinen, L. M., Savolainen, T., Vauhkonen, M., and Ketolainen, J. (2011). Electrical capacitance tomography as a

monitoring tool for high-shear mixing and granulation. *Chemical Engineering Science*, 66(18):4090 – 4100.

[S-TEC Sensor Technology, 2019] S-TEC Sensor Technology (2019). *Installation, Operation & Maintenance Manual, Density Transmitter DT-9300*.

[Saiful et al., 2015] Saiful, M., Mansor, B., Zakaria, Z., Balkhis, I., Rahim, R. A., Sahib, M. F. A., Yunos, Y. M., Sahlan, S., Bunyamin, S., Abas, K. H., Ishak, M. H. I., and Danapalasingam, K. A. (2015). Magnetic induction tomography: A brief review. *Jurnal Teknologi*, 73(3).

[Salmi, 2003] Salmi, J. A. (2003). Body Composition Assessment with Segmental Multifrequency Bioimpedance Method. Master's thesis, Department of Physiology, University of Kuopio, Kuopio, Finland.

[Sanchez Correa and David, 2018] Sanchez Correa, R. and David, J. P. (2018). Ultra-low latency communication channels for FPGA-based HPC cluster. *Integration*, 63:41 – 55.

[Scharfetter et al., 2008] Scharfetter, H., Kostinger, A., and Issa, S. (2008). Hardware for quasi-single-shot multifrequency magnetic induction tomography (MIT): the graz mk2 system. *Physiological Measurement*, 29(6):S431–S443.

[Scharfetter et al., 2001] Scharfetter, H., Lackner, H. K., and Rosell, J. (2001). Magnetic induction tomography: hardware for multi-frequency measurements in biological tissues. *Physiological Measurement*, 22(1):131–146.

[Scuffham et al., 2012] Scuffham, J. W., Wilson, M. D., Seller, P., Veale, M. C., Sellin, P. J., Jacques, S. D. M., and Cernik, R. J. (2012). A CdTe detector for hyperspectral SPECT imaging. *Journal of Instrumentation*, 7(08):P08027–P08027.

[Semelka et al., 2007] Semelka, R. C., Armao, D. M., Elias Junior, J., and Huda, W. (2007). Imaging strategies to reduce the risk of radiation in ct studies, including selective substitution with mri. *Journal of Magnetic Resonance Imaging*, 25(5):900–909.

[Shepp and Vardi, 1982] Shepp, L. A. and Vardi, Y. (1982). Maximum likelihood reconstruction for emission tomography. *IEEE Transactions on Medical Imaging*, 1(2):113–122.

[Sijbers and Postnov, 2004] Sijbers, J. and Postnov, A. (2004). Reduction of ring artefacts in high resolution micro-CT reconstructions. *Physics in Medicine and Biology*, 49(14):N247–N253.

[Silverstein et al., 2008] Silverstein, J. C., Parsad, N. M., and Tsirline, V. (2008). Automatic perceptual color map generation for realistic volume visualization. *Journal of Biomedical Informatics*, 41(6):927 – 935.

[Smith-Bindman et al., 2009] Smith-Bindman, R., Lipson, J., Marcus, R., Kim, K.-P., Mahesh, M., Gould, R., Berrington de González, A., and Miglioretti, D. L. (2009). Radiation Dose Associated With Common Computed Tomography Examinations and the Associated Lifetime Attributable Risk of Cancer. *Archives of Internal Medicine*, 169(22):2078–2086.

[Snyder and Miller, 1985] Snyder, D. L. and Miller, M. I. (1985). The use of sieves to stabilize images produced with the em algorithm for emission tomography. *IEEE Transactions on Nuclear Science*, 32(5):3864–3872.

[Snyder et al., 1987] Snyder, D. L., Miller, M. I., Thomas, L. J., and Politte, D. G. (1987). Noise and edge artifacts in maximum-likelihood reconstructions for emission tomography. *IEEE Transactions on Medical Imaging*, 6(3):228–238.

[Soleimani et al., 2006] Soleimani, M., Gómez-Laberge, C., and Adler, A. (2006). Imaging of conductivity changes and electrode movement in EIT. *Physiological Measurement*, 27(5):S103–S113.

[Soleimani and Lionheart, 2005] Soleimani, M. and Lionheart, W. R. B. (2005). Nonlinear image reconstruction for electrical capacitance tomography using experimental data. *Measurement Science and Technology*, 16(10):1987–1996.

[Soleimani and Lionheart, 2006] Soleimani, M. and Lionheart, W. R. B. (2006). Absolute conductivity reconstruction in magnetic induction tomography using a nonlinear method. *IEEE Transactions on Medical Imaging*, 25(12):1521–1530.

[Soleimani et al., 2007] Soleimani, M., Vauhkonen, M., Yang, W., Peyton, A., Kim, B. S., and Ma, X. (2007). Dynamic imaging in electrical capacitance tomography and electromagnetic induction tomography using a kalman filter. *Measurement Science and Technology*, 18(11):3287–3294.

[Somersalo et al., 1992] Somersalo, E., Cheney, M., and Isaacson, D. (1992). Existence and uniqueness for electrode models for electric current computed tomography. *SIAM Journal on Applied Mathematics*, 52(4):1023–1040.

[Stone, 1991] Stone, M. (1991). Imaging the tongue and vocal tract. *Br J Disord Commun*, 26(1):11 – 23.

[Svard et al., 2005] Svard, S. J., Hakansson, A., Backlin, A., Osifo, O., Willman, C., and Jansson, P. (2005). Nondestructive experimental determination of the pin-power distribution in nuclear fuel assemblies. *Nuclear Technology*, 151(1):70–76.

[T. Mull, 2004] T. Mull, B. Schoen, K. U. (2004). Final Report of the PKL Experimental Program within the OECD/SETH Project. *OECD / SETH*, FANP NGTT1/04/en/04.

[Takei, 2006] Takei, M. (2006). GVSPM image reconstruction for capacitance CT images of particles in a vertical pipe and comparison with the conventional method. *Measurement Science and Technology*, 17(8):2104–2112.

[Takiguchi, 2019] Takiguchi, T. (2019). Ultrasonic tomographic technique and its applications. *Applied Sciences*, 9(5).

[Teague, 2002] Teague, G. (2002). *Mass flow measurement of multi-phase mixtures by means of tomographic techniques.* University of Cape Town, Faculty of Engineering, Department of Electrical Engineering.

[Telford et al., 1976] Telford, W. M., Geldart, L. P., and Sheriff, R. E. (1976). Applied geophysics. *Geological Magazine*, 113(5):492–493.

[Tousignant et al., 1999] Tousignant, O., Hamel, L.-A., Dufour, P. C., Joly, F., Macri, J. R., McConnell, M. L., Ryan, J. M., and Jordanov, V. T. (1999). Energy and position resolution of a CdZnTe gamma-ray detector with orthogonal coplanar anodes. In James, R. B. and Schirato, R. C., editors, *Hard X-Ray, Gamma-Ray, and Neutron Detector Physics*, volume 3768, pages 38 – 48. International Society for Optics and Photonics, SPIE.

[Trakic et al., 2012] Trakic, A., Eskandarnia, N., Li, B. K., Weber, E., Wang, H., and Crozier, S. (2012). Rotational magnetic induction tomography. *Measurement Science and Technology*, 23(2):025402.

[Uecker et al., 2010] Uecker, M., Zhang, S., Voit, D., Karaus, A., Merboldt, K.-D., and Frahm, J. (2010). Real-time mri at a resolution of 20 ms. *NMR in Biomedicine*, 23(8):986–994.

[Utter and Lambeth, 2010] Utter, A. C. and Lambeth, P. G. (2010). A high-performance digital system for electrical capacitance tomography. *Medicine & Science in Sports & Exercise*, 42(2).

[Vallée et al., 2012] Vallée, C., Seidel, T., Lucas, D., Beyer, M., Prasser, H.-M., Pietruske, H., Schotz, P., and Carl, H. (2012). Counter-current flow limitation in a model of the hot leg of a pwr - comparison between air/water and steam/water experiments. *Nuclear Engineering and Design*, 245:113 – 124.

[Van Gompel et al., 2011] Van Gompel, G., Van Slambrouck, K., Defrise, M., Batenburg, K. J., de Mey, J., Sijbers, J., and Nuyts, J. (2011). Iterative correction of beam hardening artifacts in ct. *Medical Physics*, 38(S1):S36–S49.

[Vardi et al., 1985] Vardi, Y., Shepp, L. A., and Kaufman, L. (1985). A statistical model for positron emission tomography. *Journal of the American Statistical Association*, 80(389):8–20.

[Vauhkonen et al., 2001] Vauhkonen, M., Lionheart, W. R. B., Heikkinen, L. M., Vauhkonen, P. J., and Kaipio, J. P. (2001). A MATLAB package for the EIDORS project to reconstruct two-dimensional EIT images. *Physiological Measurement*, 22(1):107–111.

[Vauhkonen et al., 1998] Vauhkonen, M., Vadasz, D., Karjalainen, P. A., Somersalo, E., and Kaipio, J. P. (1998). Tikhonov regularization and prior information in electrical impedance tomography. *IEEE Transactions on Medical Imaging*, 17(2):285–293.

[Wagenknecht et al., 2013] Wagenknecht, G., Kaiser, H.-J., Mottaghy, F. M., and Herzog, H. (2013). Mri for attenuation correction in pet: methods and challenges. *Magnetic Resonance Materials in Physics, Biology and Medicine*, 26(1):99–113.

[Wang et al., 2005] Wang, B., Ji, H., Huang, Z., and Li, H. (2005). A high-speed data acquisition system for ECT based on the differential sampling method. *IEEE Sensors Journal*, 5(2):308–312.

[Wang et al., 2007] Wang, H., Lei, T., and Zhang, C. (2007). An image reconstruction algorithm based on total variation with adaptive mesh refinement for ect. *Flow Measurement and Instrumentation*, 18(5):262 – 267. Process Tomography and Flow Visualization.

[Wang et al., 2009] Wang, H., Xin, S., and Zhang, X. (2009). New progress of the digital electrical capacitance tomography system for gas/liquid two phase flow. In *2009 IEEE International Workshop on Imaging Systems and Techniques*, pages 37–40.

[Wang and Yang, 2010] Wang, H. and Yang, W. (2010). Measurement of fluidised bed dryer by different frequency and different normalisation methods with electrical capacitance tomography. *Powder Technology*, 199(1):60 – 69. Special Issue: Recent Advances in Fluid-Particle Systems.

[Wang, 2005] Wang, M. (2005). Seeing a new dimension—the past decade's developments on electrical impedance tomography. *Progress in Natural Science*, 15(sup1):1–13.

[Wang and Ma, 2006] Wang, M. and Ma, Y. (2006). Over-zero switching scheme for fast data collection operation in electrical impedance tomography. *Measurement Science and Technology*, 17(8):2078–2082.

[Wang et al., 2005] Wang, M., Yixin Ma, Holliday, N., Yunfeng Dai, Williams, R. A., and Lucas, G. (2005). A high-performance EIT system. *IEEE Sensors Journal*, 5(2):289–299.

[Warsito and Fan, 2001] Warsito, W. and Fan, L.-S. (2001). Neural network based multi-criterion optimization image reconstruction technique for imaging two- and three-phase flow systems using electrical capacitance tomography. *Measurement Science and Technology*, 12(12):2198–2210.

[Wei and Soleimani, 2012] Wei, H.-Y. and Soleimani, M. (2012). A magnetic induction tomography system for prospective industrial processing applications. *Chinese Journal of Chemical Engineering*, 20(2):406–410.

[Wi et al., 2014] Wi, H., Sohal, H., McEwan, A. L., Woo, E. J., and Oh, T. I. (2014). Multi-frequency electrical impedance tomography system with automatic self-calibration for long-term monitoring. *IEEE Transactions on Biomedical Circuits and Systems*, 8(1):119–128.

[Wilkinson et al., 2005] Wilkinson, A. J., Randall, E. W., Cilliers, J. J., Durrett, D. R., Naidoo, T., and Long, T. (2005). A 1000-measurement frames/second ERT data capture system with real-time visualization. *IEEE Sensors Journal*, 5(2):300–307.

[Wright et al., 2017] Wright, P., Basu, W., Lionheart, W., Crabb, M., and Green, P. (2017). Improved amplitude estimation of lung eit signals in the presence of transients: Experimental validation using discrete phantoms. In *Proceedings of the18th International Conference on Biomedical Applications of Electrical Impedance Tomography*, page 26.

[Wu et al., 1994] Wu, R.-S., Araujo, F. V., and Huang, L.-J. (1994). Multifrequency backscattering tomography for constant and vertically varying backgrounds. *International Journal of Imaging Systems and Technology*, 5(1):7–21.

[Xilinx325T Documentation, 2019] Xilinx325T Documentation (2019). *Kintex-7 FPGAs Data Sheet: DC and AC Switching Characteristics*.

[Yang et al., 2017a] Yang, L., Li, F., Xiong, Z., Shi, G., Niu, Y., and Li, R. (2017a). Single-shot dense depth sensing with frequency-division multiplexing fringe projection. *Journal of Visual Communication and Image Representation*, 46:139 – 149.

[Yang and Peng, 2002] Yang, W. Q. and Peng, L. (2002). Image reconstruction algorithms for electrical capacitance tomography. *Measurement Science and Technology*, 14(1):R1–R13.

[Yang et al., 1999] Yang, W. Q., Spink, D. M., York, T. A., and McCann, H. (1999). An image-reconstruction algorithm based on landweber's iteration method for electrical-capacitance tomography. *Measurement Science and Technology*, 10(11):1065–1069.

[Yang and Jia, 2017] Yang, Y. and Jia, J. (2017). A multi-frequency electrical impedance tomography system for real-time 2d and 3d imaging. *Review of Scientific Instruments*, 88(8):085110.

[Yang and Peng, 2013] Yang, Y. and Peng, L. (2013). A configurable electrical capacitance tomography system using a combining electrode strategy. *Measurement Science and Technology*, 24(7):074005.

[Yang et al., 2017b] Yang, Y., Peng, L., and Jia, J. (2017b). A novel multi-electrode sensing strategy for electrical capacitance tomography with ultra-low dynamic range. *Flow Measurement and Instrumentation*, 53:67 – 79. Process Tomography.

[Yorkey et al., 1987] Yorkey, T. J., Webster, J. G., and Tompkins, W. J. (1987). Comparing reconstruction algorithms for electrical impedance tomography. *IEEE Transactions on Biomedical Engineering*, BME-34(11):843–852.

[Zakaria et al., 2012] Zakaria, Z., Rahim, R. A., Mansor, M. S. B., Yaacob, S., Ayob, N. M. N., Muji, S. Z. M., Rahiman, M. H. F., and Aman, S. M. K. S. (2012). Advancements in transmitters and sensors for biological tissue imaging in magnetic induction tomography. *Sensors*, 12(6):7126–7156.

[Zhang and Soleimani, 2016] Zhang, M. and Soleimani, M. (2016). Simultaneous reconstruction of permittivity and conductivity using multi-frequency admittance measurement in electrical capacitance tomography. *Measurement Science and Technology*, 27(2):025405.

[Zhang et al., 2010] Zhang, X., Chen, S., Wang, H., and Zhang, Y. (2010). Fpga-based multi-frequency excitation and modulation technology in eit system. In *2010 3rd International Conference on Biomedical Engineering and Informatics*, volume 2, pages 907–911.

[Zhou and Li, 2017] Zhou, Y. and Li, X. (2017). A real-time EIT imaging system based on the split augmented Lagrangian shrinkage algorithm. *Measurement*, 110:27 – 42.

[Zhou et al., 2015] Zhou, Z., Dowrick, T., Malone, E., Avery, J., Li, N., Sun, Z., Xu, H., and Holder, D. (2015). Multifrequency electrical impedance tomography with total variation regularization. *Physiological Measurement*, 36(9):1943–1961.

[Zinan Liu et al., 2008] Zinan Liu, Zheng Xu, and Haijun Luo (2008). The application of magnetic sensor in mit. In *2008 World Automation Congress*, pages 1–4.

[Ziolkowski and Gratkowski, 2009] Ziolkowski, M. and Gratkowski, S. (2009). Weighted sum method and genetic algorithm based multiobjective optimization of an exciter for magnetic induction tomography. In *VXV International Symposium on Theoretical Engineering*, pages 1 – 5.